# Ultramafic Alteration and the Cooling of Earth and Mars

by

Joshua Murray

Submitted to the Department of Earth, Atmospheric, and Planetary Sciences
in partial fulfillment of the requirements for the degree of

DOCTOR OF PHILOSOPHY IN GEOLOGY

at the

MASSACHUSETTS INSTITUTE OF TECHNOLOGY

September 2024



Authored by: Joshua Murray
Department of Earth, Atmospheric, and Planetary Sciences
August 15, 2024

Certified by: Oliver Jagoutz
Professor of Geology, Thesis Supervisor

Accepted by: Robert van der Hilst
Schlumberger Professor of Earth and Planetary Sciences
Head of Department, Department of Earth, Atmopsheric, and Planetary Sciences

# Ultramafic Alteration and the Cooling of Earth and Mars

by

Joshua Murray

Submitted to the Department of Earth, Atmospheric, and Planetary Sciences
on August 15, 2024 in partial fulfillment of the requirements for the degree of

DOCTOR OF PHILOSOPHY IN GEOLOGY

## ABSTRACT

This thesis deals with the influence of 'ultramafic' rocks over the climate of planets. Ultramafic rocks, rich in Mg and Fe, are the most common rocks on Earth but exist primarily in the mantle and rarely outcrop on the surface. They are incredibly unstable under Earth's surface conditions where they are altered via incongruent reactions which form clay minerals, iron oxides, and ultimately release cations to the ocean. Due to their instability, they play an out-sized role in Earth's long-term carbon cycle. My first chapter investigates a hitherto unappreciated mechanism by which ultramafic rocks serve as a carbon sink, through the formation of high-surface-area clays and the resultant burial of organic carbon. I use a combination of mineral weathering models and proxy data to show that this mechanism has contributed to the glaciations of the Palaeozoic (541 - 252 Ma).

Unlike Earth, igneous rocks on the Martian surface are frequently of ultramafic composition. My second chapter argues that the alteration of these Martian ultramafic rocks was fundamental in the cooling of the planet from a habitable surface with liquid water to a cold and icy planet, largely devoid of an atmosphere. I show that the same high-surface-area clay minerals which bury organic carbon on Earth are prevalent enough on Mars to store the bulk of its initial 1-4 bar atmosphere as adsorbed methane. I postulate that this methane was formed abiotically during hydrothermal alteration of ultramafic rocks, a process which is observed in ultramafic systems on Earth. I show that this framework reconciles the histories of $\delta^{13}$C and atmospheric loss-to-space on Mars.

My final chapter quantifies the effects of the alteration of ultramafic and mafic rocks across the Taconic orogeny in Newfoundland, Canada. This collision exposed one of the most well-studied ultramafic bodies on Earth, the Bay of Islands ophiolite, and closely preceded global cooling in the Middle-Late Ordovician (470-445 Ma). I present a new method, leveraging both geochemical analysis and modelling of basin sediments, to infer ancient silicate weathering fluxes. I show that the relative weathering rate in this region increased dramatically during the Taconic orogeny. This method could be applied throughout systems with tectonically-driven changes in surface lithology to build a fuller understanding of the forces which modulate Earth's climate.

My work asks as many questions as it answers but tries to honestly portray the uncertainties associated with the application of quantitative methods in noisy, geologic systems. I hope that in trying to meaningfully constrain these processes I plant seeds of inquiry from which myself and others can one day make more concrete statements of the cause and effect between tectonics and climate.

Thesis supervisor: Oliver Jagoutz
Title: Professor of Geology

# Acknowledgments

I have needed to lean on many people and institutions in order to reach this point.

Oli Jagoutz gave me the tools and confidence to identify gaps in our collective knowledge and begin to fill them. His patience, particularly during a global pandemic, was not something I had earned but appreciate to this day. I hope to carry with me what I have learnt in field skills and scientific rigour as I plod onwards.

My time at MIT began with Kristin Bergmann's orientation class and a spring of sample dissolutions in David McGee's lab. I am grateful for the six years of conversations I have had since then with both Kristin and David. Seeing people care about fundamental science while caring about others is contagious and they have been fantastic role models for me. In addition, I'd like to thank my final committee member, Prof. Nicholas Tosca, for the time he has spent reading and giving feedback on this thesis as well as fielding my questions about clays through the years.

The multi-disciplinary nature of this work has meant I've needed to consult a range of experts outside of my committee. Those include Adam Jost, Dan Rothman, Mick Follows, Francis Macdonald, Greg Ravizza, Doug Reusch, and Edwin Kite.

The Jagoutz lab (sensu lato) was a perennially supportive environment for me. Emilie Bowman, Ben Klein, Hervé Rezeau, Cailey Condit, Claire Nichols, Amy Moser, Cameron Murphy, and Hongze Bo each taught me something new about the world and made me feel more at home in it. I'd especially like to thank Billy Shinevar, Craig Martin, and Zoe Molitor. The four of us still talk most days and my life is better for it.

They say the Green Building's architecture prevents community but in truth it cemented some lifelong friendships for me. Thank you to Diana Dumit, Joanna Millstein, and Noah Anderson for making life brighter: the dunkin coffees are on me, in perpetuity. Thank you to Julia Wilcots and Tristan Abott, the people whose company made me glad that landlords priced me out of a studio apartment. And thank you to Lily Sanborn. I could not have done this without her clever scientific eye, constant encouragement, and our weekend foraging adventures.

Outside of science, I would like to thank the friends, teammates, and co-coaches of the MIT ultimate team. In particular I'd like to thank Axis Sivitz, Miles Cruice-Barnett, Nic Arons, Henrik Boecken, and Richard Yip for helping me acclimate to the oddities of MIT. Additionally, I spent many summer evenings playing club ultimate with some mediocre teams and some great friends, especially Chris Haley and Drew Edwards whose camaraderie kept me afloat.

I am indebted to the Princeton Geosciences department (notably Blair Schoene and Adam Maloof) for inspiring this adventure. As well as other Princeton friends, Aqeel Phillips and

Nicolette D'Angelo, who supported my move to Boston and kept me sane(ish) throughout.

I have spent the last decade on the wrong side of the pond but try to carry a little Yorkshire with me. Jake Hawkyard and Georgie Millar showed me what friendship looks like and I struggle to replicate it when I am not visiting them. And of course I am forever grateful to my parents, Rachel and Ian, who took me outside at every opportunity and supported each of my endeavours. I promise to stop getting degrees now.

This PhD was fuelled by a combination of 9 Bar Espresso, Christina's Spice Shop, and Lumentation Film Lab. Its soundtrack was supplied by Adrienne Lenker, Christian Holden, Conor Oberst, Jake Ewald, Isaac Wood, Phoebe Bridgers, Robert Zimmerman, and Townes van Zandt, amongst others.

# Contents

# List of Figures

# List of Tables

# Chapter 1

# Palaeozoic cooling modulated by ophiolite weathering through organic carbon preservation

Published, *Nature Geosciences*. Murray and Jagoutz 2023

## 1.1 Abstract

Ophiolite obductions in the tropics are coeval with Phanerozoic glaciations. The exposure of mafic and ultramafic rocks is thought to trigger cooling by increasing global weatherability. However, each Palaeozoic icehouse also coincides with a $\delta^{13}C$ increase of 3 - 5‰, interpreted as an increase in organic carbon burial, not weatherability. Here we provide a framework that explains the tectonic forces behind Palaeozoic glaciations through increased organic carbon burial caused by the weathering of mafic and ultramafic lithologies in ophiolites. To evaluate the leverage ophiolite obduction has over organic carbon burial, we couple a mineral weathering model with a carbon box model. We show that the weathering of (ultra)mafic rocks can substantially enhance the preservation of organic carbon through the formation of high-surface-area smectite clays. The heightened organic carbon burial induced by an idealized ophiolite obduction causes ocean $\delta^{13}C$ to increase by ∼3.7‰. The temporal evolution and magnitude of our modelled $\delta^{13}C$ excursion approximates Palaeozoic records. We present an analysis of shale geochemistry, which shows a correlation between ultramafic provenance and total organic carbon. Our results indicate that high-surface-area clays, formed during

weathering of (ultra)mafic lithologies, exert a major control over Earth's long-term carbon cycle.

## 1.2 Introduction

Earth's climate is primarily controlled by the partial pressure of carbon dioxide ($pCO_2$) in the atmosphere (Owen et al. 1979). The major tectonic control(s) of Earth's on million-year timescales are volcanic outgassing (McKenzie et al. 2016), silicate weatherability (Kump et al. 1999) and/or organic carbon (OC) burial (Galy et al. 2007). The importance of mafic lithologies, uplift and local climate for chemical weathering has motivated recent studies that show a temporal coincidence between ophiolite obduction in the tropics and icehouse climates (Dessert et al. 2003; West et al. 2005; Jagoutz et al. 2016; Macdonald et al. 2019). These studies argue that the obduction of mafic and ultramafic rocks (rich in Ca and Mg) raises Earth's weatherability, augmenting the flux of alkaline-earth cations to the ocean and increasing carbonate precipitation for a given $pCO_2$.

The icehouse climates of the Palaeozoic era are characterized by positive excursions in records of $\delta^{13}C$, a signature of the enrichment of $^{13}C$ over $^{12}C$ (Methods). These records could be the result of weathering carbonate shelves following glacioeustatic marine regression (Kump et al. 1999). Alternatively, heightened OC burial could simultaneously explain both global cooling and positive $\delta^{13}C$ through a single feedback (Kump and Arthur 1999; Grossman et al. 2008a) but has not been causally linked to the obduction of mafic and ultramafic lithologies in the tropics during times of glaciation (Jagoutz et al. 2016; Macdonald et al. 2019).

Over 99.5% of all OC is degraded before it is buried below the upper reactive layer of marine sediment (Hedges and Keil 1995). The fraction that is preserved is protected from remineralization by adsorption on the surface of clay minerals and iron oxides. As such, mineral species with high specific surface area (SSA) provide greater protection (Lalonde et al. 2012; Hemingway et al. 2019). Shales rich in kaolinite, which has an SSA of 15 $m^2/g$,

have systematically lower total organic carbon (TOC) levels than those rich in smectite, which has an SSA of ∼800 $m^2/g$ (Kennedy et al. 2002) (Fig. 1.1e). As smectites are formed more readily under Mg-rich solutions and from Mg-rich bedrocks (Harder 1972; Nahon et al. 1982a; Brigatti and Poppi 1984; Obeso and Kelemen 2020), we outline a pathway by which (ultra)mafic rock exposures alter the long-term carbon cycle through enhanced OC preservation. We evaluate the effects of ophiolite-derived clays and subsequent OC burial, in tandem with increased weatherability, and reconcile Palaeozoic glaciations with changes in $\delta^{13}C$ and surface lithology.

## 1.3 Mineral weathering model

We present a simple model of clay formation through individual mineral weathering reactions. As fresh rocks are exposed on the surface, their constituent minerals chemically weather, first in situ and then during erosion and transportation to the continental shelf. The minerals formed during weathering and the rate of alteration depend upon the primary mineral, grain size, climate, microporosity and co-occurring mineralogy (Velde and Meunier 2008). However, the ratio between mineral weathering rates remains approximately constant (Velbel 1993). By using the most common reaction pathways and using relative reaction rates, we simplify weathering reactions of different lithologies to a tractable representation of clay formation (Methods).

We compiled the weathering reaction rates for eight common rock-forming minerals. Peridotite, gabbro and granite are treated as aggregates of their constituent minerals and serve as ultramafic, mafic and felsic endmembers, respectively. We tracked the mineralogy and SSA of each rock with increasing degree of chemical weathering, $\omega$, (Fig. 1.1). Results of our model show that ultramafic rocks, and to a lesser extent mafic rocks, rapidly form smectite clays from their Al-poor primary minerals, leading to peak SSA (250-775 $m^2/g$) sediments at $\omega = 10^{-3.6}$, before a decline in SSA as smectite is altered to silica and goethite with greater $\omega$ (Fig. 1.1). Felsic rocks weather more slowly due to their stable constituent

minerals, and the resulting kaolinite-rich sediment has low SSA (14-27 $m^2/g$), peaking around $\omega = 10^{4.4}$ before vermiculite weathers to kaolinite (Fig. 1.1).

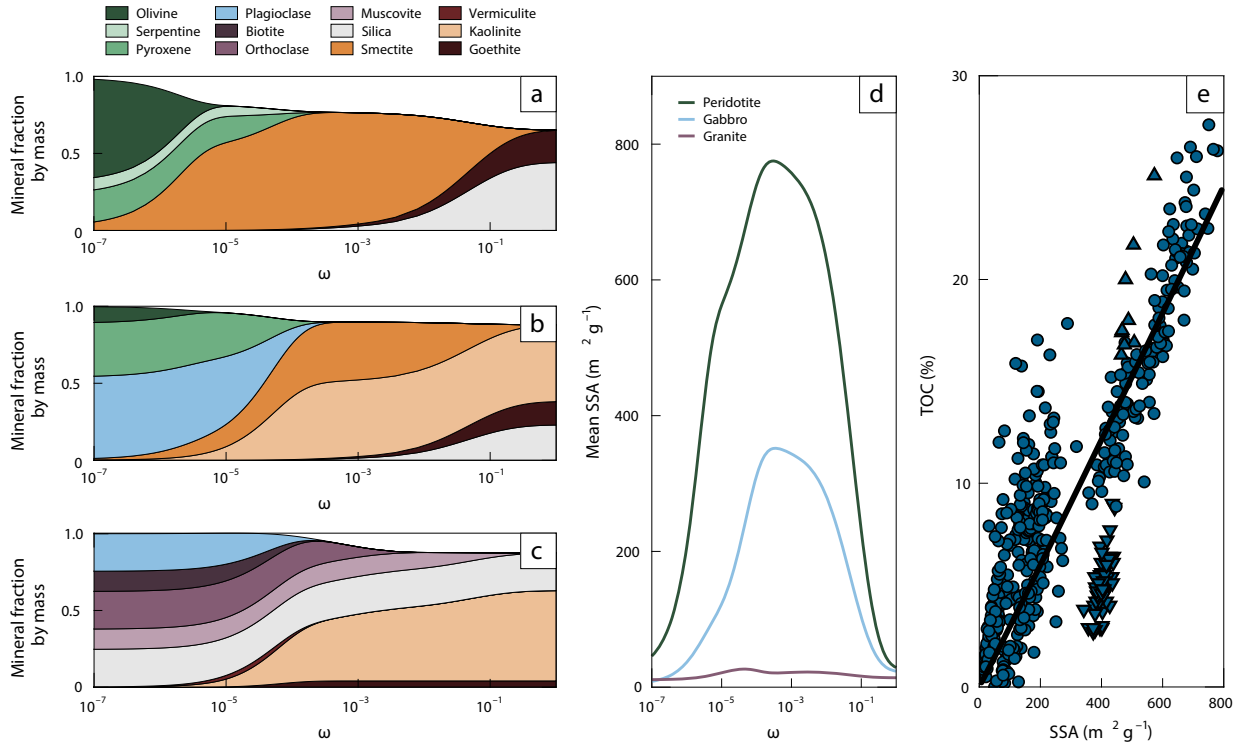


**Figure 1.1: a)**, Modelled weathering of peridotite (lherzolite) with 70% olivine, 20% pyroxene and 10% serpentine. **b)**, Modelled weathering of gabbro with 60% plagioclase, 30% pyroxene and 10% olivine. **c)**, Modelled weathering of granite with 25% plagioclase, 25% orthoclase, 12.5% muscovite, 12.5% biotite and 25% quartz. In panels a–c, mineral fraction is given as the fraction of the initial mass and progresses with increasing degree of weathering, $\omega$ (shown on a log scale). Relative weathering rates are given in Supplementary Table 1 (Methods). **d)**, SSA of the bulk rock in panels a–c as the weathering reaction progresses. **e)**, Compilation of SSA and TOC values. Downward-pointing triangles represent data in which the authors attribute TOC loss to bioturbation. Upward-pointing triangles represent data in which the authors document anoxia as contributing to high TOC values. The black line is a correlation consistent with monolayer equivalent adsorption of OC. We use this correlation to couple SSA to TOC (Methods). The same data are reproduced in Fig. 1.6 differentiated by the sample location.

## 1.4 Carbon box model

The empirical relationship between SSA and TOC (Fig. 1.1) provides a framework by which changes in lithology can force climate: mafic and ultramafic minerals create high-SSA clays that increase the preservation potential of OC. Irrespective of whether the OC is pedogenic or, more likely, marine in origin(Blattmann et al. 2019), its preservation in siliciclastic deposits

represents a transfer of carbon from the ocean-atmosphere system to the lithosphere. We adopt a linear function to describe the influence of changing SSA on OC preservation and proceed to model the carbon-cycle response to a change in surface lithology using a simple one-box model that couples the global fraction of exposed felsic, mafic and ultramafic rocks to clay mineralogy (Fig. 1.1), silicate weathering flux, OC burial, ocean phosphorus and $pCO_2$. We hold global sedimentation constant, and the silicate weathering flux refers to the mass of carbon sequestered as carbonates due to the chemical weathering of silicate minerals and the associated Ca and Mg released (Methods).

Ocean phosphorus is thought to play a critical role in OC burial through Earth history due to the limitations it places on primary productivity(Laakso and Schrag 2014). Over long timescales, if phosphorus is buried in organic matter according to the Redfield ratio, C/P of 106/1, OC burial cannot exceed the riverine flux of phosphorus, regardless of sedimentary SSA(Laakso and Schrag 2014). However, preferential recycling of phosphorus from the sediment back into the ocean has been well documented. In stratigraphic sections of organic-rich shales and anoxic conditions C/P ratios increase up to tenfold, including C/P in mineral-bound OC deposited during Ocean Anoxic Event 2 (Löhr and Kennedy 2014; Li et al. 2017; Beil et al. 2020; Percival et al. 2020). Our model treats buried C/P ratio as a function of phosphorus in the ocean, and we present model results with differing maximum burial values of C/P (Methods). Our model is not intended to fully recreate the complexities of the global carbon cycle, particularly the feedbacks that operate on short timescales, but rather to gauge the implications of increasing the fraction of siliciclastic sedimentation derived from mafic and ultramafic regions.

To approximate an ophiolite obduction, we forced the carbon box model by increasing the global surface fraction of ultramafic and mafic rocks by 0.5% each over 2 Myr from an initial 0% and 4%, respectively. This agrees with observed obduction length of 5,000 km and overthrust of 300 km (Jagoutz et al. 2016). The influence of different obduction lengths and ultramafic fractions over steady-state $\delta^{13}C$ and $pCO_2$is shown in Figs. 1.7 and 1.8. To simulate the period over which tectonic uplift is equal to erosion, we maintained the amount

of exposed ophiolite for 4 Myr, after which additional mafic and ultramafic lithologies decay exponentially (Fig. 1.2).

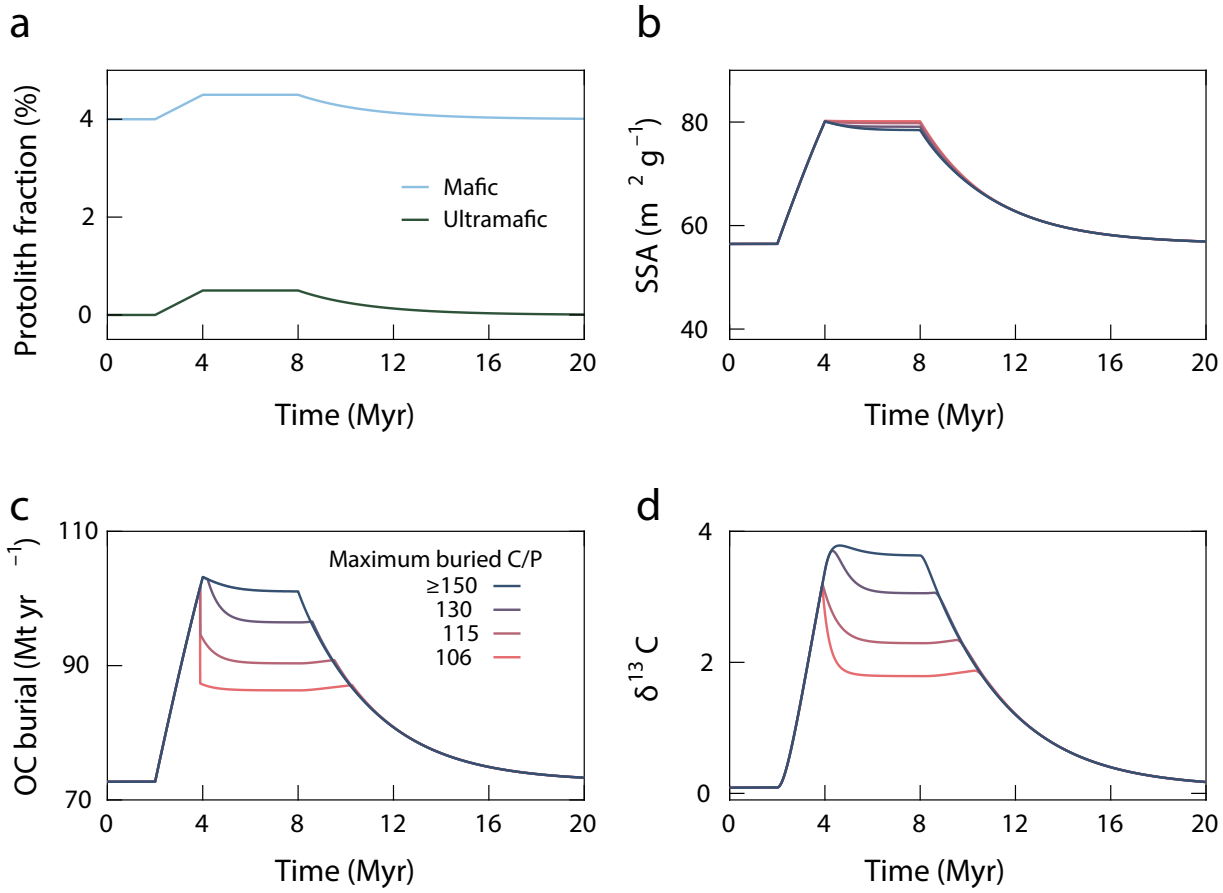


**Figure 1.2:** Line colour reflects maximum C/P ratio in buried sediment (Methods). **a)** Fractions of mafic and ultramafic lithologies on Earth's surface. Felsic lithologies provide the remaining percentage. **b)** Mean SSA of silicate weathering products. **c)** Change in OC burial as a result of the increased average SSA. **d)** Evolution of ocean $\delta^{13}$C as OC burial changes.

In our model, the emplacement of mafic and ultramafic rocks results in a 61% increase in the mean SSA of global sediment from 56 $m^2g^{-1}$ to 80 $m^2g^{-}1$ (Fig. 1.2). Assuming sufficient phosphorus recycling, the OC preservation associated with heightened SSA increases the OC burial flux from 73 MtC $yr^{-1}$ to 102 MtC $yr^{-1}$ (Fig. 1.2c). To reach steady state, decreases 3.7-fold (Fig. 1.9c) until the silicate weathering flux decreases from 127 Mt $yr^{-1}$ to 99 Mt $yr^{-1}$. This cooling lowers $\omega$ from $1.9 \times 10^4$ to $1.0 \times 10^4$, which has a minor influence over SSA (Fig. 1.2 and Fig. 1.9d). The OC burial causes a 3.7‰ positive $\delta^{13}$C excursion (Fig. 1.2d). Using a climate sensitivity of 3-4 °C (Sherwood et al. 2014) yields mean global cooling

of 6-8 °C, comparable to the changes observed at the initiation of icehouse climates (DeConto et al. 2008). Holding weatherability constant, making OC burial the sole driver of our carbon model, limits the decrease to 3.2-fold, corresponding to a 5-7 °C cooling (Fig. 1.10).

If phosphorus is not recycled, OC burial becomes phosphorus-limited 2 Myr after the onset of ophiolite obduction. This limitation is due to both a decrease in the riverine phosphorus flux as the silicate weathering flux decreases (Fig. 1.11) and an increase in OC burial (Fig. 1.2). In this scenario, OC burial is capped at 86 Mt yr-1 by the riverine phosphorus flux. The isotopic excursion remains similar in magnitude, reaching 3.6‰, but is truncated by the phosphorus limitation, causing a rapid decrease in $\delta^{13}C$ to 1.8‰. The change in atmospheric $pCO_2$ is limited to a 2-fold decrease, which is reflected in both the silicate weathering flux and the degree of weathering, $\omega$. We present intermediate values for maximum C/P of 106-150 in Fig. 1.2. For our obduction scenario, any buried C/P ratio greater than 142/1 yields identical model results for $\delta^{13}C$ and $pCO_2$ as the OC burial rate remains SSA-limited.

Alongside phosphorus, iron is thought to be a limiting nutrient in parts of the ocean(Moore et al. 2013). However, these elements are more abundant in mafic lithologies than in felsic lithologies. Average mafic phosphorus concentrations are 1.5-2.0 times those of felsic rocks while mafic and ultramafic iron concentrations are 3.6 and 5.3 times those of felsic rocks, respectively (Fig. 1.12). If scavenged in the nearshore environment, the high concentrations of essential nutrients in mafic rocks could serve to locally fertilize the ocean and further increase the burial of OC rather than limiting it. The impacts on the carbon cycle from combined ocean fertilization and OC preservation could be greater and more abrupt than is discussed herein.

## 1.5 Geologic and geochemical evidence

We compiled measured carbon isotopes across the four major Palaeozoic ice ages. The timing and extent of each glaciation is not well constrained (Methods) but is coeval with major ophiolite obductions (Macdonald et al. 2019) (Fig. 1.13). We found that ophiolite obductions

along longer suture zones coincide with greater $\delta^{13}C$ excursions (Fig. 1.3). We show representative $\delta^{13}C$ excursions from carbonate sections for the end-Ordovician, Frasnian–Famennian and end-Devonian in Fig. 1.3b. The isotopic evolution is comparable to that of our model results, showing a rapid increase, a prolonged high $\delta^{13}C$ state, before a more gradual decline (Fig. 1.3b). The end-Ordovician is well preserved in carbonate stratigraphy in Nevada, showing a singular plateau of 4‰ with a rapid onset and decrease (LaPorte et al. 2009b) (Fig. 1.3b). The Frasnian–Famennian record consists of the two positive excursions of the lower and upper Kellewasser (Buggisch and Joachimski 2006a) (Fig. 1.3b). The negative $\delta^{13}C$ shift between the lower and upper Kellewasser horizons is qualitatively similar to our phosphorus-limited model. The end-Devonian has been sampled extensively by drill cores in Iowa where it resembles the end-Ordovician excursion in both magnitude and shape (Stolfus et al. 2020a) (Fig. 1.3b). No single carbonate section captures the Permo–Carboniferous glaciation, which lasted at least 40 Myr and spanned multiple ophiolite obductions (Macdonald et al. 2019). As such, we derived the magnitude of the excursion from a $\delta^{13}C$ fossil compilation (Grossman et al. 2008a) and added a spline fit with a smoothing parameter of 0.1 (Fig. 1.13).

Isotopes of strontium and osmium have been used as proxies of silicate weathering. In both systems, mafic and ultramafic rocks are less radiogenic than their felsic counterparts with lower values of $^{87}Sr/^{86}Sr$ and $^{187}Os/^{188}Os$. Unfortunately, the Palaeozoic records of osmium are sparse, and those present are aliased due to their resolution being coarser than the ocean residence time of osmium (for example, (Finlay et al. 2010; Percival et al. 2019)). Because the concentration of Sr in mafic and ultramafic rocks is lower than in felsic lithologies, coupling our silicate weathering rates to Sr fluxes predicts a minor $^{87}Sr/^{86}Sr$ decrease from 0.7083 to 0.7080, substantially smaller than the Palaeozoic variations (Methods and Figs. 1.15 and 1.14). The change we infer from our model highlights the first-order control of strontium-rich continental rocks (Edmond 1992) and the inefficacy of $^{87}Sr/^{86}Sr$ as a diagnostic of ultramafic weathering. As Sr and Os weathering proxies are of limited use in evaluating our hypothesis, we used whole-rock geochemistry to assess the influence of ophiolite weathering

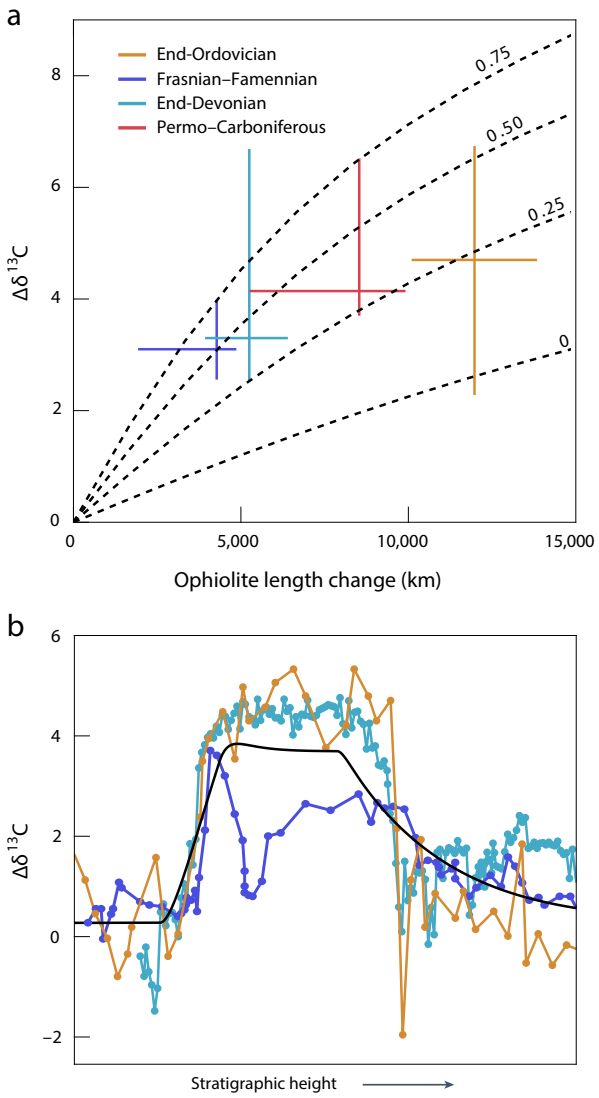


**Figure 1.3: a)** Magnitude of $\delta^{13}$C excursions ($\Delta\delta^{13}$C) and changes in ophiolite length across the four Palaeozoic glaciations. The coloured lines reflect 1 ranges of $\delta^{13}$C excursions and ophiolite length changes. The intersection of the lines represents the median $\delta^{13}$C excursion and ophiolite length change. Change in ophiolite length is derived from the sutures of ref. 8. Our compilation of $\delta^{13}$C excursions (Supplementary Table 5 and Methods) is used to constrain the magnitude of $\delta^{13}$C excursions across the end-Ordovician (n = 10), Frasnian–Famennian (n = 8) and end-Devonian (n = 10). The Permo–Carboniferous is not represented by a single stratigraphic section. Instead, we derive the size of the excursion from a comparison of brachiopod $\delta^{13}$C values at the onset of the excursion (n = 30) with $\delta^{13}$C values at the height of the excursion (n = 70) (ref. 10) (Methods and Fig. 1.13). Black dashed lines are our modelled changes in ocean $\delta^{13}$C as a function of the length and ultramafic fraction of the weathering ophiolite (0-0.75). **b)** Example $\delta^{13}$C isotope excursions from the end-Ordovician, Frasnian–Famennian and end-Devonian glaciations using the same colour scheme as panel a30,31,32. Overlain in black is the modelled isotopic excursion without phosphorus limitation (Fig. 1.2d).

over OC burial.

Our framework for lithologically induced glaciations makes a clear prediction for the

sedimentary rock record: sediments dominantly sourced from (ultra)mafic rocks should, on average, have higher TOC than those derived from felsic lithologies. Chromium has long been used as a tracer of ultramafic provenance in sedimentary rocks (Hiscott 1984a; Garver et al. 1996) given its high concentration in the upper mantle (Workman and Hart 2005) and relative immobility during weathering (Viers et al. 2009). We examined the geochemistry of 7,820 shales, mudstones, and siltstones of the Sedimentary Geochemistry and Paleoenvironments Project (SGP) for which Cr, $Al_2O_3$ and TOC data are present (Farrell et al. 2021). We used Cr/Al ratios to remove the diluting effect of carbonate minerals. After discretizing the data, we observed a systematic increase in the median and range of shale TOC with increasing Cr/Al ratio (Fig. 1.4a and Methods). We then inspected the temporal variation in Cr/Al of the same SGP samples through the Phanerozoic and showed the heightened occurrence of high-Cr/Al samples during periods of glaciation (Fig. 1.4b). Median Cr/Al is 1.4 times greater, and the Cr/Al at the 97.5th percentile ($2\sigma$) is 4.2 times greater in shales deposited during glaciations compared with shales of warmer periods. Given its short 8 kyr residence time in the ocean (Broecker and Peng 1982), the Cr is probably derived from a proximal source rock, eroding essentially contemporaneously. The same trend is observed in Co/Al and Ni/Al, both insoluble trace elements that are concentrated in mantle peridotites relative to the continental crust (Fig. 1.16). While the concentration of these elements in shales is additionally influenced by redox conditions and organic complexation, the fact that all three elemental ratios show similar trends supports our interpretation of an ultramafic signature. This correlation could be further bolstered by analysis of organo–mineral interfaces in Plio–Pleistocene sediments where an increase in detritus from the ultramafic terranes of the Southeast Asian islands $\sim$ 4 million years ago is concurrent with an increase in TOC from 0.2–0.5 wt% to 1.0–1.8 wt% (Rosenthal et al. 2018; Bayon et al. 2023).

A TOC value greater than 15%, as observed in Fig. 1.4a, may be greater than can be adsorbed to mineral surfaces and requires a combination of both high SSA and an anoxic environment (Kennedy and Wagner 2011). Even ignoring those data exceeding 15 wt%

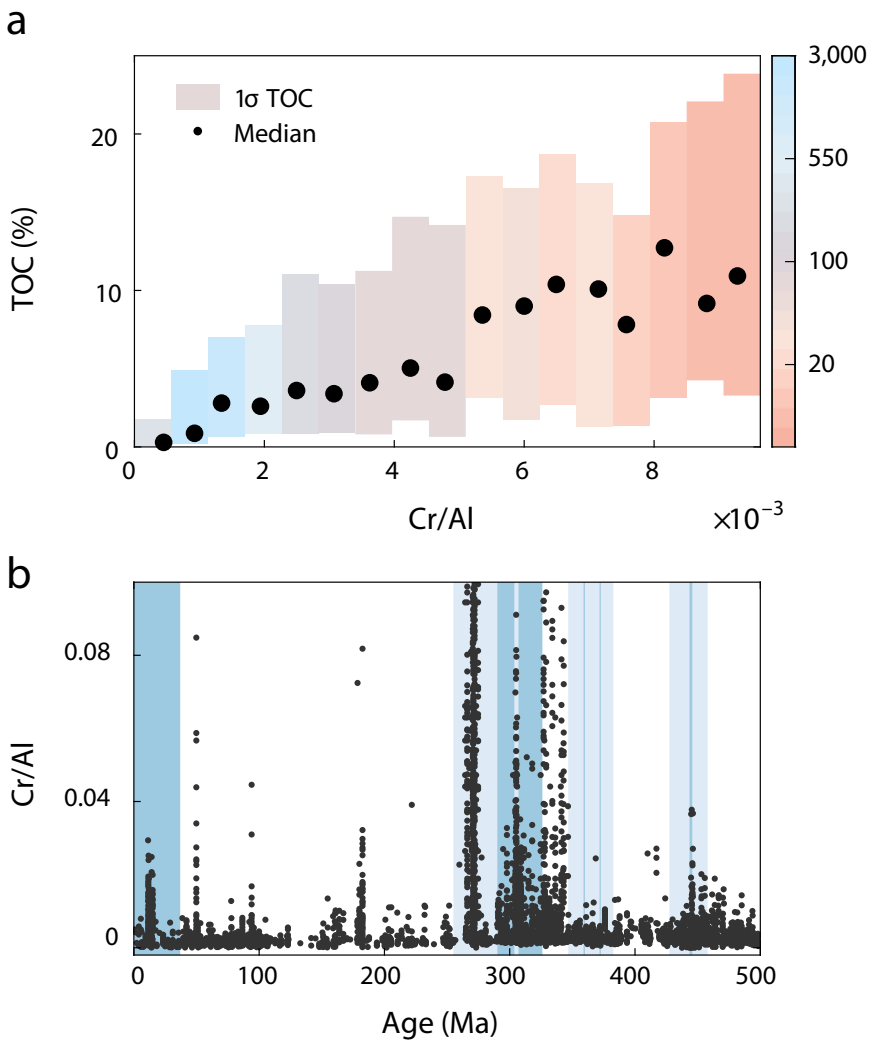


**Figure 1.4: a)** Binned mean and standard deviation of SGP samples: horizontal axis is the ratio of Cr/Al, vertical axis represents TOC. Coloured boxes represent the single standard deviation of TOC for a given Cr/Al binned range. Black points show the median within the given bin. The colour of each rectangle denotes the number of samples contributing to the mean and standard deviation. At Cr/Al values exceeding 102, the data are sparse and the relationship breaks down. This is probably caused by sorting, which concentrates chromite in coarser, clay-poor sediments. **b)** Cr/Al of SGP samples through the Phanerozoic overlain on Phanerozoic glaciations. Dark blue bars show short endmember chronologies of glaciation; pale blue bars show prolonged endmember chronologies (Methods and Supplementary Table 3). Data continue above the limits of the y axis, particularly around the Permo–Carboniferous.

TOC, the sedimentary geochemistry supports the observation that the shales with a larger ultramafic component, on average, preserve a greater fraction of OC and that those shales occur more frequently during glacial periods (Fig. 1.4 and 1.16).

Alongside the geochemical correlation in Fig. 1.4, we see evidence of ultramafic detritus (notably Cr-spinel) and slab break-off closely preceding each Palaeozoic glaciation (Figs.

1.17, 1.18, and 1.19). Although Cr-spinel provides direct evidence of ophiolite weathering, slab processes may be governing the transport of high-SSA clays. While we treat $\omega$ as a global value, dependent upon only temperature, $\omega$ is high in areas with high chemical-weathering rates and low erosion rates, where thick regoliths develop and smectite clays are further altered into iron oxides (Nahon et al. 1982a; Dessert et al. 2003). Slab break-off would cause rapid uplift, enhanced erosion, lower $\omega$ and an increase in high-SSA sedimentation. The positive feedbacks among uplift, weathering and erosion may cause punctuated cooling on timescales much faster than plate convergence.

In summary, through the framework of OC burial, we reconcile the theory of ophiolite-induced cooling with carbon isotope excursions across Palaeozoic glaciations. Our model calculations, the $\delta^{13}$C isotopic record and shale geochemistry all provide evidence to support the hypothesis that OC preservation by high-SSA clays is a major pathway by which ophiolite obduction disrupts the carbon cycle. The influence of tectonically driven clay formation and subsequent increased OC preservation could extend far beyond Phanerozoic and be relevant for ocean anoxia, great oxidation event(s), and the initiation of snowball Earth (Schrag et al. 2002; Kennedy et al. 2006; Percival et al. 2020).

## 1.6 Methods

### 1.6.1 Mineral weathering

The weathering of igneous minerals is simplified to a balanced chemical equation from primary mineral to its most common weathering product. We allow the secondary mineral to further weather if those reactions are commonly reported. Those reactions are listed below:

**Olivine**

$$8\,Mg_2SiO_4 + 2\,(Al_3{}^+, Fe_3{}^+) + 26\,H^+ \longrightarrow \tag{1.1}$$

$$Mg_{2.66}(Al, Fe)_2Si_8O_{20}(OH)_4 + 13.33\,Mg^{2+} + 8\,H_2O + 6\,H^+ \longrightarrow \tag{1.2}$$

$$2\,(Al, Fe)O(OH) + 8\,SiO_2 + 16\,Mg^{2+} + 12\,H_2O \tag{1.3}$$

$$\text{Olivine} + \text{Trivalent cation} + \text{Protons} \longrightarrow \tag{1.4}$$

$$\text{Mg-Smectite} + \text{Magnesium Ions} + \text{Water} + \text{Protons} \longrightarrow \tag{1.5}$$

$$\text{Goethite/Boehmite} + \text{Silica} + \text{Magnesium Ions} + \text{Water} \tag{1.6}$$

The weathering products of olivine are modulated not only by the composition of the primary mineral, but also by the aqueous chemistry of the groundwater (Delvigne et al. 1979). In the presence of sufficient trivalent cations, a magnesium smectite is produced (Delvigne et al. 1979; Chesworth et al. 2004; Wilson 2004). In purely ultramafic exposures where aluminium is absent, olivine can alter to talc (Noack and Duplay 1983). Any fayalite component of the olivine can be weathered to goethite after the complete dissolution of silica and magnesium, sometimes via an intermediate smectite phase and/or the precipitation of amorphous silica (Nahon et al. 1982b; Velde and Meunier 2008). Our model assumes olivine alteration occurs in the presence of adequate amounts of $Al^{3+}$ or $Fe^{3+}$, either through the local mineral assemblage or through groundwater enriched by nearby lithologies, to produce magnesian smectite. The complete dissolution of magnesium then leads to a final product

of iron (or aluminium) oxyhydroxide with amorphous silica.

**Serpentine**

$$4\,Mg_2FeSi_2O_5(OH)_4 + 12\,H^+ \longrightarrow \tag{1.7}$$

$$Mg_{0.3}Fe_3MgSi_8O_{20}(OH)_4 + 11\,H_2O + Fe^{3+} + 6.7\,Mg^{2+} \longrightarrow \tag{1.8}$$

$$4\,FeO(OH) + 8\,SiO_2 + 8\,Mg^{2+} + 12\,H_2O \tag{1.9}$$

$$\text{Serpentine (Antigorite)} + \text{Water} \longrightarrow \tag{1.10}$$

$$\text{Fe-montmorillonite} + \text{Iron Ion} + \text{Magnesium Ion} \longrightarrow \tag{1.11}$$

$$\text{Goethite} + \text{Silica} + \text{Magnesium Ion} + \text{Iron Ion} + \text{Hydroxyl Ion} \tag{1.12}$$

Given that many ultramafic rocks are hydrothermally altered prior to surface exposure, we also include the weathering of serpentine in our model. Caillaud et al. 2006 studied the alteration of serpentine in detail and found different smectite clays are formed based upon the crystal habit, and hence microporosity, of the primary mineral. Given our focus on OC protection, we treat the two smectites interchangeably as a single Al-poor, Fe-rich montmorillonite. In a similar fashion to olivine, further weathering results in the formation of iron oxides (maghemite, goethite, or haematite), which we treat as goethite for simplicity (Caillaud et al. 2006). Chlorite can be produced alongside serpentine either during weathering or low temperature hydrothermal alteration (Brigatti and Poppi 1984). The subsequent weathering of chlorite is complex, forming either interlayered smectite, vermiculite, or kaolinite prior to goethite (Brigatti and Poppi 1984; Aspandiar and Eggleton 2002).

**Pyroxene**

$$4\,MgFeSi_2O_6 + 4\,H^+ + H_2O \longrightarrow \tag{1.13}$$

$$Mg_{0.3}Fe_4Si_8O_{20}(OH)_4 + 3.7\,Mg^{2+} \longrightarrow \tag{1.14}$$

$$4\,FeO(OH) + 8\,SiO_2 + 4\,Mg^{2+} + nH_2O \tag{1.15}$$

$$\text{Hypersthene} + \text{Water} \longrightarrow \tag{1.16}$$

$$\text{Fe-Smectite} + \text{Iron Ions} + \text{Magnesium Ions} \longrightarrow \tag{1.17}$$

$$\text{Goethite} + \text{Silica} + \text{Magnesium Ion} + \text{Water} \tag{1.18}$$

We base our pyroxene alteration reaction upon the work of (Eggleton 1975). Smectite (usually the Fe-rich nontronite) is the dominant product of the weathering of both orthopyroxene and clinopyroxene (Pion 1979; Nahon et al. 1982b; Delvigne 1983; Banfield et al. 1991). Further alteration can convert pyroxene-derived smectites to talc (Eggleton and Boland 1982). Alternatively, vermiculite and goethite have been reported in some cases (Basham 1974). Again, we adopt the most commonly reported secondary mineral, smectite, as our first modelled product. The pyroxene-derived smectites usually co-occur with iron oxide minerals which we treat as the final weathering product of the reaction (Delvigne 1983; Banfield et al. 1991).

**Plagioclase feldspar**

$$CaAl_2Si_2O_8 + H_2O + 2\,H^+ \longrightarrow Al_2Si_2O_5(OH)_4 + Ca^{2+} \tag{1.19}$$

$$\text{Anorthite} + \text{Water} + \text{Protons} \longrightarrow \text{Kaolinite} + \text{Calcium Ion} \tag{1.20}$$

The dissolution of plagioclase feldspar occurs almost an order of magnitude faster than potassium feldspar (Siegel and Pfannkuch 1984). Multiple aluminous secondary phases have been documented including gibbsite, allophane, and smectite (Eswaran and Bin 1978; Anand

et al. 1985; Banfield et al. 1991). However, we assume a weathering product of kaolinite which aligns with the majority of field results (Delvigne and Martin 1970; Robertson and Eggleton 1991; Sheet and Tettenhorst 1997).

**Biotite**

$$\mathrm{KMgFe_2AlSi_3O_{10}(OH)_2 + 4\,H_2O + 5\,H^+ \longrightarrow} \tag{1.21}$$

$$\mathrm{MgFe_2AlSi_3O_{10}(OH)_2 + K^+ + 5\,H^+ \longrightarrow} \tag{1.22}$$

$$\mathrm{FeAlSi_2O_5(OH)_4 + FeO(OH) + K^+ + Mg^{2+} + Si^{4+} + 5\,H_2O} \tag{1.23}$$

$$\mathrm{Biotite + Water + Protons \longrightarrow} \tag{1.24}$$

$$\mathrm{Vermiculite + Ion + Proton \longrightarrow} \tag{1.25}$$

$$\mathrm{Kaolinite + Goethite + Ions + Water} \tag{1.26}$$

Biotite weathering is the earliest visible alteration in most granites where cleavage planes and fractures provide access for water which strips potassium ions from the interlayer sites creating expandible vermiculite (Coleman et al. 1963). Subsequent leaching of the octahedral and tetrahedral sites leads to the formation of kaolinite (Gilkes and Suddhiprakarn 1979; Meunier and Velde 1979). While direct weathering of biotite to kaolinite has been observed, we model the weathering as a piecewise reaction with equal weathering rates.

**Potassium feldspar**

$$\mathrm{KAlSi_3O_8 + 0.5\,H_2O + H^+ \longrightarrow 0.5\,Al_2Si_2O_5(OH)_4 + K^+ + 2\,Si^{4+} + 2\,O_2} \tag{1.27}$$

$$\mathrm{Orthoclase + Water + Protons \longrightarrow Kaolinite + Ions + Oxygen} \tag{1.28}$$

Potassium feldspar is leached less readily than the sodium or calcium of plagioclase which leads to a slower alteration rate. The weathering of potassium feldspar to kaolinite is the canonical mineral alteration reaction and is well documented (Eswaran and Bin 1978;

Anand et al. 1985; Banfield and Eggleton 1990; Sheet and Tettenhorst 1997). The single-phase product is, however, an oversimplification which we perpetuate. Gibbsite, allophane, and smectite have been noted in conjunction with kaolinite (Eswaran and Bin 1978; Anand et al. 1985; Banfield and Eggleton 1990).

**Muscovite**

$$2\,KAl_3Si_3O_{10}(OH)_2 + H_2O + O_2 \longrightarrow 3\,Al_2Si_2O_5(OH)_4 + K^+ \tag{1.29}$$

$$\text{Muscovite} + \text{Water} + \text{Oxygen} \tag{1.30}$$

Muscovite reactions proceed more slowly than those of biotite (Kalinowski and Schweda 1996). The hydration and leaching of potassium ions leads to the formation of kaolinite. Some vermiculite is observed (e.g., Meunier and Velde 1979) however kaolinite is the most stable and abundant weathering product (Banfield and Eggleton 1990; Robertson and Eggleton 1991; Singh and Gilkes 1991).

### 1.6.2 Treatment of weathering

We treat quartz, kaolinite and goethite as stable. In nature, weathering reactions are more complicated than represented here. For example, clays formed in weathering ophiolites can be found as purely smectite (often stevensite or montmorillonite; (Nahon et al. 1982a)) however, chlorite can be found interlayered with smectite, potentially formed during hydrothermal processes or as an intermediate weathering product (Brigatti and Poppi 1984). To consider siliciclastic mineralogy on a global scale, we idealize the weathering of each mineral independently and ignore the influence of co-occurring species. We use chemical compositions to convert modal abundances to mass fractions (Fig. 1.1).

Weathering rates depend not only on the mineralogy but also on climate and physical erosion rates. Fortunately, the ratio of weathering rates between different minerals has been shown to be broadly constant across laboratory and field experiments (Velbel 1993),

allowing us to simplify our model and use only relative weathering rates. The ratio of mineral alteration rates is given in Table A.1. Our weathering model follows the progression of alteration reactions from primary to secondary (and tertiary where necessary), where the rate of the alteration of mineral A to mineral B is proportional to the inverse square root of the mean age of the reactant mineral (Lasaga 1984):

$$dC_b/dt \propto k_a C_a \omega_a^{-1/2} \tag{1.31}$$

where $k_a$ is the rate ratio of mineral A (Table A.1), $\omega$a is the normalized age of mineral A, $C_a$ is the fraction of mineral A present in the rock. We model the reaction numerically, updating the ages and concentrations of minerals A and B (and C where necessary). Because the weathering rates are constructed relative to one another and are not absolute, $\omega$ reflects a normalized age such that by $\omega = 1$, all reactions are complete and only silica, kaolinite, and goethite remain (Fig. 1.1); $\omega$ also serves as the degree of weathering in our carbon model (Eq. 1.40 and 1.42).

We apply our weathering model to three igneous rock compositions: ultramafic, mafic and felsic. The mineralogy of those initial, igneous compositions is given in Table A.2. Mineral abundances are given as modal abundance and converted to mass to show chemical depletion. We then convert mass to SSA by the values in Table A.2. Primary minerals are assigned an SSA of 0.1 $m^2/g$ except for serpentine, which is 8 $m^2/g$ (Crespo et al. 2019), and muscovite, which has an illite SSA of 80 $m^2/g$ (Young 2012).

### 1.6.3 SSA-TOC relationship

To couple SSA to TOC, we derived an empirical relationship between the two. We compiled 483 analyses of both SSA and TOC in shales across four continents (Table A.6). Only those studies that used ethylene glycol monoethyl ether for SSA analyses were selected due to the ability of both internal and external surface area to preserve organic carbon. We seek a best-fit function of the form:

$$TOC = a \cdot SSA^b \tag{1.32}$$

However, $b$ is close to 1 for most fit parameters, and as such we simplify our idealized relationship to a proportionality:

$$TOC = a \cdot SSA \tag{1.33}$$

The value of $a$ is derived by a weighted linear regression of the SSA and TOC values in Table A.6. Weights are proportional to the sum of the normalized Euclidean distances between the sample point and all other points (eq. 1.34).

$$w_i = \sum \sqrt{\frac{{toc_i - toc_j}^2}{\overline{toc}} + \frac{{ssa_i - ssa_j}^2}{\overline{ssa}}} \tag{1.34}$$

This yields $a = 0.0306$ g/m$^2$, giving a function that maps from sediment SSA to TOC. This relationship is consistent with preservation approximately equivalent to monolayer loading of TOC on clays (Hedges and Keil 1995; Kennedy et al. 2002). We show the data and best-fit line in Fig. 1.1e. We explore the dependence on our SSA–TOC relationship in Fig. 1.20 using values of coefficients $a$ and $b$.

While mineral protection is a major control on OC burial on the continental margin (Hedges and Keil 1995; Kennedy et al. 2002; Hemingway et al. 2019), treating TOC solely as a function of SSA is an oversimplification. We ignore here the effects of temperature, sedimentation rate and bottom-water oxygen concentration. High sedimentation rates can lower the time over which OC is exposed to oxygen, increasing preservation (Hedges and Keil 1995). Similarly, ocean anoxia can reduce remineralization rates and raise TOC concentrations above monolayer equivalent values (Kennedy and Wagner 2011). The effects of temperature on OC preservation may be a feedback that is not represented within our model. Cooling increases the solubility of oxygen within water, which could serve as a negative feedback by increasing remineralization rates at higher dissolved oxygen levels. Alternatively,

respiration reactions slow considerably with lower temperature, which may act as a positive feedback. Our model serves only to isolate the effect of clay mineralogy and SSA over Earth's climate, rather than act as a complete model for sedimentation, ocean chemistry, redox and preservation on the continental margin.

We investigate the magnitude of changes induced by SSA-driven OC preservation using a simple one-box model that couples the global fraction of exposed felsic, mafic and ultramafic rocks to clay formation, silicate weathering and $p\mathrm{CO}_2$. The formation of clays is governed by the preceding descriptions while all other relationships are simplified to power laws or Arrhenius relationships.

### 1.6.4 Carbon box model

Our model follows the work of Kump and Arthur 1999. The evolution of the mass of C in the ocean–atmosphere system, $M_c$, is a balance of influxes and outfluxes:

$$\Delta M_c/\Delta t = F_v - F_{sw} - F_{org} \tag{1.35}$$

where $F_v$ is the flux of C from volcanic outgassing, metamorphic $CO_2$ release and organic carbon/pyrite weathering. Today, this value is poorly constrained. We choose 200 Mt/yr (for example, Berner et al. 1983; Burton et al. 2013; Soulet et al. 2021).

$F_{sw}$ is the flux of C from ocean–atmosphere to lithosphere due to the precipitation of carbonate minerals from silicate-derived cations. $F_{sw}$ is a function of both lithology and according to eq. 1.36:

$$F_sw = k_{sw} \cdot \lambda \cdot p\mathrm{CO}_2^{\beta} \tag{1.36}$$

where,

$$\lambda = \text{weatherability} = p_f + 3.1p_m + 8.1p_u \tag{1.37}$$

where $p_f$, $p_m$, $p_u$ = protolith fraction of felsic, mafic and ultramafic rock, respectively; $\beta$ = silicate weathering exponent = 0.22 (Berner et al. 1983); $k_{sw}$ = 25 Mt/yr; $k_{sw}$ is chosen such that $F_{sw} \approx 0.65\ F_v$ at pre-industrial conditions of $p\mathrm{CO}_2$= 280 ppm and $\lambda = 1.06$.

Calculating $p\mathrm{CO}_2$ requires assumptions about carbonate saturation in the ocean. Over the long timescales we consider here, we treat the sum of ocean [Mg] + [Ca] to be constant and assume that $M_c$ is dominantly $\mathrm{HCO}_3$. Given the residence time of Mg in the ocean is ∼13 Myr, these simplifications are reasonable. However, our estimated changes in $p\mathrm{CO}_2$ should be treated as approximations.

$$p\mathrm{CO}_2 = 280\mathrm{ppm} \cdot \left(\frac{M_c(t)}{M_c(0)}\right)^2 \tag{1.38}$$

Where $M_c(0)$ is the mass of carbon in the modern ocean–atmosphere system, 38,600,000 Mt (Kump and Arthur 1999).

$F_{org}$ is the burial of organic carbon, calculated according to equations 1.39–1.42. We consider only the sediments delivered to the continental margin and deltaic regions. $F_{org}$ can be limited either by the supply of mineral surfaces or by the supply of phosphorus to the ocean, and we use the minimum of those two constraints in calculating $F_{org}$.

Today, two-thirds of modern sediment delivery is from the mafic, tectonically active regions that constitute southeast Asia and Oceania (Milliman and Farnsworth 2013), suggesting that ophiolite obduction would increase global sedimentation rates. Conservatively, we assume that while the SSA of sediment changes, the total sediment flux remains constant. Similarly, we take $\omega$ to reflect mean global climate. In areas with high degrees of chemical weathering and low physical erosion rates, $\omega$ may be far greater than the global value, moving past $\omega = 10^{3.6}$, at which point SSA and OC burial would begin to decrease, limiting the effect of obduction (Fig. 1.1 and 1.6). Our model results do not reflect the increased local weathering in the warm, rainy tropics compared with higher latitudes (Kent and Muttoni 2013), and the outsized importance of tropical lithologies is not incorporated (Kent and Muttoni 2013; Jagoutz et al. 2016; Macdonald et al. 2019).

$$F_{os} = d \cdot F_{sed} \cdot \text{TOC}/100 \tag{1.39}$$

$$\text{SSA} = p_f \cdot G_s(\omega) + 3.1 \cdot p_m \cdot B_s(\omega) + 8.1 \cdot p_u \cdot P_s(\omega) \tag{1.40}$$

$$F_{op} = 12 \cdot M \cdot \frac{C/P}{31} \tag{1.41}$$

where,

$F_{sed}$ = global sediment flux = $14,030$Mt/yr($SyvitskiEtal.2005$)

$d$ = nearshore/deltaic fraction of sediment flux = 0.3($KuehlEtal.2005$)

$F_{os}$ = SSA-limited OC burial

$F_{op}$ = phosphorus-limited OC burial

$M_p$ = mass of available phosphorus in the ocean

$G_s$, $B_s$ and $P_s$ are the numerical functions derived from mineral weathering laws that relate $\omega$ to SSA as described in the preceding and shown in Fig. 1.1d. TOC is linked to SSA via equation (1.32). The values of 3.1 and 8.1 that appear in equations 1.37 and 1.40 parameterize the silicate weathering rates of mafic and ultramafic rocks, relative to felsic rocks, derived from the molar abundance of Ca and Mg (Rudnick and Gao 2003; Workman and Hart 2005; Gale et al. 2013). The constants 12 and 31 reflect the molar mass of carbon and phosphorus, respectively; $\omega$ is coupled to climate by the Arrhenius relationship (eq. 1.42), and temperature is approximated by a climate sensitivity equation (eq. 1.43) (Arrhenius 1896; West et al. 2005; Sherwood et al. 2014).

$$\omega = \omega_0 e^{-\frac{E_a}{R}\left(\frac{1}{T}-\frac{1}{T_0}\right)} \tag{1.42}$$

$$T = T_0 + S \cdot log_2\left(pCO_2/pCO_2(0)\right) \tag{1.43}$$

where $S$ = climate sensitivity = 3 K (Sherwood et al. 2014); $T_0$ = pre-industrial average temperature = 298 K; $pCO_2(0)$ = pre-industrial $pCO_2$= 280 ppm; $E_a$ = activation energy = 74.9 kJ (West et al. 2005); $R$ = gas constant = 8.314 kJ/K/mol; $\omega_0$ = reference weathering degree = $10^{\breve{}4}$. We constrain $\omega_0$ by compiling mineralogy from over 55,000 Deep Sea Drilling Project (DSDP) smear slides. By taking the mean modal mineralogy, we find that the terrigenous portion consists primarily of clays, silica, feldspar and iron oxides (Fig. 1.5). The presence of 7.5% feldspar and 0.5% pyroxene places $\omega_0$ between $10^5$ and $10^3$. We use $10^4$ for the results presented in Fig. 1.2 and present a sensitivity test in Fig. 1.20.

$M_P$ is modelled similarly to $M_C$ (eq. 1.35) but governed only by the riverine flux, $F_{P_{SW}}$, and OC burial divided by the buried C/P ratio.

$$F_{P_{SW}} = 0.7 \cdot F_{sw} \cdot (31/12) \cdot (p_f \cdot 0.01111 + p_m \cdot 0.0071 \cdot 3.1 + p_u \cdot 0.00069 \cdot 8.1)/\lambda \tag{1.44}$$

$$F_{P_{OC}} = F_{org}/(C/P) \cdot 31/12 \tag{1.45}$$

$$(C/P) = 106 + (C/P_{max} - 106) \cdot e^{-20\frac{M_P}{M_P(0)}} \tag{1.46}$$

The factor of 0.7 in eq. 1.44 reflects the fraction of riverine phosphorus that is bioavailable (for example, (Pacini and Gächter 1999; Stepanauskas et al. 2002)); the constants 0.0111, 0.0071 and 0.00069 are the molar ratios of P to Ca + Mg in felsic, mafic and ultramafic rocks, respectively; and e is Euler's number. In Fig. 1.2, we vary $C/P_{max}$. The value –20 in eq. 1.46 is a decay constant designed to maintain the Redfield ratio outside of very low values of $M_P$ (Fig. 1.22). $M_P(0)$ is set as $1.2 \cdot 10^5$, derived from a steady-state OC burial of 70 Mt/yr and a residence time of 69,000 yr (Broecker and Peng 1982). Given our model's lack

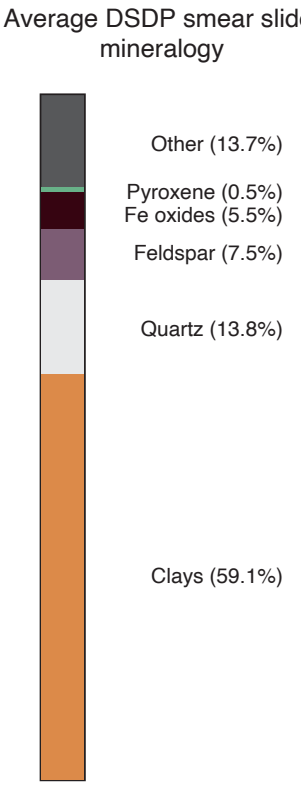


**Figure 1.5:** Average smear slide mineralogy of DSDP cores. A total of 55738 slide mineralogy descriptions were compiled by crawling the website ngdc.noaa.gov/mgg/geology/dsdp/data/smear.htm on January 18th 2023 (Deep Sea Drilling Project, 1989). Biogenous and hydrogenous minerals (e.g., carbonates, sulfates, diatoms) were removed and the residual mineral abundances reflect terrigenous weathering. "Other" consists of: zeolite (5.1%), heavy mineral (3.6%), glauconite (1.8%), opaque mineral (1.7%), rock fragment (0.50%), hornblende (0.34%), biotite (0.16%), rutile (0.097%), apatite (0.07%), zircon (0.05%), amphibole (0.04%), tourmaline (0.04%), epidote (0.03%), garnet (0.02%), cristobalite (0.02%), detrital mineral (0.02%), zoisite (0.02%), olivine (0.02%), serpentine (0.008%), detrital material (0.008%), sphalerite (0.007%), sphene (0.005%), tremolite (0.002%), anatase (0.002%), staurolite (0.001%), flourite [sic] (0.001%), glaucophane (0.001%), analcite (0.001%), spinel (0.001%), topaz (0.0002%), sillimanite (0.00001%), kyanite (0.000004%).

of negative feedbacks for high phosphorus concentrations, we artificially impose an upper limit of $2 \cdot 10^5$. Sedimentary deposits of phosphate, which are common in the rock record but minor in the modern ocean, provide a pathway by which excess phosphorus is removed from the ocean (Froelich et al. 1982).

Assuming carbonate minerals precipitate without carbon isotopic fractionation, the $\delta^{13}$C of the ocean–atmosphere system through time is controlled by the fluxes $F_v$ and $F_{org}$, as well as the size of the carbon reservoir:

$$\Delta\delta^{13}C/\Delta t = 1/M \cdot \left(\left(F_v \cdot \delta_v - \delta^{13}C\right) - F_{org} \cdot \delta_{org}\right) \tag{1.47}$$

In eq. 1.47, $\delta_V$ is the combined carbon isotopic ratio of volcanic outgassing (traditionally –5‰) and organic carbon weathering (traditionally 22‰), which we set constant at –9‰ to achieve a steady-state $\delta^{13}$C around 0‰ (Kump and Arthur 1999). $\delta_{org}$ is the fractionation of carbon, relative to the oceanic value, via photosynthesis, which we hold at 25‰(Hayes et al. 1999).

### 1.6.5 Compilation of natural records

Mean $\delta^{13}$C excursions were calculated from the chemostratigraphic sections in Table A.5 and are used in Fig. 1.3. The magnitude of each excursion was chosen by eye. Representative sections are displayed in Fig. 1.3b and 1.13, and were chosen due to their age constraints and higher temporal resolution. Our model curves are scaled uniformly in time to qualitatively match the shown sections. We linearly interpolated ages of isotopic records between the known ages listed in Table A.4. The resultant time evolution is poorly constrained, with some sections tied only by two age estimates.

The Permo–Carboniferous $\delta^{13}$C range is derived from the data of Grossman et al. 2008a. We used change-point analysis of a smoothed spline (smoothing parameter 0.1) through the data to find the onset of the $\delta^{13}$C excursion at 324.4 Ma and plateau at 308.0 Ma. We subtract each $\delta^{13}$C datum with age 324.4 ± 1 Ma (n = 30) from each $\delta^{13}$C datum with age 308.0 ± 1 Ma (n = 70) and take the median and 1 $\sigma$ range of the resultant values.

We calculate the ophiolite length change for each glaciation by interpolating the suture lengths of Macdonald et al. 2019 at 0.1 Ma resolution and subtracting the pre-glacial and post-glacial suture lengths from the syn-glacial suture lengths. We use the ages of the glaciations given in Table A.3. For the suture lengths that follow the Permo–Carboniferous, we use 255 Ma as the minimum age.

### 1.6.6 Analysis of shale geochemistry

We queried the Stanford Geochemistry and Palaeoenvironments database (Farrell et al. 2021), filtering for 'shale', 'mudstone', and 'siltstone' as the lithology. A total of 7,820 samples contained data for Cr, $Al_2O_3$ and TOC; 6,679 samples contained data for Co, Al2O3 and TOC; and 7,755 contained data for Ni, $Al_2O_3$ and TOC. We consider the ratio Cr/Al as a simple measure of ultramafic provenance. To make systematic variations more visible, we construct bins of Cr/Al and calculate the distribution of TOC within those bins. Any bin with fewer than 15 samples is ignored. In Fig. 1.4a, we show the median Cr/Al, the median TOC and the $1\sigma$ range in TOC values (16th to 84th quantiles). Figure 1.4b overlays the Phanerozoic time variation in shale Cr/Al on the abrupt and prolonged endmember glaciation chronologies (Table A.3). Similar relationships are shown in Fig. 1.16 for Co/Al and Ni/Al.

### 1.6.7 Strontium Methods

The isotopic ratio $^{87}Sr/^{86}Sr$, has long been used as a proxy of silicate weathering (e.g., Edmond 1992). Continental crust has high isotopic values and ultramafic rocks have low isotopic values. The concentration of Sr is 42 times higher in the continental crust than the mantle, meaning it is often used as a proxy of continental weathering (Rudnick et al. 2003; Workman and Hart 2005). We forward-model the response of $^{87}Sr/^{86}Sr$ to an ophiolite obduction. The increase in mafic and ultramafic rocks that we prescribe induces a small negative shift in ocean $^{87}Sr/^{86}Sr$, from 0.7084 to 0.7082 (Fig. 1.14), smaller than those observed throughout the Palaeozoic (Fig. 1.15).

The evolution of strontium isotopes within the system is governed by the fluxes of silicate weathering and hydrothermal exchange at mid ocean ridges (e.g., (Brass 1976; Li and Elderfield 2013)):

$$\Delta R_0/\Delta t = 1/M_{Sr} \cdot (J_H(R_H - R_O) + J_{SW}(R_{SW} = R_O)) \tag{1.48}$$

Where, R is the normalised isotopic ratio of the ocean-atmosphere system (O), hydrothermal exchange (H), or silicate weathering (SW). The relationship between $^{87}Sr/^{86}Sr$ and R is:

$$R = {}^{87}\text{Sr}/{}^{86}\text{Sr}/(9.43 + {}^{87}\text{Sr}/{}^{86}\text{Sr}) \tag{1.49}$$

$J$ is the Sr flux, in megatonnes, of the sources. $M_{Sr}$ is the mass of Sr in the ocean-atmosphere system, which controls the response time of $^{87}Sr/^{86}Sr_O$ to forcings: we hold $M_{Sr}$ constant at $10.6 \cdot 10^6$ MT (Francois and Walker 1992). $J_H$ and $R_H$ are also held constant, representing a flux of 0.64 MT/yr and an $^{87}Sr/^{86}Sr$ of 0.703 (Francois and Walker 1992).

The concentration of Sr in felsic, mafic, and ultramafic rocks varies significantly and as such the strontium flux, $J_{SW}$, associated with a given silicate weathering flux, $F_{SW}$, varies with lithology according to Eq. 1.50 and 1.51.

$$J_{SW} = F_{SW} \cdot r_{Sr}(p_f, p_m, p_u) \cdot 87.6/44.0 \tag{1.50}$$

$$r_{Sr}(p_f, p_m, p_u) = 10^{-6} \cdot (2900 \cdot p_f + 3.1 \cdot 370 \cdot p_m + 8.1 \cdot 8.5 \cdot p_u) \tag{1.51}$$

The values of $2900{\cdot}10^{-6}$, $370{\cdot}10^{-6}$, and $8.5{\cdot}10^{-6}$ in Eq. 1.51 are the molar ratios [Sr]/([Mg] + [Ca]) for felsic, mafic, and ultramafic components, respectively (Rudnick et al. 2003; Workman and Hart 2005; Gale et al. 2013). $^{87}Sr/^{86}Sr_{SW}$ is thus the weighted average of lithologic sources according to their Sr concentration, weathering rate, and fraction present:

$$^{87}\text{Sr}/^{86}\text{Sr}_{SW} = \frac{320 \cdot p_f^{87}\text{Sr}/^{86}\text{Sr}_f + 3.1 \cdot 129 \cdot p_m^{87}\text{Sr}/^{86}\text{Sr}_m + 8.1 \cdot 7.6 \cdot p_u^{87}\text{Sr}/^{86}\text{Sr}_u}{320 \cdot p_f + 3.1 \cdot 129 \cdot p_m + 8.1 \cdot 7.6 \cdot p_u} \tag{1.52}$$

Weightings of 320, 129, and 7.6 are applied to felsic, mafic, and ultramafic lithologies, respectively, due to their ppm concentration in those end-members (Rudnick et al. 2003; Workman and Hart 2005; Gale et al. 2013). We prescribe an $^{87}Sr/^{86}Sr$ a 0.710, 0.704, and

0.7026 for felsic, mafic, and ultramafic rocks. The felsic end-member is equal to the average non-Himalayan rivers (Edmond 1992); the mafic end-member is an average of arc-basalts (Jagoutz and Schmidt 2012); the ultramafic end-member is taken from (Workman and Hart 2005).

## 1.7 Supplementary Figures

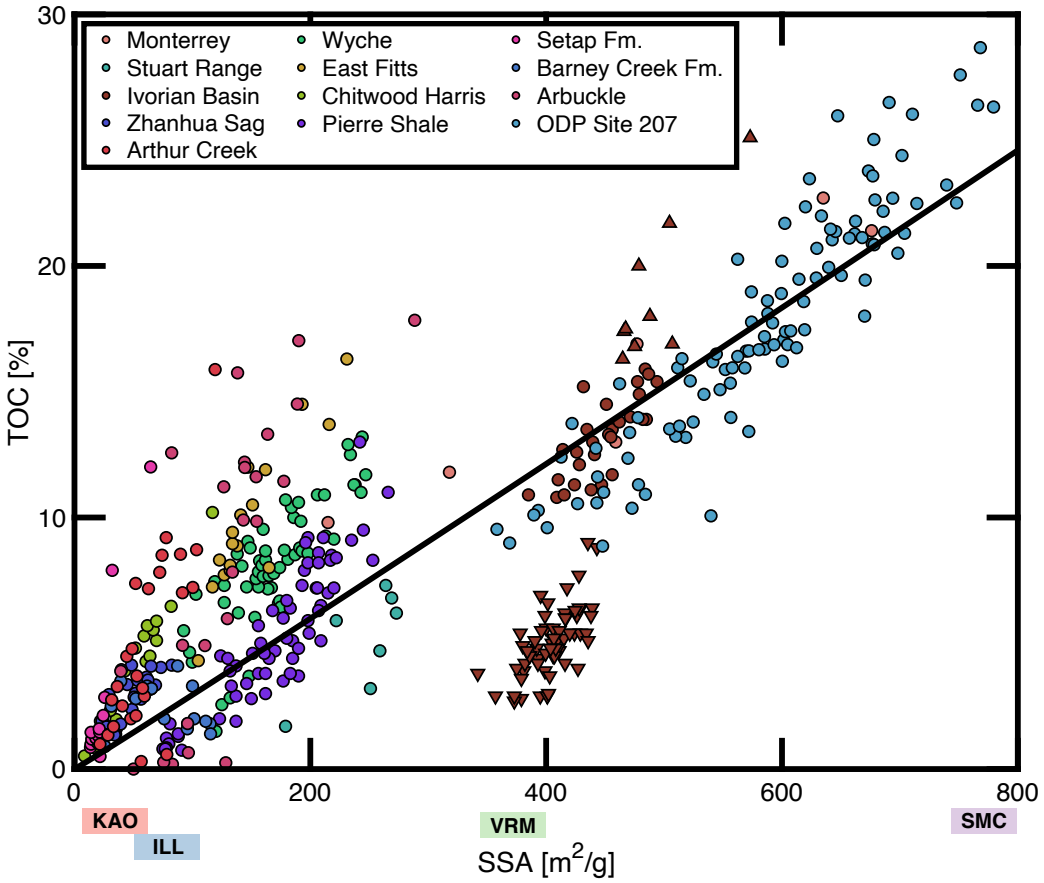


**Figure 1.6:** Compilation of SSA and TOC values with a linear fit. References for each site are given in Table. A.6 (attached). Linear fit is applied with sample weights proportional to their relative sparseness i.e., those data with fewer neighbours are weighed more strongly. The approximate SSA of kaolinite (KAO), illite (ILL), vermiculite (VRM), and smectite (SMC) is show below the SSA axis. The linear fit is in good agreement with estimates of monolayer equivalent adsorption of OC (Kennedy and Wagner 2011). Downward pointing triangles represent data in which the authors attribute TOC loss to bioturbation. Upward pointing triangles represent data in which the authors attribute heighted TOC to an anoxic environment.

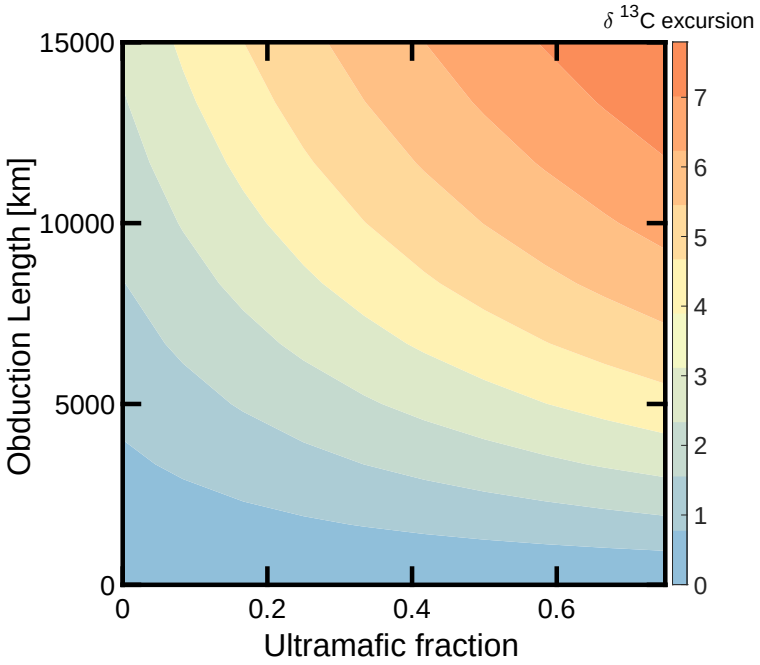


**Figure 1.7:** Influence of ultramafic (peridotite) fraction of the ophiolite and obduction length over the change in $\delta^{13}$C at maximum mafic/ultramafic extent. Each case assumes 300 km overthrust.

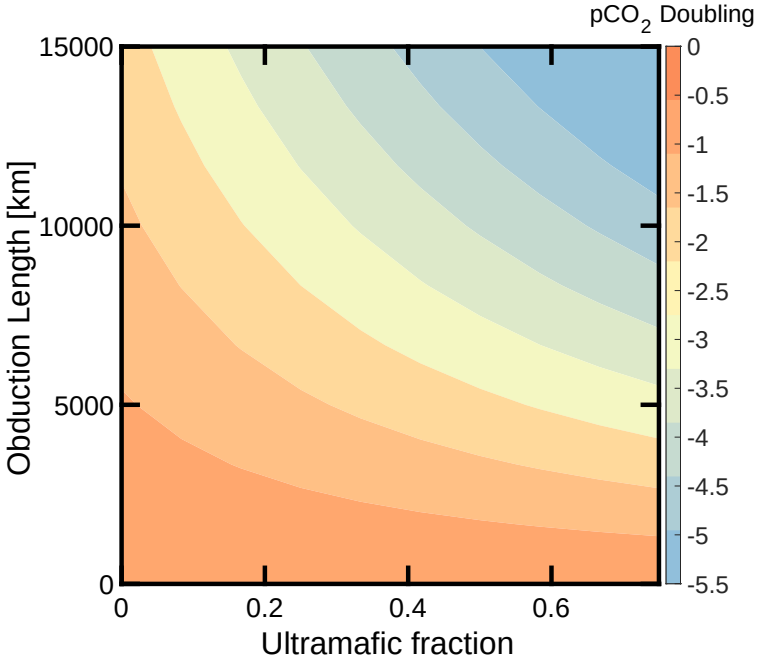


**Figure 1.8:** Influence of ultramafic (peridotite) fraction of the ophiolite and obduction length over the change in steady-state $p\mathrm{CO}_2$at maximum mafic/ultramafic extent. Each case assumes 300 km overthrust.

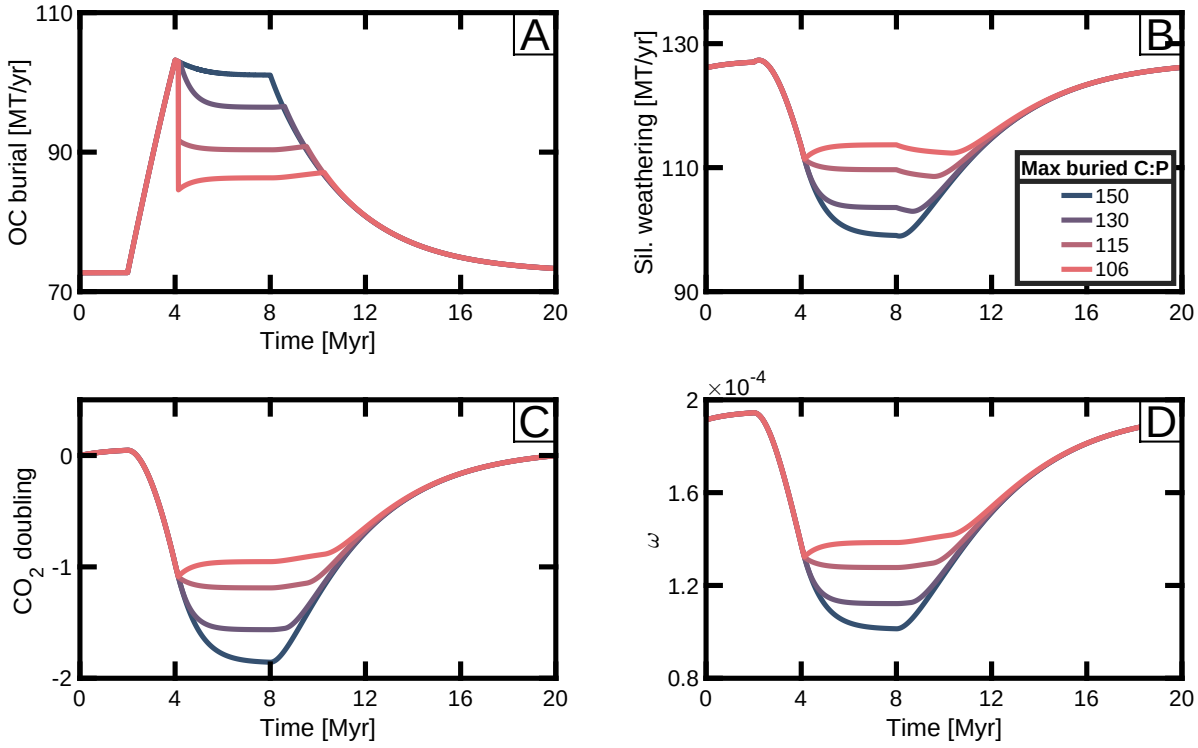


**Figure 1.9:** Carbon box model response to ophiolite forcing. A) Change in global organic carbon burial (MT of C per year). B) Silicate weathering flux decreases due to the silicate-weathering feedback and the OC burial such that the sum of silicate weathering and OC burial is approximately equal to the sources. C) Atmospheric $CO_2$ response shown as the $\log_2$ of the ratio of $pCO_2$ to the initial $pCO_2$. These estimates are sensitive to the parameterisation of the silicate-weathering feedback (Eq. M6) and serve to show and order of magnitude estimate for cooling, rather than a quantitative prediction. D) Changes in the degree of weathering, , as a result of the decrease in $pCO_2$.

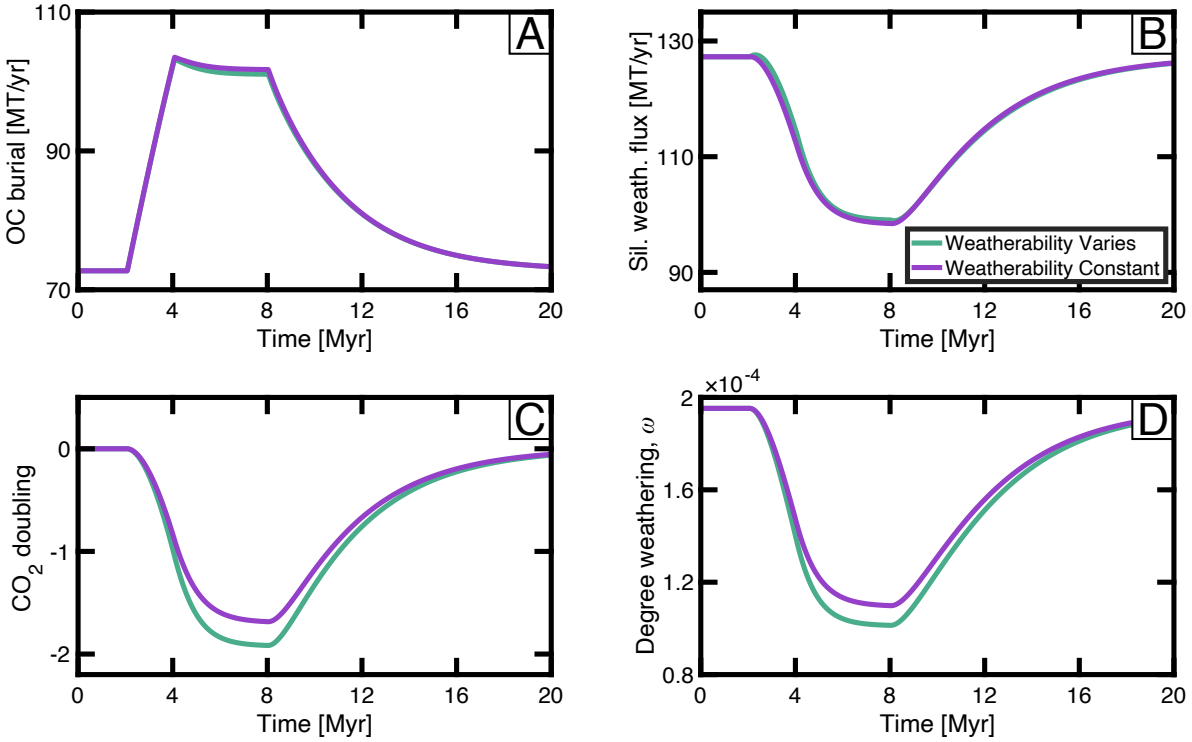


**Figure 1.10:** Comparison of model results with and without changes in weatherability. Each panel is as in Fig. 1.9. Nutrients are assumed to not be limiting. Teal lines correspond to the model simulation in which the increase in ophiolite lithology alters weatherability. Purple lines correspond to the case in which weatherability is unaltered by the increase in (ultra)mafics rocks and the system is driven solely by changes in clay mineralogy and SSA.

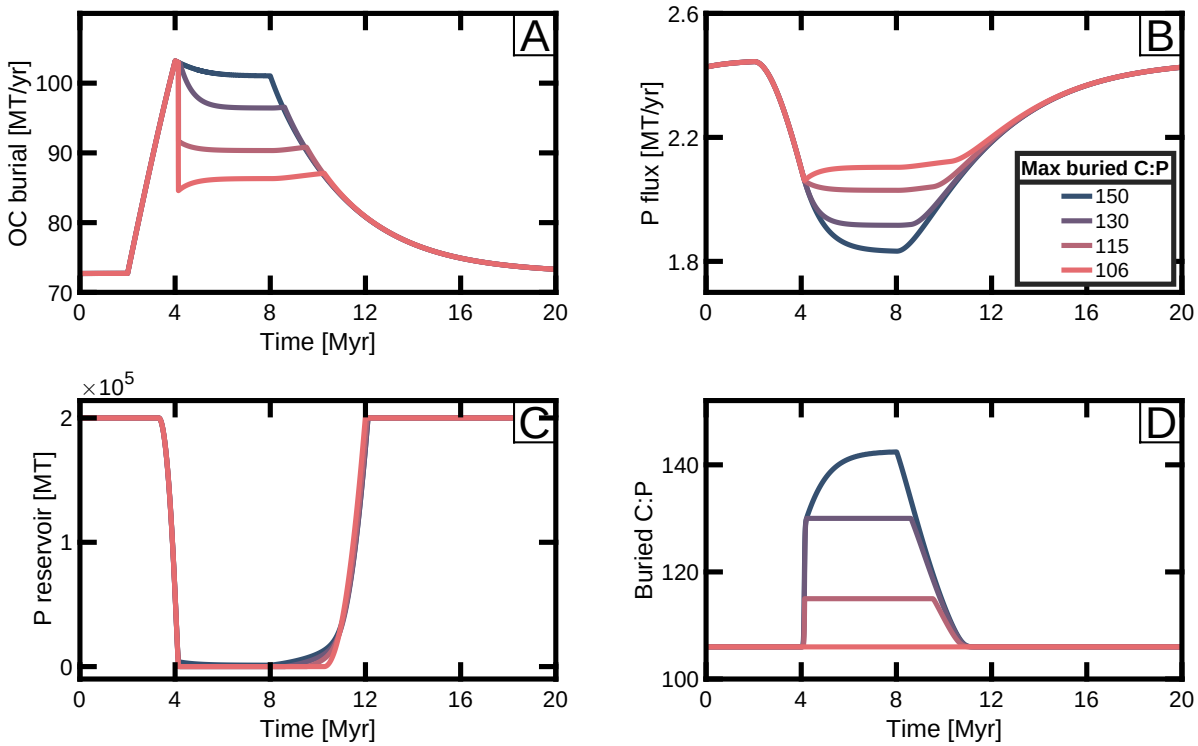


**Figure 1.11:** Changes in phosphorus as a response to increased OC burial. A) OC burial, as seen in Fig. 2C. B) Riverine flux of phosphorus, derived from Eq. M16. C) P reservoir response from the balance of M16-M18. D) Buried C:P ratio according to Eq. M18 and visualised in Fig. S18.

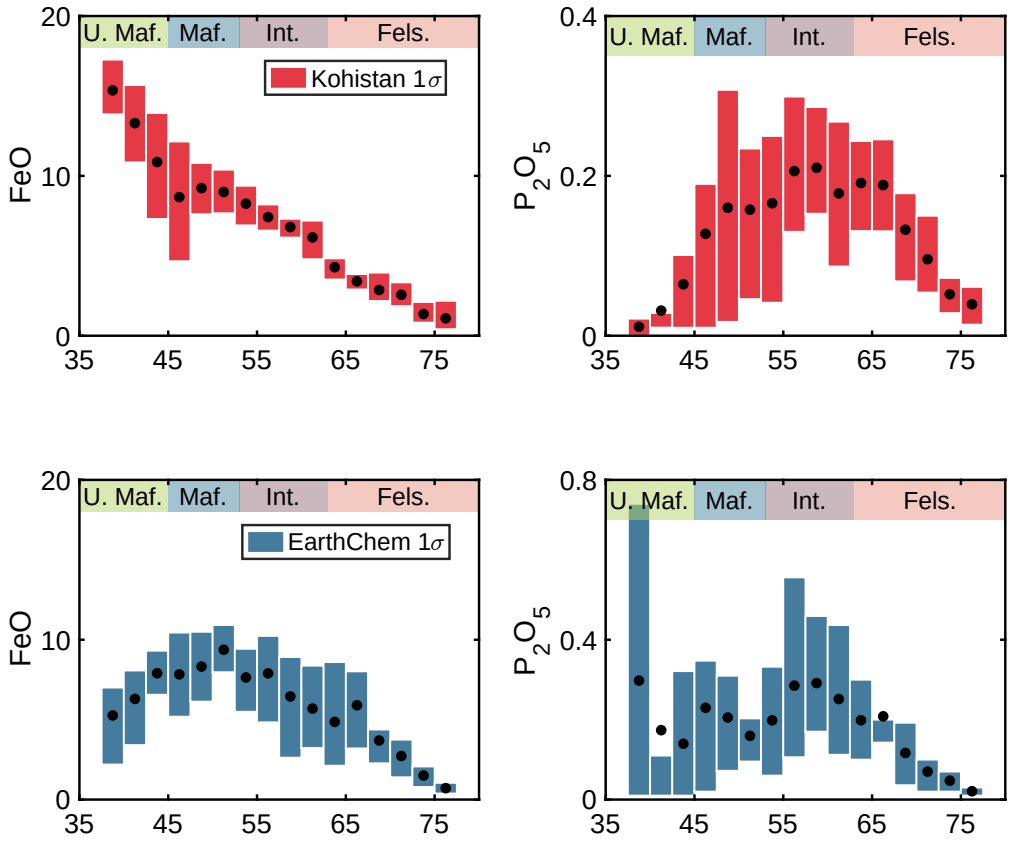


**Figure 1.12:** Igneous trends in FeO and P2O5 vs SiO2 from the Kohistan Arc (top row, Jagoutz Schmidt, 2012) and EarthChem (bottom row), showing one standard deviation of data (from the 16th to 84th quantile). Large black points represent the mean in each bin. Igneous compositions defined by SiO2 (ultramafic, mafic, intermediate, and felsic) are shown above the boxes. Note the smaller y-scale for phosphorous in the Kohistan suite compared to EarthChem.

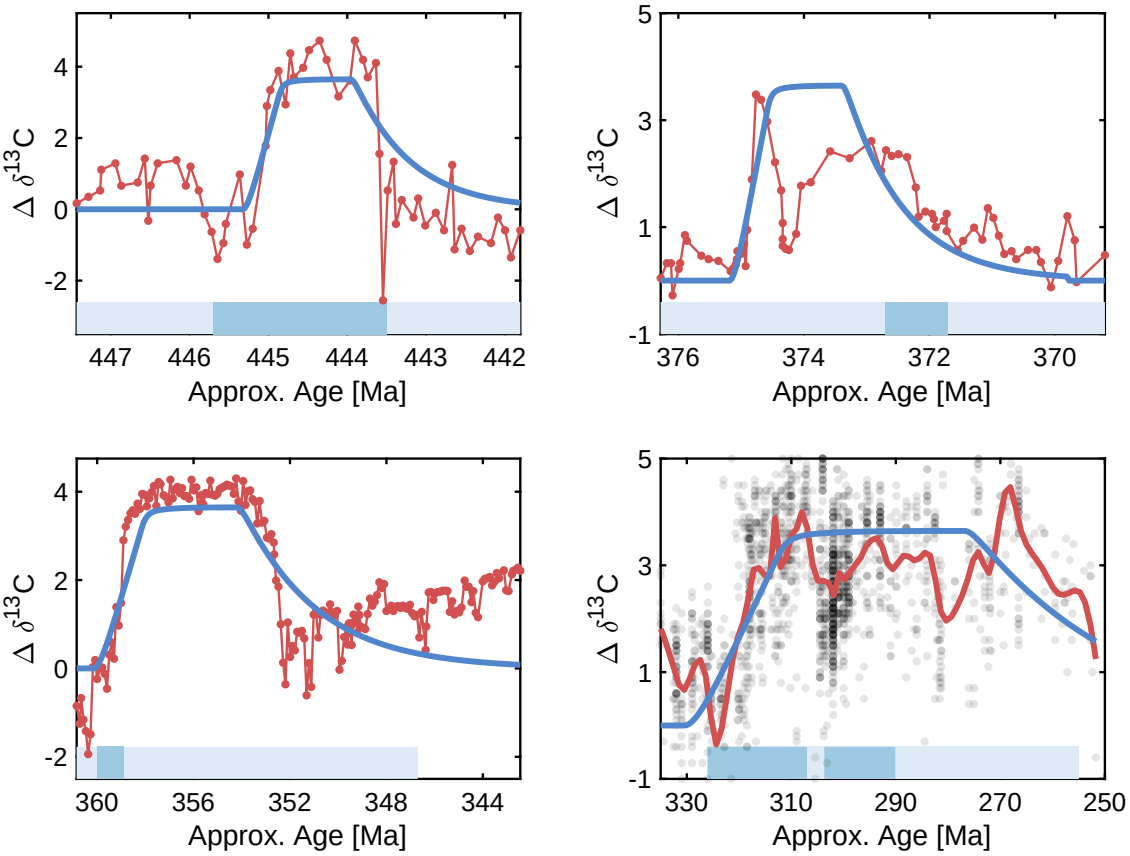


**Figure 1.13:** Examples of compiled carbon isotope excursions from the four glaciations of the Palaeozoic. Dark blue bars represent abrupt end-member chronologies of glaciation, whereas pale blue bars represent prolonged end-members (Table A.3). Our model results (blue line) are time-dilated to qualitatively correlate with the $\delta^{13}$C observations. Late Ordovician (Hirnantian) section from LaPorte et al. 2009a, Blackstone River section; Frasnian-Famennian (Kellewaser) section from Buggisch and Joachimski 2006b, Behringhausen section; End-Devonian (Hangenberg) section from Stolfus et al. 2020b; Permo-Carboniferous brachiopod data from Grossman et al. 2008a where the red line represents a splined interpolation of the data (semi-transparent black circles). Geochronology of both the excursions and glaciations are not well constrained (Table A.4, A.3).

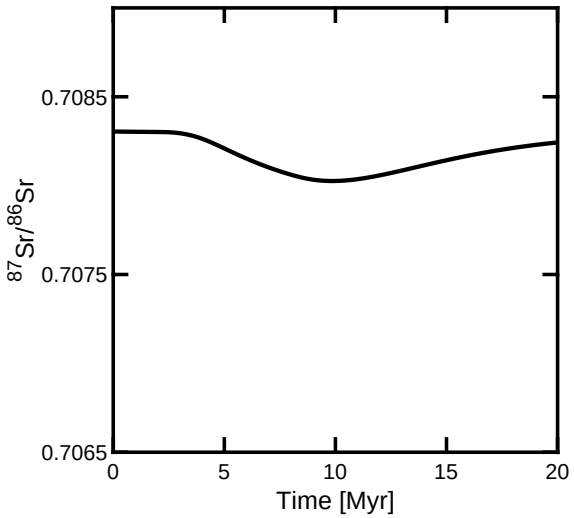


**Figure 1.14:** Modelled $^{87}Sr/^{86}Sr$ response to a 0.5% increase in mafic and ultramafic surface lithologies (Fig. 2A). The Y axis range represents total Cenozoic variation (Veizer et al. 1999).

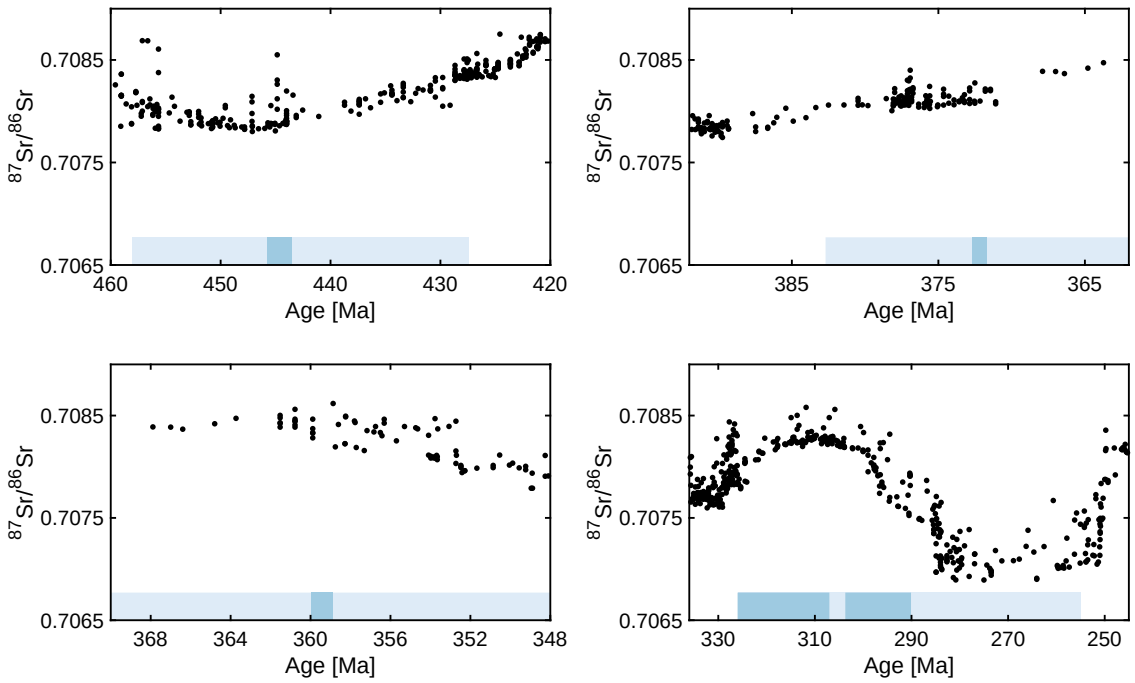


**Figure 1.15:** $^{87}Sr/^{86}Sr$ records spanning Palaeozoic glaciations. Age and $^{87}Sr/^{86}Sr$ are from the fossil data of Prokoph et al. 2008. Uncertainties in the timing of glaciation are explored in the Methods and Supplemental Information. The Y-scale represents the range of observed variation in the Phanerozoic (Veizer et al. 1999).

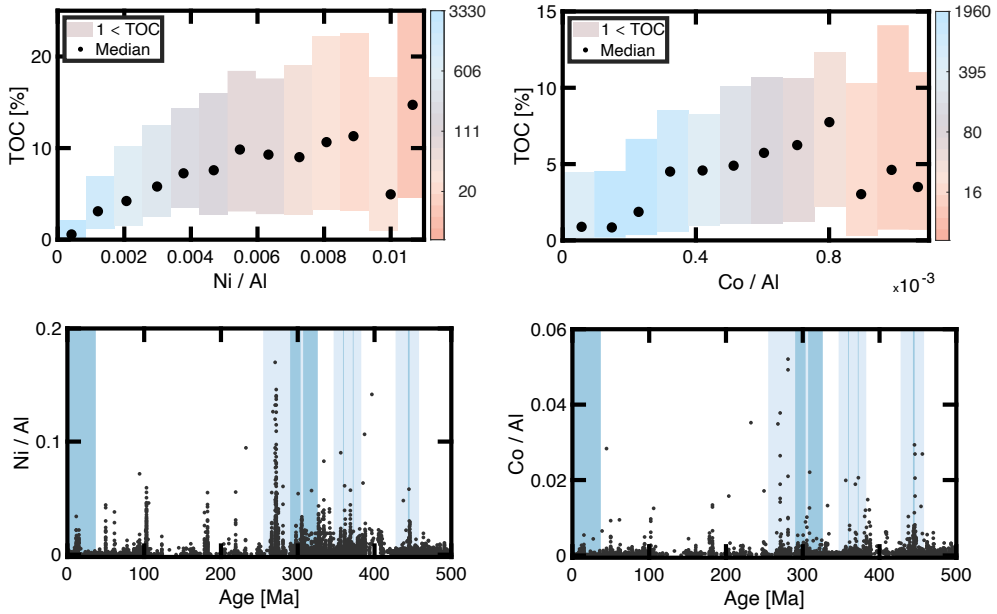


**Figure 1.16:** Alternative trace element analyses for ultramafic provenance and TOC. For A and B, the colour of the box refers to the number of samples contributing to the mean (black dot) and standard deviation (rectangle). In C and D the blue bars reflect Phanerozoic glaciations where pale blue is a prolonged chronology and dark blue is a short chronology (Table. S3). A) Binned median and standard deviation of SGP shale samples, TOC against Co/Al. B) Binned median and standard deviation of SGP shale samples, TOC against Ni/Al. C) Co/Al of SGP shale samples through the Phanerozoic. D) Ni/Al of SGP shale samples through the Phanerozoic.

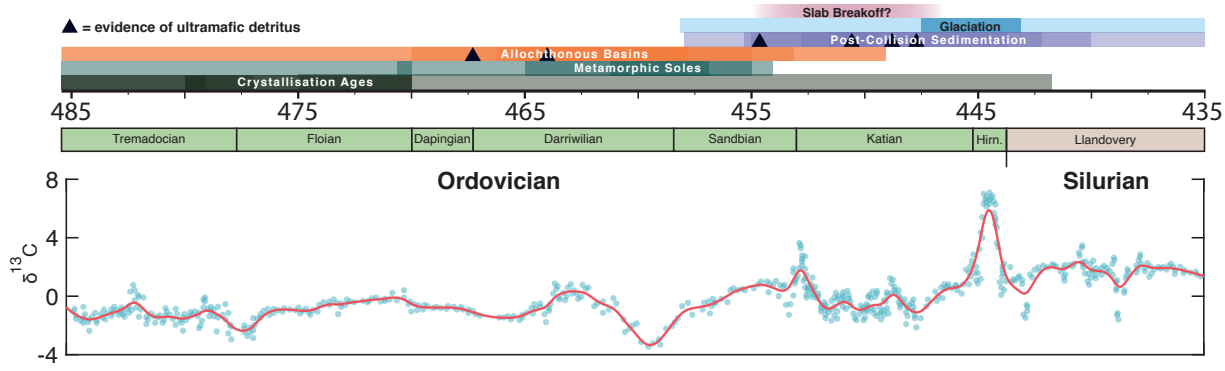


**Figure 1.17:** Non-exhaustive timeline of ophiolite obductions and resultant basin fill during the Ordovician. See attached Table A.7 for geologic constraints. Isotope record taken from Saltzman et al. 2012

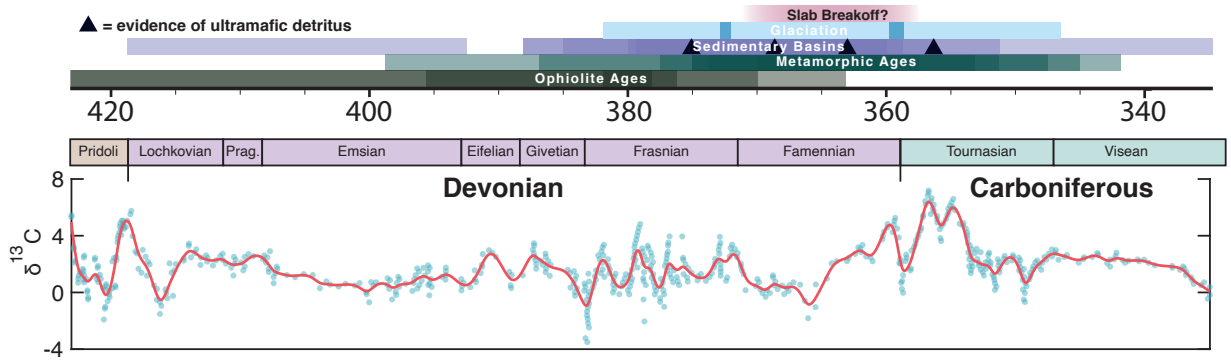


**Figure 1.18:** Non-exhaustive timeline of ophiolite obductions and resultant basin fill during the Ordovician. See attached Table A.7 for geologic constraints. Isotope record taken from Saltzman et al. 2012

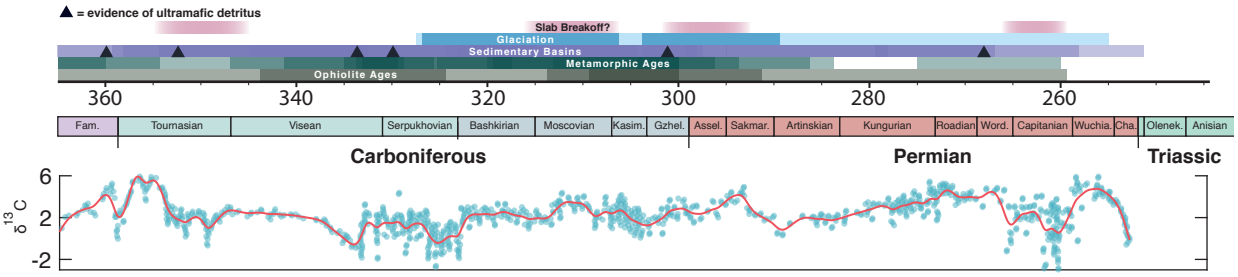


**Figure 1.19:** Non-exhaustive timeline of ophiolite obductions and resultant basin fill during the Ordovician. See attached Table A.7 for geologic constraints. Isotope record taken from Saltzman et al. 2012

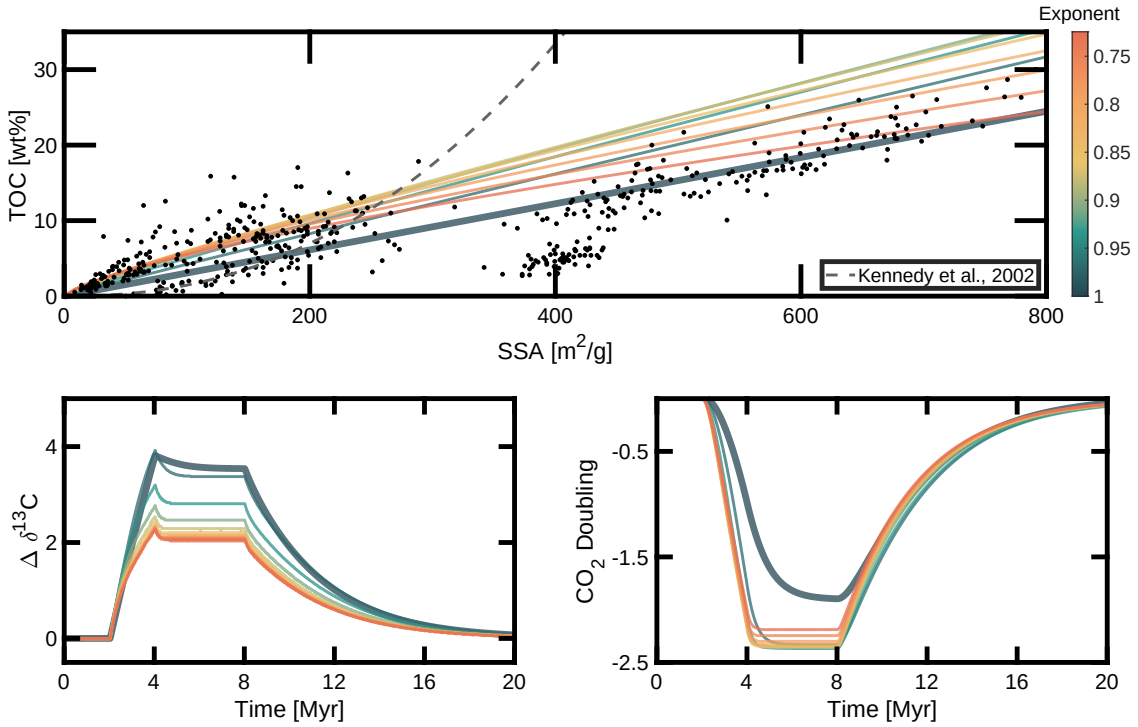


**Figure 1.20:** Range of possible SSA-TOC relationships with resultant $\delta^{13}C$ and $pCO_2$ responses. Thick, blue (exponent = 1) lines represent our chosen SSA-TOC fit and model response. A) The same data as seen in Fig. 1.6 with various power-law fits overlain. Grey dashed line is replicated from (Kennedy et al. 2002) which fails to approximate the data at high SSA values. B) Modelled $\delta^{13}C$ response to changing the SSA-TOC power law. For each simulation $\delta^{13}C$ is given relative to the initial value. C) Modelled $pCO_2$ response to changing the SSA-TOC power law. Results largely depend on the local gradient in the range of SSA 0-100 m2/g.

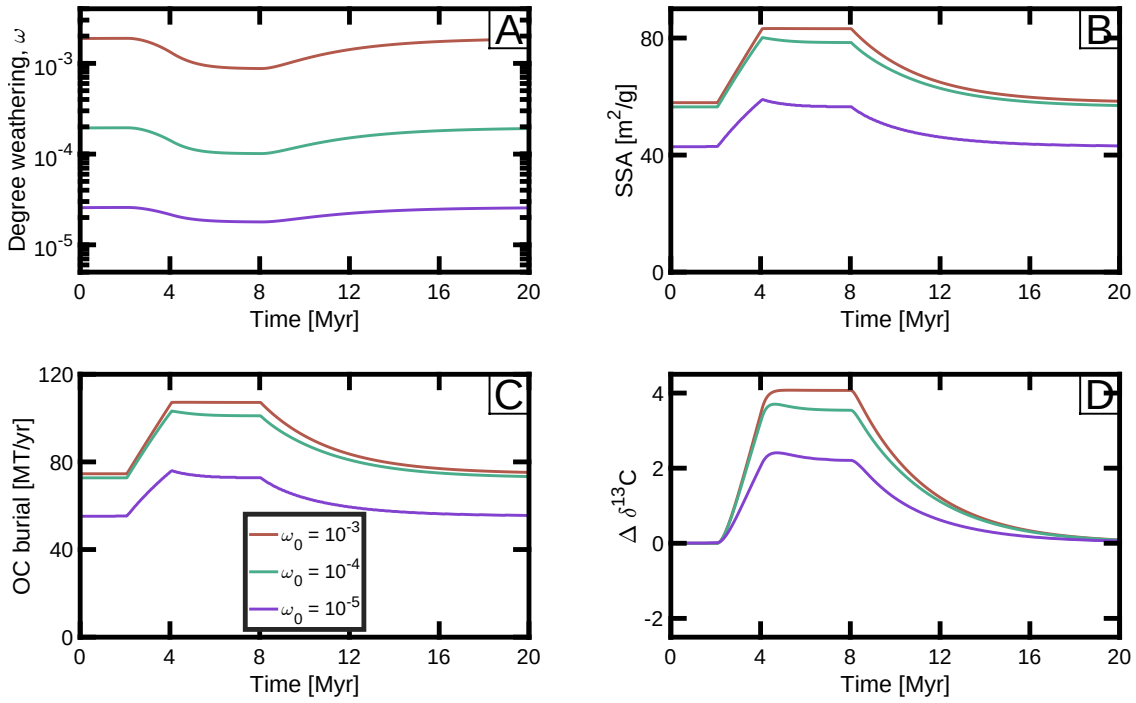


**Figure 1.21:** Influence of changing $\omega_0$ over: (A) degree of weathering; (B) SSA; (C) OC burial; and (D) resultant carbon isotope excursion.

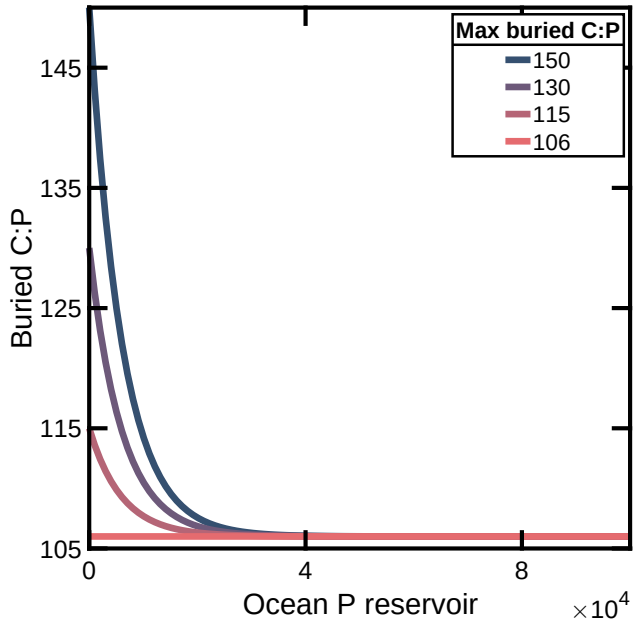


**Figure 1.22:** Chosen function to approximate P recycling during phosphorus-limited conditions.

# Chapter 2

# Olivine alteration and the loss of Mars' early atmospheric carbon

In review, *Science Advances*.

## 2.1 Abstract

The early Martian atmosphere had 0.25-4 bar of $CO_2$ but thinned rapidly around 3.5 Ga. The fate of that carbon remains poorly constrained. The hydrothermal alteration of ultramafic rocks, rich in Fe(II) and Mg, forms both abiotic methane, serpentine, and high-surface-area smectite clays. Given the abundance of ultramafic rocks and smectite in the Martian upper crust and the growing evidence of organic carbon in Martian sedimentary rocks, we quantify the effects of ultramafic alteration on the carbon cycle of early Mars. We calculate the capacity of Noachian-age clays to store organic carbon. Up to 1.7 bar of $CO_2$ can plausibly be adsorbed on clay surfaces. Coupling abiotic methanogenesis with best estimates of Mars' $\delta^{13}C$ history predicts a reservoir of 0.6–1.3 bar $CO_2$ equivalent. Such a reservoir could be utilized as an energy source for long-term missions. Our results further illustrate the control of water-rock reactions on the atmospheric evolution of planets.

## 2.2 Introduction

Geological observations of Mars indicate a dense early atmosphere ranging from 0.25 to 4 bar of $CO_2$ (Jakosky 2019; Kite 2019). However, Mars' current surface reservoir only amounts

to approximately 0.054 bar of $CO_2$, suggesting a significant loss of $CO_2$, either to space or the lithosphere (Hu et al. 2015). This decline of $CO_2$ likely occurred between the late Noachian and late Hesperian period, when sedimentary deposits reflect a transition from a 'warm and wet' to a 'cold and dry' climate (Kite 2019). The mechanism by which Mars lost its atmospheric $CO_2$ remains poorly constrained.

Photochemical models and orbiter measurements of carbon loss to space indicate an integrated escape since the Noachian of ∼1.3-6.3 mbar of $CO_2$, two orders of magnitude lower than the rates necessary to explain the removal of 0.25-4 bar (Ramstad et al. 2018; Lo et al. 2021) (see Fig. 2.6). Escape rates may have been amplified by an early magnetic dipole (Sakai et al. 2018) and/or more frequent solar storms (Jakosky et al. 2015). In addition, sizeable amounts of $CO_2$ may have been sequestered as carbonate minerals (Hu et al. 2015), however such large deposits have yet to be located (Edwards and Ehlmann 2015). The challenge in reconciling models of Martian atmospheric evolution with present-day observations often leads to the postulation of a "missing sink" of carbon (Edwards and Ehlmann 2015; Heard and Kite 2020).

Recent rover missions detected reduced organic carbon in Martian rocks (Glavin et al. 2013; Stern et al. 2022; Sharma et al. 2023). On Earth, reduced carbon species, primarily methane, can be formed abiotically during low temperature (<140 °C) serpentinization (Etiope and Whiticar 2019). The oxidation of Fe(II) in olivine to Fe(III) in serpentine, which is abundant in ultramafic terrains on Mars (Ehlmann et al. 2010; Tutolo and Tosca 2023) and is found as detrital minerals within deltaic sediments (Tice et al. 2024), liberates $H_2$ from water. Through the Sabatier reaction, this $H_2$ reacts with $CO_2$ to form methane ($CH_4$; simplified in Eq. 2.1). Similar Fischer-Tropsch Type (FTT) reactions can produce less reduced or more complex organic molecules and hydrocarbons (Berndt et al. 1996; Steele et al. 2018). Methane is unstable in the Martian atmosphere and would revert to $CO_2$ in less than 1 ka (Krasnopolsky et al. 2004; Lefevre and Forget 2009) due to photochemical degradation (Wong et al. 2003).

However, smectite clays, the most abundant hydrated mineral on the Martian surface

(Ehlmann et al. 2011), have the capacity to adsorb and protect organic carbon (Hedges and Keil 1995; Murray and Jagoutz 2023). Similar to serpentine, these clay minerals form through water-rock reactions and alteration of mafic and ultramafic rocks (Seyfried Jr and Mottl. 1982; Caillaud et al. 2006). Smectite surfaces can catalyze the polymerization and aromatization of simple organic carbon compounds (Williams et al. 2005) to complex molecules similar to those cyclic hydrocarbons detected by the Perseverance rover (Sharma et al. 2023). On Earth, tectonic processes and biological activity recycle lithospheric carbon back to the atmosphere (Hedges and Keil 1995; Kelemen and Manning 2015). On Mars, where these processes are limited or absent (Zuber 2001), mineral protected organic carbon in the crust would remain stable over long geologic timescales. Consequently, relatively small fluxes (e.g., Krissansen-Totton et al. 2018) could accumulate large lithospheric stores of organic carbon.

Here, we evaluate the role of abiotic methanogenesis and subsequent storage of methane within smectite clays in the cooling of the Martian climate. We constrain this process through a simple mass-balance model of serpentinization, estimates of the volume of clays within the crust, and a model of the evolution of carbon isotopes since the early Noachian.

## 2.3 Results

### 2.3.1 Methane Formation and Storage

Our model explores the oxidation of Fe(II) present in olivine, which was abundant on Mars through at least the early Hesperian (Mustard et al. 2005; Ehlmann and Edwards 2014), to serpentine. Eq. 2.1 shows a simplified, idealized reaction:

$$\text{Olivine} + H_2O + CO_2 \rightarrow \text{Serpentine} + \text{Magnetite} + CH_4 \tag{2.1}$$

We explore serpentinization volumes of 0-2 km GEL, within the depth of hydrated minerals on Mars (Sun and Milliken 2015) and inferred serpentinization rates on Earth (Tutolo and Tosca 2023). Our calculations show that a 2 km GEL of serpentine reduces ∼5 bar of

atmospheric $CO_2$ to methane (Fig. 2.7).

Clay minerals on Mars are exposed in craters as deep as 17 km (Sun and Milliken 2015). However, the total volume of clays remains a significant source of uncertainty. The hydrated crust stores anywhere from 16 m GEL (Mustard 2019) to 1350 m GEL of $H_2O$ (Wernicke and Jakosky 2021; upper limit), equivalent to 27 m GEL to 2260 m GEL of clay minerals (Methods). Given the uncertainty, we compute the capacity of smectite clays to store organic carbon for various total volumes (Fig. 2.1, Methods) and investigate the implications of organic carbon storage as a function of clay volume, including both the 'best estimate' of 218 – 436 m GEL smectite and the 'plausible range' from 117 m to 1440 m GEL (Wernicke and Jakosky 2021).

The methane storage capacity of different clay minerals is dependent upon both pressure and temperature. Due to its high surface area, smectite can adsorb a factor of four more methane than illite or chlorite, with a maximum adsorption of ~0.6 wt% (Figure 2.1a, Table 2.1). Integrating through the plausible volumes of smectite clay, our analysis indicates that 0.07 bar of $CO_2$ equivalent can be stored as methane within 117 m GEL and 1.7 bar in 1440 m GEL (Fig. 2.1b). The 'best estimate' clay volumes can store 0.16 – 0.4 bar of $CO_2$ as adsorbed methane. Compared to the non-polar methane, smectite can store far greater percentages (up to 32 wt%) of polar organic molecules (Shen 2004). Such molecules are measured in Martian mudstones (Glavin et al. 2013; Eigenbrode et al. 2018), and can form abiotically in smectite interlayer spaces (Williams et al. 2005). In this regard, methane serves as a conservative estimate compared to the adsorption of possible compounds on clay surfaces. Below 500 m depth the maximum adsorbed methane concentration is relatively constant (Fig. 2.1a), indicating that the relationship between clay thickness and stored organic carbon is approximately linear (Fig. 2.1b). The depth distribution of the total clay volume is less influential: a 1000 m thick surface layer of pure smectite can store 1.1 bar, whereas an equal volume distributed evenly throughout the upper 10 km can store 1.3 bar (Fig. 2.8).

Our calculations show Martian clays could store multiple bar of $CO_2$ equivalent. Reducing

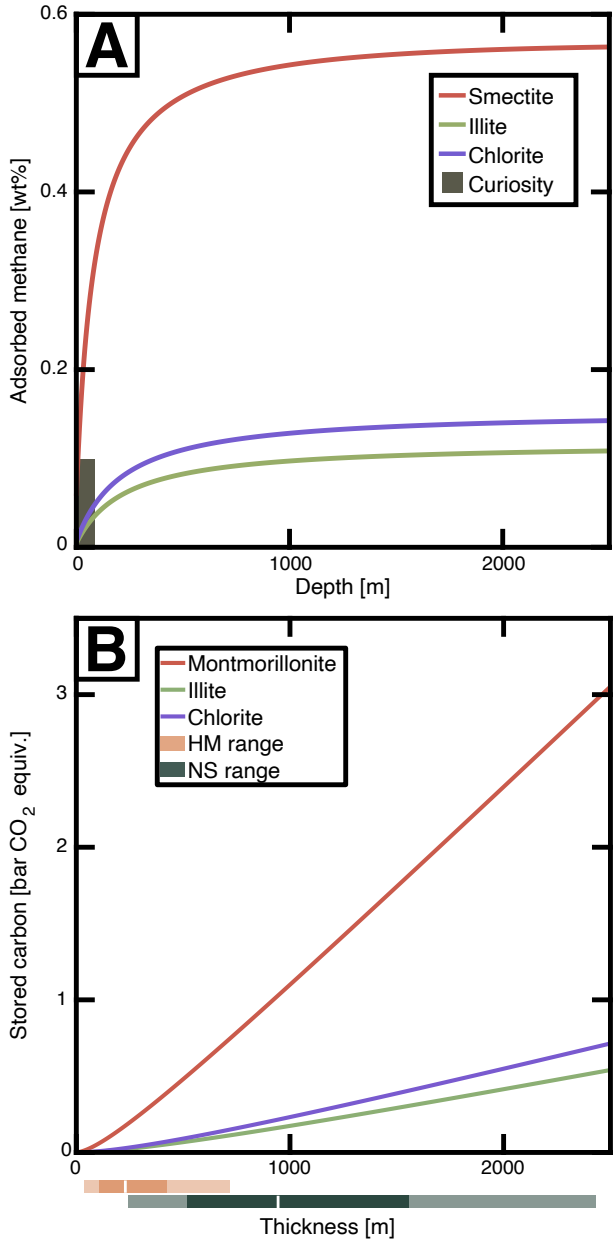


**Figure 2.1:** Capacity for smectite clays to store organic carbon. a) Calculations of adsorbed methane, shown at total organic carbon (TOC), on smectite, illite, and chlorite as a function of depth. Estimates are based upon experimental data of Langmuir adsorption assuming an early Martian geotherm and crustal density (Methods). The grey bar shows the possible range of TOC in a mudstone sample in Gale crater (Stern et al. 2022). b) Integrated TOC, converted to $CO_2$ atmospheric pressure, as a function of clay mineralogy and global equivalent layer (GEL) thickness. The orange and green boxes reflect the one and two standard deviation estimates of smectite clay volumes based upon the formation of hydrated minerals (HM) and near-surface (NS) estimates, respectively (Wernicke and Jakosky 2021; Methods).

1.7 bar of $CO_2$ to organic compounds would require ~700m GEL depth of serpentinization (Fig. 2.7). On Earth, serpentinization of a 700 m thick layer would take between 10 ka and

100 Ma (Beinlich et al. 2020; Leong et al. 2021). While serpentine is observed on Mars today (Ehlmann et al. 2010), the extent of serpentinization in the subsurface is hard to estimate and could be obscured by subsequent alteration of serpentine to smectite since the Noachian (Caillaud et al. 2006).

### 2.3.2 Isotopic History

Abiotic methanogenesis preferentially incorporates light carbon isotopes (Etiope and Whiticar 2019). Consequently, the conversion of atmospheric $CO_2$ to mineral-bound $CH_4$ would lead to the fractionation of the carbon isotopic composition of the surface reservoir (Fig. 2.2). To model the change in isotopic composition of atmospheric $CO_2$ for varying GEL thicknesses of smectite clays and initial atmospheric pressure, we employ a Monte Carlo method (Fig. 2.2, Methods). We use a fractionation factor of -14 ± 3‰ for methanogenesis, consistent with observations of abiotic systems on Earth (Etiope and Whiticar 2019; Methods). For the 'lowest plausible' clay volume of 117 m GEL, we calculate an atmospheric enrichment of 0.4-1.8‰, depending on the initial atmospheric pressure of $CO_2$. The 'best estimate' of clay volumes yields atmospheric enrichment in $\delta^{13}C$ of 1.9‰to 14‰. The 'highest plausible' volumes of 1440 m GEL stores 1.7 bar of $CO_2$ and would enrich $\delta^{13}C$ by 15-50‰, depending on the initial atmosphere (Fig. 2.2).

We place our predictions of $\delta^{13}C$ changes associated with methanogenesis within the constraints imposed by the atmospheric evolution of carbon isotopes on Mars. Today, heavy carbon is strongly enriched, with atmospheric $\delta^{13}C$ measured as 48± 4‰ (Webster et al. 2013), while the early atmosphere likely reflected mantle $\delta^{13}C$ values of -30 to -20‰ (Wright et al. 1992; Hu et al. 2015). Enriching atmospheric $\delta^{13}C$ from mantle values to present-day levels necessitates an increase of up to ∼80‰ over Mars' history (Fig. 2.2b). This enrichment is attributed, at least partially, to atmospheric escape. We combine modelled fractionation factors for photodissociation of $CO_2$ (Hu et al. 2015) with best estimates of atmospheric escape of atomic carbon (Lo et al. 2021) and project $\delta^{13}C$ back to the Noachian

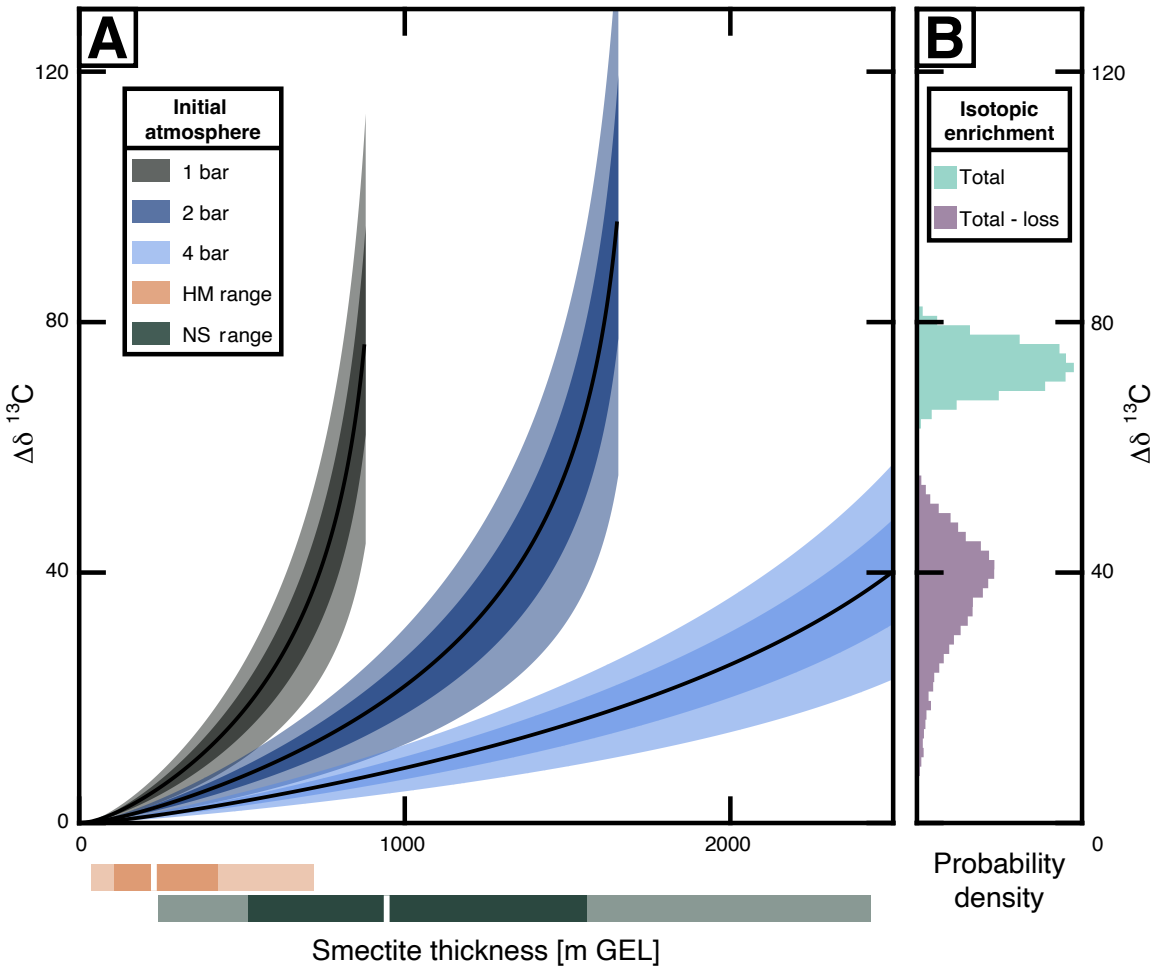


**Figure 2.2:** Predicted change in atmospheric $\delta^{13}$C for a variable volume of smectite clays saturated with abiotic methane. A) Colored segments reflect different initial Martian atmospheric pressures. Data are shown with median (black line), 1 standard deviation (near-opaque field), and 2 standard deviations (semi-transparent field). The orange and green boxes reflect the one and two standard deviation estimates of smectite clay thickness as shown in Fig. 2.1. B) Probability density of changes in $\delta^{13}$C for the total enrichment since 4.5 Ga (turquoise) and the total enrichment which cannot be explained by current estimates of atmospheric loss alone (purple).

(see Methods; Fig. 2.2b). We find integrated atmospheric loss since 4.0 Ga can account for $34^{+11}_{-6}$ ‰ of isotopic enrichment (Fig. 2.2b). The remaining $38^{+7}_{-11}$‰ of enrichment must be attributable to a process not included in these integrated estimates of loss to space. Loss rates could be significantly greater in the past (Jakosky et al. 2015; Sakai et al. 2018), particularly if oxygen escape is derived from $CO_2$ photodissociation rather than $H_2O$ (Jakosky et al. 2018). However, modern loss rates of carbon are ∼2 orders of magnitude lower than oxygen loss rates (Jakosky et al. 2018; Ramstad et al. 2018) and enhanced loss in the early solar

system is difficult to quantify, particularly if $\delta^{13}$C enrichment is driven by a combination of geologic and atmospheric mechanisms.

Here we explore the effect of abiotic methanogenesis on the history of $\delta^{13}$C and consider the extent to which water-rock reactions can bridge the gap between early magmatic $\delta^{13}$C values and the $\delta^{13}$C inferred through the extrapolation of modern atmospheric loss (Lo et al. 2021). Figure 2.3 overlays the change in atmospheric $\delta^{13}$C associated with various GEL thicknesses of organic matter bearing smectite clay, for an initial 2 bar $CO_2$ atmosphere. Subsequently, we evaluate the size of organic reservoir, formed by abiotic methanogenesis, required to explain the isotopic discrepancy (Fig. 2.2b).

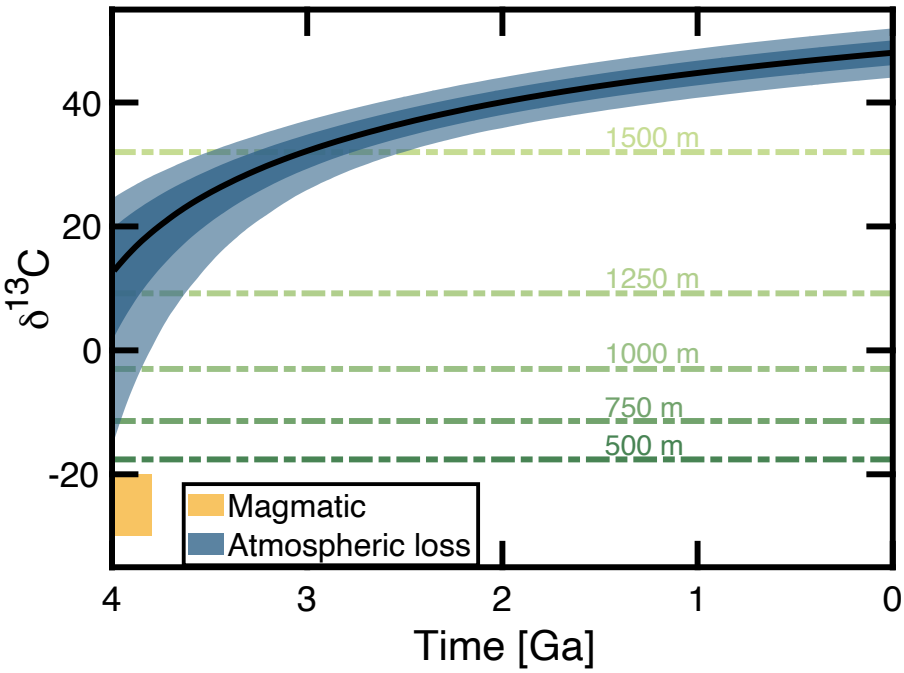


**Figure 2.3:** Enrichment of Martian $\delta^{13}$C since 4.0 Ga due to atmospheric escape and volume-dependent enrichment by mineral-bound organic carbon. The blue field is calculated by projecting the modern atmospheric composition backwards with best estimates of photodissociation and solar evolution (Claire et al. 2012; Lo et al. 2021; Methods). The median, one standard deviation, and two standard deviations, are displayed as the black line, near-opaque field, and semi-transparent field. The magmatic composition of Martian meteorites is shown as a yellow bar (40). Green dashed lines show the median $\delta^{13}$C predicted by smectite clays of various GEL thicknesses for an initial atmosphere of two bar $CO_2$. See Fig. 2.9 for a comparable figure with other loss estimates and initial atmospheric pressures.

To do so, we use a Bayesian treatment of clay volumes, isotopic fractionation, initial $\delta^{13}$C, and present conditions, to calculate the conditional probability distribution of organic carbon

in the Martian crust given the isotopic composition of the atmosphere at 4 Ga (Methods). For an initial atmospheric $CO_2$ pressure of 1 bar, an organic carbon reservoir equivalent to $0.65^{+0.13}_{-0.30}$ bar $CO_2$ best recreates the available data (Fig. 2.4). An initial atmospheric pressure of 2 bar is best fit by an organic carbon reservoir equivalent to $1.25^{+0.29}_{-0.69}$ bar $CO_2$. Such organic carbon reservoirs equate to total masses of 0.69-1.33 PT of carbon. To reduce that amount of carbon requires at least 280 m - 510 m GEL of serpentinization (Fig. 2.7), and at least 670 - 1100 m GEL of smectite to adsorb and protect the carbon in the crust (Fig. 2.1). Reaching serpentinization depths of 510 m by the end of the Hesperian period requires rates of $\sim 5 \cdot 10^{-9}$ km/yr, which is slower than the most conservative estimates of serpentinization reaction fronts on Earth (Leong et al. 2021; Tutolo and Tosca 2023). If, on the other hand, rates of serpentinization on early Mars matched the fastest estimates on Earth today, the serpentinization front would require only 5 kyr to reach 510 m (Beinlich et al. 2020).

Absent of a secondary mechanism which reduced atmosphere $\delta^{13}C$, for an initial atmosphere of 1 and 2 bar, respectively, we find that the mineral bound organic carbon reservoir cannot exceed masses equivalent to 0.85 bar and 1.7 bar, else atmospheric $\delta^{13}C$ is enriched beyond modern values (Fig. 2.2). This corresponds to an upper limit in methane-saturated smectite clays of 800 m GEL and 1500 m GEL, respectively (Fig 2.1b), consistent with the 'highest plausible' limits derived from estimates of crustal $H_2O$ (Mustard 2019; Wernicke and Jakosky 2021).

An initial atmosphere of 4 bar requires greater than 2 km GEL of smectite clay minerals and associated methane in order to recreate the isotopic enrichment observed today (Fig. 2.2, Fig. 2.10). Such a volume is beyond the plausible limit of hydrated minerals on Mars (Wernicke and Jakosky 2021). If the early Martian atmosphere were as thick as 4 bar, other processes, which either concentrates carbon within the crust beyond methane adsorption or markedly increase the rate of atmospheric escape (Jakosky 2019), would be necessary to explain the loss of carbon.

In addition to carbon, hydrogen is fractionated during the formation of methane. Using

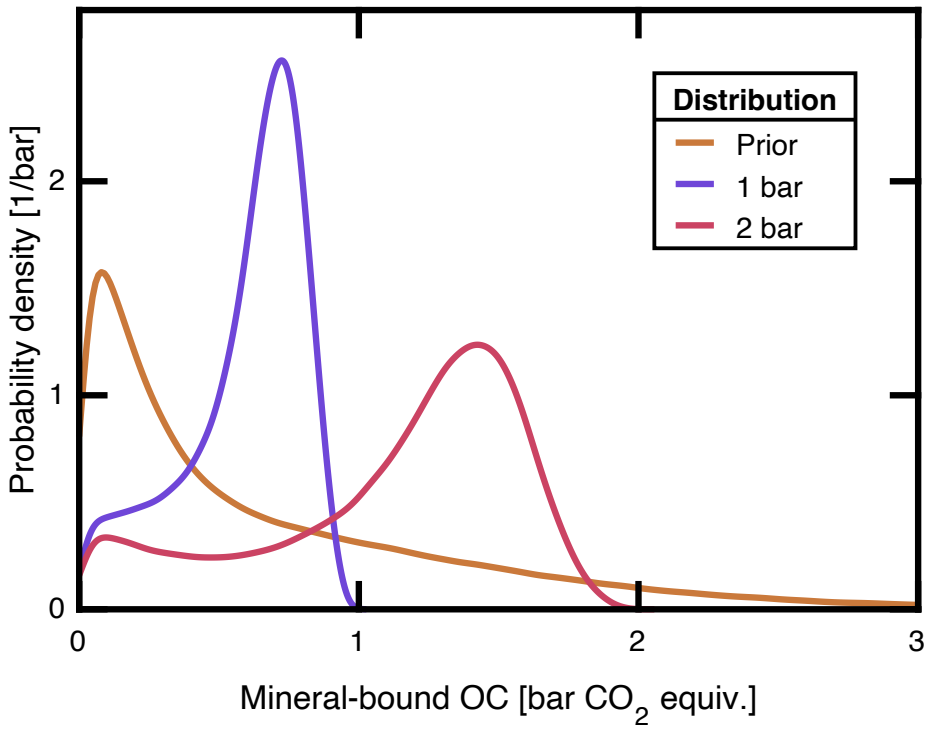


**Figure 2.4:** Prior and posterior probability distributions of organic carbon in the Martian crust. The prior distribution (orange line) is calculated according to the combined near-surface and hydrated mineral estimates of $H_2O$ in the Martian crust (Wernicke and Jakosky 2021; Methods) and converted to organic carbon by the calculations shown in Fig. 2.1b. Posterior distributions are conditional upon an initial one bar atmosphere (purple line) and an initial two bar atmosphere (red line). Posterior distributions reflect the organic carbon reservoir required to replicate $\delta^{13}C$ predicted by atmospheric escape models. Comparable figures are presented in the Supplementary Information with prior distributions derived solely from near-surface estimates and hydrated mineral formation (Fig. 2.11 & 2.12).

a fractionation factor of 325 ± 50‰(Etiope and Whiticar 2019, Table 2.1), we estimate an enrichment in D/H of 0.01-0.4 VSMOW, depending on the initial atmospheric pressure of $CO_2$ and the size of the water reservoir at 4 Ga (Fig. 2.14). An enrichment of 0.4 VSMOW is minor in comparison to the ∼5 VSMOW enrichment in D/H since the Noachian which was driven largely by atmospheric escape (Webster et al. 2013; Scheller et al. 2021). The large uncertainties in hydrogen escape rates through time, including the dependency on solar EUV (Lillis et al. 2017), the effect of dust storms (Stone et al. 2020; Chaffin et al. 2021), and the changes in orbital obliquity (Jakosky et al. 1995), pose a barrier to relating abiotic methanogenesis to the history of Martian D/H. Due to these uncertainties, we refrain from using D/H as a constraint to infer the size of the organic carbon reservoir. Future models of

Martian D/H may benefit from the inclusion of abiotic methanogenesis but only if loss-driven hydrogen fractionation through time is known to greater precision than ∼0.5 VSMOW.

## 2.4 Discussion

Our results demonstrate that serpentinization indeed could have formed a large organic carbon reservoir due to the reduction of atmospheric $CO_2$. This reservoir, stored and protected on clay mineral surfaces since the Noachian, could represent the postulated 'missing sink' of carbon on Mars. We demonstrate that Mars' climatic and carbon isotopic history can be explained with the inclusion of an organic carbon reservoir equivalent to ∼0.4 – 1.5 bar of $CO_2$. Given that we do not attempt to model the effects of an early magnetic field and solar storms, our integrate loss estimates likely reflect a lower bound (Lo et al. 2021, Methods). It follows that the size of the organic carbon reservoir is an upper bound. The $\delta^{13}C$ enrichment (Fig. 2.2b) can thus be partitioned between the storage of organic molecules on clay surfaces (this paper) and unquantified processes which enhance the loss to space of $CO_2$.

Our estimates are sensitive to the inferred isotopic history of the Martian atmosphere and the estimates of clay thickness on Mars. For example, if early Martian $\delta^{13}C$ were comparable to Earth's mantle, -5‰, then the size of a clay-bound organic carbon reservoir would necessarily decrease in order to conform with modern atmospheric values. Alternatively, if the false detection of smectite is pervasive due to its indistinguishable adsorption bands compared to hisingerite (Fe-rich serpentine) (Tutolo and Tosca 2023), then our prior distribution of smectite volume is an overestimate. However, hisingerite has high specific surface area (662 - 758 $m^2/g$, similar to that of smectite; Shayan 1984) and could adsorb substantial stores of organic carbon itself.

The bounds placed on the organic carbon reservoir could be further constrained by measurements of organic carbon within Martian mudstones, particularly in the subsurface, to investigate the depth-dependence predicted in Fig. 2.1a. On Earth, we can garner greater understanding through study of abiotic methanogenesis in serpentinites of compositions more

similar to those on Mars (Tutolo and Tosca 2023), and through laboratory measurements which constrain isotopic fractionation during the formation of complex organic molecules within the interlayer space of smectites (Williams et al. 2005).

Traditionally, 2 wt% TOC is seen as a minimum for economical extraction of gas from shale (Wang and Gale 2009). However, space exploration need not be profitable and 0.5 wt% could provide a valuable fuel source. If extracted, Martian organic carbon, particularly methane, could be used as a propellent for farther space missions or return flights (Neill et al. 2009; Palmer 2021). Alternatively, methane and subsequent hydrogen acts as a potent greenhouse gas in the Martian atmosphere (Ramirez et al. 2014) and could be used more effectively for terraforming than other accessible carbon reservoirs (Jakosky and Edwards 2018). Processes which further concentrate organic carbon in shales or in traps would make these ventures more achievable and justifies searching for such concentrated deposits in the subsurface.

Our results may have ramifications beyond Mars' climate history. Given that tectonic processes have overturned and obscured most Hadean and Archaean crust on Earth, Mars provides the best window into planetary processes in the 1 Gyr after accretion. Our results show that aqueous alteration and serpentinization of (ultra-)mafic rocks are critical processes for the exchange of hydrogen and carbon between the ocean-atmosphere and the lithosphere and can meaningfully influence the $CO_2$ budget of a planet's atmosphere. Our model of abiotic methanogenesis and storage, shown in the schematic Figure 2.5, which is minor on Earth today, may be a widespread, fundamental process in the atmospheric evolution of young rocky planets with an (ultra-)mafic crust. The formation and adsorption of organic molecules formed soon after planetary accretion could even be integral to the development of life (Oparin 1953; Williams et al. 2005). However, in the absence of tectonic overturning, the adsorption of organic carbon onto clay surfaces may represent an irreversible loss of atmospheric carbon, further tying plate tectonics to planetary habitability even in the absence of significant carbonate deposits (Kasting and Catling 2003).

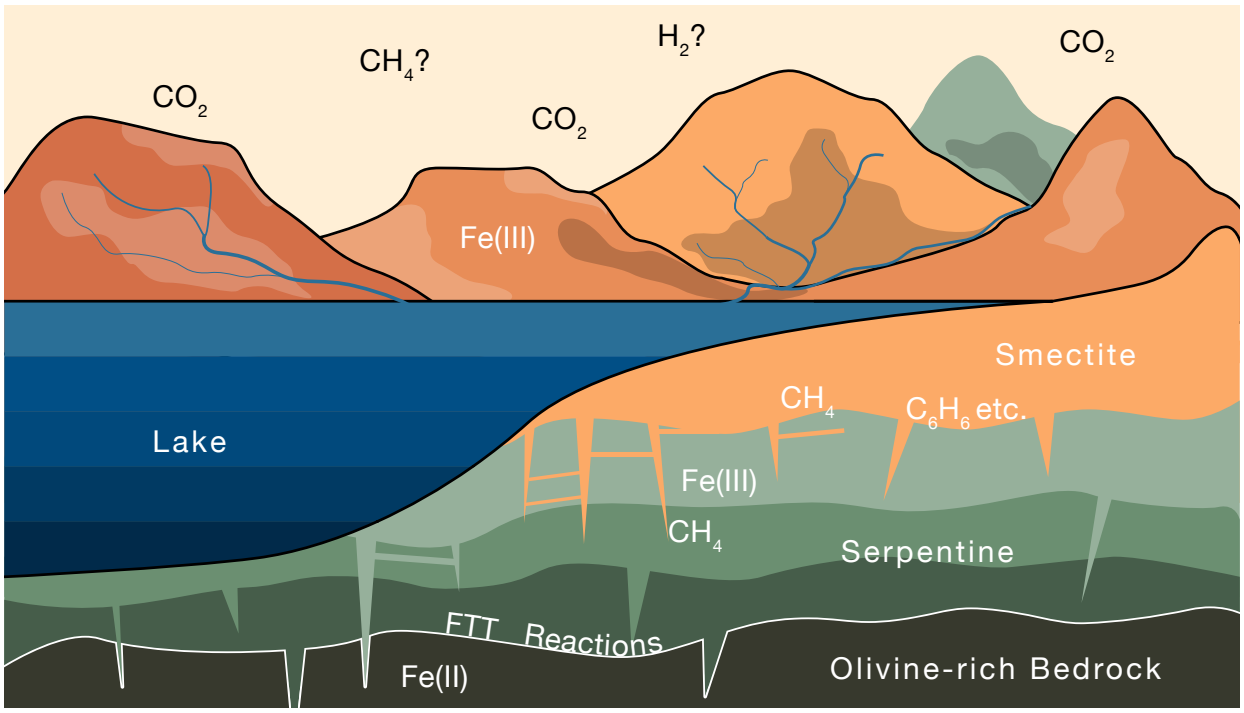


**Figure 2.5:** Schematic for our framework of organic carbon sequestration on early Mars. Ultramafic rocks are hydrothermally altered in the subsurface to form serpentine, smectite, and methane. Methane is adsorbed in the smectite interlayer space where it may further react to form complex organic molecules (Williams et al. 2005). Combined, these reactions amass geologically significant stores of carbon within the crust.

## 2.5 Methods

### 2.5.1 Abiotic methanogenesis

To investigate the relationship between abiotic methanogenesis and serpentinization volume, we assume that reactant olivine has a forsterite number of 0.6 and an Fe(II)/ΣFe of 1 (Koeppen and Hamilton 2008). We use a forsterite density of 3300 kg/m$^3$ and a fayalite density of 4400 kg/m$^3$. We model olivine alteration to serpentine with a final Fe(II)/ΣFe of 0.4 (Tutolo and Tosca 2023). We explore global equivalent layer (GEL) depths of 0 km to 2 km, consistent with 1 Ga of the slowest estimates of the migration of serpentinization reaction fronts (Leong et al. 2021) and the maximum total volume of hydrated minerals in the Martian crust (Fig. 2.8). We follow the chemical equation of Oze and Sharma 2005 in which six mols of fayalite form one mol of methane. GEL thicknesses of serpentinization are

then converted to mols of olivine, mols of methane, and finally atmospheric pressure of $CO_2$ (Fig. 2.7).

### 2.5.2 Methane adsorption

The adsorption of methane on clay surfaces is dependent upon the mineralogy, pressure, and temperature. We assume an upper crustal density of 3100 kg/m$^3$ (Baratoux et al. 2014; Wieczorek et al. 2022), a clay density of 2300 kg/m$^3$, a surface temperature of 0°C, and a Martian geotherm of 15 K/km (Clifford 1991). We convert depth to temperature and calculate the Langmuir coefficient, $K$, according to Eq. 2.2 (Ji et al. 2012):

$$ln(K) = \frac{q}{RT} + \frac{\Delta S^0}{R} - ln(p^0) \tag{2.2}$$

Where $q$ is the heat of adsorption; $\Delta S^0$ is the standard entropy of adsorption; $R$ is the gas constant; $T$ is temperature; and $(p^0)$ is the standard pressure, 1 bar.

We then calculate the adsorption of methane, $\Gamma$, according to the Langmuir coefficient (Eq. 2.3):

$$\Gamma = \Gamma_{max} \frac{K \cdot P}{K \cdot P + 1} \tag{2.3}$$

For smectite, illite, and chlorite, the values, of $q$, $\Delta S^0$, and $\Gamma_{max}$, are given in Table 2.1 (Ji et al. 2012). We use numerical integration of $\Gamma$ with depth, to derive the total adsorption of methane for a given thickness of smectite (Fig. 2.1).

### 2.5.3 Clay Volumes

The total volume of clay minerals in the Martian crust is a major control to the history of water on Mars, however constraining clay abundance and water content at depth remains challenging (Clifford 1991; Mustard 2019; Wernicke and Jakosky 2021). We derive our range of smectite volumes from two existing estimates of water sequestered in the crust: the first

is constrained by the $H_2O$ necessary to form hydrated minerals; the second is constrained by estimates of $H_2O$ in the near-surface of Mars (Wernicke and Jakosky 2021). The prior distribution for our inferred reservoir of organic carbon is evenly sampled from the hydrated mineral distribution and near-surface distribution (Wernicke and Jakosky 2021; Fig. 2.4) and we present the results for each distribution separately within the Supplementary Information (Fig. 2.11 and 2.12).

The majority (62%) of detected hydrated minerals on Mars are smectite clays (Wernicke and Jakosky 2021). A further 23% are chlorite (Wernicke and Jakosky 2021), which is formed primarily by the diagenetic alteration of smectite (Ehlmann et al. 2011). Adsorbed organic matter is retained during the diagenesis of smectite (Kennedy et al. 2014). As such, we assume that 85% of hydrated minerals in the Martian crust were smectite clays or remain as smectite clays. We convert mineral-bound $H_2O$ estimates to GEL thickness of smectite clay assuming a water content of 22 wt% and a density of 2300 kg/m$^3$. This results in a conversion factor of 1.68 from $H_2O$ [m GEL] to smectite clay [m GEL] (see Fig. 2.13) for a comparison. The 'plausible' range of water sequestered within the crust, 70 - 860 m GEL (Wernicke and Jakosky 2021), is thus equivalent to 117 - 1440 m GEL of smectite clay.

### 2.5.4 Isotopic fractionation during abiotic methanogenesis

We use a Monte Carlo method to randomly sample the fractionation factor of abiotic methanogenesis and model the subsequent isotopic enrichment of $^{13}C$ in the atmosphere. We generate a fractionation factor according to the normal distribution -14 $\pm$ 3‰(Table 2.1). Distinguishing biotic and abiotic methane signatures on Earth is challenging, however biotic methane tends to have a lighter signature than abiotic methane (although both processes preferentially incorporate $^{12}C$). The range -14 $\pm$ 3‰ is chosen to reflect the majority of samples studied in the Semail and Al Farfar ophiolites (Etiope and Whiticar 2019), as well as the abiotic methane catalyzed by chromium spinel (Etiope et al. 2018) which is detected in Jezero Crater (Tice et al. 2024).

As methane reacts within the smectite interlayer space to form more complex organic compounds, carbon may be fractionated again. If some of the organic carbon were then freed to the atmosphere, the fractionation during complex abiotic polymerization and aromatization reactions would play a role in the atmospheric evolution of $\delta^{13}C$. These reactions have not been well-studied from an isotopic standpoint, and remain a source of uncertainty in our model. We suggest that, given the tendency for abiotic ethane to incorporate more $^{12}C$ than does abiotic methane (Etiope et al. 2018; Etiope and Whiticar 2019), our fractionation factors are more likely to underestimate the strength of fractionation than overestimate. Similarly, abiotic methanogenesis tends to be incorporate more $^{12}C$ at lower temperatures (Etiope and Ionescu 2015). Given a cooler Martian geotherm and surface temperatures, serpentinization on Noachian Mars may have fractionated carbon more strongly than the ophiolite complexes we use as analogues.

To calculate the change in $\delta^{13}C$ of the atmosphere, we run simulations with a given starting atmospheric pressure of $CO_2$ and a global thickness of smectite clays. We then calculate the ratio of carbon which could be sequestered as mineral-bound methane, relative to the starting atmospheric carbon. We use this ratio of sequestered carbon and the fractionation factor discussed above to calculate the change in atmospheric $\delta^{13}C$ by the Rayleigh equation (Fig. 2.2).

We use the same methodology to calculate the influence of abiotic methanogenesis on hydrogen isotopes. We use a D/H range of -325‰± 50‰ for abiotic methane, relative to the source $H_2O$ (14). The resulting change in atmospheric D/H is shown in Fig. 2.14.

### 2.5.5 Atmospheric Escape and $\delta^{13}C$

Estimates of atmospheric escape can be derived via multiple methods. The loss of O to space, as measured by MAVEN (e.g. (Lillis et al. 2017)), can be tied to $CO_2$ photodissociation but may be derived primarily from the photodissociation of $H_2O$ (Jakosky 2019; Heard and Kite 2020). Alternatively, the isotopic fractionation since the Noachian has been used to

estimate the amount of $CO_2$ loss assuming a fractionation factor for photodissociation of CO (Hu et al. 2015). However, the mechanism of carbon loss outlined here also enriches carbon isotopes in the atmosphere so we cannot use modern $\delta^{13}C$ to constrain both methanogenesis and atmospheric loss. Instead, we use recently calculated total modern loss rates which include photodissociation, dissociative recombination, electron impact dissociation, and photoionization (Lo et al. 2021). We scale the total modern loss with the intensity of the solar Lyman continuum (Eq. 2.4) (Claire et al. 2012; Lo et al. 2021). The relationship between the flux of photons in the Lyman continuum and the photodissociation of $CO_2$ is unknown (Hu et al. 2015). We assume a power law with an exponent sampled from a lognormal distribution with mean 1.5 and standard deviation 0.25.

$$F_c = \left(F_0(4.5 - t)^{\beta_{lym}}\right)^{\alpha_{lym}} \tag{2.4}$$

We apply a total carbon isotope fractionation factor of 0.6, which is calculated specifically for photodissociation of CO (Hu et al. 2015). We project loss rates backwards from the present to 4 Ga, adding carbon back into the atmosphere and tracking the resultant $\delta^{13}C$. A full set of model parameters is given in Table 2.1. In the Supplementary Information, we provide an alternative history of $\delta^{13}C$ using the ion loss rates from solar wind-driven ion escape, constrained by the Mars Express orbiter (Fig. 2.9) (Ramstad et al. 2018).

### 2.5.6 Inference of the organic carbon reservoir

Assuming that abiotic methanogenesis is responsible for the previously unaccounted enrichment in $^{13}C$, we can put estimates on the amount of organic carbon stored in Martian clays.

Once again, we use Monte Carlo simulations to generate two separate distributions of $\delta^{13}C$: the first from mineral-bound abiotic methane; the second from rewinding 4 Ga of atmospheric loss. Our prior distribution for methane-driven $\delta^{13}C$ is derived from the estimated probability distribution of water in hydrated minerals on Mars (Fig. 4 of Wernicke and Jakosky 2021) converted to clay volume. We then use Bayes' theorem to calculate the

posterior distribution of mineral-bound organic carbon according to the likelihood (the probability distribution of $\delta^{13}C$ at 4 Ga according to our model of atmospheric escape) and the prior (the probability distribution of $\delta^{13}C$ beginning from magmatic values and enriched by abiotic methanogenesis). We handle the probabilities numerically via weighted resampling with replacement of the parameters in the abiotic methanogenesis model.

For an initial atmosphere of 4 bar $CO_2$, only 3% of simulations of methanogenesis exceed the $\delta^{13}C$ inferred from atmosphere escape i.e., for our framework to bridge the gap between magmatic values and modern values requires loss rates which are improbably high or fractionation factors for abiotic methanogenesis which are improbably low. As such, we do not include the posterior distribution of mineral-bound organic carbon for a 4 bar atmosphere in Fig. 2.4 and suggest that another process would likely be necessary to remove such a large reservoir of carbon. For completeness, the posterior distribution is shown in Fig. 2.10.

## 2.6 Supplementary Information

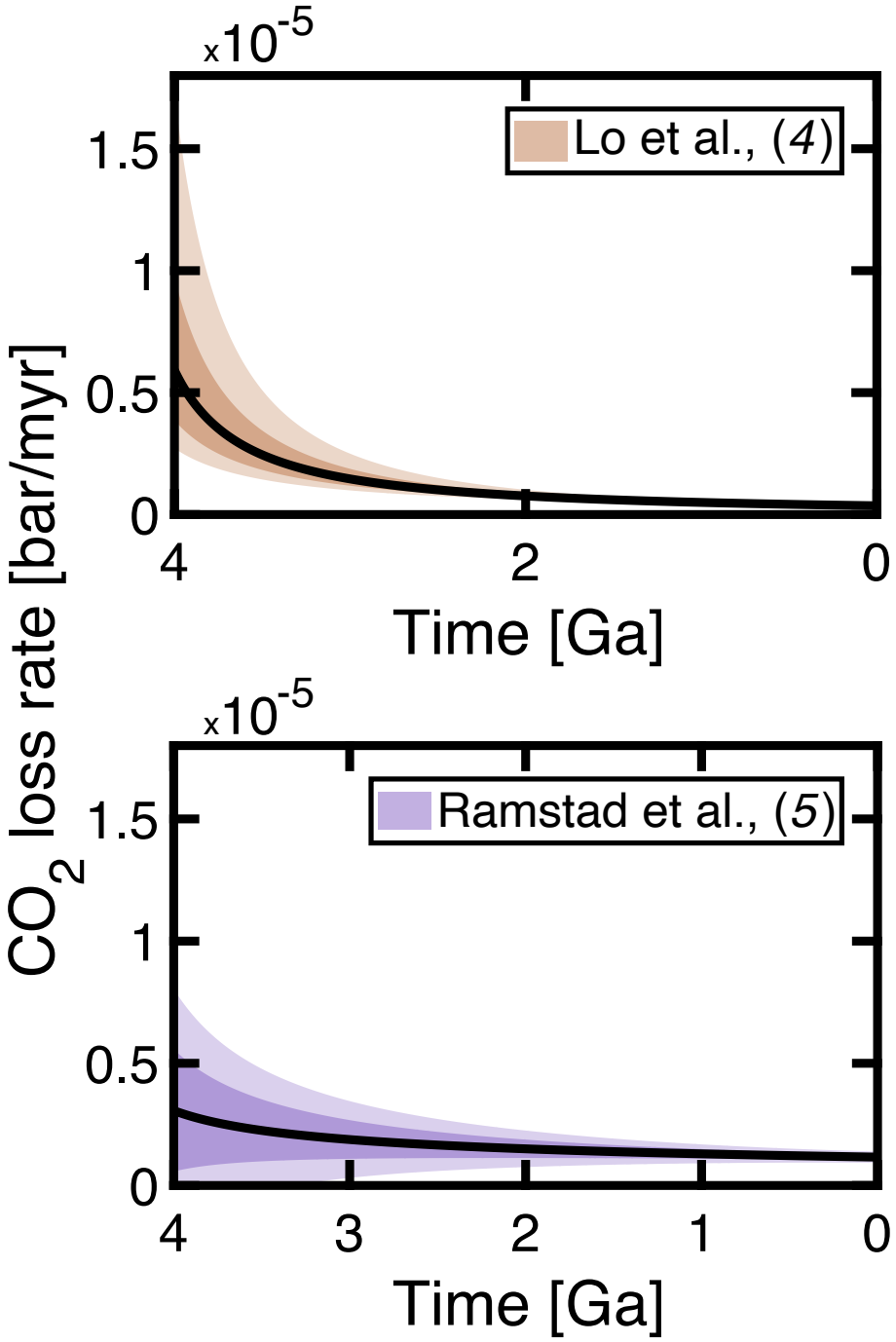


**Figure 2.6:** Modelled atmospheric loss of $CO_2$ since 4 Ga. Loss rates are derived from Lo et al., Lo et al. 2021 (top) and Ramstad et al. 2018 (bottom). The median, one standard deviation, and two standard deviations, are displayed as the black line, near-opaque field, and semi-transparent field.

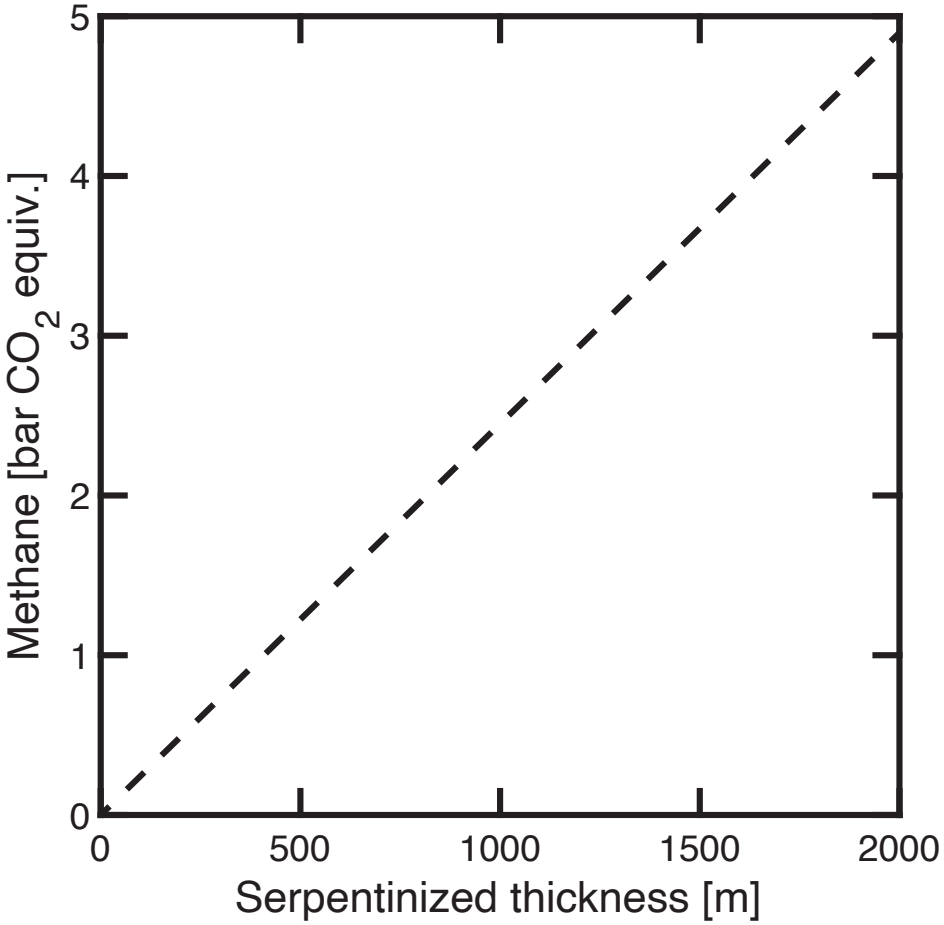


**Figure 2.7:** Abiotic methane formed due to oxidation of iron for a given thickness of serpentinized material. Thickness refers to a Global Equivalent Layer (GEL) and could be distributed throughout the upper crust. The total mass of methane is converted to the equivalent bar of $CO_2$ reduced to form that methane.

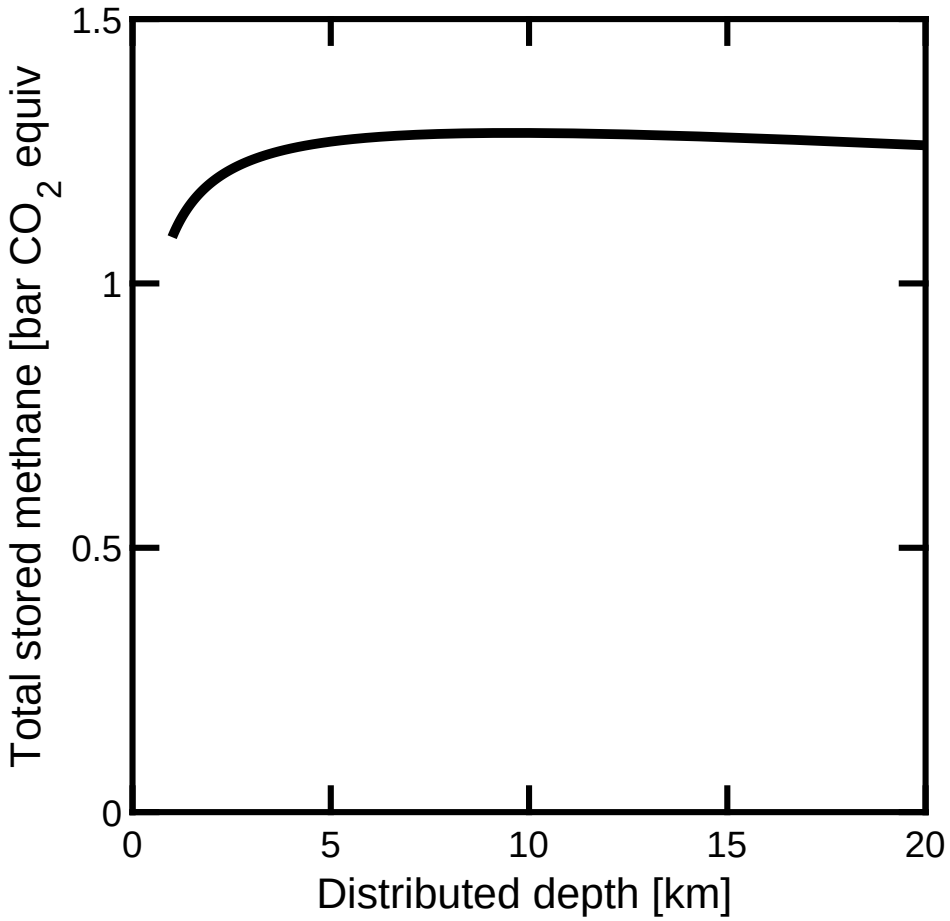


**Figure 2.8:** Total methane stored within smectite clays as a function of the distribution of those clays. The x axis, 'distributed depth', is the depth over which 1000 m of smectite clay is uniformly distributed i.e., a distributed depth of 10 km indicates a 10% abundance of smectite clay over those 10 km.

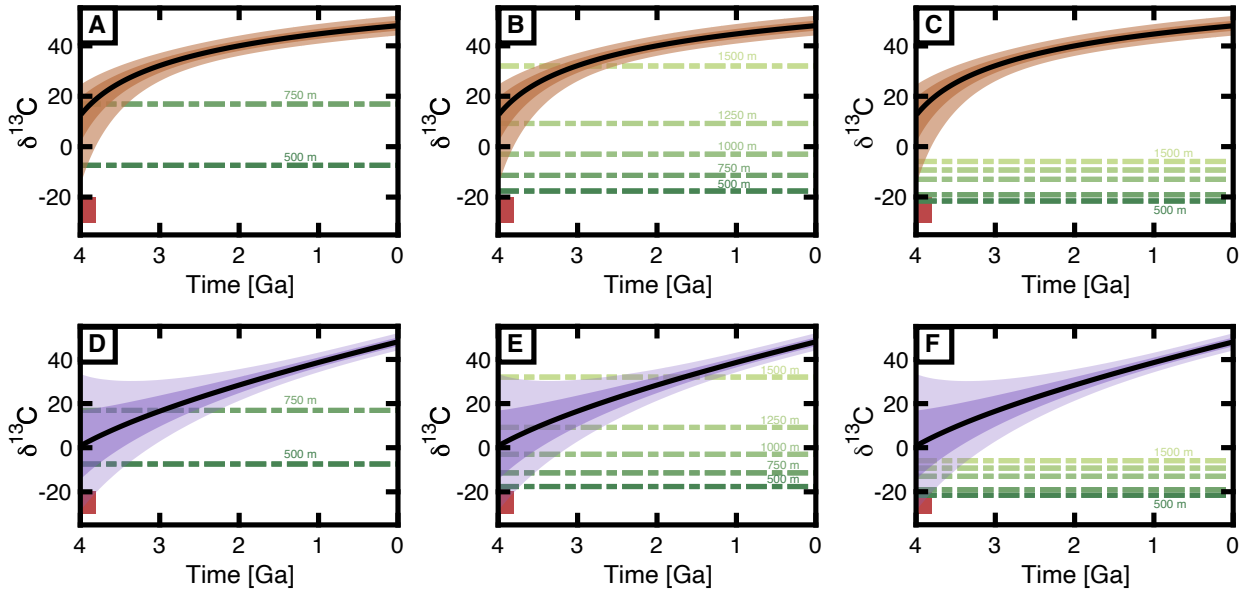


**Figure 2.9:** Modelled loss-driven enrichment of Martian $\delta^{13}$C since 4.0 Ga. The brown field (a, b, and c) is calculated from the loss rates of (Claire et al. 2012; Lo et al. 2021) (Methods). The purple field (d, e, and f) is calculated from (Ramstad et al. 2018) (Methods). The median, one standard deviation, and two standard deviations are displayed as the black line, near-opaque field, and semi-transparent field. The magmatic composition of Martian meteorites is shown as a red bar (Wright et al. 1992). Green dashed lines show the median $\delta^{13}$C predicted by smectite clays of various GEL thicknesses for an initial atmosphere of 1 bar $CO_2$ (a and d), 2 bar $CO_2$ (b and e), and 4 bar CO2 (c and f).

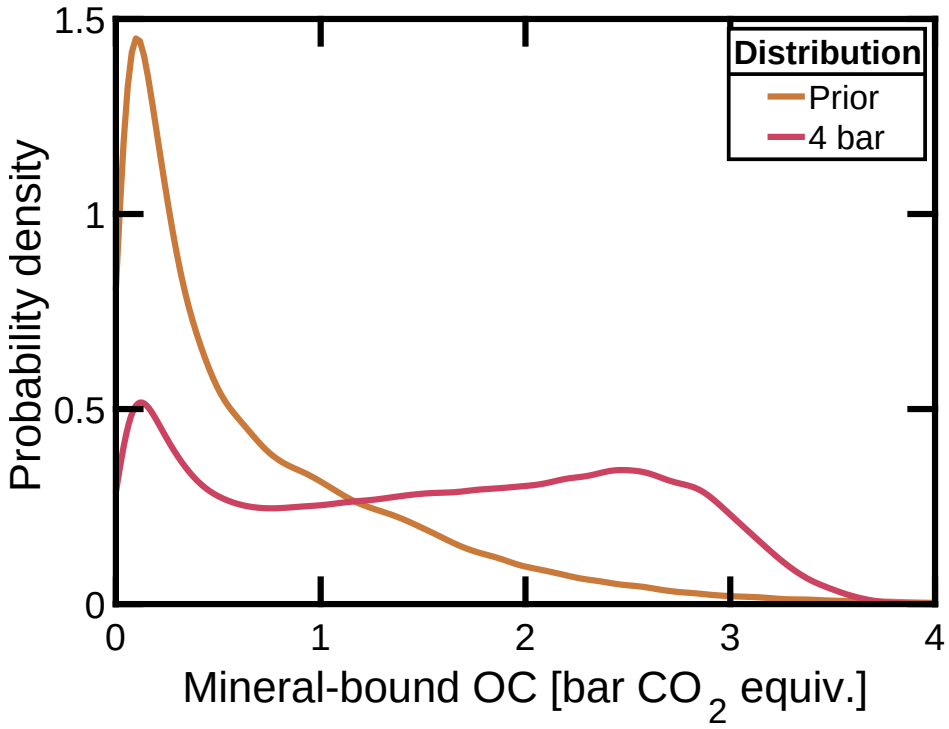


**Figure 2.10:** Prior and 4-bar posterior probability distributions of organic carbon in the Martian crust required to replicate $\delta^{13}$C predicted by atmospheric escape models. The prior distribution (orange line) is calculated according to estimates of H2O in hydrated minerals of the Martian crust (Wernicke and Jakosky 2021; Methods) and converted to organic carbon by the calculations shown in Fig. 2.1b. Posterior distribution (red line) is calculated according to an initial 4 bar atmosphere.

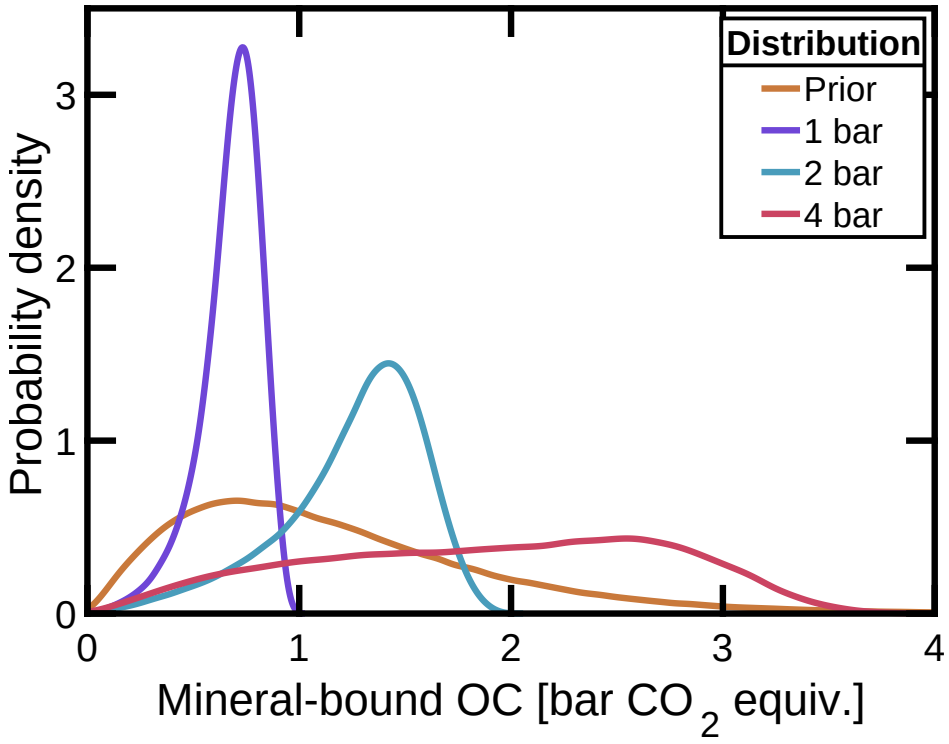


**Figure 2.11:** Near-surface Prior and posterior probability distributions of organic carbon in the Martian crust. The prior distribution (orange line) is calculated according to near-surface estimates of $H_2O$ in the Martian crust (Wernicke and Jakosky 2021; Methods) and converted to organic carbon by the calculations shown in Fig. 2.1b. Posterior distributions are conditional upon an initial one bar atmosphere (purple line) and an initial two bar atmosphere (blue line), and an initial four bar atmosphere (red line). Posterior distributions reflect the organic carbon reservoir required to replicate $\delta^{13}C$ predicted by atmospheric escape models.

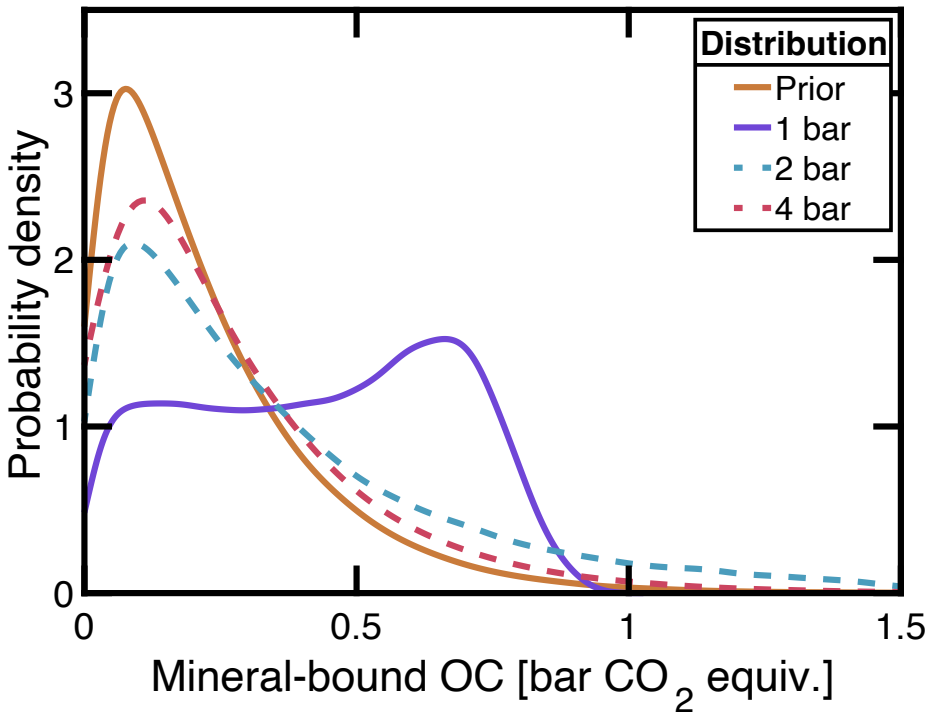


**Figure 2.12:** Hydrated-mineral Prior and posterior probability distributions of organic carbon in the Martian crust. The prior distribution (orange line) is calculated according to near-surface estimates of $H_2O$ in the Martian crust (Wernicke and Jakosky 2021; Methods) and converted to organic carbon by the calculations shown in Fig. 2.1b. Posterior distributions are conditional upon an initial one bar atmosphere (purple line) and an initial two bar atmosphere (blue line), and an initial four bar atmosphere (red line). Posterior distributions reflect the organic carbon reservoir required to replicate $\delta^{13}C$ predicted by atmospheric escape models. Dashed lines reflect those model simulations for which the model is unable to sequester the initial atmosphere within clay minerals i.e. the total clay-bound organic carbon necessary to reconcile modern $\delta^{13}C$ is unlikely given the imposed hydrate-mineral prior.

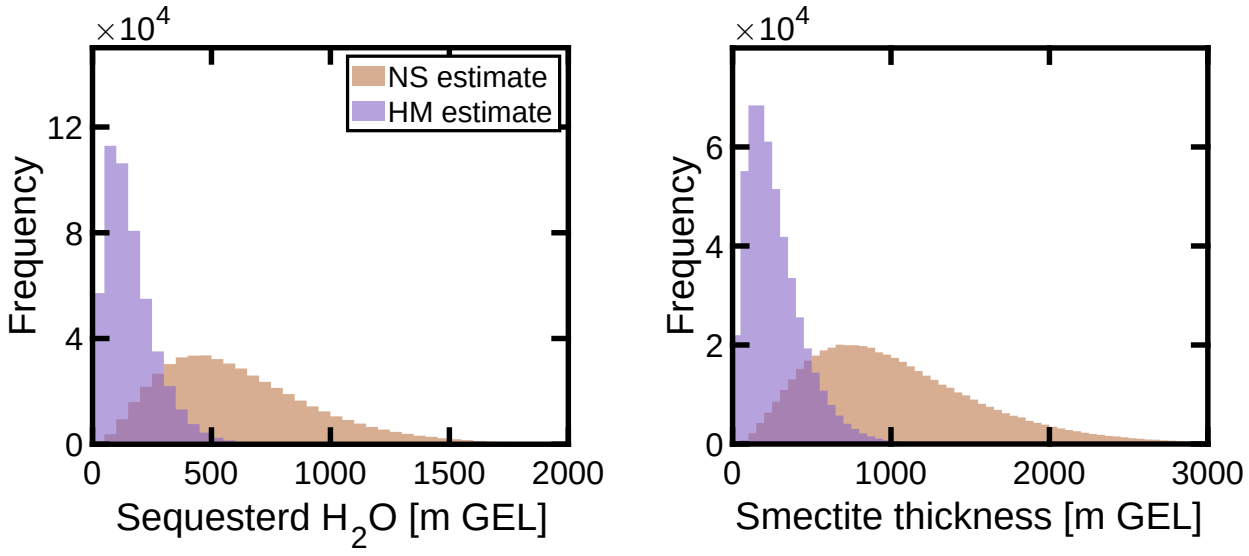


**Figure 2.13:** Probability distribution of crustal $H_2O$ and smectite clay [m global equivalent layer] used as a prior in our inference model, shown as frequency of simulations (n = 500,000). A) $H_2O$ sequestered in the Martian crust replicated from (Wernicke and Jakosky 2021; see their Fig. 4). Brown histogram reflects the estimate based upon near-surface concentration of $H_2O$, extrapolated to depth; purple histogram reflects the estimate based upon the requisite water to form hydrated minerals (HM) at depth. B) Probability distribution of smectite thickness following our conversion from total $H_2O$ to smectite clay (see Methods).

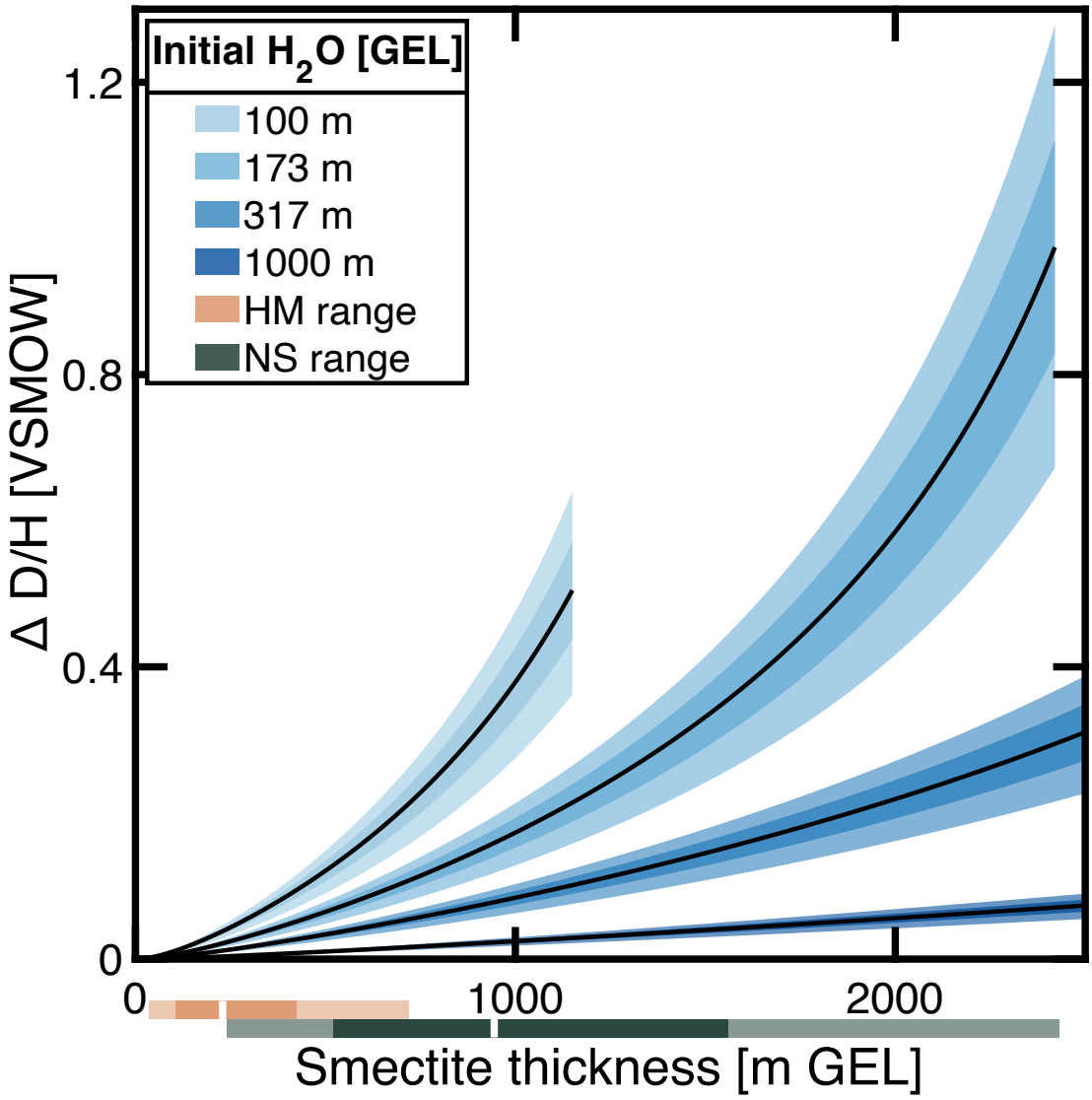


**Figure 2.14:** Predicted change in atmospheric D/H for a variable thickness of smectite clays saturated with abiotic methane. Colored segments reflect different initial thicknesses of atmosphere. Data are shown with median (black line), 1 standard deviation (near-opaque field), and 2 standard deviations (semi-transparent field). The range from 173 – 317 m is the preferred initial $H_2O$ inventory of Wernicke and Jakosky 2021.

| Process | Variable | Mean | Stdev | Distribution | Unit | Reference(s) |
|---|---|---|---|---|---|---|
| Carbon loss | C loss fractionation | 0.6 | | single value | | Hu et al. 2015 |
| Carbon loss | Modern $CO_2$ | 0.054 | | single value | bar | Hu et al. 2015 |
| Carbon loss | Modern $CO_2$ loss | $6.12 \cdot 10^{23}$ | | single value | C atoms/second | Lo et al. 2021 |
| Carbon loss | C loss, lyman power law | 1.5 | 0.25 | lognormal | | See discussion in Hu et al. 2015 |
| Carbon loss | Lyman limit time exponent | -0.86 | | single value | | Claire et al. 2012 |
| Methanogenesis | Carbon fractionation | -14 | 3 | normal distribution | ‰ | Etiope and Whiticar 2019 |
| Methanogenesis | Hydrogen fractionation | -325 | 50 | normal distribution | ‰ | Etiope and Whiticar 2019 |
| Methanogenesis | Forsterite number | 0.6 | | single value | | Koeppen and Hamilton 2008 |
| Methanogenesis | Initial Fe(II)/Fe(TOT) | 1 | | single value | | Charge balance |
| Methanogenesis | Final Fe(II)/Fe(TOT) | 0.4 | | single value | | Tutolo and Tosca 2023 |
| Methanogenesis | Serpentinization Depth | 1 | | Uniform: 0 to 2 | km | Mustard 2019; Tutolo and Tosca 2023 |
| Methane storage | Clay thickness – HM estimate | 315 | 211 | gamma distribution | m | Derived from Wernicke and Jakosky 2021, Fig. 4. |
| Methane storage | Clay thickness – NS estimate | 1,235 | 673 | gamma distribution | m | Derived from Wernicke and Jakosky 2021, Fig. 4. |
| Methane storage | $q$ | 16.6, 10.3, 9.4 | | Single value. SMC, ILL, CHL | kJ/mol | Ji et al. 2012 |
| Methane storage | $\Gamma_{max}$ | 0.38, 0.079, 0.103 | | Single value. SMC, ILL, CHL | mmol/g | Ji et al. 2012 |
| Methane storage | $\Delta S_0$ | -79.5, -65.3, -64.8 | | Single value. SMC, ILL, CHL | J/mol/K | Ji et al. 2012 |

**Table 2.1:** Parameters used in Monte Carlo simulations of abiotic methanogenesis and atmospheric escape.

# Chapter 3

# Reconstructing weathering fluxes associated with the Taconic orogeny, Newfoundland

## 3.1 Abstract

Secular changes in Earth's weatherability have been invoked as a driver of global cooling due to a temporal coincidence between arc-continent collisions and icehouse climates. However, investigating a causality between these tectonic events and cooling requires a quantification of weathering rates for ancient, largely eroded terranes. Here we present a new methodology for estimating changes in silicate weathering rates from the geochemistry of siliciclastic sediments. We show that the amount of CaO and MgO chemically weathered from igneous rocks and deposited as siliciclastic sediment can be estimated to within ∼2.5 wt%. We apply our method to Late Cambrian to Silurian forearc sediments of the Taconic orogeny in Newfoundland, Canada. We show a sharp increase in the silicate weathering rate in the Middle Ordovician, coincident with a decrease in global temperatures inferred through proxy data.

## 3.2 Introduction

Rather than monotonic warming or cooling, Earth's steady-state climate varies over million-year timescales from warm climates to glacial climates (Frakes et al. 1992; Isbell et al. 2003).

This climate variability has been tied to mass extinction (Sheehan 1973; Stanley 2016) and evolution (Raup 1994; Hoffman 2009). The process(es) which drives variations in Earth's climate remains debated (France-Lanord and Derry 1997; Kump et al. 1999; McKenzie et al. 2016; Dalton et al. 2022). At least throughout the Phanerozoic, Earth's glacial climates coincide with arc-continent collisions and ophiolite obductions within the tropical rainbelt (Jagoutz et al. 2016; Macdonald et al. 2019; Park et al. 2020). However, the mechanism (if any) by which these collisions modulate Earth's climate remains unresolved (Guo et al. 2008; Torres et al. 2014; Murray and Jagoutz 2023).

In order to interrogate the causality between arc-continent collision and Earth's climate, we present a method for constraining the silicate weathering flux associated with the weathering of an ancient terrane. Historically, estimates of silicate weathering are either qualitative (Nesbitt and Young 1982; Nesbitt and Wilson 1992) or rely upon direct measurements of the primary rocks from which the siliciclastic sediments are derived (France-Lanord and Derry 1997). Using the geochemistry of immobile (insoluble) elements in a basin sediment, we show it is possible to estimate the average composition of the source rock. Comparing the inferred source rock geochemistry with the residual alkaline earth elements present in the siliciclastic portion of the sedimentary rocks yields a total amount of CaO and MgO transferred to the ocean, per unit mass of sediment. Incorporating the deposition rate of those siliciclastic sediments, we can estimate the $CO_2$ consumption associated with the weathering of that terrane.

We apply our methodology to the allochthonous and autochthonous sediments of the Taconic orogeny in Newfoundland, Canada. The Taconic orogeny began around 488 Ma (Staal et al. 2012), when the southern edge of Laurentia, oriented approximately east-west within the tropical rainbelt (Swanson-Hysell and Macdonald 2017), collided with the Taconic arc system. The collision caused the obduction of ophiolites from the Scandinavian Caledonides to Newfoundland and as far south as Alabama. The erosion of these ophiolites filled the new accommodation with siliciclastic sediments (Waldron et al. 1998; Hibbard 2000). A simplified timeline of these tectonic changes is presented in Fig. 3.1. Given the tempo-

ral coincidence between the Taconic orogeny and the glacial climate during the Hirnantian (Goldberg et al. 2021), an increase in Earth's global *weatherability* has been invoked as the primary driver of Late Ordovician cooling (Kump et al. 1999; Swanson-Hysell and Macdonald 2017; Macdonald et al. 2019).

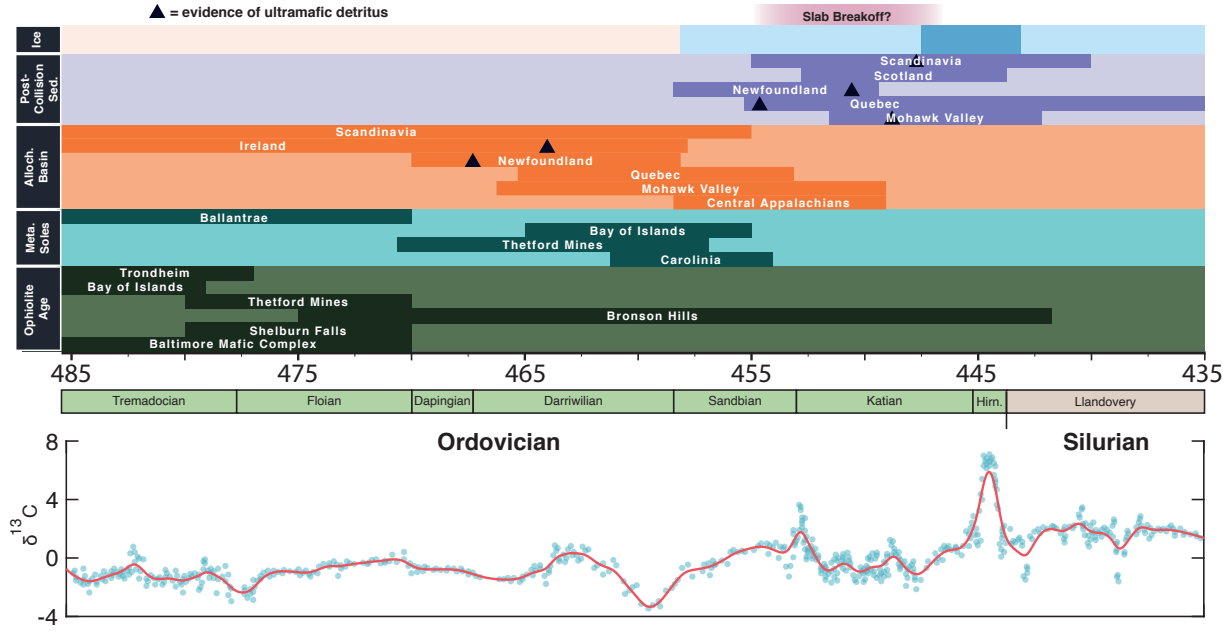


**Figure 3.1:** Expanded timeline of Ordovician arc-continent collisions detailing the crystallisation age, metamorphic age, and basin sediment associated with Taconic and Caledonian orogenies. Ultramafic detritus, as evidenced by detrital chromite, is shown as black triangles within the basin sediments. The presence of polar ice is represented by the pale blue and dark blue bars. See attached Table A.7 for geologic constraints. Isotope record taken from Saltzman et al. 2012.

Our calculations support the hypothesis that Taconic weathering was at least partially responsible for Middle-Late Ordovician cooling. We show that carbon consumption driven by the silicate weathering flux in Newfoundland increased by at least an order of magnitude in the Middle Ordovician (Dapingian and Lower Darriwilian) and during a second pulse (Sandbian and Katian), driven locally by flexural loading of Taconic allochthons in Quebec (White et al. 2020), and recorded by the Long Point group in Newfoundland.

## 3.3 Methods

### 3.3.1 Sedimentary geochemistry and biostratigraphy

The autochthonous and allocations sedimentary rocks in Newfoundland have been well correlated and biostratigraphically dated (e.g., Stevens 1970; James and Stevens 1986; Quinn 1992; Quinn et al. 1999; White et al. 2019). We collected 65 siliciclastic rock samples from coastal outcrops in November 2021, spanning the Late Cambrian to Late Silurian (e.g., Fig. 3.2). These samples include interbedded siliciclastics from pre-collisional platform carbonates (Cow Head Group and equivalent Table Head Group), syn-collisional forearc basin and trench slope sediments (Lower Head Formation, and Goose Tickle Group), and post-collisional foreland basin sediments (Long Point group and Clam Bank Group).

Through a review of the existing literature, we ascribe ages and thicknesses to each group and formation, as well as each 'bed' within the Cow Head Group (James and Stevens 1986). The ages are constrained by biostratigraphic studies of conodonts and graptolites which are correlated to GTS2020 (Gradstein et al. 2020) and detailed in Table 3.5. Similarly, we use best estimates of unit thicknesses (Table 3.5) in order to calculate sedimentation rate per unit area.

We analysed 29 of the samples for whole rock geochemistry. We selected samples from each major unit which showed minimal evidence of secondary alteration. The location and inferred age of each sample is given in Table 3.4. Approximately 50g of each samples was powedered in a tungsten carbide ring and puck mill, homogenised, fused into a glass bead, and measured via X-ray fluorescence at the Hamilton Analytical Lab. Whole rock major element and trace element data are presented in Table 3.1 and 3.2.

### 3.3.2 Carbonate leaching

In order to measure the carbonate composition, we acid leach the samples and analyse the leachate. This step follows the whole rock analysis such that any trace elements which inform

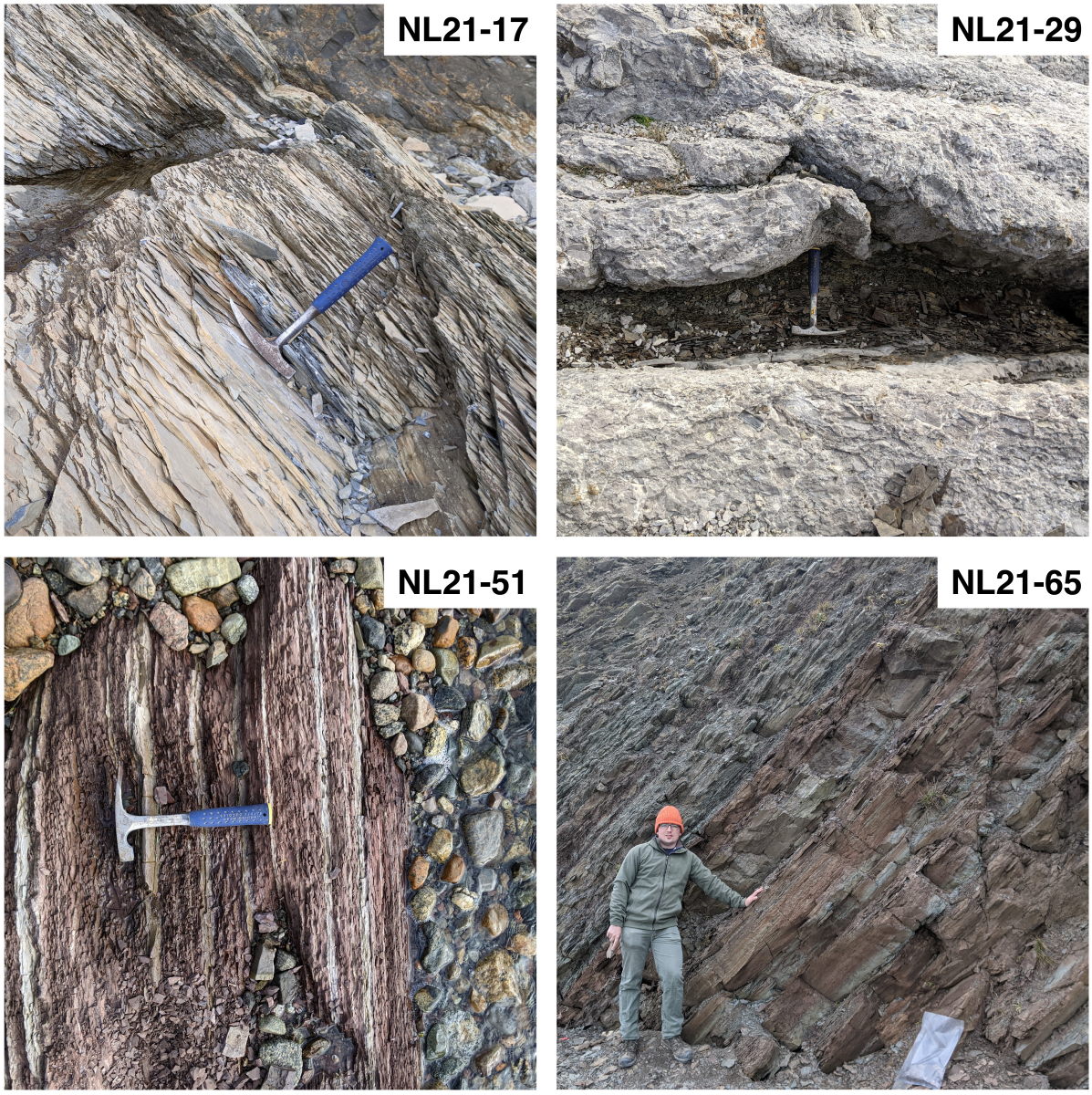


**Figure 3.2:** Four example outcrops collected in November 2021. Rock hammer and field assistant (175 cm) for scale. Blue handle of the hammer points stratigraphically up. NL21-65 is overturned and the up direction is to the right.

the provenance of the rock, particularly those bound on clay surfaces, are unaffected by the acid leach.

For consistency, we leached the same powders which were homogenised and fused for X-ray fluorescence. We weighed approximately 4 mg of each sample and a 0 g procedural blank into 15 ml centrifuge tubes before adding 4 ml of 2.5% acetic acid. Weak acetic acid

was chosen as it has been shown to fully dissolve dolomite without introducing significant contamination from clay minerals (Li et al. 2021). The samples were agitated in an ultrasonic bath for 30 minutes before being centrifuged at 4000 RPM for 5 minutes. The supernatant (acetic acid) of each sample was poured off into a syringe and filtered through a 0.1 $\mu$m Luer Lock filter into a second centrifuge tube. We then added 4 ml of Milli-Q water and agitated the sampled for a further 30 minutes. The samples were then centrifuged for a second time and the supernatant was poured off into a syringe, filtered through a clean 0.1 $\mu$m Luer Lock filter, and added to the centrifuge tube with the acetic acid. The $\sim$8 ml of leachate was dried in a 60°C bead bath for 6 days. The resultant salts were redissolved in 5 ml of 2% nitric acid and vortexed to ensure complete dissolution. A flowchart of the leaching protocol is presented in Fig. 3.3.

We sub-sampled 1 ml aliquots for analysis on the quadrupole ICP-MS at the MIT Center for Environmental Health Sciences. We collected counts of $^{23}$Mg, $^{43}$Ca, and $^{44}$Ca and converted to [Mg] and [Ca] as ppm via a standard calibration curve (Fig. 3.4). We bracketed every five of our samples with a 25% concentration standard (17.678 ppm Mg and 66.567 ppm Ca) to ensure the calibration was consistent throughout.

By subtracting the carbonate fraction from the whole-rock geochemistry and re-normalising the resulting data, we calculate the composition of the siliciclastic sediment.

### 3.3.3 Primary rock inference

We present a new method for calculating the average alkaline earth concentration of the primary rock from which the sediments are derived.

MgO and CaO are particularly soluble during chemical weathering (Nesbitt and Wilson 1992; Nesbitt et al. 1996) and the present concentration holds little information about the initial. However, in unaltered igneous rocks, Mg and Ca correlate well with other, less mobile elements, due to their partitioning during magmatic differentiation. These relationships can be approximately linear, such as the depletion of MgO and Ni during differentiation from

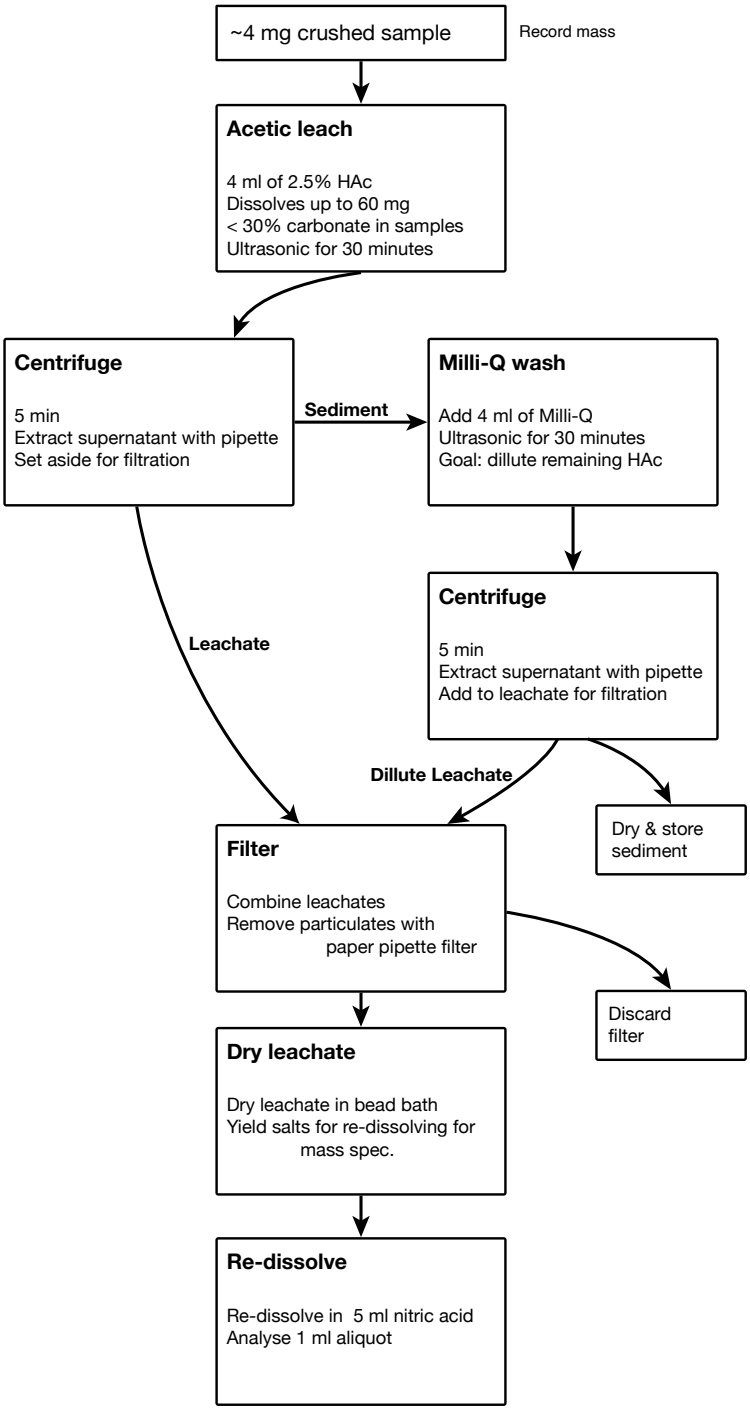


**Figure 3.3:** Protocol for leaching carbonate minerals from mixed siliciclastic samples.

ultramafic to felsic rocks (Fig. 3.13), or non-linear such as the differentiation of $TiO_2$, governed by the crystallisation of Fe-Ti oxides, and CaO, governed by the crystallisation of plagioclase feldspar and clinopyroxene (Fig. 3.13, Jagoutz and Schmidt 2012).

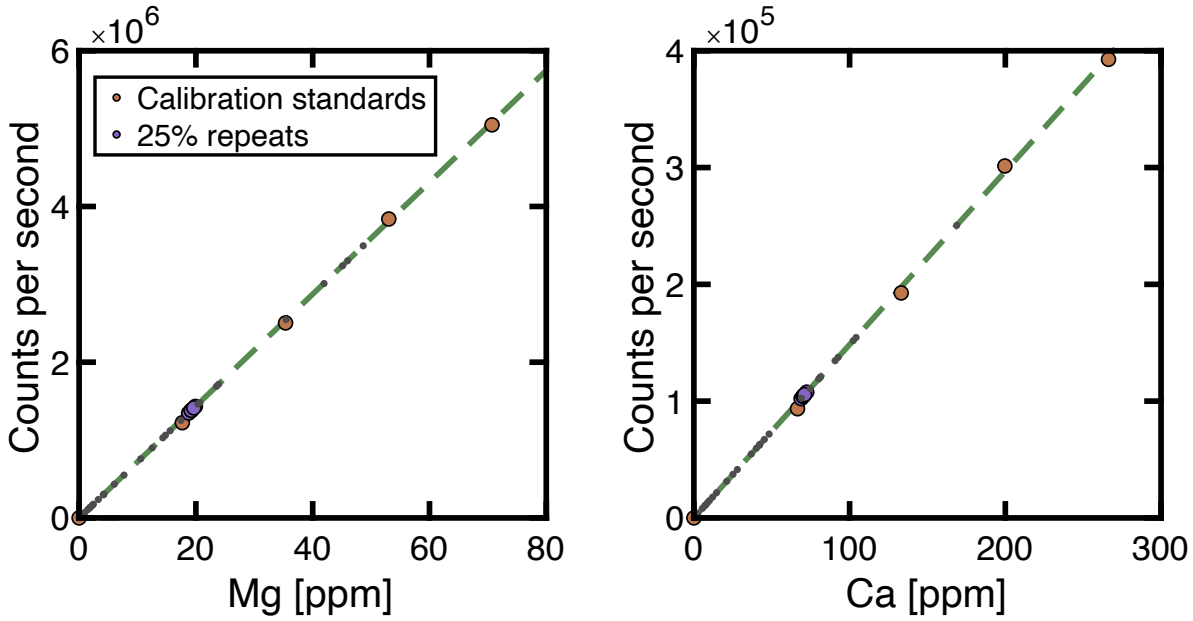


**Figure 3.4:** Calibration curve used for quadrupole ICP-MS analysis of dissolved carbonate. Here we display counts of $^{25}$Mg and $^{43}$Ca. The calibration curve uses standards dissolved volumetrically to 0%, 25%, 50%, 75%, and 100% concentrations. Purple points are repetitions of the 25% standard, conducting periodically throughout analysis of our samples (grey points).

We select the immobile elements $Al_2O_3$, Cr, FeO, Nb, Ni, $TiO_2$, and Zr as predictors in a Guassian process regression (GPR) model. GPR models are probabilistic, machine learning algorithms which assume parameters can be related through Guassian distributions and non-linear covariance functions or *kernels* (Rasmussen and Williams 2006). The specific elements were chosen as predictor variables due to their recalcitrance during weathering and their depletion or enrichment in the crust relative to the mantle (Fig. 3.5).

We create synthetic sedimentary geochemical suites from igneous rock compositions of the PetDB database[1]. For each synthetic suite we mix three samples, one felsic/intermediate, $\vec{F}$, one mafic, $\vec{M}$, and one ultramafic, $\vec{U}$, with uniformly random proportions $(\alpha, \beta, \gamma)$. To simulate the dissolution of mobile elements, we reduce the concentration of the mobile elements MgO, CaO, $Na_2O$, and $K_2O$ ($\vec{C}_{mob}$), by a fourth, independent random variable, $d$

[1]The data were downloaded from the PetDB Database (https://search.earthchem.org/) on 5 October, 2023, using the following parameters: material=igneous, igneous: ultramafic, igneous: mafic, igneous: intermediate, igneous: felsic. Of the ∼20,000 total samples, the dataset contains 503 felsic/intermediate samples, 9051 mafic samples, and 223 ultramafic samples with the necessary set of mobile and immobile geochemical data.

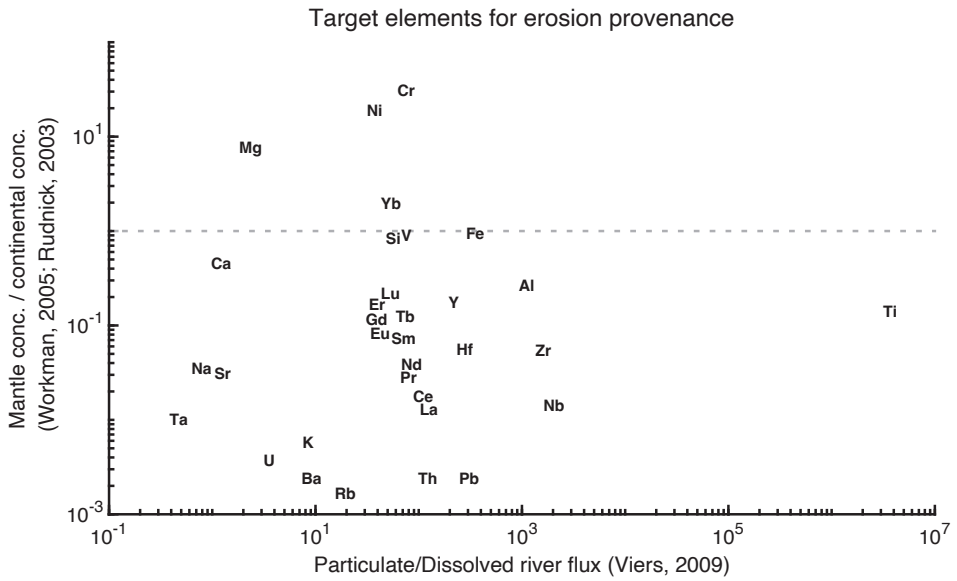


**Figure 3.5:** Scatter diagram showing the utility of commonly analysed elements as indicators of primary lithology. $x$ axis represents the solubility of an element during weathering (data from Viers et al. 2009). $y$ axis shows the relative enrichment or depletion of each element in the continental crust relative to the depleted MORB mantle (Rudnick et al. 2003; Workman and Hart 2005)

(the degree of weathering, Eq. 3.1), which is uniform random between 0 and 1.

$$\vec{C}_{mob} = (1-d)\left(\alpha\vec{F}_{mob} + \beta\vec{M}_{mob} + \gamma\vec{U}_{mob}\right). \tag{3.1}$$

$$\vec{C}_{imm} = \frac{\alpha\vec{F}_{mob} + \beta\vec{M}_{mob} + \gamma\vec{U}_{mob}}{1 - \left(\sum(\alpha\vec{F}_{mob} + \beta\vec{M}_{mob} + \gamma\vec{U}_{mob}) - \sum\vec{C}_{mob}\right)} \tag{3.2}$$

As a result of the dissolution of mobile elements, the concentration of immobile elements increases (Eq. 3.2).

We create 10,000 synthetic geochemical suites in this way. We use 5,000 of the resultant immobile element sets, $\vec{C}_{imm}$, to predict the *initial* CaO and MgO, prior to dissolution. The trained model reports root mean squared errors (RMSE) of 1.47 wt% and 2.37 wt% for CaO and MgO, respectively. The other 5,000 data serve as test data and we present the relationship between predicted and actual values (Fig. 3.6). The CaO and MgO test data are matched with RMSE of 1.54 wt% and 2.38 wt%, respectively.

We apply the trained GPR model on our siliciclastic sediments from Newfoundland to

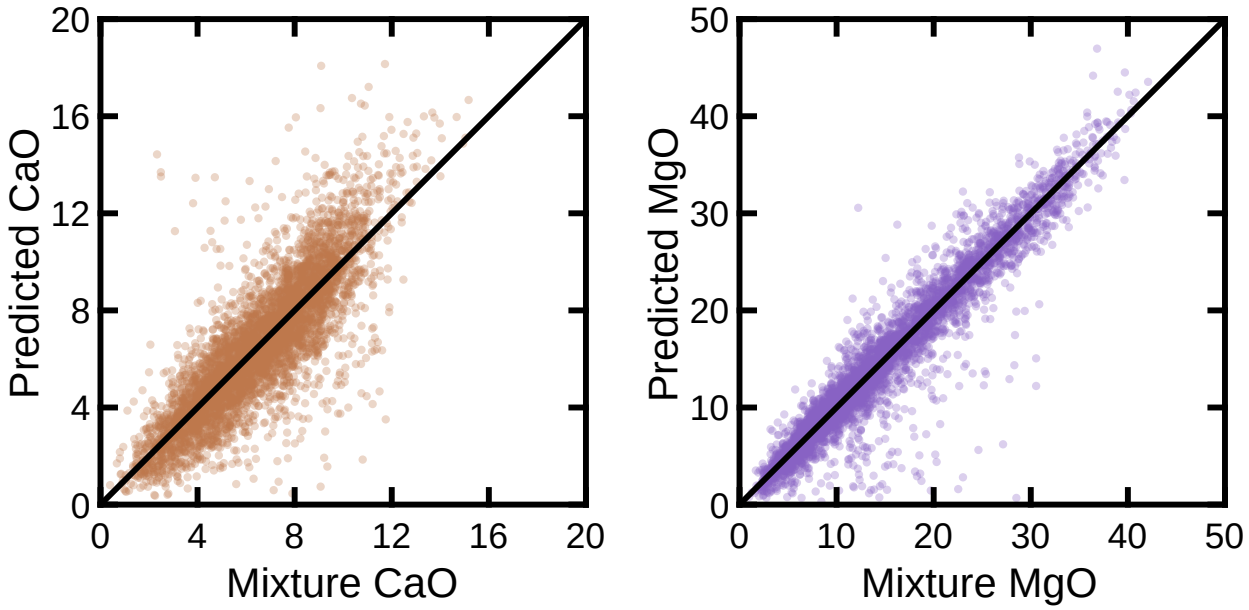


**Figure 3.6:** Test results of our GPR model for inferring CaO and MgO, applied to synthetic geochemical data of mixed ultramafic, mafic, and felsic/intermediate compositions. n = 5000.

estimate the loss of Ca and Mg associated with the emplacement of the Bay of Islands ophiolite.

## 3.4 Results

We report whole rock geochemistry in Table 3.1 and 3.2. Major element carbonate geochemisty is provided in Table 3.3. The carbonate data are presented relative to theoretical dolomite in Fig. 3.7. Of our samples, the highest carbonate concentration was observed in sample NL21-26 and calculated as 61.6% by mass. The inferred siliciclastic composition from subtracting the carbonate composition from the whole rock data is presented stratigraphically in Fig. 3.8.

Starting around 480 Ma, in the upper beds of the Cow Head Group, we see increased CaO and MgO within the silicate fraction of the rocks (Fig. 3.8). The upper limit of CaO increases from $\sim$ 1 wt% to 2-4 wt%. MgO increases from $\sim$ 2 wt% to 4-8 wt%. These increases coincide with similar increases in Ni, Cr, and FeO (Fig. 3.8). Ni and Cr in our samples increase from $\sim$ 50 ppm to 100-150 ppm and $\sim$ 75 ppm to 200-500 ppm, respectively.

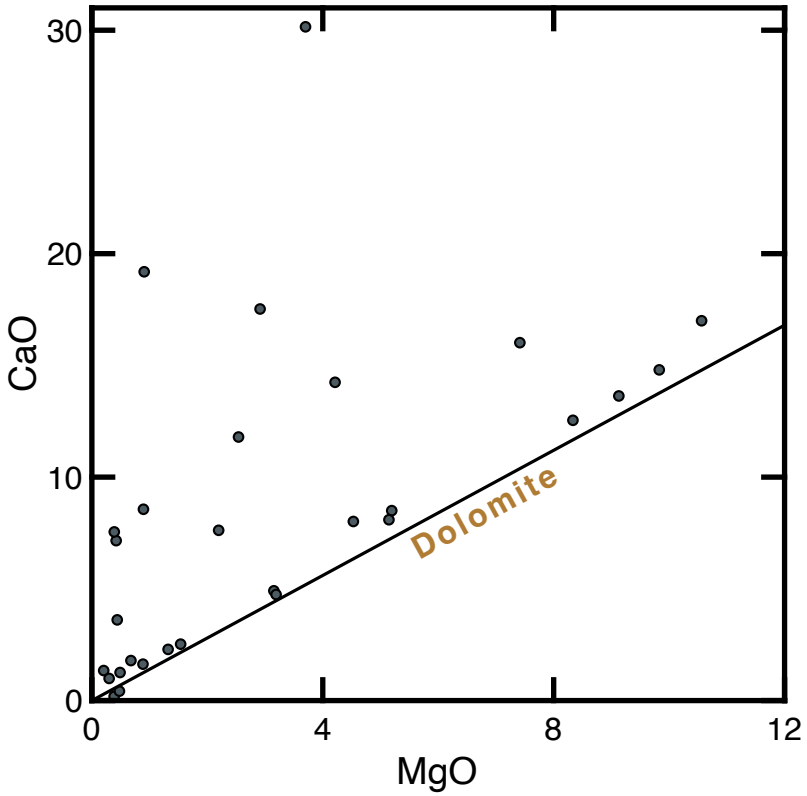


**Figure 3.7:** Scatter diagram showing CaO and MgO of carbonate minerals dissolved from our samples. The theoretical dolomite line (1:1 Ca:Mg) is shown.

FeO increases from an initial $\sim$ 5 wt% in the Late Cambrian and Early Ordovician to 6-7.5 wt% in the Middle and Late Ordovician. The elements which are enriched in felsic rocks (Al, Zr, Nb, Ti; see Fig. 3.5) are less variable, however $Al_2O_3$ decreases from an initial 18 wt% in the lower Cow Head Group (503 Ma) to as low as 7.3 wt% at the top of the Cow Head Group (569 Ma). The Clam Bank Formation of the Late Silurian and Early Devonian (Dix et al. 2023) has a similar geochemistry to the Late Cambrian and Early Ordovician sediments of the lower Cow Head Group, implying a return to a similar weathering lithology.

We use the immobile elements in Fig. 3.8 to predict the initial primary rock composition through the GPR model (Methods). The inferred primary MgO and CaO is shown in Fig. 3.9, showing that primary MgO and CaO increase in tandem with the mafic immobile elements. Primary CaO increases around 480 Ma from $\sim$5 wt% to as much as 13 wt%. The change in primary MgO is less marked than CaO, but still increases from 2.5-4 wt% to 3-7 wt%.

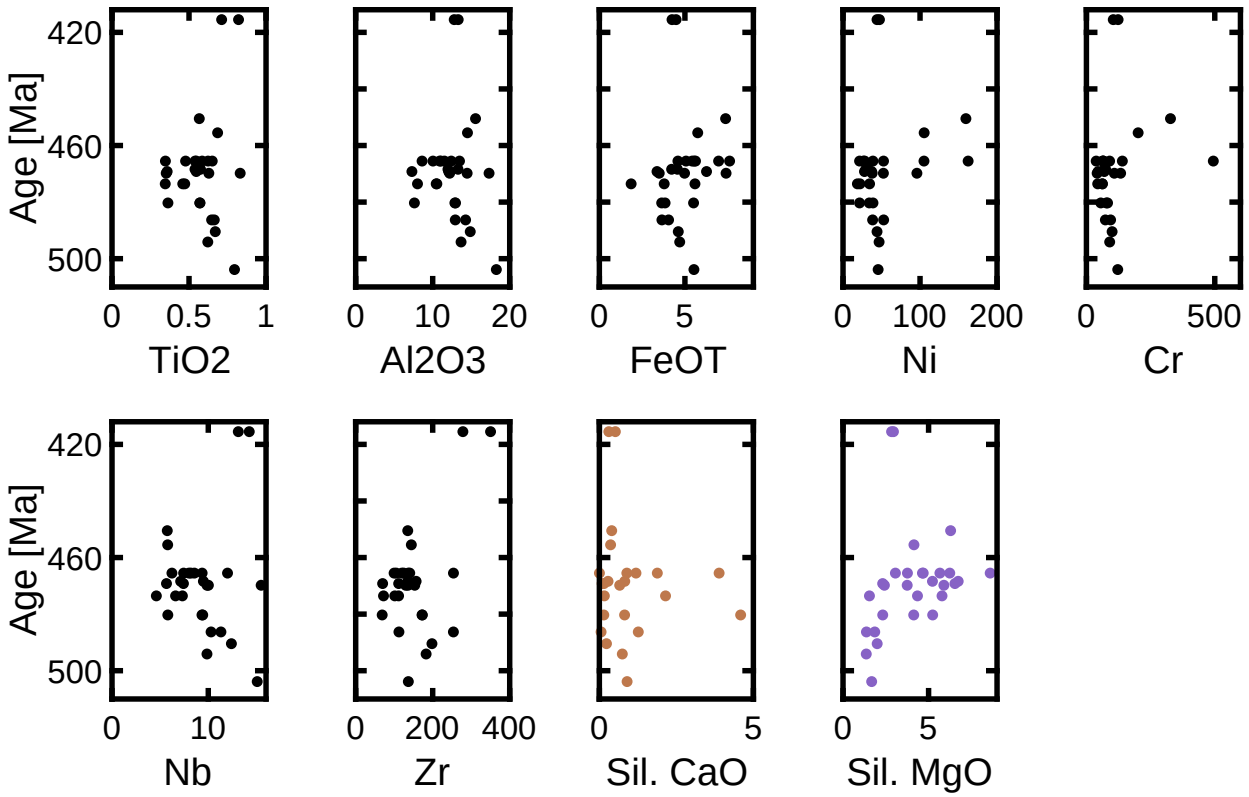


**Figure 3.8:** Immobile elements (predictor variables), CaO, and MgO of Newfoundland sediments. These data are recalculated by subtracting the carbonate chemistry from the whole-rock X-ray fluorescence data and renormalalising the resultant dataset. Ages are derived from the biostratigraphic constraints outlined in Table 3.5

Next, we use the inferred primary geochemistry (Fig. 3.9) and the measured siliciclastic geochemistry (Fig. 3.8) to estimate the loss of CaO and MgO from the weathering of pre-collisional, syn-collisional, and post-collisional rocks (Fig. 3.10). We find predominantly positive values, implying the inferred primary CaO and MgO is greater than the measured values of the siliclastic sediment. Average CaO loss is calculated as 6.2 wt% with peak values of 12.6 and 12.8 wt% between 480 and 470 Ma. Average MgO loss is 0.4 wt% but we calculate multiple negative values, as low as -2.9 wt%, between 480 and 460 Ma (see Discussion). Peak MgO loss is found between 480 and 470 Ma at 4.5 wt%.

By using our compiled thickness and age estimates (Table 3.5), we calculate sedimentation rates. We take average CaO and MgO loss for each sampled unit, interpolating between units for those which were not measured, and multiply by sedimentation rates to calculate a flux of CaO and MgO per unit area. We normalise these values to our maximum calculated CaO

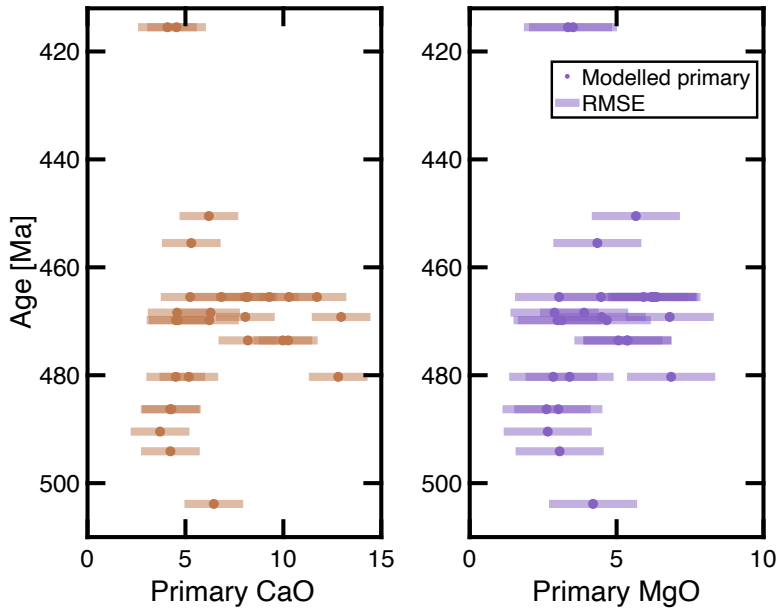


**Figure 3.9:** Primary CaO and MgO inferred through Gaussian Process Regression (Methods). We show the uncertainy according to the RMSE of the trained model.

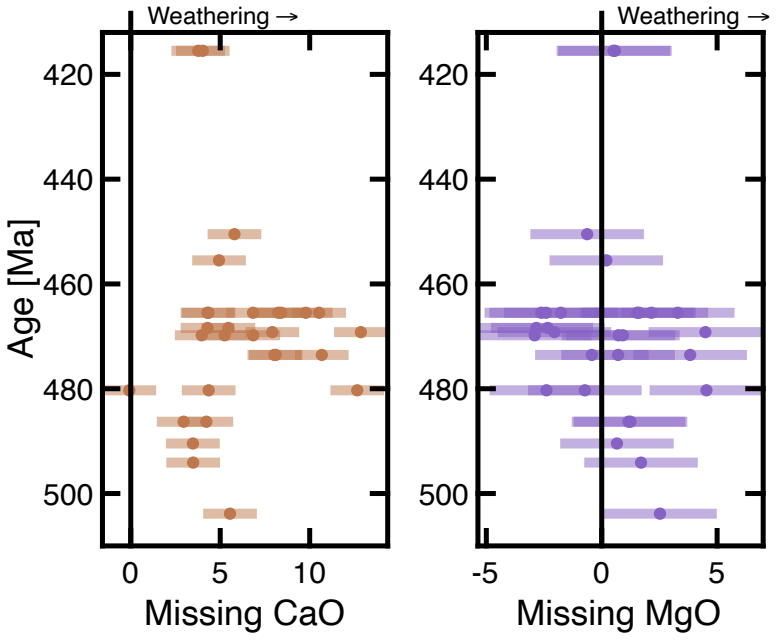


**Figure 3.10:** Inferred primary CaO and MgO minus the measure silicate CaO and MgO. Weathering causes greater loss, pushing values in the positive $x$ direction. Negative $x$ values imply either an underestimation in our inference of initial alkaline earth elements or precipitation of authigenic CaO-rich or MgO-rich silicate minerals, sometimes referred to as 'reverse weathering'.

flux to show the relative weathering flux through time (Fig. 3.11). The low sedimentation rate and inferred CaO-poor primary lithologies yield low relative Ca fluxes (0.07 - 0.2) in the

Late Cambrian and Early Ordovician. The Ca flux increases by a factor of 10 around 470 Ma, beginning with upper Cow Head Group (beds 12-14 (James and Stevens 1986)). These values continue through the Lower Head Formation until 463 Ma prior to a depositional hiatus (the Taconic unconformity). The Loudres Formation of the Long Point Group (458 - 453 Ma) has a low sedimentation rate and low depletion in CaO, yielding low fluxes of Ca (Fig. 3.11 and Fig. 3.10). However, the high sedimentation rate of the Winterhouse Formation (453-448 Ma) drives high Ca fluxes, reaching the maximum normalised value of 1. In comparison, Mg fluxes are muted and consistently less than 8% of the maximum Ca flux. The most notable feature of our inferred Mg flux is the -0.16 flux of Mg in bed 14 of the Cow Head Group (469-468 Ma). This negative value implies a net consumption of Mg by the sedimentary rocks (see Discussion).

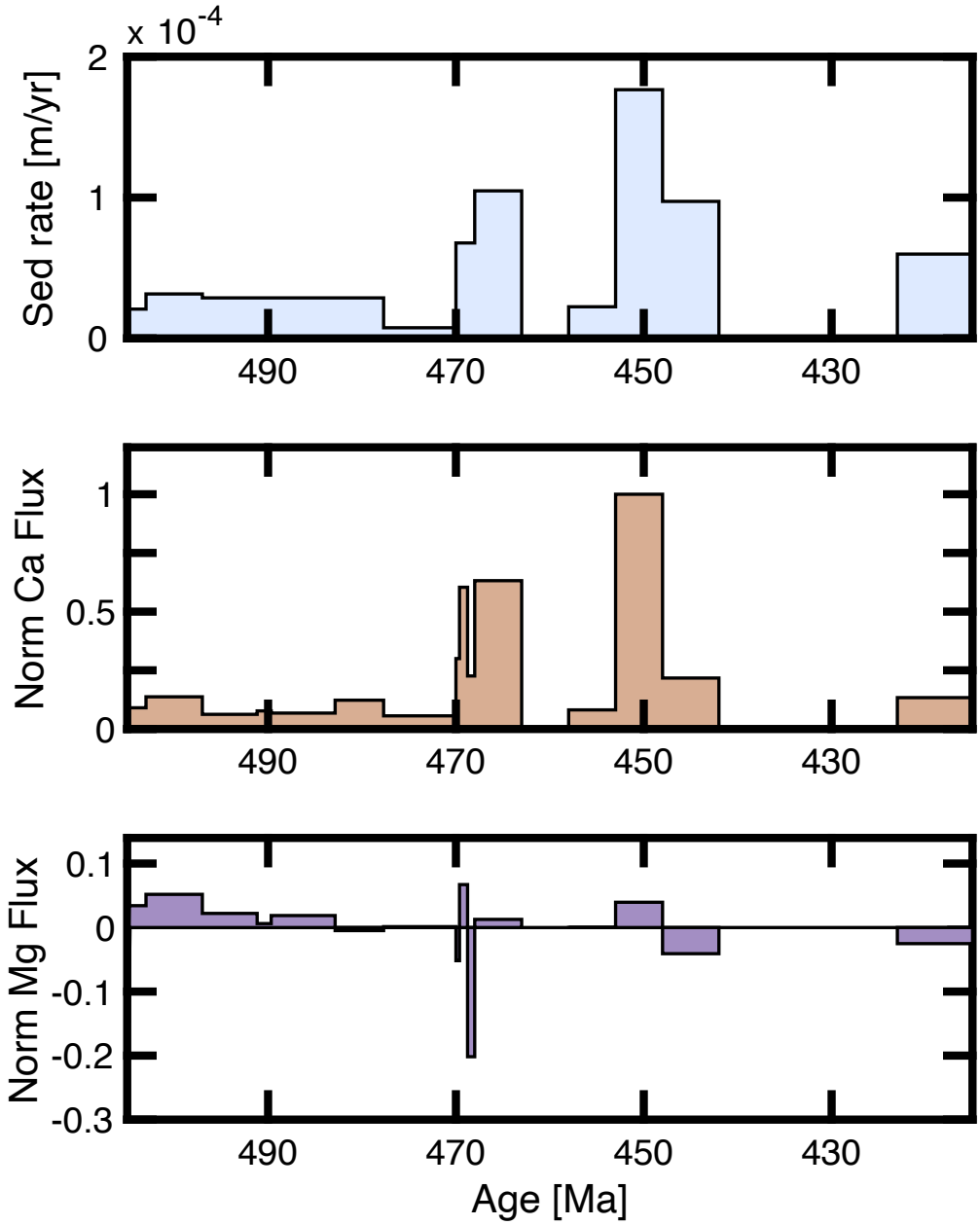


**Figure 3.11:** Calculated flux of sediment (a), Ca (b), and Mg (c) from the weathering and erosion of Newfoundland terranes. Ca and Mg fluxes are normalised to the maximum flux of Ca to show the relative weathering rate through time.

| | Major elements (wt % oxides) | | | | | | | | | | |
|---|---|---|---|---|---|---|---|---|---|---|---|
| **Sample** | **SiO2** | **TiO2** | **Al2O3** | **FeO*** | **MnO** | **MgO** | **CaO** | **Na2O** | **K2O** | **P2O5** | **LOI** |
| **21-5** | 62.87 | 0.644 | 13.64 | 5.40 | 0.067 | 4.10 | 1.69 | 2.68 | 2.43 | 0.131 | 5.37 |
| **21-7** | 57.80 | 0.541 | 14.87 | 7.05 | 0.075 | 6.39 | 0.57 | 2.59 | 3.87 | 0.102 | 5.07 |
| **21-8** | 61.30 | 0.490 | 12.08 | 4.15 | 0.020 | 6.29 | 2.78 | 1.24 | 3.47 | 0.140 | 7.29 |
| **21-13** | 68.82 | 0.445 | 9.86 | 3.57 | 0.015 | 4.99 | 1.78 | 0.72 | 2.89 | 0.073 | 5.62 |
| **21-15** | 46.09 | 0.469 | 10.79 | 3.71 | 0.025 | 8.92 | 8.51 | 0.96 | 3.44 | 0.080 | 15.30 |
| **21-16** | 68.20 | 0.565 | 9.10 | 4.16 | 0.049 | 4.65 | 3.61 | 1.82 | 1.36 | 0.099 | 5.69 |
| **21-17** | 32.43 | 0.338 | 7.01 | 2.82 | 0.054 | 12.77 | 15.26 | 0.30 | 2.27 | 0.046 | 25.71 |
| **21-19** | 35.96 | 0.284 | 6.59 | 4.14 | 0.080 | 13.45 | 13.66 | 0.41 | 1.32 | 0.058 | 23.32 |
| **21-20** | 40.53 | 0.387 | 8.52 | 2.92 | 0.020 | 1.75 | 19.65 | 0.12 | 5.09 | 0.094 | 17.55 |
| **21-21** | 38.75 | 0.411 | 9.12 | 2.83 | 0.026 | 4.14 | 17.67 | 0.17 | 4.67 | 0.087 | 19.83 |
| **21-26** | 21.53 | 0.296 | 6.80 | 2.06 | 0.031 | 4.32 | 30.49 | 0.09 | 4.45 | 0.099 | 28.08 |
| **21-27** | 42.76 | 0.417 | 8.35 | 2.36 | 0.033 | 5.41 | 15.06 | 0.30 | 4.93 | 0.149 | 18.02 |
| **21-29** | 62.62 | 0.637 | 13.70 | 3.88 | 0.018 | 1.61 | 1.04 | 0.42 | 8.73 | 0.187 | 4.42 |
| **21-30** | 39.28 | 0.414 | 9.40 | 2.78 | 0.036 | 8.99 | 11.82 | 0.49 | 4.49 | 0.116 | 20.68 |
| **21-34** | 74.38 | 0.320 | 7.42 | 1.72 | 0.013 | 2.75 | 1.64 | 0.41 | 2.46 | 0.052 | 7.88 |
| **21-35** | 57.02 | 0.258 | 5.26 | 2.43 | 0.023 | 4.21 | 11.86 | 0.47 | 1.40 | 0.222 | 14.40 |
| **21-39** | 65.36 | 0.308 | 6.47 | 3.09 | 0.040 | 2.39 | 7.28 | 0.38 | 3.66 | 0.470 | 7.14 |
| **21-40** | 51.91 | 0.476 | 10.75 | 4.59 | 0.100 | 6.60 | 5.60 | 0.36 | 5.84 | 0.114 | 12.42 |
| **21-44** | 44.92 | 0.339 | 7.78 | 4.13 | 0.523 | 9.42 | 9.68 | 0.39 | 3.18 | 0.065 | 18.68 |
| **21-49** | 61.54 | 0.526 | 11.61 | 6.02 | 0.014 | 6.76 | 0.56 | 0.88 | 3.30 | 0.112 | 6.88 |
| **21-50** | 28.96 | 0.268 | 5.58 | 1.97 | 0.135 | 13.70 | 17.38 | 0.59 | 1.49 | 0.214 | 28.87 |
| **21-51** | 30.46 | 0.303 | 6.38 | 3.11 | 0.225 | 12.58 | 15.79 | 0.43 | 2.37 | 0.083 | 27.21 |
| **21-52** | 38.38 | 0.190 | 4.73 | 2.78 | 0.162 | 9.99 | 16.67 | 0.51 | 1.11 | 0.137 | 24.13 |
| **21-55** | 53.31 | 0.455 | 10.47 | 6.42 | 0.255 | 6.37 | 4.60 | 0.36 | 3.80 | 0.107 | 13.24 |
| **21-57** | 66.28 | 0.551 | 10.26 | 5.22 | 0.040 | 3.56 | 1.32 | 0.73 | 2.32 | 0.107 | 8.70 |
| **21-62** | 58.25 | 0.286 | 9.92 | 2.84 | 0.038 | 4.16 | 7.03 | 0.07 | 2.66 | 0.104 | 13.17 |
| **21-63** | 49.76 | 0.706 | 14.69 | 6.28 | 0.079 | 3.57 | 7.02 | 0.64 | 3.59 | 0.137 | 12.78 |
| **21-64** | 57.10 | 0.660 | 10.28 | 3.41 | 0.083 | 3.26 | 8.98 | 1.57 | 2.92 | 0.142 | 10.21 |
| **21-65** | 66.67 | 0.675 | 12.63 | 4.25 | 0.047 | 3.18 | 1.55 | 1.79 | 3.40 | 0.137 | 5.14 |

**Table 3.1:** X-ray fluorescence analysis of major elements.

| | Trace elements (ppm) | | | | | | | | | | | | | | | | | | | | | |
|---|---|---|---|---|---|---|---|---|---|---|---|---|---|---|---|---|---|---|---|---|---|---|
| **Sample** | **Ni** | **Cr** | **V** | **Sc** | **Cu** | **Zn** | **Ga** | **Ba** | **Rb** | **Sr** | **Y** | **Zr** | **Hf** | **Nb** | **La** | **Ce** | **Nd** | **Sm** | **Dy** | **Yb** | **Th** | **Pb** |
| **21-5** | 99 | 189 | 107 | 15.6 | 43 | 60 | 14 | 396 | 63 | 129 | 19 | 136 | 3.7 | 5.4 | 24 | 48 | 23 | 4.0 | 3.4 | 1.4 | 8 | 13 |
| **21-7** | 152 | 313 | 96 | 21.8 | 23 | 75 | 19 | 425 | 61 | 173 | 18 | 129 | 3.5 | 5.5 | 37 | 63 | 24 | 3.3 | 3.2 | 1.6 | 7 | 18 |
| **21-8** | 29 | 68 | 115 | 10.8 | 22 | 74 | 14 | 647 | 123 | 125 | 15 | 143 | 3.0 | 6.5 | 28 | 51 | 24 | 4.3 | 2.8 | 1.2 | 10 | 16 |
| **21-13** | 32 | 59 | 213 | 9.5 | 55 | 102 | 12 | 373 | 110 | 72 | 9 | 105 | 2.3 | 6.9 | 19 | 40 | 14 | 2.6 | 2.1 | 2.2 | 10 | 15 |
| **21-15** | 39 | 81 | 101 | 9.7 | 48 | 51 | 13 | 436 | 116 | 112 | 12 | 97 | 2.4 | 7.5 | 23 | 34 | 15 | 2.2 | 2.5 | 1.6 | 6 | 11 |
| **21-16** | 147 | 448 | 87 | 11.7 | 22 | 50 | 11 | 301 | 39 | 129 | 16 | 230 | 5.8 | 7.4 | 16 | 39 | 14 | 2.0 | 2.9 | 1.5 | 7 | 9 |
| **21-17** | 15 | 47 | 36 | 5.4 | 7 | 28 | 9 | 217 | 87 | 100 | 10 | 71 | 2.3 | 6.2 | 17 | 34 | 14 | 2.6 | 2.1 | 0.9 | 5 | 2 |
| **21-19** | 23 | 39 | 41 | 4.9 | 7 | 49 | 7 | 148 | 48 | 95 | 11 | 59 | 1.8 | 4.4 | 15 | 34 | 11 | 2.2 | 2.3 | 2.0 | 5 | 5 |
| **21-20** | 29 | 56 | 74 | 5.8 | 20 | 59 | 10 | 294 | 70 | 150 | 10 | 114 | 3.2 | 6.1 | 15 | 37 | 12 | 2.3 | 2.3 | 1.5 | 5 | 18 |
| **21-21** | 27 | 61 | 70 | 6.6 | 20 | 26 | 12 | 270 | 78 | 123 | 9 | 121 | 3.5 | 7.6 | 14 | 33 | 15 | 3.1 | 2.2 | 1.9 | 7 | 17 |
| **21-26** | 17 | 45 | 33 | 2.0 | 11 | 17 | 10 | 191 | 44 | 291 | 8 | 51 | 1.7 | 5.6 | 19 | 31 | 12 | 2.4 | 2.1 | 1.8 | 3 | 7 |
| **21-27** | 25 | 48 | 261 | 5.8 | 30 | 65 | 11 | 396 | 81 | 109 | 14 | 164 | 4.0 | 6.6 | 17 | 36 | 16 | 3.2 | 3.0 | 1.7 | 5 | 19 |
| **21-29** | 51 | 90 | 193 | 11.1 | 77 | 38 | 19 | 493 | 124 | 69 | 14 | 108 | 3.1 | 10.9 | 17 | 39 | 14 | 2.6 | 2.8 | 1.1 | 12 | 26 |
| **21-30** | 16 | 60 | 59 | 6.6 | 8 | 21 | 13 | 394 | 101 | 92 | 11 | 125 | 3.5 | 6.8 | 16 | 33 | 14 | 2.7 | 2.4 | 1.8 | 8 | 5 |
| **21-34** | 17 | 41 | 78 | 6.8 | 54 | 45 | 9 | 351 | 86 | 58 | 6 | 67 | 2.0 | 4.3 | 8 | 19 | 7 | 1.9 | 1.6 | 1.6 | 5 | 7 |
| **21-35** | 27 | 33 | 103 | 6.2 | 48 | 73 | 7 | 268 | 45 | 204 | 15 | 50 | 1.9 | 4.1 | 14 | 30 | 14 | 2.7 | 3.1 | 1.5 | 4 | 12 |
| **21-39** | 33 | 48 | 116 | 5.1 | 33 | 169 | 7 | 205 | 52 | 165 | 18 | 58 | 2.0 | 4.9 | 18 | 38 | 19 | 3.6 | 4.1 | 1.1 | 7 | 22 |
| **21-40** | 28 | 65 | 64 | 8.7 | 21 | 50 | 14 | 431 | 131 | 67 | 13 | 144 | 3.7 | 7.9 | 24 | 45 | 18 | 3.1 | 2.8 | 1.9 | 7 | 9 |
| **21-44** | 16 | 46 | 50 | 6.5 | 5 | 33 | 11 | 252 | 106 | 74 | 12 | 75 | 2.4 | 4.9 | 19 | 38 | 12 | 2.4 | 2.4 | 2.5 | 6 | 5 |
| **21-49** | 27 | 67 | 78 | 11.3 | 6 | 76 | 15 | 294 | 137 | 68 | 12 | 107 | 2.0 | 7.1 | 25 | 48 | 18 | 3.3 | 2.5 | 2.2 | 10 | 7 |
| **21-50** | 14 | 33 | 53 | 2.6 | 14 | 29 | 6 | 186 | 49 | 111 | 15 | 63 | 2.3 | 4.4 | 18 | 37 | 17 | 3.9 | 3.0 | 1.2 | 5 | 18 |
| **21-51** | 12 | 35 | 39 | 4.1 | 4 | 29 | 7 | 231 | 81 | 86 | 12 | 78 | 2.5 | 5.2 | 17 | 38 | 16 | 3.5 | 2.3 | 1.8 | 3 | 9 |
| **21-52** | 15 | 21 | 42 | 3.4 | 26 | 35 | 5 | 159 | 35 | 130 | 12 | 69 | 2.4 | 3.4 | 11 | 31 | 12 | 2.7 | 2.6 | 1.0 | 3 | 12 |
| **21-55** | 44 | 55 | 69 | 9.4 | 42 | 61 | 12 | 369 | 150 | 57 | 15 | 101 | 2.2 | 7.2 | 28 | 65 | 25 | 4.4 | 2.9 | 1.1 | 10 | 14 |
| **21-57** | 99 | 132 | 94 | 13.2 | 28 | 67 | 14 | 273 | 81 | 53 | 14 | 99 | 2.9 | 7.5 | 20 | 44 | 20 | 4.3 | 2.8 | 1.8 | 7 | 11 |
| **21-62** | 31 | 34 | 70 | 9.3 | 27 | 48 | 10 | 295 | 81 | 123 | 18 | 110 | 3.2 | 8.0 | 23 | 43 | 19 | 3.7 | 3.3 | 2.9 | 12 | 44 |
| **21-63** | 81 | 113 | 117 | 16.0 | 38 | 267 | 19 | 462 | 129 | 86 | 22 | 130 | 3.4 | 13.1 | 41 | 73 | 32 | 5.7 | 3.8 | 1.6 | 14 | 5 |
| **21-64** | 35 | 99 | 68 | 9.2 | 94 | 53 | 11 | 369 | 85 | 140 | 28 | 282 | 7.2 | 11.5 | 32 | 68 | 30 | 5.5 | 4.5 | 2.1 | 11 | 10 |
| **21-65** | 45 | 99 | 79 | 10.8 | 15 | 71 | 17 | 640 | 100 | 154 | 22 | 264 | 6.6 | 12.4 | 32 | 61 | 27 | 4.9 | 3.9 | 2.6 | 11 | 8 |

**Table 3.2:** X-ray fluorescence analysis of trace elements.

| Sample | Weight [mg] | Mg [ppm] | Ca [ppm] | Nitric mass | MgO (wt%) | CaO (wt%) |
|---|---|---|---|---|---|---|
| NL21-05 | 3.983 | 0.970 | 7.573 | 5.04545 | 0.20 | 1.34 |
| NL21-07 | 4.094 | 1.877 | 1.071 | 5.04545 | 0.39 | 0.18 |
| NL21-08 | 4.204 | 7.687 | 15.031 | 5.04545 | 1.54 | 2.53 |
| NL21-13 | 3.961 | 4.170 | 9.141 | 5.04545 | 0.89 | 1.63 |
| NL21-15 | 3.847 | 20.723 | 43.651 | 5.04545 | 4.53 | 8.01 |
| NL21-16 | 4.28 | 2.235 | 21.883 | 5.04545 | 0.44 | 3.61 |
| NL21-17 | 3.859 | 45.106 | 80.853 | 5.04545 | 9.83 | 14.80 |
| NL21-19 | 4.232 | 41.940 | 75.148 | 5.04545 | 8.33 | 12.54 |
| NL21-20 | 3.844 | 4.142 | 104.429 | 5.04545 | 0.91 | 19.19 |
| NL21-21 | 4.137 | 14.336 | 102.634 | 5.04545 | 2.91 | 17.52 |
| NL21-26 | 3.963 | 17.442 | 169.166 | 5.04545 | 3.70 | 30.15 |
| NL21-27 | 4.061 | 20.345 | 81.886 | 5.04545 | 4.21 | 14.24 |
| NL21-29 | 4.125 | 1.466 | 5.783 | 5.04545 | 0.30 | 0.99 |
| NL21-30 | 3.867 | 23.888 | 46.532 | 5.04545 | 5.19 | 8.50 |
| NL21-34 | 3.836 | 6.024 | 12.438 | 5.04545 | 1.32 | 2.29 |
| NL21-35 | 4.146 | 12.526 | 69.229 | 5.04545 | 2.54 | 11.79 |
| NL21-39 | 3.761 | 1.881 | 38.110 | 5.04545 | 0.42 | 7.16 |
| NL21-40 | 4.158 | 15.589 | 28.921 | 5.04545 | 3.15 | 4.91 |
| NL21-44 | 3.846 | 23.536 | 44.061 | 5.04545 | 5.15 | 8.09 |
| NL21-49 | 4.026 | 2.284 | 2.404 | 5.04545 | 0.48 | 0.42 |
| NL21-50 | 3.873 | 48.648 | 93.196 | 5.04545 | 10.56 | 17.00 |
| NL21-51 | 4.237 | 45.996 | 81.772 | 5.04545 | 9.13 | 13.63 |
| NL21-52 | 4.02 | 35.444 | 91.151 | 5.04545 | 7.41 | 16.02 |
| NL21-55 | 3.896 | 14.786 | 26.176 | 5.04545 | 3.19 | 4.75 |
| NL21-57 | 4.093 | 3.292 | 10.373 | 5.04545 | 0.68 | 1.79 |
| NL21-62 | 4.04 | 10.552 | 43.581 | 5.04545 | 2.20 | 7.62 |
| NL21-63 | 3.896 | 1.798 | 41.633 | 5.04545 | 0.39 | 7.55 |
| NL21-64 | 4.009 | 4.259 | 48.592 | 5.04545 | 0.89 | 8.56 |
| NL21-65 | 4.202 | 2.440 | 7.470 | 5.04545 | 0.49 | 1.26 |
| B1 | | 0.016 | 0.130 | | | |

**Table 3.3:** Geochemistry of dissolved carbonates. Analytical uncertainty (RSD) varies between 0.5% and 3% of ppm values. B1 is a procedural blank

## 3.5 Discussion

We infer that the dissolution protocol successfully dissolved the carbonate present in the rocks, regardless of whether the carbonate were dolomite, calcite, or mixed calcite-dolomite (Fig. 3.7). The proximity of the carbonate CaO and MgO data to the dolomite line, even

for high MgO values, implies that the carbonate was dissolved irrespective of the carbonate mineralogy. Those samples with high XRF loss on ignition (LOI) correlate with samples with higher CaO and MgO in the dissolved carbonate analysis (Fig. 3.14). Given complete dissolution, the inferred siliciclastic composition ought to be accurate to within the analytical uncertainty of the ICP-MS analysis ($\leq$0.5 wt%; Table. 3.3). X-ray diffraction of the leached sediments would test the extent of carbonate dissolution but has not been performed at this time.

It follows that the uncertainty in our CaO and MgO loss is primarily derived from the inferred composition of primary rocks from which the sediments are derived. RMSE of 1.45 wt% and 2.37 wt% for CaO and MgO respectively are substantial and make quantitative statements of silicate weathering challenging (Fig. 3.10). Despite this, the highest values of primary MgO and CaO from 480 to 460 Ma are more than 2 RMSE greater than the Late Cambrian and Early Ordovician values (Fig. 3.9). Thus, the observed increase in missing CaO and the increase in variability in missing MgO (Fig. 3.10) likely reflects a genuine change in source lithology and weathering.

The negative values observed in lost MgO (Fig. 3.10) imply that MgO in those siliciclastic sediments is greater than the inferred igneous rock(s) from which the sediment is derived. Residual dolomite could explain this gain in MgO, however, as discussed above, the data suggest that carbonate minerals were fully dissolved and accounted for in our procedure. Further, one would expect missing CaO to show negative values in tandem with the MgO if dolomite were the driving mechanism of this enrichment.

An alternative explanation is that reworking and sorting of the sediments en route to the basin could alter the concentration of immobile elements. Specifically, the relative reduction of concentration in mafic elements (e.g., Cr in chromite, Ti in ilmenite, Ni in smectite clays) relative to felsic elements (Zr in zircon, Al in clay), would lead to an underestimation of MgO in the primary lithology. In Fig. 3.12 we show the elemental ratios of Zr/Sc and Th/Sc relative to turbidites of McLennan et al. 1990. Zr/Sc and Th/Sc have been used as a proxy for secondary weathering and sorting of basin sediments (McLennan et al. 1993).

The proximity of our samples to the line of compositional variation suggests that significant reworking to modify their trace element composition is unlikely.

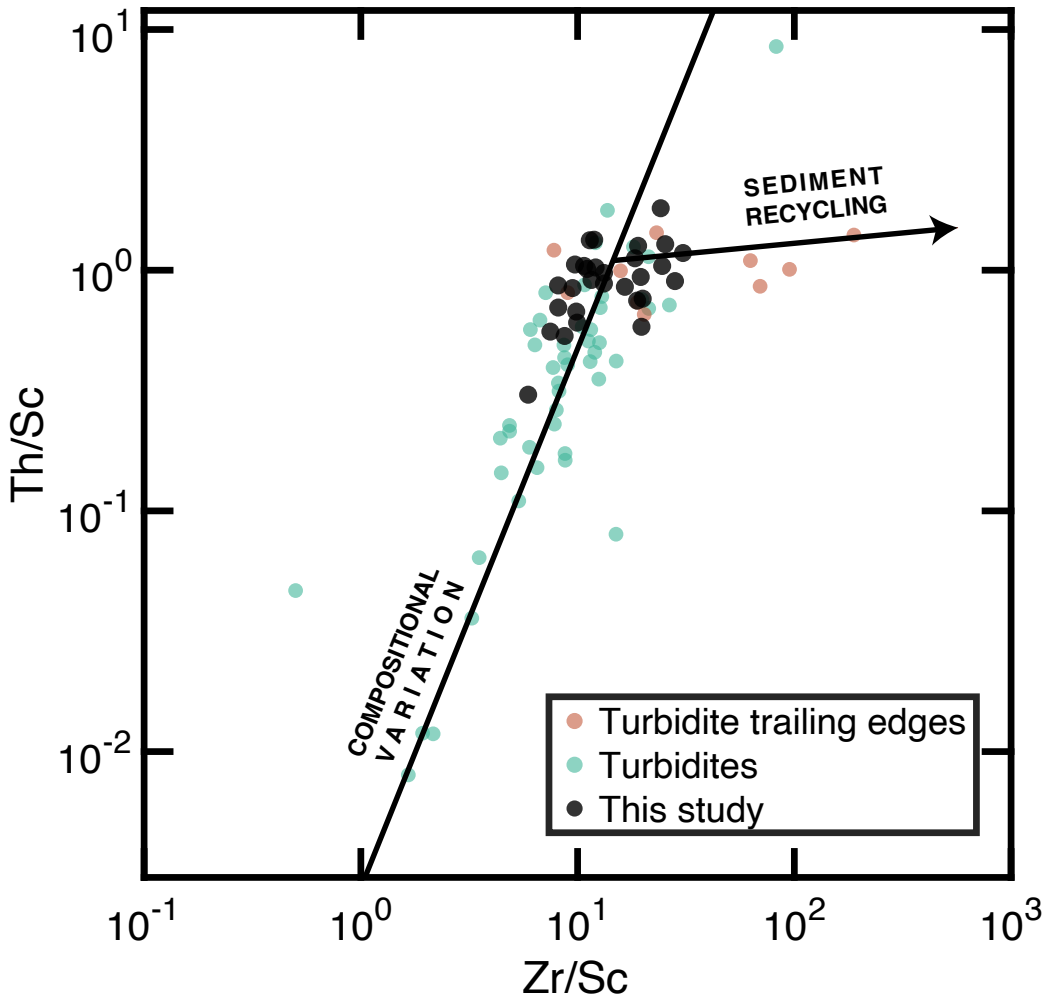


**Figure 3.12:** Comparison of Zr/Sc and Th/Sc in Newfoundland samples (black points) to turbidite samples of McLennan et al. 1990 (turquoise and red dots). Deviation from the line of compositional variation is used to fingerprint samples which have been reworked and sorted (McLennan et al. 1993).

Our favoured explanation for the negative values in lost MgO is that a substantial amount of MgO in our samples is present as authigenic clays. Magnesium is well-mixed in the global ocean with a residence time of 13 Ma (Broecker and Peng 1982) and authigenic clays provide one of the major sink of Mg (Sun et al. 2016). Given the residence time, authigenic clays may have precipitated Mg derived from the weathering of distal terranes, millions of years prior and increased the MgO in the silicate phase of the sedimentary rocks we analysed.

In order to convert missing Ca and Mg to fluxes, we need to estimate the sedimentation

rate through time. We consider the basin to be of fixed size and incorporate the entire thickness of sediment for each unit (both carbonate and siliciclastic). In the case of the Cow Head Group, where the majority of the stratigraphy is limestone and dolostone (James and Stevens 1986), this serves as an upper bound. As such, our sedimentation rates, and hence relative Ca and Mg fluxes before 470 Ma, are overestimates. Despite this overestimate, the first pulse of notable weathering from 470 Ma to 463 Ma, coincides with bed 12 of the Cow Head Group and shows an order of magnitude increase in Ca flux. This increase in weathering precedes the Hirnantian glaciation by at least 10 Ma, but does coincide with a sharp increase in brachiopod $\delta^{18}O$ (Goldberg et al. 2021), reflecting global cooling which may have been a necessary prerequisite to the icehouse climate.

The second pulse in sedimentation, following the hiatus which followed the Lower Head Formation, has been linked with loading of the crust during the later phase of the Taconic orogeny in Quebec (White et al. 2020). We calculate that within Newfoundland alone, the weathering flux in the Winterhouse Formation (453-448 Ma), was 32% greater than the weathering flux during the deposition of the Lower Head Formation. This second pulse aligns more closely with other basin deposits along the Laurentian margin from Quebec to Pennsylvania between 450 and 440 Ma (Hiscott et al. 1986; White et al. 2020).

To quantify these fluxes, we need to assume the aerial size of the basin fill sediment. Given the substantial faulting and erosion since the Ordovician (e.g., Waldron et al. 1998), as well as the lack of outcrop outside of coastal cliff faces, we hold the basin area constant. We assume a collisional length of 500 km (the modern-day length of the western coast of Newfoundland) and a basin width of 150 km (such that the sediment reach as far as Anticosti Island (White et al. 2020)). We calculate maximum $CO_2$ consumption of 1.6 Mt/yr during the Winterhouse Formation and 1.26 Mt/yr during the Lower Head Formation, just 0.7% and 0.5% of modern $CO_2$ consumption by silicate weathering, respectively (Hartmann et al. 2009).

These low carbon consumption rates may point to underestimates within our methodology. This could stem from the lack of Mg depletion in our geochemical analysis (Fig. 3.10);

from underestimating the basin size, which would increase a factor of ∼5 if sedimentation extended from Newfoundland to Pennsylvania, and a factor of ∼15 if sedimentation includes the entire margin from the Scandinavian Caledonides to Alabama (e.g., Macdonald et al. 2019); from the presence of authigenic species, particularly apatite, causing a high CaO concentration which does not represent loss from the source rocks, however $P_2O_5$ concentrations suggest phosphate phases are minor (Table. 3.1); or from a lack of precision in biostratigraphic ages which yield 'smoothed' sedimentation rates and motivate further use of high-precision geochronology to parse rapid pulses of sedimentation (e.g., Macdonald et al. 2017a).

Alternatively, these low consumption rates could imply a different mechanism is required to explain Ordovician cooling. Volcanic outgassing may have been lower, making Earth's climate more sensitive to changes in weathering rate (McKenzie et al. 2016). Or finally, organic carbon burial associated with black shales deposited during the Sandbian and Katian (Hiscott et al. 1986) could provide a secondary contemporaneous sink of carbon associated with the Taconic orogeny (Murray and Jagoutz 2023).

Applying the methodology outlined here along the length of the Taconic and Caledonian foreland basin, in tandem with estimates of organic carbon burial rates, could provide greater insight into the carbon cycle forcings of the Late Ordovician.

## 3.6 Conclusion

We present a new method for constraining the silicate weathering flux associated with siliciclastic sedimentation. The combination of dissolution and provenance modelling provides both qualitative and quantitative estimates on silicate weathering through the history of a sedimentary environment. We apply our method to the Taconic orogeny during the early Palaeozoic in Newfoundland, Canada. We find an order-of-magnitude increase in Ca flux closely following the arrival of the Bay of Islands ophiolite (470 - 463 Ma) but Mg fluxes are minor in comparison to Ca. These low Mg fluxes could reflect the precipitation of clay

minerals following deposition. The influence of changing weathering fluxes over Ordovician climate could be further constrained by the application of our method along the entirety of the Taconic foreland basin.

## 3.7 Supplemental Information

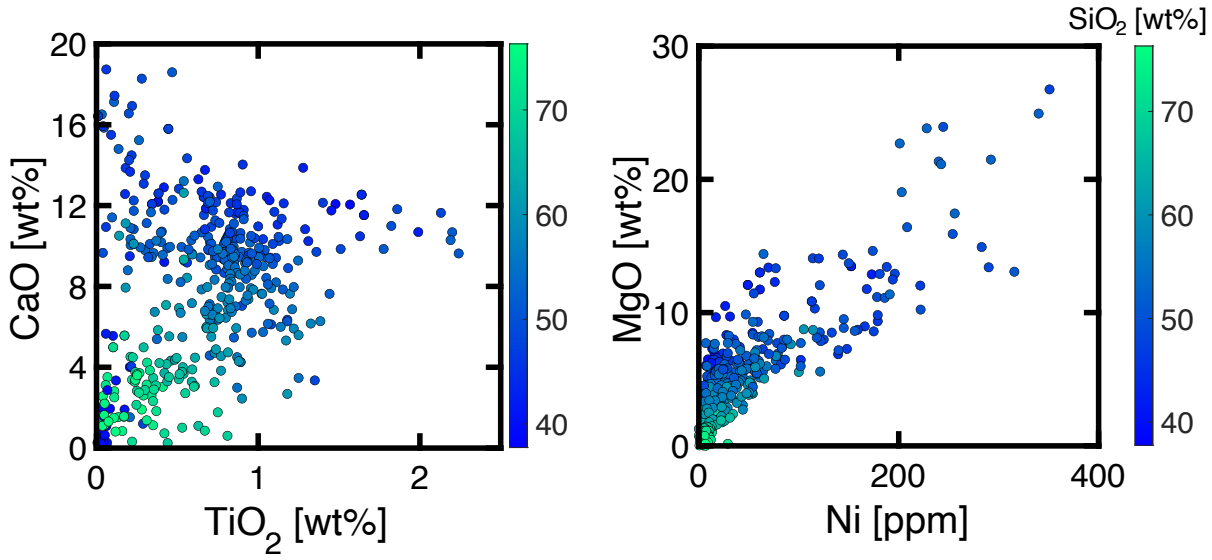


**Figure 3.13:** Example magmatic differentiation trends showing CaO vs $TiO_2$ (left) and MgO and Ni (right), coloured by $SiO_2$. CaO is partitioned into the melt until the saturation of plagioclase and clinopyroxene and enriched by the crystallisation of other minerals. $TiO_2$ behaves somewhat similarly but is governed by the precipitation of Fe-Ti oxides (e.g., ilmenite). MgO and Ni crystallise early during differentiation in olivine and sulfide minerals, respectively.

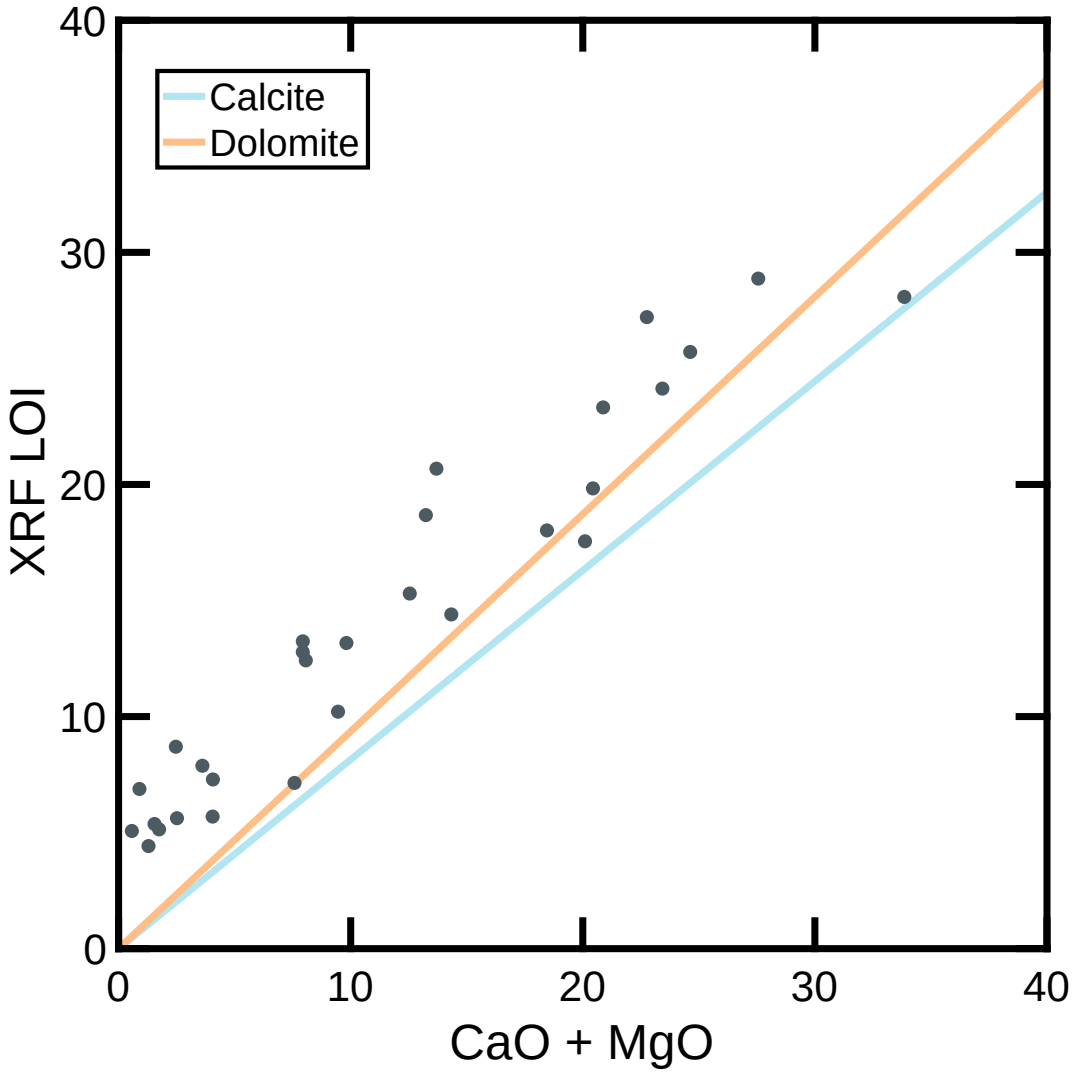


**Figure 3.14:** Scatter diagram showing the sum of CaO and MgO measured in dissolved carbonate compared to the LOI measured during glass bead formation prior to XRF analysis. Coloured lines reflect theoretical composition of calcite and dolomite. Presence of $H_2O$ drives LOI values above that of pure carbonate.

| Sample | Group | Formation | Member | Bed # | Lat | Lon | Max age | Min age |
|---|---|---|---|---|---|---|---|---|
| **NL-21-5** | Long Point | Winterhouse | | | 48.6545 | -58.9989 | 453 | 448 |
| **NL-21-7** | Long Point | Misty Point | | | 48.6557 | -58.9973 | 448 | 442 |
| **NL-21-8** | Cow Head Group | Shallow Bay | Lobster Cove | 14 | 49.6018 | -57.9550 | 468.8 | 468 |
| **NL-21-13** | Cow Head Group | Shallow Bay | Factory Cove | 11 | 49.6022 | -57.9557 | 477.1 | 470 |
| **NL-21-15** | Cow Head Group | Shallow Bay | Factory Cove | 12 | 49.6019 | -57.9555 | 470 | 496.6 |
| **NL-21-16** | Lower Head Sandstone | | | | 49.6016 | -57.9545 | 468 | 463 |
| **NL-21-17** | Lower Head Sandstone | | | | 49.6015 | -57.9543 | 468 | 463 |
| **NL-21-19** | Lower Head Sandstone | | | | 49.6016 | -57.9548 | 468 | 463 |
| **NL-21-20** | Cow Head Group | Shallow Bay | Tuckers Cove | 6 | 49.9230 | -57.8203 | 497 | 491.2 |
| **NL-21-21** | Cow Head Group | Shallow Bay | Tuckers Cove | 7 | 49.9230 | -57.8203 | 491.2 | 489.7 |
| **NL-21-26** | Cow Head Group | Shallow Bay | Downes Point | 3 | 49.9224 | -57.8142 | 504.7 | 503 |
| **NL-21-27** | Cow Head Group | Shallow Bay | Stearing island | 8 | 49.9160 | -57.8313 | 489.7 | 482.9 |
| **NL-21-29** | Cow Head Group | Shallow Bay | Stearing island | 8 | 49.9159 | -57.8306 | 489.7 | 482.9 |
| **NL-21-30** | Cow Head Group | Shallow Bay | Factory Cove | 9 | 49.9160 | -57.8303 | 482.9 | 477.7 |
| **NL-21-34** | Cow Head Group | Shallow Bay | Factory Cove | 11 | 49.9156 | -57.8297 | 477.1 | 470 |
| **NL-21-35** | Cow Head Group | Shallow Bay | Factory Cove | 13 | 49.9160 | -57.8283 | 469.6 | 468.8 |
| **NL-21-39** | Cow Head Group | Green Point Fm | Broom Point | 9 | 49.7650 | -57.9142 | 482.9 | 477.7 |
| **NL-21-40** | Cow Head Group | Green Point Fm | St Pauls | 9 | 49.7645 | -57.9140 | 482.9 | 477.7 |
| **NL-21-44** | Cow Head Group | Green Point Fm | St Pauls | 11 | 49.7637 | -57.9145 | 477.1 | 470 |
| **NL-21-49** | Cow Head Group | Green Point Fm | St Pauls | 13 | 49.8606 | -57.7875 | 469.6 | 468.8 |
| **NL-21-50** | Lower Head Sandstone | | | | 49.8606 | -57.7874 | 468.8 | 468 |
| **NL-21-51** | Lower Head Sandstone | | | | 49.8630 | -57.7843 | 468 | 463 |
| **NL-21-52** | Lower Head Sandstone | | | | 49.7706 | -57.9026 | 468 | 463 |
| **NL-21-55** | Lower Head Sandstone | | | | 49.7838 | -57.8397 | 468 | 463 |
| **NL-21-57** | Lower Head Sandstone | | | | 49.7832 | -57.8400 | 468 | 463 |
| **NL-21-62** | Table Head | Table Cove | | 12 | 48.5916 | -58.9203 | 470 | 469.6 |
| **NL-21-63** | Table Head | Black Cove | | 12 | 48.5920 | -58.9217 | 470 | 469.6 |
| **NL-21-64** | | Clam Bank Fm | | | 48.6512 | -59.0119 | 423 | 408 |
| **NL-21-65** | | Clam Bank Fm | | | 48.6511 | -59.0118 | 423 | 408 |

**Table 3.4:** Sample locations, units, and inferred ages.

| Unit | Max [Ma] | Min [Ma] | Method | Ref | Thick [m] | Ref |
|---|---|---|---|---|---|---|
| **Clam Bank** | 423 | 408 | Ludlow-Pragian | Dix et al. 2023 | 600 | Dix et al. 2023 |
| **Misty Point** | 448 | 442 | Katian-Hirnantian | Quinn et al. 1999; White et al. 2019 | 390 | Quinn et al. 1999 |
| **Winter-house** | 453 | 448 | Katian | Quinn et al. 1999; White et al. 2019 | 590 | Quinn et al. 1999 |
| **Loudres** | 458 | 453 | Sandbian | Quinn et al. 1999; White et al. 2019 | 75 | Bergström et al. 1974 |
| **Lower Head** | 468 | 463 | Dapingian-Darwillian | Quinn et al. 1999; White et al. 2019 | 350 | Quinn 1988 |
| **CH 14** | 468.8 | 468 | Dw1 | Bergström et al. 2009; Stouge 2012 | 18.8 | Stevens 1970; Coniglio 1985 |
| **CH 13** | 469.6 | 468.8 | Interpolation | | 21.1 | James and Stevens 1986 |
| **CH 12** | 470 | 469.6 | Dp1 | Bergström et al. 2009; Stouge 2012 | 9.4 | James and Stevens 1986 |
| **CH 11** | 477.1 | 470 | Interpolation | | 19.5 | James and Stevens 1986 |
| **CH 10** | 477.7 | 477.1 | Fl1 | Bergström et al. 2009; Stouge 2012 | 1.6 | James and Stevens 1986 |
| **CH 9** | 482.9 | 477.7 | Interpolation | | 53.9 | James and Stevens 1986 |
| **CH 8** | 489.7 | 482.9 | Interpolation | | 71.1 | James and Stevens 1986 |
| **CH 7** | 491.2 | 489.7 | Interpolation | | 15.6 | James and Stevens 1986 |
| **CH 6** | 497 | 491.2 | Franconian | Won and Iams 2002 | 60.9 | James and Stevens 1986 |
| **CH 5** | 501.9 | 497 | Interpolation | | 56.3 | James and Stevens 1986 |
| **CH 4** | 503 | 501.9 | Interpolation | | 12.5 | James and Stevens 1986 |
| **CH 3** | 504.7 | 503 | Interpolation | | 12.5 | James and Stevens 1986 |
| **CH 2** | 504.8 | 504.7 | Interpolation | | 0.8 | James and Stevens 1986 |
| **CH 1** | 506 | 504.8 | | White et al. 2019 | 9.4 | James and Stevens 1986 |

**Table 3.5:** Biostratigraphic constraints on the age of units of the Cambrian-Devonian margin of Newfoundland.

# Appendix A

# Supporting tables for Chapter 1

## A.1 Tables

**Table A.1:** Relative dissolution rates of common rock forming minerals.

| **Mineral** | **Dissolution rate ratio k (relative to plagioclase)** | **Reference Mineral[1], Reference** |
|---|---|---|
| Quartz | 0 | Assumed to be stable |
| Muscovite | 0.0053[2] | Biotite, Kalinowski and Schweda 1996 |
| K-Feldspar | 0.13 | Plagioclase, Siegel and Pfannkuch 1984 |
| Biotite & Vermiculite | 1.0 | Plagioclase, Cygan et al. 1989; Kalinowski and Schweda 1996 |
| Plagioclase Feldspar | 1 | Set as 1 |
| Amphibole | 2.0 | Plagioclase, Mast and Drever 1987 |
| Pyroxene | 1.1 | Olivine, Luce et al. 1972 |
| Serpentine | 0.91 | Olivine, Luce et al. 1972 |
| Olivine | 25 | Plagioclase, Siegel and Pfannkuch 1984 |
| Smectite | 0.0053 | Comparable to muscovite. Cama et al. 2000 |

[1]Not all minerals have been compared directly to plagioclase. As such, we use some studies that compare dissolution rates to biotite or olivine, both of which have been measured relative to plagioclase.

[2]Data taken from Siegel and Pfannkuch 1984, parabolic fit added and rate constants compared.

**Table A.2:** Mineral mass data and SSA of each mineral considered here. Right three columns give the modal abundances of three modelled starting lithologies.

| | Mineral density (g/cm3) | Mineral molar mass (g) | Mineral SSA (m2/g) | Starting lithology (in modal fraction) | | |
|---|---|---|---|---|---|---|
| | | | | Peridotite | Basalt | Granite |
| Olivine | 3.3 | 141 | 0.1 | 0.7 | 0.1 | 0 |
| Serpentine | 2.6 | 309 | 8 Crespo et al. 2019 | 0.1 | 0 | 0 |
| Pyroxene | 3.4 | 232 | 0.1 | 0.2 | 0.3 | 0 |
| Plagioclase | 2.6 | 278 | 0.1 | 0 | 0.6 | 0.25 |
| Biotite | 2.8 | 287 | 0.1 | 0 | 0 | 0.125 |
| K-Feldspar | 2.6 | 278 | 0.1 | 0 | 0 | 0.25 |
| Muscovite | 2.8 | 398 | 80 Young 2012 | 0 | 0 | 0.125 |
| Quartz | 2.6 | 60 | 0.1 | 0 | 0 | 0.25 |
| Smectite | 2.3 | 366 | 800 Young 2012 | / | / | / |
| Vermiculite | 2.5 | 441 | 400 Yong et al. 2012 | / | / | / |
| Kaolinite | 2.6 | 258 | 15 Young 2012 | / | / | / |
| Goethite | 3.8 | 89 | 80 Villalobos et al. 2003 | / | / | / |

**Table A.3:** Ages used for the timing of icehouse climates.

| Event Description | Age (Ma) | Stage or Biostrat. Constraint | Method | Ref. |
|---|---|---|---|---|
| Late Ordovician Long: start | 458 | Caradoc | Tillites (N. Af, S. Am) | Frakes et al. 1992 |
| Late Ordovician Long: end | 427.4 | Wenlock | Tillites (N. Af, S. Am) | Frakes et al. 1992 |
| Late Ordovician Short: start | 445.7 | / | Clumped Carbonate Isotopes | Finnegan et al. 2011 |
| Late Ordovician Short: end | 443.5 | / | Clumped Carbonate Isotopes | Finnegan et al. 2011 |
| end-Devonian Long: start | 382.7 | Frasnian | Glacial deposits: S. Am, Cent. Af | Isbell et al. 2003 |
| end-Devonian Long: end | 346.7 | Tournasian | Glacial deposits: S. Am, Cent. Af | Isbell et al. 2003 |
| Fras-Fam Short: start | 372.7 | Triangularis Conodonts | Sea level regression | Johnson et al. 1985 |
| Fras-Fam Short: end | 371.7 | Triangularis Conodonts | Sea level transgression | Johnson et al. 1985 |
| end-Fam Short: start | 360 | Miospores | Diamictites | Lakin 2016 |
| end-Fam Short: end | 358.9 | Miospores | Diamictites | Lakin 2016 |
| Permo-Carbon Long Start | 326 | Namurian | Diamictites | Isbell et al. 2003 |
| Permo-Carbon Long End | 255 | Lopingian | Diamictites | Isbell et al. 2003 |
| Permo-Carb Glacial II | 326 | Namurian | Diamictites (S. Am, Aus., Tibet) | Isbell et al. 2003 |
| Permo-Carb Glacial II | 307 | Early Westphalian | Diamictites (S. Am, Aus., Tibet) | Isbell et al. 2003 |
| Permo-Carb Glacial III | 303.7 | Stephanian | Diamictite (S. Am., Af., Arabia, Ant., Ind., Aus.) | Isbell et al. 2003 |
| Permo-Carb Glacial III | 290.1 | Sakmarian | Diamictite (S. Am., Af., Arabia, Ant., Ind., Aus.) | Isbell et al. 2003 |
| Cenozoic Antarctic | 35 | / | $\delta^{18}O$ | Zachos et al. 2001 |

**Table A.4:** Age constraints used for plotting $\delta^{13}$Cexcursions across Palaeozoic glaciations.

| Excursion | Strat. Height (m) | Age (Ma) | Method | Citation(s) |
|---|---|---|---|---|
| Fras-Fam | 1.1858 | 375.06 | Conodont Biostratigraphy | Buggisch and Joachimski 2006b |
| Fras-Fam | 2.0708 | 374.24 | Conodont Biostratigraphy | Buggisch and Joachimski 2006b |
| Fras-Fam | 2.4071 | 372.77 | Conodont Biostratigraphy | Buggisch and Joachimski 2006b |
| Fras-Fam | 2.8761 | 371.96 | Conodont Biostratigraphy | Buggisch and Joachimski 2006b |
| Fras-Fam | 3.6903 | 370.62 | Conodont Biostratigraphy | Buggisch and Joachimski 2006b |
| end-Fam | -64 | 348 | Kinderhookian-Osagean Boundary | Stolfus et al. 2020b |
| end-Fam | -99.4 | 359.3 | end-Devonian | Stolfus et al. 2020b |
| Late Ord | 19.48 | 445.2 | Base of Hirnantian | LaPorte et al. 2009a |
| Late Ord | 37.79 | 443.1 | Top of Hirnantian | LaPorte et al. 2009a |

**Table A.5:** Compilation of $\delta^{13}$Cfor sections for the four Palaeozoic glaciations with the approximate size of the excursion for each section and the average for each glaciation.

| **Glaciation** | **Source** | $\delta^{13}$**Cexcursion** | **Average** |
|---|---|---|---|
| Hirnantian | LaPorte et al. 2009a: Vinini Creek | 7.6 | 4.68 |
| Hirnantian | LaPorte et al. 2009a: Monitor Range | 6.8 | |
| Hirnantian | LaPorte et al. 2009a: Blackstone River | 5.2 | |
| Hirnantian | Young et al. 2010 | 6.1 | |
| Hirnantian | Demski et al. 2015: M-6-79 | 1.7 | |
| Hirnantian | Demski et al. 2015: M-10-86 | 2.2 | |
| Hirnantian | Gorjan et al. 2012 | 6.2 | |
| Hirnantian | Mauviel and Desrochers 2016 | 3.8 | |
| Hirnantian | Melchin and Holmden 2006: Truro Island | 3 | |
| Hirnantian | Melchin and Holmden 2006: Eleanor Lake | 4.2 | |
| Frasnian | Buggisch and Joachimski 2006b: Benner | 2.6 | 3.275 |
| Frasnian | Buggisch and Joachimski 2006b: Beringhausen | 3.3 | |
| Frasnian | Buggisch and Joachimski 2006b: Vogelsberg | 3.2 | |
| Frasnian | Chen et al. 2005: Baisha | 3 | |
| Frasnian | Chen et al. 2005: Fuhe | 3 | |
| Frasnian | Joachimski et al. 2002: Devil's Gate | 3.7 | |
| Frasnian | Joachimski et al. 2002: Morocco | 5 | |
| Frasnian | Savage et al. 2006 | 2.4 | |
| Famennian | Buggisch and Joachimski 2006b: Benner | 2.5 | 3.771 |
| Famennian | Buggisch and Joachimski 2006b: la Serre | 3 | |
| Famennian | Cramer et al. 2008 | 3.4 | |
| Famennian | Kaiser 2005: Grune Schneid | 0.9 | |
| Famennian | Kaiser 2005: Trolp | 3.2 | |
| Famennian | Kumpan et al. 2014: Gendron Celles | 2.6 | |
| Famennian | Kumpan et al. 2014: les Ardennes | 3.6 | |
| Famennian | Myrow et al. 2013: Cement Creek | 7.7 | |
| Famennian | Qie et al. 2015: Long'an | 3.8 | |
| Famennian | Saltzman 2005 | 7 | |
| Permo-Carb | Grossman et al. 2008b | 3.6 | 3.6 |

**Table A.6:** Compilation of SSA and TOC data

| Ref Method | Sample Number | Formation | SSA | TOC | Section |
|---|---|---|---|---|---|
| Rahman et al. 2017 | M59 | Monterrey | 318 | 11.8 | |
| Rahman et al. 2017 | M62 | Monterrey | 676 | 21.4 | |
| Rahman et al. 2017 | M22 | Monterrey | 459 | 13 | |
| Rahman et al. 2017 | M28 | Monterrey | 477 | 16.9 | |
| Rahman et al. 2017 | M33 | Monterrey | 635 | 22.7 | |
| Rahman et al. 2017 | M21 | Monterrey | 215 | 9.8 | |
| Rahman et al. 2017 | S43 | Stuart Range | 273 | 6.2 | |
| Rahman et al. 2017 | S81 | Stuart Range | 222 | 5.9 | |
| Rahman et al. 2017 | S08 | Stuart Range | 259 | 4.7 | |
| Rahman et al. 2017 | S77 | Stuart Range | 264 | 7.3 | |
| Rahman et al. 2017 | S64 | Stuart Range | 269 | 6.8 | |
| Rahman et al. 2017 | S12 | Stuart Range | 179 | 1.7 | |
| Rahman et al. 2017 | S26 | Stuart Range | 251 | 3.2 | |
| Kennedy and Wagner 2011 | D65R-5W-123-124 | Ivorian Basin | 424 | 11.3 | |
| Kennedy and Wagner 2011 | D65R-5W-124-125 | Ivorian Basin | 385 | 10.9 | |
| Kennedy and Wagner 2011 | D65R-5W-127-128 | Ivorian Basin | 439 | 6.4 | |
| Kennedy and Wagner 2011 | D65R-5W-129-130 | Ivorian Basin | 424 | 5.4 | |
| Kennedy and Wagner 2011 | D65R-5W-136-137 | Ivorian Basin | 399 | 3.9 | |
| Kennedy and Wagner 2011 | D65R-5W-146-147 | Ivorian Basin | 395 | 2.9 | |
| Kennedy and Wagner 2011 | D65R-6W-2-3 | Ivorian Basin | 401 | 2.9 | |
| Kennedy and Wagner 2011 | D65R-6W-9-10 | Ivorian Basin | 357 | 2.9 | |
| Kennedy and Wagner 2011 | D65R-6W-10-11 | Ivorian Basin | 402 | 3 | |
| Kennedy and Wagner 2011 | D65R-6W-12-13 | Ivorian Basin | 403 | 3.7 | |
| Kennedy and Wagner 2011 | D65R-6W-15-16 | Ivorian Basin | 407 | 5.1 | |
| Kennedy and Wagner 2011 | D65R-6W-18-19 | Ivorian Basin | 428 | 6.3 | |
| Kennedy and Wagner 2011 | D65R-6W-23-24 | Ivorian Basin | 409 | 10.8 | |
| Kennedy and Wagner 2011 | D65R-6W-24-25 | Ivorian Basin | 456 | 11.7 | |
| Kennedy and Wagner 2011 | D65R-6W-26-27 | Ivorian Basin | 441 | 12.5 | |
| Kennedy and Wagner 2011 | D65R-6W-29-30 | Ivorian Basin | 456 | 13.5 | |
| Kennedy and Wagner 2011 | D65R-6W-32-33 | Ivorian Basin | 494 | 15.4 | |
| Kennedy and Wagner 2011 | D65R-6W-38-39 | Ivorian Basin | 507 | 16.9 | |
| Kennedy and Wagner 2011 | D65R-6W-41-42 | Ivorian Basin | 573 | 25.1 | |
| Kennedy and Wagner 2011 | D65R-6W-43-44 | Ivorian Basin | 466 | 17.4 | |
| Kennedy and Wagner 2011 | D65R-6W-44-45 | Ivorian Basin | 479 | 14.9 | |
| Kennedy and Wagner 2011 | D65R-6W-47-48 | Ivorian Basin | 405 | 5 | |
| Kennedy and Wagner 2011 | D65R-6W-49-50 | Ivorian Basin | 400 | 5.6 | |
| Kennedy and Wagner 2011 | D65R-6W-51-52 | Ivorian Basin | 426 | 6.1 | |
| Kennedy and Wagner 2011 | D65R-6W-52-53 | Ivorian Basin | 428 | 6.4 | |
| Kennedy and Wagner 2011 | D65R-6W-56-57 | Ivorian Basin | 409 | 5.1 | |
| Kennedy and Wagner 2011 | D65R-6W-57-58 | Ivorian Basin | 427 | 4 | |

| | | | | | |
|---|---|---|---|---|---|
| Kennedy and Wagner 2011 | D65R-6W-61-62 | Ivorian Basin | 407 | 4.8 | |
| Kennedy and Wagner 2011 | D65R-6W-66-67 | Ivorian Basin | 411 | 4.7 | |
| Kennedy and Wagner 2011 | D65R-6W-67-68 | Ivorian Basin | 416 | 4.2 | |
| Kennedy and Wagner 2011 | D65R-6W-70-71 | Ivorian Basin | 381 | 3.9 | |
| Kennedy and Wagner 2011 | D65R-6W-78-79 | Ivorian Basin | 379 | 2.8 | |
| Kennedy and Wagner 2011 | D65R-6W-79-80 | Ivorian Basin | 373 | 2.7 | |
| Kennedy and Wagner 2011 | D65R-6W-82-83 | Ivorian Basin | 373 | 2.9 | |
| Kennedy and Wagner 2011 | D65R-6W-88-89 | Ivorian Basin | 393 | 4.4 | |
| Kennedy and Wagner 2011 | D65R-6W-89-90 | Ivorian Basin | 375 | 4 | |
| Kennedy and Wagner 2011 | D65R-6W-90-91 | Ivorian Basin | 393 | 4.2 | |
| Kennedy and Wagner 2011 | D65R-6W-92-93 | Ivorian Basin | 396 | 5.5 | |
| Kennedy and Wagner 2011 | D65R-6W-96-97 | Ivorian Basin | 447 | 11.3 | |
| Kennedy and Wagner 2011 | D65R-6W-98-99 | Ivorian Basin | 462 | 13.8 | |
| Kennedy and Wagner 2011 | D65R-6W-99-100 | Ivorian Basin | 453 | 13.3 | |
| Kennedy and Wagner 2011 | D65R-6W-100-101 | Ivorian Basin | 485 | 13.9 | |
| Kennedy and Wagner 2011 | D65R-6W-101-102 | Ivorian Basin | 482 | 13.9 | |
| Kennedy and Wagner 2011 | D65R-6W-103-104 | Ivorian Basin | 484 | 15.9 | |
| Kennedy and Wagner 2011 | D65R-6W-106-107 | Ivorian Basin | 443 | 8.8 | |
| Kennedy and Wagner 2011 | D65R-6W-107-108 | Ivorian Basin | 438 | 6.1 | |
| Kennedy and Wagner 2011 | D65R-6W-109-110 | Ivorian Basin | 415 | 5.2 | |
| Kennedy and Wagner 2011 | D65R-6W-113-114 | Ivorian Basin | 429 | 5.4 | |
| Kennedy and Wagner 2011 | D65R-6W-114-115 | Ivorian Basin | 434 | 5.4 | |
| Kennedy and Wagner 2011 | D65R-6W-116-117 | Ivorian Basin | 420 | 5.4 | |
| Kennedy and Wagner 2011 | D65R-6W-120-121 | Ivorian Basin | 410 | 4.8 | |
| Kennedy and Wagner 2011 | D65R-6W-130-131 | Ivorian Basin | 406 | 4.5 | |
| Kennedy and Wagner 2011 | D65R-6W-134-135 | Ivorian Basin | 407 | 4.5 | |
| Kennedy and Wagner 2011 | D65R-6W-145-146 | Ivorian Basin | 379 | 3.6 | |
| Kennedy and Wagner 2011 | D65R-7W-0-2 | Ivorian Basin | 342 | 3.8 | |
| Kennedy and Wagner 2011 | D65R-7W-2-3 | Ivorian Basin | 382 | 4.2 | |
| Kennedy and Wagner 2011 | D65R-7W-4-5 | Ivorian Basin | 392 | 4.8 | |
| Kennedy and Wagner 2011 | D65R-7W-6-7 | Ivorian Basin | 386 | 4.5 | |
| Kennedy and Wagner 2011 | D65R-7W-8-9 | Ivorian Basin | 378 | 5.4 | |
| Kennedy and Wagner 2011 | D65R-7W-9-10 | Ivorian Basin | 399 | 6.1 | |
| Kennedy and Wagner 2011 | D65R-7W-10-11 | Ivorian Basin | 406 | 5.6 | |
| Kennedy and Wagner 2011 | D65R-7W-11-12 | Ivorian Basin | 395.3 | 6.9 | |
| Kennedy and Wagner 2011 | D65R-7W-15-16 | Ivorian Basin | 415.3 | 10.9 | |
| Kennedy and Wagner 2011 | D65R-7W-16-17 | Ivorian Basin | 428.2 | 12.1 | |
| Kennedy and Wagner 2011 | D65R-7W-17-18 | Ivorian Basin | 410.2 | 11.5 | |
| Kennedy and Wagner 2011 | D65R-7W-18-19 | Ivorian Basin | 439.5 | 13 | |
| Kennedy and Wagner 2011 | D65R-7W-19-20 | Ivorian Basin | 414.1 | 12.7 | |
| Kennedy and Wagner 2011 | D65R-7W-21-22 | Ivorian Basin | 451.1 | 14.5 | |
| Kennedy and Wagner 2011 | D65R-7W-22-23 | Ivorian Basin | 471.4 | 14 | |

| | | | | | |
|---|---|---|---|---|---|
| Kennedy and Wagner 2011 | D65R-7W-24-25 | Ivorian Basin | 477.5 | 15.4 | |
| Kennedy and Wagner 2011 | D65R-7W-26-27 | Ivorian Basin | 486.9 | 15.7 | |
| Kennedy and Wagner 2011 | D65R-7W-27-28 | Ivorian Basin | 454.9 | 13.2 | |
| Kennedy and Wagner 2011 | D65R-7W-31-32 | Ivorian Basin | 464.9 | 16.3 | |
| Kennedy and Wagner 2011 | D65R-7W-32-33 | Ivorian Basin | 431.6 | 15.2 | |
| Kennedy and Wagner 2011 | D65R-7W-33-34 | Ivorian Basin | 467.4 | 17.5 | |
| Kennedy and Wagner 2011 | D65R-7W-37-38 | Ivorian Basin | 435.6 | 5.1 | |
| Kennedy and Wagner 2011 | D65R-7W-39-40 | Ivorian Basin | 411.1 | 5.5 | |
| Kennedy and Wagner 2011 | D65R-7W-40-41 | Ivorian Basin | 415.8 | 6.2 | |
| Kennedy and Wagner 2011 | D65R-7W-41-42 | Ivorian Basin | 424.5 | 6.3 | |
| Kennedy and Wagner 2011 | D65R-7W-46-47 | Ivorian Basin | 416.7 | 6 | |
| Kennedy and Wagner 2011 | D65R-7W-49-50 | Ivorian Basin | 406.5 | 5.2 | |
| Kennedy and Wagner 2011 | D66R-1W-50-51 | Ivorian Basin | 380.2 | 4.9 | |
| Kennedy and Wagner 2011 | D66R-1W-57-58 | Ivorian Basin | 384 | 4.7 | |
| Kennedy and Wagner 2011 | D66R-1W-74-75 | Ivorian Basin | 399.5 | 4.6 | |
| Kennedy and Wagner 2011 | D66R-1W-79-80 | Ivorian Basin | 390.5 | 5.1 | |
| Kennedy and Wagner 2011 | D66R-1W-82-83 | Ivorian Basin | 401.4 | 6.6 | |
| Kennedy and Wagner 2011 | D66R-1W-85-86 | Ivorian Basin | 417.7 | 7.2 | |
| Kennedy and Wagner 2011 | D66R-1W-86-87 | Ivorian Basin | 435.4 | 9 | |
| Kennedy and Wagner 2011 | D66R-1W-87-88 | Ivorian Basin | 438.2 | 11.1 | |
| Kennedy and Wagner 2011 | D66R-1W-90-91 | Ivorian Basin | 434.6 | 13.5 | |
| Kennedy and Wagner 2011 | D66R-1W-93-94 | Ivorian Basin | 425.9 | 12.6 | |
| Kennedy and Wagner 2011 | D66R-1W-95-96 | Ivorian Basin | 475 | 16.8 | |
| Kennedy and Wagner 2011 | D66R-1W-98-99 | Ivorian Basin | 488 | 18 | |
| Kennedy and Wagner 2011 | D66R-1W-112-113 | Ivorian Basin | 478.6 | 20 | |
| Kennedy and Wagner 2011 | D66R-1W-115-116 | Ivorian Basin | 504.6 | 21.7 | |
| Kennedy and Wagner 2011 | D66R-1W-117-118 | Ivorian Basin | 427.8 | 7.7 | |
| Kennedy and Wagner 2011 | D66R-1W-119-120 | Ivorian Basin | 408.1 | 4.8 | |
| Kennedy and Wagner 2011 | D66R-120-121 | Ivorian Basin | 403.7 | 4.8 | |
| Kennedy and Wagner 2011 | D66R-1W-122-123 | Ivorian Basin | 416.2 | 6 | |
| Kennedy et al. 2014 | n/a | Wyche | 120 | 1.5 | |
| Kennedy et al. 2014 | n/a | Wyche | 125 | 2.56 | |
| Kennedy et al. 2014 | n/a | Wyche | 132 | 2.83 | |
| Kennedy et al. 2014 | n/a | Wyche | 148 | 3.69 | |
| Kennedy et al. 2014 | n/a | Wyche | 99.9 | 4.25 | |
| Kennedy et al. 2014 | n/a | Wyche | 97.6 | 4.64 | |
| Kennedy et al. 2014 | n/a | Wyche | 92.6 | 5.5 | |
| Kennedy et al. 2014 | n/a | Wyche | 103 | 6.95 | |
| Kennedy et al. 2014 | n/a | Wyche | 119 | 7.45 | |
| Kennedy et al. 2014 | n/a | Wyche | 127 | 7.3 | |
| Kennedy et al. 2014 | n/a | Wyche | 127 | 6.62 | |
| Kennedy et al. 2014 | n/a | Wyche | 139 | 6.21 | |

| | | | | | |
|---|---|---|---|---|---|
| Kennedy et al. 2014 | n/a | Wyche | 153 | 6.03 | |
| Kennedy et al. 2014 | n/a | Wyche | 173 | 6.59 | |
| Kennedy et al. 2014 | n/a | Wyche | 174 | 6.68 | |
| Kennedy et al. 2014 | n/a | Wyche | 175 | 6.44 | |
| Kennedy et al. 2014 | n/a | Wyche | 167 | 7.21 | |
| Kennedy et al. 2014 | n/a | Wyche | 164 | 7.16 | |
| Kennedy et al. 2014 | n/a | Wyche | 156 | 7.24 | |
| Kennedy et al. 2014 | n/a | Wyche | 146 | 7.24 | |
| Kennedy et al. 2014 | n/a | Wyche | 142 | 8.07 | |
| Kennedy et al. 2014 | n/a | Wyche | 138 | 8.55 | |
| Kennedy et al. 2014 | n/a | Wyche | 147 | 9.05 | |
| Kennedy et al. 2014 | n/a | Wyche | 149 | 8.79 | |
| Kennedy et al. 2014 | n/a | Wyche | 154 | 7.57 | |
| Kennedy et al. 2014 | n/a | Wyche | 156 | 7.84 | |
| Kennedy et al. 2014 | n/a | Wyche | 157 | 8.28 | |
| Kennedy et al. 2014 | n/a | Wyche | 159 | 8.1 | |
| Kennedy et al. 2014 | n/a | Wyche | 162 | 8.31 | |
| Kennedy et al. 2014 | n/a | Wyche | 162 | 8.67 | |
| Kennedy et al. 2014 | n/a | Wyche | 160 | 7.66 | |
| Kennedy et al. 2014 | n/a | Wyche | 165 | 7.69 | |
| Kennedy et al. 2014 | n/a | Wyche | 169 | 7.78 | |
| Kennedy et al. 2014 | n/a | Wyche | 174 | 8.01 | |
| Kennedy et al. 2014 | n/a | Wyche | 181 | 8.34 | |
| Kennedy et al. 2014 | n/a | Wyche | 178 | 8.7 | |
| Kennedy et al. 2014 | n/a | Wyche | 187 | 8.52 | |
| Kennedy et al. 2014 | n/a | Wyche | 191 | 8.79 | |
| Kennedy et al. 2014 | n/a | Wyche | 193 | 8.67 | |
| Kennedy et al. 2014 | n/a | Wyche | 198 | 8.58 | |
| Kennedy et al. 2014 | n/a | Wyche | 213 | 9.26 | |
| Kennedy et al. 2014 | n/a | Wyche | 220 | 9.14 | |
| Kennedy et al. 2014 | n/a | Wyche | 160 | 9.53 | |
| Kennedy et al. 2014 | n/a | Wyche | 186 | 10 | |
| Kennedy et al. 2014 | n/a | Wyche | 192 | 9.85 | |
| Kennedy et al. 2014 | n/a | Wyche | 184 | 10.4 | |
| Kennedy et al. 2014 | n/a | Wyche | 190 | 10.6 | |
| Kennedy et al. 2014 | n/a | Wyche | 179 | 10.7 | |
| Kennedy et al. 2014 | n/a | Wyche | 206 | 10.9 | |
| Kennedy et al. 2014 | n/a | Wyche | 212 | 10.9 | |
| Kennedy et al. 2014 | n/a | Wyche | 238 | 11.3 | |
| Kennedy et al. 2014 | n/a | Wyche | 237 | 11.3 | |
| Kennedy et al. 2014 | n/a | Wyche | 243 | 11 | |
| Kennedy et al. 2014 | n/a | Wyche | 247 | 11.7 | |

| | | | | | |
|---|---|---|---|---|---|
| Kennedy et al. 2014 | n/a | Wyche | 234 | 12.5 | |
| Kennedy et al. 2014 | n/a | Wyche | 232 | 12.9 | |
| Kennedy et al. 2014 | n/a | Wyche | 244 | 13.2 | |
| Kennedy et al. 2014 | n/a | East Fitts | 105 | 4.31 | |
| Kennedy et al. 2014 | n/a | East Fitts | 117 | 7.24 | |
| Kennedy et al. 2014 | n/a | East Fitts | 127 | 7.72 | |
| Kennedy et al. 2014 | n/a | East Fitts | 132 | 7.9 | |
| Kennedy et al. 2014 | n/a | East Fitts | 132 | 8.1 | |
| Kennedy et al. 2014 | n/a | East Fitts | 165 | 8.01 | |
| Kennedy et al. 2014 | n/a | East Fitts | 123 | 8.31 | |
| Kennedy et al. 2014 | n/a | East Fitts | 138 | 8.87 | |
| Kennedy et al. 2014 | n/a | East Fitts | 134 | 8.96 | |
| Kennedy et al. 2014 | n/a | East Fitts | 134 | 9.41 | |
| Kennedy et al. 2014 | n/a | East Fitts | 141 | 10.1 | |
| Kennedy et al. 2014 | n/a | East Fitts | 151 | 10.5 | |
| Kennedy et al. 2014 | n/a | East Fitts | 147 | 12 | |
| Kennedy et al. 2014 | n/a | East Fitts | 162 | 11.9 | |
| Kennedy et al. 2014 | n/a | East Fitts | 216 | 13.7 | |
| Kennedy et al. 2014 | n/a | East Fitts | 193 | 14.5 | |
| Kennedy et al. 2014 | n/a | East Fitts | 231 | 16.3 | |
| Kennedy et al. 2014 | n/a | Chitwood Harris | 8.52 | 0.519 | |
| Kennedy et al. 2014 | n/a | Chitwood Harris | 19.2 | 0.785 | |
| Kennedy et al. 2014 | n/a | Chitwood Harris | 15.8 | 1.08 | |
| Kennedy et al. 2014 | n/a | Chitwood Harris | 25.9 | 1.38 | |
| Kennedy et al. 2014 | n/a | Chitwood Harris | 22 | 1.91 | |
| Kennedy et al. 2014 | n/a | Chitwood Harris | 25.3 | 1.79 | |
| Kennedy et al. 2014 | n/a | Chitwood Harris | 35.4 | 1.59 | |
| Kennedy et al. 2014 | n/a | Chitwood Harris | 35.4 | 1.97 | |
| Kennedy et al. 2014 | n/a | Chitwood Harris | 30.4 | 2.33 | |
| Kennedy et al. 2014 | n/a | Chitwood Harris | 52.8 | 2.8 | |
| Kennedy et al. 2014 | n/a | Chitwood Harris | 42.7 | 3.9 | |
| Kennedy et al. 2014 | n/a | Chitwood Harris | 60.7 | 4.28 | |
| Kennedy et al. 2014 | n/a | Chitwood Harris | 64 | 4.49 | |
| Kennedy et al. 2014 | n/a | Chitwood Harris | 51.7 | 4.81 | |
| Kennedy et al. 2014 | n/a | Chitwood Harris | 69.6 | 5.11 | |
| Kennedy et al. 2014 | n/a | Chitwood Harris | 59 | 5.29 | |
| Kennedy et al. 2014 | n/a | Chitwood Harris | 66.8 | 5.53 | |
| Kennedy et al. 2014 | n/a | Chitwood Harris | 61.8 | 5.7 | |
| Kennedy et al. 2014 | n/a | Chitwood Harris | 69.6 | 5.88 | |
| Kennedy et al. 2014 | n/a | Chitwood Harris | 82 | 6.47 | |
| Kennedy et al. 2014 | n/a | Chitwood Harris | 117 | 10.2 | |
| Kennedy et al. 2002 | CH-MS-12 | Pierre Shale | 137 | 1.9 | |

| | | | | | |
|---|---|---|---|---|---|
| Kennedy et al. 2002 | CH-MS-11 | Pierre Shale | 162 | 3 | |
| Kennedy et al. 2002 | CH-MS-10 | Pierre Shale | 150 | 2.8 | |
| Kennedy et al. 2002 | CH-MS-9 | Pierre Shale | 137 | 2.9 | |
| Kennedy et al. 2002 | CH-MS-8 | Pierre Shale | 185 | 5.1 | |
| Kennedy et al. 2002 | CH-MS-7 | Pierre Shale | 180 | 5.2 | |
| Kennedy et al. 2002 | CH-MS-6 | Pierre Shale | 218 | 8.5 | |
| Kennedy et al. 2002 | CH-MS-5 | Pierre Shale | 217 | 8.3 | |
| Kennedy et al. 2002 | CH-MS-4 | Pierre Shale | 222 | 8.4 | |
| Kennedy et al. 2002 | CH-MS-3 | Pierre Shale | 235 | 9.1 | |
| Kennedy et al. 2002 | CH-MS-2 | Pierre Shale | 253 | 8.3 | |
| Kennedy et al. 2002 | CH-MS-1 | Pierre Shale | 158 | 5 | |
| Kennedy et al. 2002 | CH-SS-16 | Pierre Shale | 242 | 13 | |
| Kennedy et al. 2002 | CH-SS-15 | Pierre Shale | 266 | 11 | |
| Kennedy et al. 2002 | CH-SS-14 | Pierre Shale | 198 | 9.2 | |
| Kennedy et al. 2002 | CH-SS-13 | Pierre Shale | 245 | 9.5 | |
| Kennedy et al. 2002 | CH-SS-12 | Pierre Shale | 211 | 9.2 | |
| Kennedy et al. 2002 | CH-SS-11 | Pierre Shale | 195 | 7.9 | |
| Kennedy et al. 2002 | CH-SS-10 | Pierre Shale | 190 | 3.7 | |
| Kennedy et al. 2002 | CH-SS-9 | Pierre Shale | 185 | 4.4 | |
| Kennedy et al. 2002 | CH-SS-8 | Pierre Shale | 198 | 8.2 | |
| Kennedy et al. 2002 | CH-SS-7 | Pierre Shale | 190 | 4.8 | |
| Kennedy et al. 2002 | CH-SS-6 | Pierre Shale | 196 | 9 | |
| Kennedy et al. 2002 | CH-SS-5 | Pierre Shale | 215 | 7 | |
| Kennedy et al. 2002 | CH-2-4 | Pierre Shale | 177 | 3.5 | |
| Kennedy et al. 2002 | CH-SS-3 | Pierre Shale | 183 | 6.4 | |
| Kennedy et al. 2002 | CH-SS-2 | Pierre Shale | 198 | 5.9 | |
| Kennedy et al. 2002 | CH-SS-1 | Pierre Shale | 180 | 6.7 | |
| Kennedy et al. 2002 | CH-GS-13 | Pierre Shale | 183 | 3.8 | |
| Kennedy et al. 2002 | CH-GS-12 | Pierre Shale | 205 | 7.2 | |
| Kennedy et al. 2002 | CH-GS-11 | Pierre Shale | 156 | 3.8 | |
| Kennedy et al. 2002 | CH-GS-10 | Pierre Shale | 133 | 3.3 | |
| Kennedy et al. 2002 | CH-GS-9 | Pierre Shale | 88 | 1.3 | |
| Kennedy et al. 2002 | CH-GS-8 | Pierre Shale | 81 | 1.8 | |
| Kennedy et al. 2002 | CH-GS-7 | Pierre Shale | 88 | 1.4 | |
| Kennedy et al. 2002 | Ch-GS-6 | Pierre Shale | 75 | 0.8 | |
| Kennedy et al. 2002 | CH-GS-5 | Pierre Shale | 78 | 1.231 | |
| Kennedy et al. 2002 | CH-GS-4 | Pierre Shale | 80 | 1 | |
| Kennedy et al. 2002 | CH-GS-3 | Pierre Shale | 78 | 0.8462 | |
| Kennedy et al. 2002 | CH-GS-2 | Pierre Shale | 91 | 0.75 | |
| Kennedy et al. 2002 | CH-GS-1 | Pierre Shale | 77 | 0.8 | |
| Kennedy et al. 2002 | Rb-MS-5 | Pierre Shale | 162 | 3.8 | |
| Kennedy et al. 2002 | RB-MS-4 | Pierre Shale | 170 | 4.7 | |

| | | | | | |
|---|---|---|---|---|---|
| Kennedy et al. 2002 | RB-MS-3 | Pierre Shale | 165 | 4.4 | |
| Kennedy et al. 2002 | RB-MS-2 | Pierre Shale | 168 | 6.3 | |
| Kennedy et al. 2002 | RB-MS-1 | Pierre Shale | 193 | 7.3 | |
| Kennedy et al. 2002 | RB-SS-16 | Pierre Shale | 156 | 5.7 | |
| Kennedy et al. 2002 | RB-SS-15 | Pierre Shale | 207 | 8.6 | |
| Kennedy et al. 2002 | RB-SS-14 | Pierre Shale | 177 | 6 | |
| Kennedy et al. 2002 | RB-SS-13 | Pierre Shale | 207 | 8.2 | |
| Kennedy et al. 2002 | RB-SS-12 | Pierre Shale | 206 | 7.2 | |
| Kennedy et al. 2002 | RB-SS-11 | Pierre Shale | 209 | 6.5 | |
| Kennedy et al. 2002 | RB-SS-10 | Pierre Shale | 124 | 4.5 | |
| Kennedy et al. 2002 | RB-SS-9 | Pierre Shale | 207 | 6.3 | |
| Kennedy et al. 2002 | RB-SS-8 | Pierre Shale | 130 | 4.4 | |
| Kennedy et al. 2002 | RB-SS-7 | Pierre Shale | 146 | 3.4 | |
| Kennedy et al. 2002 | RB-SS-6 | Pierre Shale | 199 | 5.4 | |
| Kennedy et al. 2002 | RB-SS-5 | Pierre Shale | 209 | 5.1 | |
| Kennedy et al. 2002 | RB-SS-4 | Pierre Shale | 220 | 7.2 | |
| Kennedy et al. 2002 | RB-SS-3 | Pierre Shale | 151 | 4.6 | |
| Kennedy et al. 2002 | RB-SS-2 | Pierre Shale | 137 | 4.1 | |
| Kennedy et al. 2002 | RB-SS-1 | Pierre Shale | 96 | 1.8 | |
| Kennedy et al. 2002 | RB-GS-3 | Pierre Shale | 161 | 4.6 | |
| Kennedy et al. 2002 | RB-GS-2 | Pierre Shale | 123 | 2 | |
| Kennedy et al. 2002 | RB-GS-1 | Pierre Shale | 132 | 3.9 | |
| Zhu et al. 2020 | T-12 | Zhanhua Sag | 53 | 2.89 | |
| Zhu et al. 2020 | T-16 | Zhanhua Sag | 82.5 | 4.13 | |
| Zhu et al. 2020 | T-19 | Zhanhua Sag | 64.1 | 3.17 | |
| Zhu et al. 2020 | T-23 | Zhanhua Sag | 68.7 | 3.34 | |
| Zhu et al. 2020 | T-29 | Zhanhua Sag | 51.7 | 3.01 | |
| Zhu et al. 2020 | T-31 | Zhanhua Sag | 50.6 | 2.86 | |
| Zhu et al. 2020 | T-35 | Zhanhua Sag | 48.8 | 2.37 | |
| Zhu et al. 2020 | T-44 | Zhanhua Sag | 39.2 | 1.79 | |
| Zhu et al. 2020 | T-47 | Zhanhua Sag | 44.7 | 3.36 | |
| Zhu et al. 2020 | T-51 | Zhanhua Sag | 61 | 3.65 | |
| Zhu et al. 2020 | T-55 | Zhanhua Sag | 29.2 | 2.96 | |
| Zhu et al. 2020 | T-58 | Zhanhua Sag | 48.4 | 4.13 | |
| Zhu et al. 2020 | T-63 | Zhanhua Sag | 53.7 | 3.52 | |
| Zhu et al. 2020 | T-67 | Zhanhua Sag | 56.4 | 2.78 | |
| Zhu et al. 2020 | T-72 | Zhanhua Sag | 73.3 | 4.04 | |
| Zhu et al. 2020 | T-79 | Zhanhua Sag | 64.9 | 4.09 | |
| Zhu et al. 2020 | T-82 | Zhanhua Sag | 62.3 | 3.54 | |
| Zhu et al. 2020 | T-89 | Zhanhua Sag | 33.1 | 2.57 | |
| Zhu et al. 2020 | T-99 | Zhanhua Sag | 39.8 | 3.95 | |
| Zhu et al. 2020 | T-107 | Zhanhua Sag | 23.3 | 1.91 | |

| | | | | | |
|---|---|---|---|---|---|
| Zhu et al. 2020 | T-120 | Zhanhua Sag | 34.9 | 1.38 | |
| Zhu et al. 2020 | T-126 | Zhanhua Sag | 33.8 | 1.36 | |
| Zhu et al. 2020 | T-128 | Zhanhua Sag | 21.8 | 1.35 | |
| Zhu et al. 2020 | T-141 | Zhanhua Sag | 27.1 | 1.68 | |
| Zhu et al. 2020 | T-145 | Zhanhua Sag | 20.9 | 1.32 | |
| Zhu et al. 2020 | T-148 | Zhanhua Sag | 26.2 | 1.37 | |
| Zhu et al. 2020 | T-151 | Zhanhua Sag | 24.2 | 1.28 | |
| Fosu-Duah et al. 2016 | SF1 | Setap Fm. | 21.67 | 0.5 | |
| Fosu-Duah et al. 2016 | SF2 | Setap Fm. | 13.63 | 0.86 | |
| Fosu-Duah et al. 2016 | SF3 | Setap Fm. | 13.98 | 0.99 | |
| Fosu-Duah et al. 2016 | SF4 | Setap Fm. | 19.2 | 1.06 | |
| Fosu-Duah et al. 2016 | SF5 | Setap Fm. | 14.67 | 1.19 | |
| Fosu-Duah et al. 2016 | SF6 | Setap Fm. | 18.86 | 1.22 | |
| Fosu-Duah et al. 2016 | SF7 | Setap Fm. | 18.17 | 1.23 | |
| Fosu-Duah et al. 2016 | SF8 | Setap Fm. | 24.9 | 1.26 | |
| Fosu-Duah et al. 2016 | SF9 | Setap Fm. | 20.27 | 1.32 | |
| Fosu-Duah et al. 2016 | SF10 | Setap Fm. | 14.08 | 1.46 | |
| Fosu-Duah et al. 2016 | SF11 | Setap Fm. | 21.37 | 1.47 | |
| Fosu-Duah et al. 2016 | SF12 | Setap Fm. | 20.97 | 1.6 | |
| Fosu-Duah et al. 2016 | SF13 | Setap Fm. | 24.41 | 2.13 | |
| Fosu-Duah et al. 2016 | SF14 | Setap Fm. | 25.67 | 2.85 | |
| Fosu-Duah et al. 2016 | SF15 | Setap Fm. | 32.03 | 7.9 | |
| Fosu-Duah et al. 2016 | SF16 | Setap Fm. | 64.62 | 12.01 | |
| Baruch et al. 2015 | LV09-1 | Barney Creek Fm. | 25.8 | 0.9 | |
| Baruch et al. 2015 | LV09-2* | Barney Creek Fm. | 31.2 | 2.5 | |
| Baruch et al. 2015 | LV09-3 | Barney Creek Fm. | 39.3 | 3.5 | |
| Baruch et al. 2015 | LV09-4 | Barney Creek Fm. | 65.1 | 3.2 | |
| Baruch et al. 2015 | LV09-5 | Barney Creek Fm. | 61.6 | 3.3 | |
| Baruch et al. 2015 | GR7-1 | Barney Creek Fm. | 76.1 | 2 | |
| Baruch et al. 2015 | GR7-2 | Barney Creek Fm. | 115 | 1.8 | |
| Baruch et al. 2015 | GR7-3* | Barney Creek Fm. | 100.1 | 3.3 | |
| Baruch et al. 2015 | GR7-4 | Barney Creek Fm. | 111.3 | 1.9 | |
| Baruch et al. 2015 | GR7-5 | Barney Creek Fm. | 95.7 | 1.6 | |
| Baruch et al. 2015 | MCA5-1* | Barney Creek Fm. | 52 | 2.8 | |
| Baruch et al. 2015 | MCA5-2 | Barney Creek Fm. | 65.3 | 3.2 | |
| Baruch et al. 2015 | MCA5-3 | Barney Creek Fm. | 101.5 | 2 | |
| Baruch et al. 2015 | MCA5-4 | Barney Creek Fm. | 87.5 | 4.1 | |
| Baruch et al. 2015 | McA5-5 | Barney Creek Fm. | 115.4 | 1.4 | |
| Fraser 2012 | 3-23-00/1 | Arbuckle | 50.07 | 0 | |
| Fraser 2012 | 3-23-00/2 | Arbuckle | 288.54 | 17.84 | |
| Fraser 2012 | 3-23-00/3 | Arbuckle | 128.31 | 0.25 | |
| Fraser 2012 | 3-23-00/6 | Arbuckle | 126.62 | 11.22 | |

| | | | | | |
|---|---|---|---|---|---|
| Fraser 2012 | 3-23-00/8R | Arbuckle | 143.22 | 9.9 | |
| Fraser 2012 | 3-23-00/9R | Arbuckle | 110.61 | 4.91 | |
| Fraser 2012 | 3-23-00/10A | Arbuckle | 91.65 | 4.92 | |
| Fraser 2012 | 3-23-00/10B | Arbuckle | 154.52 | 9.85 | |
| Fraser 2012 | 3-23-00/11R | Arbuckle | 39.29 | 3.89 | |
| Fraser 2012 | 3-23-00/12 | Arbuckle | 83.08 | 0.19 | |
| Fraser 2012 | 3-23-00/13 | Arbuckle | 75.66 | 0.27 | |
| Fraser 2012 | 3-23-00/14 | Arbuckle | 133.92 | 7.83 | |
| Fraser 2012 | 3-23-00/15 | Arbuckle | 163.82 | 13.31 | |
| Fraser 2012 | 3-23-00/17 | Arbuckle | 177.55 | 11.44 | |
| Fraser 2012 | 3-23-00/19 | Arbuckle | 154.06 | 11.62 | |
| Fraser 2012 | 3-23-00/20 | Arbuckle | 144.23 | 12.2 | |
| Fraser 2012 | 3-23-00/21 | Arbuckle | 189 | 14.51 | |
| Fraser 2012 | 3-23-00/22 | Arbuckle | 190.22 | 17.03 | |
| Fraser 2012 | 3-23-00/23 | Arbuckle | 144.43 | 11.99 | |
| Fraser 2012 | 3-23-00/24 | Arbuckle | 138.32 | 15.75 | |
| Fraser 2012 | 3-23-00/25 | Arbuckle | 82.42 | 12.57 | |
| Fraser 2012 | 3-23-00/28 | Arbuckle | 129.65 | 5.98 | |
| Fraser 2012 | 3-23-00/29 | Arbuckle | 95.95 | 1.81 | |
| Fraser 2012 | 3-23-00/31 | Arbuckle | 96.59 | 0.65 | |
| Löhr and Kennedy 2014 | 45-46 | ODP Site 207 | 677.9 | 25 | |
| Löhr and Kennedy 2014 | 54-55 | ODP Site 207 | 662.4 | 21.8 | |
| Löhr and Kennedy 2014 | 65-66 | ODP Site 207 | 592 | 17.7 | |
| Löhr and Kennedy 2014 | 84-85 | ODP Site 207 | 673.3 | 23.8 | |
| Löhr and Kennedy 2014 | 95-96 | ODP Site 207 | 422 | 13.7 | |
| Löhr and Kennedy 2014 | 105-106 | ODP Site 207 | 562.4 | 20.3 | |
| Löhr and Kennedy 2014 | 115-116 | ODP Site 207 | 587.7 | 18.6 | |
| Löhr and Kennedy 2014 | 125-126 | ODP Site 207 | 556.6 | 14 | |
| Löhr and Kennedy 2014 | 144-145 | ODP Site 207 | 574.2 | 17.8 | |
| Löhr and Kennedy 2014 | 10-11 | ODP Site 207 | 650.3 | 19.6 | |
| Löhr and Kennedy 2014 | 20-21 | ODP Site 207 | 600.3 | 16.2 | |
| Löhr and Kennedy 2014 | 70-71 | ODP Site 207 | 661.6 | 21.3 | |
| Löhr and Kennedy 2014 | 81-82 | ODP Site 207 | 701.8 | 24.4 | |
| Löhr and Kennedy 2014 | 90-91 | ODP Site 207 | 511.6 | 16 | |
| Löhr and Kennedy 2014 | 100-101 | ODP Site 207 | 633.4 | 22 | |
| Löhr and Kennedy 2014 | 110-111 | ODP Site 207 | 791.2 | 30 | |
| Löhr and Kennedy 2014 | 119-120 | ODP Site 207 | 768.2 | 28.7 | |
| Löhr and Kennedy 2014 | 130-131 | ODP Site 207 | 647.2 | 26 | |
| Löhr and Kennedy 2014 | 10-11 | ODP Site 207 | 623.3 | 23.5 | |
| Löhr and Kennedy 2014 | 19-20 | ODP Site 207 | 541.3 | 16.2 | |
| Löhr and Kennedy 2014 | 30-31 | ODP Site 207 | 400.9 | 9.6 | |
| Löhr and Kennedy 2014 | 40-41 | ODP Site 207 | 426.6 | 10.5 | |

| | | | | | |
|---|---|---|---|---|---|
| Löhr and Kennedy 2014 | 51-52 | ODP Site 207 | 690.9 | 26.5 | |
| Löhr and Kennedy 2014 | 60-61 | ODP Site 207 | 358.3 | 9.5 | |
| Löhr and Kennedy 2014 | 70-71 | ODP Site 207 | 462.3 | 15.3 | |
| Löhr and Kennedy 2014 | 80-81 | ODP Site 207 | 677 | 23.6 | |
| Löhr and Kennedy 2014 | 90-91 | ODP Site 207 | 602.4 | 21.7 | |
| Löhr and Kennedy 2014 | 100-101 | ODP Site 207 | 412.7 | 12.4 | |
| Löhr and Kennedy 2014 | 110-111 | ODP Site 207 | 779.4 | 26.3 | |
| Löhr and Kennedy 2014 | 120-121 | ODP Site 207 | 369.1 | 9 | |
| Löhr and Kennedy 2014 | 130-131 | ODP Site 207 | 443.6 | 11.6 | |
| Löhr and Kennedy 2014 | 5-6 | ODP Site 207 | 676.6 | 20.9 | |
| Löhr and Kennedy 2014 | 5-6 | ODP Site 207 | 599.4 | 18.9 | |
| Löhr and Kennedy 2014 | 15-16 | ODP Site 207 | 569.6 | 16.6 | |
| Löhr and Kennedy 2014 | 27-28 | ODP Site 207 | 477.9 | 14 | |
| Löhr and Kennedy 2014 | 35-36 | ODP Site 207 | 442.2 | 12.8 | |
| Löhr and Kennedy 2014 | 45-46 | ODP Site 207 | 572 | 16.6 | |
| Löhr and Kennedy 2014 | 55-56 | ODP Site 207 | 601.4 | 17.1 | |
| Löhr and Kennedy 2014 | 67-68 | ODP Site 207 | 547.5 | 15.1 | |
| Löhr and Kennedy 2014 | 77-78 | ODP Site 207 | 556.2 | 15.3 | |
| Löhr and Kennedy 2014 | 95-96 | ODP Site 207 | 571.8 | 13.4 | |
| Löhr and Kennedy 2014 | 105-106 | ODP Site 207 | 604.8 | 16.9 | |
| Löhr and Kennedy 2014 | 115-116 | ODP Site 207 | 518.4 | 13.2 | |
| Löhr and Kennedy 2014 | 75-76 | ODP Site 207 | 619.9 | 22.3 | |
| Löhr and Kennedy 2014 | 85-86 | ODP Site 207 | 393.3 | 10.3 | |
| Löhr and Kennedy 2014 | 94-95 | ODP Site 207 | 678.9 | 22.6 | |
| Löhr and Kennedy 2014 | 104-105 | ODP Site 207 | 515.2 | 16.3 | |
| Löhr and Kennedy 2014 | 116-117 | ODP Site 207 | 443 | 10.6 | |
| Löhr and Kennedy 2014 | 125-126 | ODP Site 207 | 639.6 | 19.9 | |
| Löhr and Kennedy 2014 | 135-136 | ODP Site 207 | 642.6 | 21 | |
| Löhr and Kennedy 2014 | 145-146 | ODP Site 207 | 614.4 | 19.5 | |
| Löhr and Kennedy 2014 | 9-10 | ODP Site 207 | 629.1 | 19.5 | |
| Löhr and Kennedy 2014 | 20-21 | ODP Site 207 | 469.4 | 12.4 | |
| Löhr and Kennedy 2014 | 30-31 | ODP Site 207 | 509.8 | 13.2 | |
| Löhr and Kennedy 2014 | 40-41 | ODP Site 207 | 562.5 | 16.4 | |
| Löhr and Kennedy 2014 | 119-120 | ODP Site 207 | 710.6 | 26 | |
| Löhr and Kennedy 2014 | 20-21 | ODP Site 207 | 585.5 | 16.7 | |
| Löhr and Kennedy 2014 | 31-32 | ODP Site 207 | 852.7 | 33.4 | |
| Löhr and Kennedy 2014 | 39-40 | ODP Site 207 | 751.2 | 27.6 | |
| Löhr and Kennedy 2014 | 52-53 | ODP Site 207 | 765.9 | 26.4 | |
| Löhr and Kennedy 2014 | 65-66 | ODP Site 207 | 698.3 | 20.5 | |
| Löhr and Kennedy 2014 | 75-76 | ODP Site 207 | 687.1 | 21.3 | |
| Löhr and Kennedy 2014 | 87-88 | ODP Site 207 | 645.5 | 21.4 | |
| Löhr and Kennedy 2014 | 97-98 | ODP Site 207 | 641.2 | 21.5 | |

| | | | | | |
|---|---|---|---|---|---|
| Löhr and Kennedy 2014 | 110-111 | ODP Site 207 | 599.9 | 20.2 | |
| Löhr and Kennedy 2014 | 120-121 | ODP Site 207 | 574 | 19 | |
| Löhr and Kennedy 2014 | 130-131 | ODP Site 207 | 588 | 18.1 | |
| Löhr and Kennedy 2014 | 140-141 | ODP Site 207 | 629.5 | 20.7 | |
| Löhr and Kennedy 2014 | 11-12 | ODP Site 207 | 522.2 | 15.4 | |
| Löhr and Kennedy 2014 | 20-21 | ODP Site 207 | 580.4 | 16.7 | |
| Löhr and Kennedy 2014 | 60-61 | ODP Site 207 | 544.3 | 16.5 | |
| Löhr and Kennedy 2014 | 70-71 | ODP Site 207 | 551.9 | 15.9 | |
| Löhr and Kennedy 2014 | 71-72 | ODP Site 207 | 447.9 | 8.9 | |
| Löhr and Kennedy 2014 | 122-123 | ODP Site 207 | 612.4 | 16.7 | |
| Löhr and Kennedy 2014 | 5-6 | ODP Site 207 | 670.5 | 19.4 | |
| Löhr and Kennedy 2014 | 16-17 | ODP Site 207 | 678.2 | 20.8 | |
| Löhr and Kennedy 2014 | 28-29 | ODP Site 207 | 504.7 | 13.5 | |
| Löhr and Kennedy 2014 | 35-36 | ODP Site 207 | 685.8 | 22.2 | |
| Löhr and Kennedy 2014 | 45-46 | ODP Site 207 | 389.6 | 10.1 | |
| Löhr and Kennedy 2014 | 55-56 | ODP Site 207 | 714.3 | 22.5 | |
| Löhr and Kennedy 2014 | 65-66 | ODP Site 207 | 618.4 | 18.6 | |
| Löhr and Kennedy 2014 | 75-76 | ODP Site 207 | 739.6 | 23.2 | |
| Löhr and Kennedy 2014 | 85-86 | ODP Site 207 | 748.1 | 22.5 | |
| Löhr and Kennedy 2014 | 95-96 | ODP Site 207 | 703.9 | 21.3 | |
| Löhr and Kennedy 2014 | 105-106 | ODP Site 207 | 539.8 | 10.1 | |
| Löhr and Kennedy 2014 | 115-116 | ODP Site 207 | 602.9 | 17.4 | |
| Löhr and Kennedy 2014 | 125-126 | ODP Site 207 | 568.5 | 15.9 | |
| Löhr and Kennedy 2014 | 10-11 | ODP Site 207 | 533.8 | 14.9 | |
| Löhr and Kennedy 2014 | 20-21 | ODP Site 207 | 668 | 21.1 | |
| Löhr and Kennedy 2014 | 50-51 | ODP Site 207 | 670.1 | 18 | |
| Löhr and Kennedy 2014 | 60-61 | ODP Site 207 | 557.9 | 16 | |
| Löhr and Kennedy 2014 | 71-72 | ODP Site 207 | 693.9 | 22.7 | |
| Löhr and Kennedy 2014 | 80-81 | ODP Site 207 | 657.2 | 21.1 | |
| Löhr and Kennedy 2014 | 89-90 | ODP Site 207 | 513 | 13.6 | |
| Löhr and Kennedy 2014 | 100-101 | ODP Site 207 | 472.8 | 10.4 | |
| Löhr and Kennedy 2014 | 5-6 | ODP Site 207 | 478.3 | 11.3 | |
| Löhr and Kennedy 2014 | 15-16 | ODP Site 207 | 593.3 | 16.9 | |
| Löhr and Kennedy 2014 | 25-26 | ODP Site 207 | 484.2 | 10.9 | |
| Löhr and Kennedy 2014 | 35-36 | ODP Site 207 | 585.2 | 17.2 | |
| Löhr and Kennedy 2014 | 45-46 | ODP Site 207 | 607.4 | 17.4 | |
| Löhr and Kennedy 2014 | 55-56 | ODP Site 207 | 619.2 | 17.5 | |
| Löhr and Kennedy 2014 | 65-66 | ODP Site 207 | 470.8 | 13.4 | |
| Löhr and Kennedy 2014 | 75-76 | ODP Site 207 | 524.7 | 13.8 | |
| Löhr and Kennedy 2014 | 5-6 | ODP Site 207 | 448.8 | 11 | |
| Sturman 2012 | B2.873 | Arthur Creek | 47.76 | 2 | Baldwin |
| Sturman 2012 | B2.876 | Arthur Creek | 56.57 | 0.3 | Baldwin |

| | | | | | |
|---|---|---|---|---|---|
| Sturman 2012 | B2.879 | Arthur Creek | 59.28 | 2.9 | Baldwin |
| Sturman 2012 | B2.881 | Arthur Creek | 78.28 | 0.58 | Baldwin |
| Sturman 2012 | B2.883 | Arthur Creek | 57.71 | 3.22 | Baldwin |
| Sturman 2012 | B2.886 | Arthur Creek | 40.57 | 2.51 | Baldwin |
| Sturman 2012 | B2.888 | Arthur Creek | 52.96 | 3.7 | Baldwin |
| Sturman 2012 | B2.89 | Arthur Creek | 52.16 | 2.12 | Baldwin |
| Sturman 2012 | B2.893 | Arthur Creek | 100.35 | 7.22 | Baldwin |
| Sturman 2012 | B2.894 | Arthur Creek | 103.56 | 8.72 | Baldwin |
| Sturman 2012 | B2.897 | Arthur Creek | 77.79 | 9.2 | Baldwin |
| Sturman 2012 | B2.9 | Arthur Creek | 72.3 | 7.82 | Baldwin |
| Sturman 2012 | B2.903 | Arthur Creek | 91.54 | 7.01 | Baldwin |
| Sturman 2012 | B2.906 | Arthur Creek | 74.28 | 8.5 | Baldwin |
| Sturman 2012 | M2.819 | Arthur Creek | 28.36 | 1.35 | MacIntyre |
| Sturman 2012 | M2828 | Arthur Creek | 21.58 | 0.99 | MacIntyre |
| Sturman 2012 | M2.837 | Arthur Creek | 33.11 | 1.69 | MacIntyre |
| Sturman 2012 | M2.843 | Arthur Creek | 31.57 | 2.75 | MacIntyre |
| Sturman 2012 | M2852 | Arthur Creek | 36.29 | 3.28 | MacIntyre |
| Sturman 2012 | M2858 | Arthur Creek | 44.36 | 4.48 | MacIntyre |
| Sturman 2012 | M2861 | Arthur Creek | 48.94 | 4.78 | MacIntyre |
| Sturman 2012 | M2.870 | Arthur Creek | 62.75 | 7.17 | MacIntyre |
| Sturman 2012 | M2.876 | Arthur Creek | 89.91 | 8.54 | MacIntyre |
| Sturman 2012 | M2.879 | Arthur Creek | 51.89 | 7.38 | MacIntyre |
| Sturman 2012 | M2894 | Arthur Creek | 119.27 | 15.88 | MacIntyre |

**Table A.7:** Compilation of geologic ages of Ordovician, Devonian, and Permo-Carboniferous ophiolite obductions

| | Location | Age Type | Age Max | Age Min | Refs |
|---|---|---|---|---|---|
| **Ord.** | Scandinavian Caledonides | Crystallisation | 497 | 477 | Pedersen and Furnes 1991<br>Yoshinobu et al. 2002;<br>Slagstad et al. 2014 |
| | | Allochthonous Sediment | Cambrian | 455 | Barnes et al. 2007; Greiling and Garfunkel 2007 |
| | | Autochtonous Sediment | 455 | Mid Llandovery | Björlykke 1974; Yoshinobu et al. 2002 |
| | | Ophiolite detritus | Early Ashgill | / | Björlykke 1974 |
| | | Slab Breakoff? | 448 | | Yoshinobu et al. 2002 |
| | Scotland/Ireland Caledonides | Metamorphic Sole | 486 | 470 | Bluck et al. 1980 |
| | | South Mayo Seds | Tremadoc | Llanvirn | Wrafter and Graham 1989 |
| | | Post-collision flysch | 453 | 447 | Oliver et al. 2000 |
| | | Ophiolite detritus | lower Llanvirn | | Wrafter and Graham 1989 |
| | Newfoundland | Crystallisation | 489 | 479 | Jenner et al. 1991 |
| | | Metamorphic Sole | 465 | 455 | Dallmeyer and Williams 1975 |
| | | Allochthonous Sediment | 470 | 458 | Waldron et al. 1998 |
| | | Autochthonous Sediment | Sandbian | Silurian | Waldron et al. 1998; Quinn et al. 1999 |
| | | Ophiolite detritus I | 470 | 460 | Waldron et al. 1998 |
| | | Ophiolite detritus II | middle Caradoc | | Quinn et al. 1999 |
| | Quebec | Crystallisation | 480 | 470 | Tremblay et al. 2011 |
| | | Metamorphic Sole | 471 | 457 | Tremblay et al. 2011 |
| | | Allochthonous Sediment | Arenig | middle Caradoc | Hiscott et al. 1986 |
| | | Autochthonous Sediment | Sandbian | Silurian | Larmagnat and Neuweiler 2015;<br>Desrochers et al. 2010 |
| | | Ophiolite detritus | 455 | | De Souza et al. 2014 |
| | Central Apps | Crystallisation | 480 | 442 | Karabinos et al. 1998; Valley et al. 2020 |
| | | Allochthonous Sediment | 466 | Lower Ashgill | Berg et al. 1983; Macdonald et al. 2017b |

| | | | | | |
|---|---|---|---|---|---|
| | | Autochthonous Sediment | 452 | 442 | Hiscott 1984b; Macdonald et al. 2017b |
| | | Ophiolite Detritus | Upper Cincinattian | | Garver et al. 1996; Joy et al. 2000 |
| | | Slab Breakoff? | 455 | | Macdonald et al. 2017b |
| | Southern Apps | Crystallisation | 510 | 470 | Shaw and Wasserburg 1984 |
| | | Metamorphic Sole | 461 | 454 | Moecher et al. 2004; Miller et al. 2010 |
| **Dev.** | Tianshan | Crystallisation | 425 | 363 | Wang et al. 2011 |
| | | Metamorphism | 375 | 356 | Wang et al. 2011 |
| | | Sediment | Givetian | Tournasian | Yu 2001; Yu and Shougang 2006 |
| | Magnitogorsk | Crystallisation | Emsian | Famennian | Artyushkova and Maslov 1998; Artyuszkova and Maslov 2008 |
| | | Metamorphic Sole | 387 | 357 | Willner et al. 2002 |
| | | Sediment | 376 | 356 | Willner et al. 2002 |
| | | Ophiolite detritus | Upper Frasnian | Tournasian | Willner et al. 2002 |
| | Armorica | Crystallisation | Early Ordovician | mid Devonian | Ballèvre et al. 2009 |
| | | Metamorphic Sole | 370 | 360 | Bosse et al. 2005 |
| | | Sediment | 380 | 360 | Macdonald et al. 2019 |
| | Avalonia/ Meguma/ Suwanee | Crystallisation | Cambrian | Ordovician | Staal et al. 2012 |
| | | Metamorphic Sole | 375 | 345 | Trupe et al. 2003; Staal et al. 2012; Merschat et al. 2005 |
| | | Sediment | Givetian | Lower Visean | Swezey 2002 |
| | | Slab breakoff/ rollback? | Famennian | 357 | Moran et al. 2007; Hibbard et al. 2010; Staal et al. 2012 |
| | Chilenia/Cuyania | Crystallisation | 577 | | Basei et al. 1998 |
| | | Metamorphism | 399 | 353 | Ramos et al. 2000 |
| | | Sedimentation | 380 | 330 | Herve et al. 2013 |
| | New England Orogen (E. Aust) | Crystallisation | Cambrian | Ordovician | Sano et al. 2004 |
| | | Faulting | Westphalian | Early Permian | Roberts et al. 2006; Phillips et al. 2015 |

| | | | | |
|---|---|---|---|---|
| | Back-arc basin | Stephanian | Asselian | Roberts et al. 2006 |
| | Ophiolite detritus | Early Permian | | Allan and Leitch 1990 |
| | Slab breakoff/ rollback? | 302 | 300 | Collins et al. 1993; Jenkins et al. 2002 |
| Klondike Orogen (Yukon) | Crystallisation | 310 | 260 | Staal et al. 2018; Parsons et al. 2019 |
| | Collision | 275 | 252 | Johnston et al. 2007; Parsons et al. 2019 |
| | Forearc Sediment | 251 | 235 | Beranek and Mortensen 2011 |
| | Slab Breakoff? | 265 | 260 | Parsons et al. 2019 |
| Hercynian/Variscan | Crystallisation | 479 | | Ribeiro et al. 2010 |
| | Metamorphic Sole | 370 | 328 | Ribeiro et al. 2010 |
| | Foreland basins | Famennian | Gzhelian | Skrzypek et al. 2012; Kroner and Romer 2013 |
| | Ophiolite detritus | 354 | 332 | Geisler et al. 2005 |
| | Slab breakoff? | 355 | 345 | Jesus et al. 2007 |
| Trans-Altai | Crystallisation | 475 | 372 | Han et al. 2010 |
| | Deformation | Late Devonian | Early Carboniferous | Kröner et al. 2010 |
| | Sediment | 390 | 315 | Kröner et al. 2010 |
| | Ophiolite detritus | Late Devonian | Carboniferous | Lamb and Badarch 1997 |
| Tianshan | Crystallisation | 344 | 325 | Han et al. 2010 |
| | Metamorphism | 346 | 302 | Gao and Klemd 2003; Su et al. 2010; Klemd et al. 2005 |
| | Sediment | Bashkirian | End Carboniferous | Wang et al. 2006; Huang et al. 2018 |
| | Slab breakoff? | 316 | 300 | Han et al. 2010; Yuan et al. 2010; Wang et al. 2010 |
| Urals | Crystallisation | Ordovician | Devonian | Puchkov 2009 |
| | Exhumation | 335 | 300 | Leech and Stockli 2000 |
| | Sediment | Early Permian | Guadalupian | Rakhimov et al. 2021 |
| | Ophiolite detritus | Kazanian | | Rakhimov et al. 2021 |
| Iran | Crystallisation | 460 | 300 | Moghadam and Stern 2014 |
| | Metamorphism | 320 | 282 | Moghadam and Stern 2014 |
| | Sediment | 295 | 250 | Moghadam and Stern 2014 |
| Mauritanides | Metamorphism | 333 | 300 | Goff et al. 2001; Caby and Kienast 2009 |

| | | | | | |
|---|---|---|---|---|---|
| | | Sediment | Tournasian | Early Westphalian | Hoepffner et al. 2005 |
| | Tuarkyr | Sediment | Mid Carboniferous | Wordian | Garzanti and Gaetani 2002 |
| | | Ophiolite detritus | Late Carboniferous | | Garzanti and Gaetani 2002 |
| | Caltepec | Metamorphism I | 353 | 337 | Middleton et al. 2007; Keppie et al. 2010 |
| | | Metamorphism II | 305 | 293 | Keppie et al. 2010 |
| | | Crystallisation | 313 | 291 | Grajales-Nishimura et al. 2018 |
| | | Sediment I | 374 | 305 | Dostal and Keppie 2009 |
| | | Sediment II | 280 | 268 | Centeno-García et al. 2009 |
| | Alleghanian/ Ouachita | Metamorphism | 320 | 265 | Secor Jr and Dallmeyer. 1986 |
| | | Sediment | Namurian | Wolfcampian | Swezey 2002; Shaulis et al. 2012 |
| | | Ophiolite detritus | 345 | 320 | Shaulis et al. 2012 |

# References


Allan, A.D. and E.C. Leitch (1990). "The tectonic significance of unconformable contacts at the base of Early Permian sequences, southern New England Fold Belt". en. In: *Australian Journal of Earth Sciences* 37.1, pp. 43–49.

Anand, R.R., R.J. Gilkes, T.M. Armitage, and J.W. Hillyer (1985). "Feldspar weathering in lateritic saprolite". en. In: *Clays and Clay Minerals* 33.1, pp. 31–43.

Arrhenius, Svante (1896). "XXXI. On the influence of carbonic acid in the air upon the temperature of the ground". In: *The London, Edinburgh, and Dublin Philosophical Magazine and Journal of Science* 41.251, pp. 237–276.

Artyushkova, O.V. and Victor A. Maslov (1998). "Paleontological Substantiation of the Stratigraphic Subdivision of Pre-Famennian Volcanogenic Complexes in the Verkhneural'sk and Magnitogorsk Regions [in Russian". en. In: *IG UNTs RAN*. Ufa.

Artyuszkova, O.V. and Victor A. Maslov (2008). "Detailed correlation of the Devonian deposits in the South Urals and some aspects of their formation". en. In: *Bulletin of Geosciences* 83.4, pp. 391–399.

Aspandiar, Mehrooz F. and Richard A. Eggleton (2002). "Weathering of chlorite: I. Reactions and products in microsystems controlled by the primary mineral". en. In: *Clays and Clay Minerals* 50.6, pp. 685–698.

Ballèvre, Michel, Valérie Bosse, Céline Ducassou, and Pavel Pitra (2009). "Palaeozoic history of the Armorican Massif: models for the tectonic evolution of the suture zones". In: *Comptes rendus géoscience* 341.2-3, pp. 174–201.

Banfield, Jillian F. and Richard A. Eggleton (1990). "Analytical transmission electron microscope studies of plagioclase, muscovite, and K-feldspar weathering". en. In: *Clays and Clay Minerals* 38.1, pp. 77–89.

Banfield, Jillian F., Blair F. Jones, and David R. Veblen (1991). "An AEM-TEM study of weathering and diagenesis, Abert Lake". en. In: *Geochimica et Cosmochimica Acta* 55.10, pp. 2781–2793.

Baratoux, David, Henri Samuel, Chloé Michaut, Michael J. Toplis, Marc Monnereau, Mark Wieczorek, Raphaël Garcia, and Kei Kurita (2014). "Petrological constraints on the density of the Martian crust". en. In: *Journal of Geophysical Research: Planets* 119.7, pp. 1707–1727.

Barnes, Calvin G., Carol D. Frost, Aaron S. Yoshinobu, Kelsey McArthur, Melanie A. Barnes, Charlotte M. Allen, Øystein Nordgulen, and Tore Prestvik (2007). "Timing of sedimentation, metamorphism, and plutonism in the Helgeland Nappe Complex, north-central Norwegian Caledonides". en. In: *Geosphere* 3.6, pp. 683–703.

Baruch, Elizabeth T., Martin J. Kennedy, Stefan C. Löhr, and David N. Dewhurst (2015). "Feldspar dissolution-enhanced porosity in Paleoproterozoic shale reservoir facies from the Barney Creek Formation (McArthur Basin, Australia". no. In: *AAPG Bulletin* 99.9, pp. 1745–1770.

Basei, M., V.A. Ramos, G.I. Vujovich, and S. Poma (1998). "El basamento metamórfico de la Cordillera Frontal de Mendoza: nuevos datos geocronológicos e isotópicos". es. In: *Congreso Latinoamericano de Geología* 10, pp. 412–417.

Basham, I.R. (1974). "Mineralogical changes associated with deep weathering of gabbro in Aberdeenshire". en. In: *Clay Minerals* 10.3, pp. 189–202.

Bayon, Germain, Martin Patriat, Yves Godderis, Anne Trinquier, Patrick De Deckker, Denise K Kulhanek, Ann Holbourn, and Yair Rosenthal (2023). "Accelerated mafic weathering in Southeast Asia linked to late Neogene cooling". In: *Science Advances* 9.13, eadf3141.

Beil, Sebastian, Wolfgang Kuhnt, Ann Holbourn, Florian Scholz, Julian Oxmann, Klaus Wallmann, Janne Lorenzen, Mohamed Aquit, and El Hassane Chellai (2020). "Cretaceous oceanic anoxic events prolonged by phosphorus cycle feedbacks". In: *Climate of the Past* 16.2, pp. 757–782.

Beinlich, Andreas, Timm John, Johannes C Vrijmoed, Masako Tominaga, Tomas Magna, and Yuri Y Podladchikov (2020). "Instantaneous rock transformations in the deep crust driven by reactive fluid flow". In: *Nature Geoscience* 13.4, pp. 307–311.

Beranek, Luke P. and James K. Mortensen (2011). "The timing and provenance record of the Late Permian Klondike orogeny in northwestern Canada and arc-continent collision along western North America". en. In: *Tectonics* 30.5.

Berg, T.M., M.K. McInerney, J.H. Way, and D.B. MacLachlan (1983). "Stratigraphic correlation chart of Pennsylvania: Pennsylvania Geological Survey, 4th ser". en. In: *General Geology Report* 75, 1. sheet.

Bergström, Stig M, Xu Chen, Juan Carlos Gutiérrez-Marco, and Andrei Dronov (2009). "The new chronostratigraphic classification of the Ordovician System and its relations to major regional series and stages and to $\delta$13C chemostratigraphy". In: *Lethaia* 42.1, pp. 97–107.

Bergström, Stig M, John Riva, and Marshall Kay (1974). "Significance of conodonts, graptolites, and shelly faunas from the Ordovician of western and north-central Newfoundland". In: *Canadian Journal of Earth Sciences* 11.12, pp. 1625–1660.

Berndt, Michael E., Douglas E. Allen, and William E. Seyfried Jr (1996). "Reduction of CO2 during serpentinization of olivine at 300 C and 500 bar". en. In: *Geology* 24.4, pp. 351–354.

Berner, Robert A, Antonio C Lasaga, and Robert M Garrels (1983). "Carbonate-silicate geochemical cycle and its effect on atmospheric carbon dioxide over the past 100 million years". In: *Am. J. Sci.;(United States)* 283.7.

Björlykke, Knut (1974). "Geochemical and mineralogical influence of Ordovician Island Arcs on epicontinental clastic sedimentation. A study of Lower Palaeozoic sedimentation in the Oslo Region, Norway". In: *Sedimentology* 21.2, pp. 251–272.

Blattmann, Thomas M, Zhifei Liu, Yonghua Zhang, Yulong Zhao, Negar Haghipour, Daniel B Montluçon, Michael Plötze, and Timothy I Eglinton (2019). "Mineralogical control on the fate of continentally derived organic matter in the ocean". In: *Science* 366.6466, pp. 742–745.

Bluck, B.J., A.N. Halliday, M. Aftalion, and R.M. Macintyre (1980). "Age arid origin of Ballantrae ophiolite and its significance to the Caledonian orogeny and Ordovician time scale". en. In: *Geology* 8.10, pp. 492–495.

Bosse, Valérie, Gilbert Féraud, Michel Ballevre, Jean-Jacques Peucat, and Michel Corsini (2005). "Rb–Sr and 40Ar/39Ar ages in blueschists from the Ile de Groix (Armorican Massif, France): Implications for closure mechanisms in isotopic systems". en. In: *Chemical Geology* 220.1-2, pp. 21–45.

Brass, Garrett W. (1976). "The variation of the marine 87Sr86Sr ratio during Phanerozonic time: interpretation using a flux model". en. In: *Geochimica et Cosmochimica Acta* 40.7, pp. 721–730.

Brigatti, Maria Franca and Luciano Poppi (1984). "'Corrensite-like minerals' in the Taro and Ceno Valleys, Italy". In: *Clay minerals* 19.1, pp. 59–66.

Broecker, Wallace S and Tsung-Hung Peng (1982). *Tracers in the Sea*. Vol. 690. Lamont-Doherty Geological Observatory, Columbia University Palisades, New York.

Buggisch, Werner and Michael M Joachimski (2006a). "Carbon isotope stratigraphy of the Devonian of Central and Southern Europe". In: *Palaeogeography, Palaeoclimatology, Palaeoecology* 240.1-2, pp. 68–88.

— (2006b). "Carbon isotope stratigraphy of the Devonian of Central and Southern Europe". en. In: *Palaeogeography, Palaeoclimatology, Palaeoecology* 240.1-2, pp. 68–88.

Burton, Michael R, Georgina M Sawyer, and Domenico Granieri (2013). "Deep carbon emissions from volcanoes". In: *Reviews in Mineralogy and Geochemistry* 75.1, pp. 323–354.

Caby, Renaud and J.R. Kienast (2009). "Neoproterozoic and Hercynian metamorphic events in the Central Mauritanides: implications for the geodynamic evolution of West Africa". en. In: *Journal of African Earth Sciences* 53.3, pp. 122–136.

Caillaud, J., D. Proust, and D. Righi (2006). "Weathering sequences of rock-forming minerals in a serpentinite: influence of microsystems on clay mineralogy". en. In: *Clays and Clay Minerals* 54.1, pp. 87–100.

Cama, Jordi, Jiwchar Ganor, Carles Ayora, and C.Antonio Lasaga (2000). "Smectite dissolution kinetics at 80 C and pH 8.8". en. In: *Geochimica et Cosmochimica Acta* 64.15, pp. 2701–2717.

Centeno-García, Elena, Claudia C. Mendoza-Rosales, and Gilberto Silva-Romo (2009). "Sedimentología de la Formación Matzitzi (Paleozoico superior) y significado de sus componentes volcánicos, región de Los

Reyes Metzontla-San Luis Atolotitlán, Estado de Puebla". es. In: *Revista mexicana de ciencias geológicas* 26.1, pp. 18–36.

Chaffin, M.S. et al. (2021). "Martian water loss to space enhanced by regional dust storms". en. In: *Nature Astronomy* 5.10, pp. 1036–1042.

Chen, Daizhao, Hairuo Qing, and Renwei Li (2005). "The Late Devonian Frasnian–Famennian (F/F) biotic crisis: insights from 13Ccarb, 13Corg and 87Sr/86Sr isotopic systematics". en. In: *Earth and Planetary Science Letters* 235.1-2, pp. 151–166.

Chesworth, Ward, Jean Dejou, Pierre Larroque, and Eduardo Garcia Rodeja (2004). "Alteration of olivine in a basalt from central France". en. In: *Catena* 56.1-3, pp. 21–30.

Claire, Mark W., John Sheets, Martin Cohen, Ignasi Ribas, Victoria S. Meadows, and David C. Catling (2012). "The evolution of solar flux from 0.1 nm to 160 m: quantitative estimates for planetary studies". en. In: *The Astrophysical Journal* 757.1, p. 95.

Clifford, Stephen M. (1991). "The role of thermal vapor diffusion in the subsurface hydrologic evolution of Mars". en. In: *Geophysical Research Letters* 18.11, pp. 2055–2058.

Coleman, N.T., F.H. LeRoux, and John G. Cady (1963). "Biotite-hydrobiotite-vermiculite in soils". la. In: *Nature* 198.4878, pp. 409–410.

Collins, W.J., R. Offler, T.R. Farrell, and B. Landenberger (1993). *A revised Late Palaeozoic-Early Mesozoic tectonic history for the southern New England Fold Belt*. en. New England Orogen, eastern Australia.

Coniglio, Mario (1985). "Origin and diagenesis of fine-grained slope sediments: Cow Head Group (Cambro-Ordovician), western Newfoundland". PhD thesis. Memorial University of Newfoundland.

Cramer, Bradley D., Matthew R. Saltzman, J.E. Day, and B.J. Witzke (2008). *Record of the Late Devonian Hangenberg global positive carbon-isotope excursion in an epeiric sea setting: carbonate production, organic-carbon burial and paleoceanography during the Late Famennian*. en.

Crespo, Rivero, Miguel A., Dolores Pereira Gómez, María V.Villa García, José M.Gallardo Amores, and Vicente Sánchez Escribano (2019). "Characterization of serpentines from different regions by transmission electron microscopy, X-ray diffraction, BET specific surface area and vibrational and electronic spectroscopy". en. In: *Fibers* 7.5, p. 47.

Cygan, Randall T., William H. Casey, Mark B. Boslough, Henry R. Westrich, Martin J. Carr, and George R. Holdren Jr (1989). "Dissolution kinetics of experimentally shocked silicate minerals". en. In: *Chemical Geology* 78.3-4, pp. 229–244.

Dallmeyer, R.D. and Harold Williams (1975). "40Ar/39Ar ages from the Bay of Islands metamorphic aureole: their bearing on the timing of Ordovician ophiolite obduction". en. In: *Canadian Journal of Earth Sciences* 12.9, pp. 1685–1690.

Dalton, Colleen A, Douglas S Wilson, and Timothy D Herbert (2022). "Evidence for a global slowdown in seafloor spreading since 15 Ma". In: *Geophysical Research Letters* 49.6, e2022GL097937.

De Souza, Stephane, Alain Tremblay, and Gilles Ruffet (2014). "Taconian orogenesis, sedimentation and magmatism in the southern Quebec–northern Vermont Appalachians: Stratigraphic and detrital mineral record of Iapetan suturing". In: *American journal of science* 314.7, pp. 1065–1103.

DeConto, Robert M, David Pollard, Paul A Wilson, Heiko Pälike, Caroline H Lear, and Mark Pagani (2008). "Thresholds for Cenozoic bipolar glaciation". In: *Nature* 455.7213, pp. 652–656.

Delvigne, Jean (1983). "Micromorphology of the alteration and weathering of pyroxenes in the Koua Bocca ultramafic intrusion, Ivory-Coast, western Africa". en. In: *Sciences Géologiques, bulletins et mémoires* 72.1, pp. 57–68.

Delvigne, Jean, E.B.A. Bisdom, J. Sleeman, and G. Stoops (1979). *Olivines, their pseudomorphs and secondary products*. en.

Delvigne, Jean and H. Martin (1970). "Analyse à la microsonde électronique de l'altération d'un plagioclase en kaolinite par l'intermédiaire d'une phase amorphe". fr. In: *Cah. Office Rech. Sci. Tech. Outre-Mer (ORSTOM), Sér. Géol* 2, pp. 259–295.

Demski, Matthew W., Benjamin J. Wheadon, Lori A. Stewart, Robert J. Elias, Graham A. Young, Godfrey S. Nowlan, and Edward P. Dobrzanski (2015). "Hirnantian strata identified in major intracratonic basins of central North America: implications for uppermost Ordovician stratigraphy". en. In: *Canadian Journal of Earth Sciences* 52.1, pp. 68–76.

Desrochers, André, Claude Farley, Aicha Achab, Esther Asselin, and John F. Riva (2010). "A far-field record of the end Ordovician glaciation: the Ellis Bay Formation, Anticosti Island, Eastern Canada". en. In: *Palaeogeography, Palaeoclimatology, Palaeoecology* 296.3-4, pp. 248–263.

Dessert, Céline, Bernard Dupré, Jérôme Gaillardet, Louis M François, and Claude J Allègre (2003). "Basalt weathering laws and the impact of basalt weathering on the global carbon cycle". In: *Chemical Geology* 202.3-4, pp. 257–273.

Dix, George R, Geoff Pignotta, and Shawna E White (2023). "Initial development and sedimentary provenance of a middle Paleozoic foreland basin: Clam Bank Formation, western Newfoundland". In: *Canadian Journal of Earth Sciences* 60.11, pp. 1573–1596.

Dostal, Jaroslav and J.D. Keppie (2009). "Geochemistry of low-grade clastic rocks in the Acatlán Complex of southern Mexico: Evidence for local provenance in felsic–intermediate igneous rocks". en. In: *Sedimentary Geology* 222.3-4, pp. 241–253.

Edmond, JM (1992). "Himalayan tectonics, weathering processes, and the strontium isotope record in marine limestones". In: *Science* 258.5088, pp. 1594–1597.

Edwards, C.S. and B.L. Ehlmann (2015). "Carbon sequestration on Mars". en. In: *Geology* 43, pp. 863–866.

Eggleton, Richard A. (1975). "Nontronite topotaxial after hedenbergite". en. In: *American Mineralogist: Journal of Earth and Planetary Materials* 60.11-12, pp. 1063–1068.

Eggleton, Richard A. and J.N. Boland (1982). "Weathering of enstatite to talc through a sequence of transitional phases". en. In: *Clays and Clay Minerals* 30.1, pp. 11–20.

Ehlmann, B.L., J.F. Mustard, and S.Lf Murchie (2010). "Geologic setting of serpentine deposits on Mars". en. In: *Geophysical research letters* 37.6.

Ehlmann, Bethany L. and Christopher S. Edwards (2014). "Mineralogy of the Martian surface". en. In: *Annual Review of Earth and Planetary Sciences* 42, pp. 291–315.

Ehlmann, Bethany L., John F. Mustard, Roger N. Clark, Gregg A. Swayze, and Scott L. Murchie (2011). "Evidence for low-grade metamorphism, hydrothermal alteration, and diagenesis on Mars from phyllosilicate mineral assemblages". en. In: *Clays and Clay Minerals* 59.4, pp. 359–377.

Eigenbrode, Jennifer L, Roger E Summons, Andrew Steele, Caroline Freissinet, Maëva Millan, Rafael Navarro-González, Brad Sutter, Amy C McAdam, Heather B Franz, Daniel P Glavin, et al. (2018). "Organic matter preserved in 3-billion-year-old mudstones at Gale crater, Mars". In: *Science* 360.6393, pp. 1096–1101.

Eswaran, H. and Wong Chaw Bin (1978). "A Study of a Deep Weathering Profile on Granite in Peninsular Malaysia: I". en. In: *Physico-Chemical and Micromorphological Properties." Soil Science Society of America Journal* 42.1, pp. 144–149.

Etiope, G. and A. Ionescu (2015). "Low-temperature catalytic CO 2 hydrogenation with geological quantities of ruthenium: a possible abiotic CH 4 source in chromitite-rich serpentinized rocks". en. In: *Geofluids* 15.3, pp. 438–452.

Etiope, Giuseppe, E. Ifandi, Manuela Nazzari, B.Tsikouras Monia Procesi, Guido Ventura, Andrew Steele, Roberto Tardini, and P. Szatmari (2018). "Widespread abiotic methane in chromitites". la. In: *Scientific reports* 8.1, p. 8728.

Etiope, Giuseppe and M.J. Whiticar (2019). "Abiotic methane in continental ultramafic rock systems: Towards a genetic model". fy. In: *Applied Geochemistry* 102, pp. 139–152.

Farrell, Úna C, Rifaat Samawi, Savitha Anjanappa, Roman Klykov, Oyeleye O Adeboye, Heda Agic, Anne-Sofie C Ahm, Thomas H Boag, Fred Bowyer, Jochen J Brocks, et al. (2021). "The sedimentary geochemistry and paleoenvironments project". In: *Geobiology* 19.6, pp. 545–556.

Finlay, Alexander J, David Selby, and Darren R Gröcke (2010). "Tracking the Hirnantian glaciation using Os isotopes". In: *Earth and Planetary Science Letters* 293.3-4, pp. 339–348.

Finnegan, Seth, Kristin Bergmann, John M. Eiler, David S. Jones, David A. Fike, Ian Eisenman, Nigel C. Hughes, Aradhna K. Tripati, and Woodward W. Fischer (2011). "The magnitude and duration of Late Ordovician–Early Silurian glaciation". en. In: *Science* 331.6019, pp. 903–906.

Fosu-Duah, E.L., E. Padmanabhan, and J.G. Vintaned (2016). "Variations in specific surface area of some oligocene-Miocene shales". en. In: *Journal of Scientific Research and Development* 3, pp. 33–43.

Frakes, Lawrence A., Jane E. Francis, and Jozef I. Syktus (1992). *Climate modes of the Phanerozoic*. en.

France-Lanord, Christian and Louis A. Derry (1997). "Organic carbon burial forcing of the carbon cycle from Himalayan erosion". en. In: *Nature* 390.6655, pp. 65–67.

Francois, Louis M. and J.C. Walker (1992). "Modelling the Phanerozoic carbon cycle and climate: constraints from the 87Sr/86Sr isotopic ratio of seawater". en. In: *American Journal of Science* 292.2, pp. 81–135.

Fraser, Samuel Alex (2012). "Nanoscale imaging of the Woodford Shale, Oklahoma, USA: Organic matter preservation as clay-organic nanocomposites". en. In: *PhD diss.*

Froelich, PN, ML Bender, NA Luedtke, GR Heath, and T DeVries (1982). "The marine phosphorus cycle". In: *American Journal of Science* 282.4, pp. 474–511.

Gale, Allison, Colleen A Dalton, Charles H Langmuir, Yongjun Su, and Jean-Guy Schilling (2013). "The mean composition of ocean ridge basalts". In: *Geochemistry, Geophysics, Geosystems* 14.3, pp. 489–518.

Galy, Valier, Christian France-Lanord, Olivier Beyssac, Pierre Faure, Hermann Kudrass, and Fabien Palhol (2007). "Efficient organic carbon burial in the Bengal fan sustained by the Himalayan erosional system". In: *Nature* 450.7168, pp. 407–410.

Gao, J. and R. Klemd (2003). "Formation of HP–LT rocks and their tectonic implications in the western Tianshan Orogen, NW China: geochemical and age constraints". en. In: *Lithos* 66.1-2, pp. 1–22.

Garver, JI, PR Royce, and TA Smick (1996). "Chromium and nickel in shale of the Taconic foreland; a case study for the provenance of fine-grained sediments with an ultramafic source". In: *Journal of Sedimentary Research* 66.1, pp. 100–106.

Garzanti, E. and M. Gaetani (2002). "Unroofing history of late Paleozoic magmatic arcs within the "Turan plate"(Tuarkyr, Turkmenistan". en. In: *Sedimentary Geology* 151.1-2, pp. 67–87.

Geisler, Thorsten, Roland Vinx, Nergui Martin-Gombojav, and Robert T. Pidgeon (2005). "Ion microprobe (SHRIMP) dating of detrital zircon grains from quartzites of the Eckergneiss Complex, Harz Mountains (Germany): implications for the provenance and the geological history". en. In: *International Journal of Earth Sciences* 94.3, pp. 369–384.

Gilkes, R.J. and Anchalee Suddhiprakarn (1979). "Biotite alteration in deeply weathered granite. I. Morphological, mineralogical, and chemical properties". en. In: *Clays and Clay Minerals* 27.5, pp. 349–360.

Glavin, Daniel P, Caroline Freissinet, Kristen E Miller, Jennifer L Eigenbrode, Anna E Brunner, Arnaud Buch, Brad Sutter, P Douglas Archer Jr, Sushil K Atreya, William B Brinckerhoff, et al. (2013). "Evidence for perchlorates and the origin of chlorinated hydrocarbons detected by SAM at the Rocknest aeolian deposit in Gale Crater". In: *Journal of Geophysical Research: Planets* 118.10, pp. 1955–1973.

Goff, Le, Catherine Guerrot Élisabeth, Gilbert Maurin, Véra Johan, Monique Tegyey, and Mustapha Ben Zerga (2001). "Découverte d'éclogites hercyniennes dans la chaine septentrionale des Mauritanides (Afrique de l'Ouest". fr. In: *Comptes Rendus de l'Académie des Sciences-Series IIA-Earth and Planetary Science* 333.11, pp. 711–718.

Goldberg, Samuel L, Theodore M Present, Seth Finnegan, and Kristin D Bergmann (2021). "A high-resolution record of early Paleozoic climate". In: *Proceedings of the National Academy of Sciences* 118.6, e2013083118.

Gorjan, Paul, Kunio Kaiho, David A. Fike, and Chen Xu (2012). "Carbon-and sulfur-isotope geochemistry of the Hirnantian (Late Ordovician) Wangjiawan (Riverside) section, South China: Global correlation and environmental event interpretation". en. In: *Palaeogeography, Palaeoclimatology, Palaeoecology* 337, pp. 14–22.

Gradstein, Felix M, JG Ogg, Mark D Schmitz, and GM eds Ogg (2020). *The geologic time scale*. Elsevier.

Grajales-Nishimura, José Manuel, Mario Alfredo Ramos-Arias, Luigi Solari, Gustavo Murillo-Muñetón, Elena Centeno-García, Peter Schaaf, and Ricardo Torres-Vargas (2018). "The Juchatengo complex: an upper-level ophiolite assemblage of late Paleozoic age in Oaxaca, southern Mexico". en. In: *International Journal of Earth Sciences* 107.3, pp. 1005–1031.

Greiling, Reinhard O. and Zvi Garfunkel (2007). "An Early Ordovician (Finnmarkian?) foreland basin and related lithospheric flexure in the Scandinavian Caledonides". en. In: *American Journal of Science* 307.2, pp. 527–553.

Grossman, Ethan L, Thomas E Yancey, Thomas E Jones, Peter Bruckschen, Boris Chuvashov, SJ Mazzullo, and Horng-sheng Mii (2008a). "Glaciation, aridification, and carbon sequestration in the Permo-Carboniferous: the isotopic record from low latitudes". In: *Palaeogeography, Palaeoclimatology, Palaeoecology* 268.3-4, pp. 222–233.

Grossman, Ethan L., Thomas E. Yancey, Thomas E. Jones, Peter Bruckschen, S.J.Mazzullo Boris Chuvashov, and Horng-sheng Mii (2008b). "Glaciation, aridification, and carbon sequestration in the Permo-

Carboniferous: the isotopic record from low latitudes". en. In: *Palaeogeography, Palaeoclimatology, Palaeoecology* 268.3-4, pp. 222–233.

Guo, ZT, Bainian Sun, ZS Zhang, SZ Peng, GQ Xiao, JY Ge, QZ Hao, YS Qiao, MY Liang, JF Liu, et al. (2008). "A major reorganization of Asian climate by the early Miocene". In: *Climate of the Past* 4.3, pp. 153–174.

Han, Bao-Fu, Zhao-Jie Guo, Zhi-Cheng Zhang, Lei Zhang, Jia-Fu Chen, and Biao Song (2010). "Age, geochemistry, and tectonic implications of a late Paleozoic stitching pluton in the North Tian Shan suture zone, western China". en. In: *Bulletin* 122.3-4, pp. 627–640.

Harder, Hermann (1972). "The role of magnesium in the formation of smectite minerals". In: *Chemical Geology* 10.1, pp. 31–39.

Hartmann, Jens, Nils Jansen, Hans H Dürr, Stephan Kempe, and Peter Köhler (2009). "Global CO2-consumption by chemical weathering: What is the contribution of highly active weathering regions?" In: *Global and Planetary Change* 69.4, pp. 185–194.

Hayes, John M, Harald Strauss, and Alan J Kaufman (1999). "The abundance of 13C in marine organic matter and isotopic fractionation in the global biogeochemical cycle of carbon during the past 800 Ma". In: *Chemical Geology* 161.1-3, pp. 103–125.

Heard, Andy W. and Edwin S. Kite (2020). "A probabilistic case for a large missing carbon sink on Mars after 3.5 billion years ago". en. In: *Earth and Planetary Science Letters* 531, p. 116001.

Hedges, John I and Richard G Keil (1995). "Sedimentary organic matter preservation: an assessment and speculative synthesis". In: *Marine chemistry* 49.2-3, pp. 81–115.

Hemingway, Jordon D, Daniel H Rothman, Katherine E Grant, Sarah Z Rosengard, Timothy I Eglinton, Louis A Derry, and Valier V Galy (2019). "Mineral protection regulates long-term global preservation of natural organic carbon". In: *Nature* 570.7760, pp. 228–231.

Herve, Francisco, M. Calderón, C.M. Fanning, Robert J. Pankhurst, and E. Godoy (2013). "Provenance variations in the Late Paleozoic accretionary complex of central Chile as indicated by detrital zircons". en. In: *Gondwana Research* 23.3, pp. 1122–1135.

Hibbard, James (2000). "Docking Carolina: mid-Paleozoic accretion in the southern Appalachians". In: *Geology* 28.2, pp. 127–130.

Hibbard, James P., Cees R. Staal, and Douglas W. Rankin (2010). *Comparative analysis of the geological evolution of the northern and southern Appalachian orogen: Late Ordovician-Permian*. en.

Hiscott, R.N., K.T. Pickering, and D.R. Beeden (1986). "Progressive filling of a confined Middle Ordovician foreland basin associated with the Taconic Orogeny, Quebec, Canada". en. In: *Foreland basins*, pp. 307–325.

Hiscott, Richard N (1984a). "Ophiolitic source rocks for Taconic-age flysch: trace-element evidence". In: *Geological Society of America Bulletin* 95.11, pp. 1261–1267.

— (1984b). "Ophiolitic source rocks for Taconic-age flysch: Trace-element evidence". en. In: *Geological Society of America Bulletin* 95.11, pp. 1261–1267.

Hoepffner, Christian, Abderahmane Soulaimani, and Alain Piqué (2005). "The moroccan hercynides". en. In: *Journal of African Earth Sciences* 43.1-3, pp. 144–165.

Hoffman, Paul F (2009). "Pan-glacial—A third state in the climate system". In: *Geology Today* 25.3, pp. 100–107.

Hu, Renyu, David M. Kass, Bethany L. Ehlmann, and Yuk L. Yung (2015). "Tracing the fate of carbon and the atmospheric evolution of Mars". en. In: *Nature communications* 6.1, p. 10003.

Huang, Bo, Dong Fu, Timothy Kusky, Kunpeng Ruan, Wenxiao Zhou, and Xionghua Zhang (2018). "Sedimentary provenance in response to Carboniferous arc-basin evolution of East Junggar and North Tianshan belts in the southwestern Central Asian Orogenic Belt". en. In: *Tectonophysics* 722, pp. 324–341.

Isbell, John L., Paul A. Lenaker, Rosemary A. Askin, Molly F. Miller, and Loren E. Babcock (2003). "Reevaluation of the timing and extent of late Paleozoic glaciation in Gondwana: Role of the Transantarctic Mountains". en. In: *Geology* 31.11, pp. 977–980.

Jagoutz, Oliver, Francis A Macdonald, and Leigh Royden (2016). "Low-latitude arc–continent collision as a driver for global cooling". In: *Proceedings of the National Academy of Sciences* 113.18, pp. 4935–4940.

Jagoutz, Oliver and Max W. Schmidt (2012). "The formation and bulk composition of modern juvenile continental crust: The Kohistan arc". en. In: *Chemical Geology* 298, pp. 79–96.

Jakosky, B.M. et al. (2018). "Loss of the Martian atmosphere to space: Present-day loss rates determined from MAVEN observations and integrated loss through time". en. In: *Icarus* 315, pp. 146–157.
Jakosky, Bruce M. (2019). "The CO2 inventory on Mars". en. In: *Planetary and Space Science* 175, pp. 52–59.
Jakosky, Bruce M. and Christopher S. Edwards (2018). "Inventory of CO2 available for terraforming Mars". en. In: *Nature astronomy* 2.8, pp. 634–639.
Jakosky, Bruce M., Joseph M. Grebowsky, Janet G. Luhmann, J. Connerney, F. Eparvier, Robert Ergun, and Jasper Halekas (2015). "MAVEN observations of the response of Mars to an interplanetary coronal mass ejection". en. In: *Science* 350.6261, p. 0210.
Jakosky, Bruce M., Bradley G. Henderson, and Michael T. Mellon (1995). "Chaotic obliquity and the nature of the Martian climate". en. In: *Journal of Geophysical Research: Planets* 100.E1, pp. 1579–1584.
James, NP and RK Stevens (1986). *Stratigraphy and correlation of the Cambro–Ordovician Cow Head Group, Western Newfoundland*. Geological Survey of Canada.
Jenkins, R.B., B. Landenberger, and W.J. Collins (2002). "Late Palaeozoic retreating and advancing subduction boundary in the New England fold belt, New South Wales". en. In: *Australian Journal of Earth Sciences* 49.3, pp. 467–489.
Jenner, G.A., G.R. Dunning, J. Malpas, M. Brown, and T. Brace (1991). "Bay of Islands and Little Port complexes, revisited: age, geochemical and isotopic evidence confirm suprasubduction-zone origin". en. In: *Canadian journal of Earth sciences* 28.10, pp. 1635–1652.
Jesus, A.P., J. Munhá, A. Mateus, C. Tassinari, and Allen Phillip Nutman (2007). "The Beja layered gabbroic sequence (Ossa-Morena Zone, Southern Portugal): geochronology and geodynamic implications". en. In: *Geodinamica Acta* 20.3, pp. 139–157.
Ji, Liming, Tongwei Zhang, Kitty L. Milliken, Junli Qu, and Xiaolong Zhang (2012). "Experimental investigation of main controls to methane adsorption in clay-rich rocks". en. In: *Applied Geochemistry* 27.12, pp. 2533–2545.
Joachimski, M.M., R.D. Pancost, K.H. Freeman, C. Ostertag-Henning, and W. Buggisch (2002). "Carbon isotope geochemistry of the Frasnian–Famennian transition". zu. In: *Palaeogeography, Palaeoclimatology, Palaeoecology* 181.1-3, pp. 91–109.
Johnson, J.G., Gilbert Klapper, and Ch A. Sandberg (1985). "Devonian eustatic fluctuations in Euramerica". en. In: *Geological Society of America Bulletin* 96.5, pp. 567–587.
Johnston, S.T., D. Canil, and L.H. Heaman (2007). "Permian exhumation of the Buffalo Pitts orogenic peridotite massif, northern Cordillera, Yukon". ny. In: *Canadian Journal of Earth Sciences* 44.3, pp. 275–286.
Joy, Michael P., Charles E. Mitchell, and Soumava Adhya (2000). "Evidence of a tectonically driven sequence succession in the Middle Ordovician Taconic foredeep". en. In: *Geology* 28.8, pp. 727–730.
Kaiser, Sandra I. (2005). "Mass extinctions, climatic and oceanographic changes at the Devonian, Carboniferous boundary". en. In: *PhD*.
Kalinowski, Birgitta E. and Peter Schweda (1996). "Kinetics of muscovite, phlogopite, and biotite dissolution and alteration at pH 1–4, room temperature". en. In: *Geochimica et cosmochimica acta* 60.3, pp. 367–385.
Karabinos, Paul, Scott D. Samson, J.Christopher Hepburn, and Heather M. Stoll (1998). "Taconian orogeny in the New England Appalachians: collision between Laurentia and the Shelburne Falls arc". en. In: *Geology* 26.3, pp. 215–218.
Kasting, James F. and David Catling (2003). "Evolution of a habitable planet". en. In: *Annual Review of Astronomy and Astrophysics* 41.1, pp. 429–463.
Kelemen, P.B. and C.E. Manning (2015). "Reevaluating carbon fluxes in subduction zones, what goes down, mostly comes up". en. In: *Proceedings of the National Academy of Sciences 112*, pp. 3997–4006.
Kennedy, Martin, Mary Droser, Lawrence M Mayer, David Pevear, and David Mrofka (2006). "Late Precambrian oxygenation; inception of the clay mineral factory". In: *Science* 311.5766, pp. 1446–1449.
Kennedy, Martin J, David R Pevear, and Ronald J Hill (2002). "Mineral surface control of organic carbon in black shale". In: *Science* 295.5555, pp. 657–660.
Kennedy, Martin J and Thomas Wagner (2011). "Clay mineral continental amplifier for marine carbon sequestration in a greenhouse ocean". In: *Proceedings of the National Academy of Sciences* 108.24, pp. 9776–9781.

Kennedy, Martin John, Stefan Carlos Löhr, Samuel Alex Fraser, and Elizabeth Teresa Baruch (2014). "Direct evidence for organic carbon preservation as clay-organic nanocomposites in a Devonian black shale; from deposition to diagenesis". en. In: *Earth and Planetary Science Letters* 388, pp. 59–70.

Kent, Dennis V and G Muttoni (2013). "Modulation of Late Cretaceous and Cenozoic climate by variable drawdown of atmospheric pCO 2 from weathering of basaltic provinces on continents drifting through the equatorial humid belt". In: *Climate of the Past* 9.2, pp. 525–546.

Keppie, J.Duncan, R.D. Nance, M.A. Ramos-Arias, J.K.W. Lee, J. Dostal, A. Ortega-Rivera, and J.B. Murphy (2010). "Late Paleozoic subduction and exhumation of Cambro-Ordovician passive margin and arc rocks in the northern Acatlán Complex, southern Mexico: Geochronological constraints". en. In: *Tectonophysics* 495.3-4, pp. 213–229.

Kite, Edwin S. (2019). "Geologic constraints on early Mars climate". en. In: *Space Science Reviews* 215, pp. 1–47.

Klemd, R., M. Bröcker, B.Rt Hacker, J. Gao, P. Gans, and K. Wemmer (2005). "New age constraints on the metamorphic evolution of the high-pressure/low-temperature belt in the western Tianshan Mountains, NW China". en. In: *The Journal of Geology* 113.2, pp. 157–168.

Koeppen, William C. and Victoria E. Hamilton (2008). "Global distribution, composition, and abundance of olivine on the surface of Mars from thermal infrared data". en. In: *Journal of Geophysical Research: Planets* 113.E5.

Krasnopolsky, Vladimir A., Jean Pierre Maillard, and Tobias C. Owen (2004). "Detection of methane in the martian atmosphere: evidence for life?" en. In: *Icarus* 172.2, pp. 537–547.

Krissansen-Totton, J., S. Olson, and D.C. Catling (2018). "Disequilibrium biosignatures over Earth history and implications for detecting exoplanet life". en. In: *Science advances* 4, p. 5747.

Kroner, U. and Rolf L. Romer (2013). "Two plates—many subduction zones: the Variscan orogeny reconsidered". en. In: *Gondwana Research* 24.1, pp. 298–329.

Kröner, Alfred, Jérémie Lehmann, Karel Schulmann, Antoine Demoux, Ondrej Lexa, Dondov Tomurhuu, Pavla Štípská, Dunyi Liu, and Michael T.D. Wingate (2010). "Lithostratigraphic and geochronological constraints on the evolution of the Central Asian Orogenic Belt in SW Mongolia: Early Paleozoic rifting followed by late Paleozoic accretion". en. In: *American Journal of Science* 310.7, pp. 523–574.

Kuehl, Steven A, Mead A Allison, Steven L Goodbred, and HERMANN Kudrass (2005). "The ganges-brahmaputra delta". In.

Kump, Lee R, MA Arthur, ME Patzkowsky, MT Gibbs, DS Pinkus, and PM Sheehan (1999). "A weathering hypothesis for glaciation at high atmospheric pCO2 during the Late Ordovician". In: *Palaeogeography, Palaeoclimatology, Palaeoecology* 152.1-2, pp. 173–187.

Kump, Lee R and Michael A Arthur (1999). "Interpreting carbon-isotope excursions: carbonates and organic matter". In: *Chemical Geology* 161.1-3, pp. 181–198.

Kumpan, Tomáš, Ondřej Bábek, Jiří Kalvoda, Tomáš Matys Grygar, and Jiří Frýda (2014). "Sea-level and environmental changes around the Devonian–Carboniferous boundary in the Namur–Dinant Basin (S Belgium, NE France): a multi-proxy stratigraphic analysis of carbonate ramp archives and its use in regional and interregional correlations". en. In: *Sedimentary Geology* 311, pp. 43–59.

Laakso, Thomas A and Daniel P Schrag (2014). "Regulation of atmospheric oxygen during the Proterozoic". In: *Earth and Planetary Science Letters* 388, pp. 81–91.

Lakin, Jon Andrew (2016). "Glaciation and extinction at the Devonian-Carboniferous boundary; high palaeolatitude record of the Bolivian Altiplano". en. PhD diss., University of Southampton.

Lalonde, Karine, Alfonso Mucci, Alexandre Ouellet, and Yves Gélinas (2012). "Preservation of organic matter in sediments promoted by iron". In: *Nature* 483.7388, pp. 198–200.

Lamb, Melissa A. and Gombosuren Badarch (1997). "Paleozoic sedimentary basins and volcanic-arc systems of Southern Mongolia: new stratigraphic and sedimentologic constraints". en. In: *International Geology Review* 39.6, pp. 542–576.

LaPorte, D.F., C. Holmden, W.P. Patterson, J.D. Loxton, M.J. Melchin, C.E. Mitchell, S.C. Finney, and H.D. Sheets (2009a). "Local and global perspectives on carbon and nitrogen cycling during the Hirnantian glaciation". en. In: *Palaeogeography, Palaeoclimatology, Palaeoecology* 276.1-4, pp. 182–195.

— (2009b). "Local and global perspectives on carbon and nitrogen cycling during the Hirnantian glaciation". In: *Palaeogeography, Palaeoclimatology, Palaeoecology* 276.1-4, pp. 182–195.

Larmagnat, Stephanie and Fritz Neuweiler (2015). "Taphonomic filtering in Ordovician bryozoan carbonate mounds, Trenton group, Montmorency falls, Quebec, Canada". en. In: *Palaios* 30.3, pp. 169–180.

Lasaga, Antonio C (1984). "Chemical kinetics of water-rock interactions". In: *Journal of geophysical research: solid earth* 89.B6, pp. 4009–4025.

Leech, Mary L. and Daniel F. Stockli (2000). "The late exhumation history of the ultrahigh-pressure Maksyutov Complex, south Ural Mountains, from new apatite fission track data". en. In: *Tectonics* 19.1, pp. 153–167.

Lefevre, Franck and François Forget (2009). "Observed variations of methane on Mars unexplained by known atmospheric chemistry and physics". en. In: *Nature* 460.7256, pp. 720–723.

Leong, James Andrew M, Tucker Ely, and Everett L Shock (2021). "Decreasing extents of Archean serpentinization contributed to the rise of an oxidized atmosphere". In: *Nature communications* 12.1, p. 7341.

Li, Gaojun and Henry Elderfield (2013). "Evolution of carbon cycle over the past 100 million years". en. In: *Geochimica et Cosmochimica Acta* 103, pp. 11–25.

Li, Yanfang, Tongwei Zhang, Geoffrey S Ellis, and Deyong Shao (2017). "Depositional environment and organic matter accumulation of Upper Ordovician–Lower Silurian marine shale in the Upper Yangtze Platform, South China". In: *Palaeogeography, Palaeoclimatology, Palaeoecology* 466, pp. 252–264.

Li, Youlian, Chaofeng Li, Zhuyin Chu, and Jinghui Guo (2021). "Evaluation and optimisation of the dissolution method for bulk analysis of carbonate neodymium isotopic composition based on chemical leaching of carbonate certified reference materials". In: *Microchemical Journal* 171, p. 106880.

Lillis, R.J. et al. (2017). "Photochemical escape of oxygen from Mars: First results from MAVEN in situ data". en. In: *Journal of Geophysical Research: Space Physics* 122.3, pp. 3815–3836.

Lo, Daniel Y., Roger V. Yelle, Robert J. Lillis, and Justin I. Deighan (2021). "Carbon photochemical escape rates from the modern Mars atmosphere". en. In: *Icarus* 360, p. 114371.

Löhr, SC and MJ Kennedy (2014). "Organomineral nanocomposite carbon burial during Oceanic Anoxic Event 2". In: *Biogeosciences* 11.18, pp. 4971–4983.

Luce, Robert W., Robert W. Bartlett, and George A. Parks (1972). "Dissolution kinetics of magnesium silicates". la. In: *Geochimica et Cosmochimica Acta* 36.1, pp. 35–50.

Macdonald, Francis A, Paul M Karabinos, James L Crowley, Eben B Hodgin, Peter W Crockford, and John W Delano (2017a). "Bridging the gap between the foreland and hinterland II: Geochronology and tectonic setting of Ordovician magmatism and basin formation on the Laurentian margin of New England and Newfoundland". In: *American Journal of Science*.

Macdonald, Francis A, Nicholas L Swanson-Hysell, Yuem Park, Lorraine Lisiecki, and Oliver Jagoutz (2019). "Arc-continent collisions in the tropics set Earth's climate state". In: *Science* 364.6436, pp. 181–184.

Macdonald, Francis A., Paul M. Karabinos, James L. Crowley, Eben B. Hodgin, Peter W. Crockford, and John W. Delano (2017b). "Bridging the gap between the foreland and hinterland II: Geochronology and tectonic setting of Ordovician magmatism and basin formation on the Laurentian margin of New England and Newfoundland". en. In: *American Journal of Science* 317.5, pp. 555–596.

Mast, M.Alisa and James I. Drever (1987). "The effect of oxalate on the dissolution rates of oligoclase and tremolite". en. In: *Geochimica et Cosmochimica Acta* 51.9, pp. 2559–2568.

Mauviel, Alain and André Desrochers (2016). "A high-resolution, continuous 13C record spanning the Ordovician–Silurian boundary on Anticosti Island, eastern Canada". en. In: *Canadian Journal of Earth Sciences* 53.8, pp. 795–801.

McKenzie, N Ryan, Brian K Horton, Shannon E Loomis, Daniel F Stockli, Noah J Planavsky, and Cin-Ty A Lee (2016). "Continental arc volcanism as the principal driver of icehouse-greenhouse variability". In: *Science* 352.6284, pp. 444–447.

McLennan, SM, S Hemming, DK McDaniel, and GN Hanson (1993). "Geochemical approaches to sedimentation, provenance, and tectonics". In: *Geological Society of America, Special Papers*.

McLennan, SM, SR Taylor, Malcolm T McCulloch, and JB Maynard (1990). "Geochemical and Nd Sr isotopic composition of deep-sea turbidites: crustal evolution and plate tectonic associations". In: *Geochimica et cosmochimica acta* 54.7, pp. 2015–2050.

Melchin, Michael J. and Chris Holmden (2006). "Carbon isotope chemostratigraphy in Arctic Canada: sea-level forcing of carbonate platform weathering and implications for Hirnantian global correlation". en. In: *Palaeogeography, Palaeoclimatology, Palaeoecology* 234.2-4, pp. 186–200.

Merschat, Arthur J., Robert D. Hatcher Jr, and Timothy L. Davis (2005). "The northern Inner Piedmont, southern Appalachians, USA: kinematics of transpression and SW-directed mid-crustal flow". en. In: *Journal of Structural Geology* 27.7, pp. 1252–1281.

Meunier, A. and B. Velde (1979). "Weathering mineral facies in altered granites: the importance of local small-scale equilibria". en. In: *Mineralogical Magazine* 43.326, pp. 261–268.

Middleton, Matt, J.Duncan Keppie, J.Brendan Murphy, Brent V. Miller, R.Damian Nance, Amabel Ortega-Rivera, and James K.W. Lee (2007). "PTt constraints on exhumation following subduction in the Rheic Ocean from eclogitic rocks in thevAcatlán complex of southern México". en. In: *The geology of Peri-Gondwana: The Avalonian-Cadomian belt, adjoining cratons and the Rheic Ocean: Geological Society of America, Special Paper*. Vol. 423, pp. 489–509.

Miller, Brent V., Kevin G. Stewart, and Donna L. Whitney (2010). *Three tectonothermal pulses recorded in eclogite and amphibolite of the Eastern Blue Ridge, southern Appalachians*. en.

Milliman, John D and Katherine L Farnsworth (2013). *River discharge to the coastal ocean: a global synthesis*. Cambridge University Press.

Moecher, David P., Scott D. Samson, and Calvin F. Miller (2004). "Precise time and conditions of peak Taconian granulite facies metamorphism in the southern Appalachian orogen, USA, with implications for zircon behavior during crustal melting events". en. In: *The Journal of Geology* 112.3, pp. 289–304.

Moghadam, Hadi Shafaii and Robert J. Stern (2014). "Ophiolites of Iran: Keys to understanding the tectonic evolution of SW Asia:(I) Paleozoic ophiolites". en. In: *Journal of Asian Earth Sciences* 91, pp. 19–38.

Moore, CM, MM Mills, KR Arrigo, I Berman-Frank, L Bopp, PW Boyd, ED Galbraith, RJ Geider, C Guieu, SL Jaccard, et al. (2013). "Processes and patterns of oceanic nutrient limitation". In: *Nature geoscience* 6.9, pp. 701–710.

Moran, Patrick C., Sandra M. Barr, Chris E. White, and Michael A. Hamilton (2007). "Petrology, age, and tectonic setting of the Seal Island Pluton, offshore southwestern Nova Scotia". en. In: *Canadian Journal of Earth Sciences* 44.10, pp. 1467–1478.

Murray, Joshua and Oliver Jagoutz (2023). "Palaeozoic cooling modulated by ophiolite weathering through organic carbon preservation". en. In: *Nature Geoscience* 17.1, pp. 88–93.

Mustard, J.F., F. Poulet, A. Gendrin, J.-P. Bibring, Y. Langevin, B. Gondet, N. Mangold, G. Bellucci, and F. Altieri (2005). "Olivine and pyroxene diversity in the crust of Mars". en. In: *Science* 307.5715, pp. 1594–1597.

Mustard, John F. (2019). "Sequestration of volatiles in the Martian crust through hydrated minerals: A significant planetary reservoir of water". en. In: *Volatiles in the martian crust*. Elsevier, pp. 247–263.

Myrow, Paul M., Anne Hanson, Anna S. Phelps, Jessica R. Creveling, Justin V. Strauss, David A. Fike, and Robert L. Ripperdan (2013). "Latest Devonian (Famennian) global events in western Laurentia: variations in the carbon isotopic record linked to diagenetic alteration below regionally extensive unconformities". en. In: *Palaeogeography, Palaeoclimatology, Palaeoecology* 386, pp. 194–209.

Nahon, D, F Colin, and Y Tardy (1982a). "Formation and distribution of Mg, Fe, Mn-smectites in the first stages of the lateritic weathering of forsterite and tephroite". In: *Clay Minerals* 17.3, pp. 339–348.

— (1982b). "Formation and distribution of Mg, Fe, Mn-smectites in the first stages of the lateritic weathering of forsterite and tephroite". en. In: *Clay Minerals* 17.3, pp. 339–348.

Neill, Todd, Donald Judd, Eric Veith, and Donald Rousar (2009). "Practical uses of liquid methane in rocket engine applications". en. In: *Acta Astronautica* 65.5-6, pp. 696–705.

Nesbitt, HW and RE Wilson (1992). "Recent chemical weathering of basalts". In: *American Journal of science* 292.10, pp. 740–777.

Nesbitt, HW, GM Young, SM McLennan, and RR Keays (1996). "Effects of chemical weathering and sorting on the petrogenesis of siliciclastic sediments, with implications for provenance studies". In: *The journal of geology* 104.5, pp. 525–542.

Nesbitt, HW and Grant M Young (1982). "Early Proterozoic climates and plate motions inferred from major element chemistry of lutites". In: *nature* 299.5885, pp. 715–717.

Noack, Yves and Joëlle Duplay (1983). "Talc and weathering-hydro thermal alteration boundary". en. In: *Sciences Géologiques, bulletins et mémoires 72* 1, pp. 121–130.

Obeso, Juan Carlos de and Peter B Kelemen (2020). "Major element mobility during serpentinization, oxidation and weathering of mantle peridotite at low temperatures". In: *Philosophical Transactions of the Royal Society A* 378.2165, p. 20180433.

Oliver, G.J.H., F. Chen, R. Buchwaldt, and E. Hegner (2000). "Fast tectonometamorphism and exhumation in the type area of the Barrovian and Buchan zones". en. In: *Geology* 28.5, pp. 459–462.

Oparin, A.I. (1953). *The origin of life*. la.

Owen, Tobias, Robert D Cess, and Veerabhadran Ramanathan (1979). "Enhanced CO2 greenhouse to compensate for reduced solar luminosity on early Earth". In: *Nature* 277.5698, pp. 640–642.

Oze, Christopher and Mukul Sharma (2005). "Have olivine, will gas: Serpentinization and the abiogenic production of methane on Mars". en. In: *Geophysical research letters* 32.10.

Pacini, Nic and René Gächter (1999). "Speciation of riverine particulate phosphorus during rain events". In: *Biogeochemistry* 47.1, pp. 87–109.

Palmer, Chris (2021). "SpaceX starship lands on Earth, but manned missions to Mars will require more". en. In: *Engineering* 7.10, pp. 1345–1347.

Park, Yuem, Pierre Maffre, Yves Goddéris, Francis A Macdonald, Eliel SC Anttila, and Nicholas L Swanson-Hysell (2020). "Emergence of the Southeast Asian islands as a driver for Neogene cooling". In: *Proceedings of the National Academy of Sciences* 117.41, pp. 25319–25326.

Parsons, A.J., A. Zagorevski, J.J. Ryan, W.C. McClelland, C.R. Staal, M.J. Coleman, and M.L. Golding (2019). "Petrogenesis of the Dunite Peak ophiolite, south-central Yukon, and the distinction between upper-plate and lower-plate settings: A new hypothesis for the late Paleozoic–early Mesozoic tectonic evolution of the Northern Cordillera". en. In: *Bulletin* 131.1-2, pp. 274–298.

Pedersen, R.B. and H. Furnes (1991). "Geology, magmatic affinity and geotectonic environment of some Caledonian ophiolites in Norway". en. In: *Journal of Geodynamics* 13.2-4, pp. 183–203.

Percival, LME, DPG Bond, M Rakociński, L Marynowski, AVS Hood, T Adatte, JE Spangenberg, and KB Föllmi (2020). "Phosphorus-cycle disturbances during the Late Devonian anoxic events". In: *Global and planetary change* 184, p. 103070.

Percival, LME, David Selby, DPG Bond, Michal Rakociński, Grzegorz Racki, Leszek Marynowski, Thierry Adatte, JE Spangenberg, and KB Föllmi (2019). "Pulses of enhanced continental weathering associated with multiple Late Devonian climate perturbations: Evidence from osmium-isotope compositions". In: *Palaeogeography, Palaeoclimatology, Palaeoecology* 524, pp. 240–249.

Phillips, Glen, R. Offler, Daniela Rubatto, and David Phillips (2015). "High-pressure metamorphism in the southern New England Orogen: Implications for long-lived accretionary orogenesis in eastern Australia". en. In: *Tectonics* 34.9, pp. 1979–2010.

Pion, Jean-Claude (1979). "Altération des massifs cristallins basiques en zone tropicale sèche. Etude de quelques toposéquences en Haute-Volta". fr. In: *Persée-Portail des revues scientifiques en SHS* 57.1.

Prokoph, A., G.A. Shields, and J. Veizer (2008). "Compilation and time-series analysis of a marine carbonate 18O, 13C, 87Sr/86Sr and 34S database through Earth history". en. In: *Earth-Science Reviews* 87.3-4, pp. 113–133.

Puchkov, Victor N. (2009). "The diachronous (step-wise) arc–continent collision in the Urals". en. In: *Tectonophysics* 479.1-2, pp. 175–184.

Qie, Wenkun, Jiangsi Liu, Jitao Chen, Xiangdong Wang, Horng-sheng Mii, Xionghua Zhang, Xing Huang, Le Yao, Thomas J. Algeo, and Genming Luo (2015). "Local overprints on the global carbonate 13C signal in Devonian–Carboniferous boundary successions of South China". en. In: *Palaeogeography, Palaeoclimatology, Palaeoecology* 418, pp. 290–303.

Quinn, L., S.H. Williams, David A.T. Harper, and E.N.K. Clarkson (1999). "Late Ordovician foreland basin fill: Long Point Group of onshore western Newfoundland". en. In: *Bulletin of Canadian Petroleum Geology* 47.1, pp. 63–80.

Quinn, Louise A (1988). "Distribution and significance of Ordovician flysch units in western Newfoundland". In: *Geological Survey of Canada, Paper* 88.1B, pp. 119–127.

Quinn, Louise Anne (1992). "Foreland and trench slope basin sandstones of the Goose Tickle Group and Lower Head Formation, western Newfoundland". PhD thesis. Memorial University of Newfoundland.

Rahman, Habibur M., Martin Kennedy, Stefan Löhr, and David N. Dewhurst (2017). "Clay-organic association as a control on hydrocarbon generation in shale". cy. In: *Organic Geochemistry* 105, pp. 42–55.

Rakhimov, Ildar R., Evgenii V. Pushkarev, and Irina A. Gottman (2021). "Chromite Paleoplacer in the Permian Sediments at the East Edge of the East European Platform: Composition and Potential Sources". en. In: *Minerals* 11.7, p. 691.

Ramirez, Ramses M., Ravi Kopparapu, Michael E. Zugger, Tyler D. Robinson, Richard Freedman, and James F. Kasting (2014). "Warming early Mars with CO2 and H2". en. In: *Nature Geoscience* 7.1, pp. 59–63.

Ramos, Victor A., Mónica Escayola, Diana I. Mutti, and Graciela I. Vujovich (2000). "Proterozoic-early Paleozoic ophiolites of the Andean basement". en. In: *Ophiolites and oceanic crust: new insights from field studies and the Ocean Drilling Program* 349, p. 331.

Ramstad, Robin, Stas Barabash, Yoshifumi Futaana, Hans Nilsson, and Mats Holmström (2018). "Ion escape from Mars through time: an extrapolation of atmospheric loss based on 10 years of Mars Express measurements". en. In: *Journal of Geophysical Research: Planets* 123.11, pp. 3051–3060.

Rasmussen, Carl Edward and Christopher KI Williams (2006). *Gaussian processes for machine learning*. the MIT Press, Massachusetts Institute of Technology.

Raup, David M (1994). "The role of extinction in evolution." In: *Proceedings of the National Academy of Sciences* 91.15, pp. 6758–6763.

Ribeiro, A., J. Munhá, P.E. Fonseca, A. Araújo, J.C. Pedro, A. Mateus, C. Tassinari, G. Machado, and A. Jesus (2010). "Variscan ophiolite belts in the Ossa-Morena Zone (Southwest Iberia): Geological characterization and geodynamic significance". en. In: *Gondwana Research* 17.2-3, pp. 408–421.

Roberts, John, R. Offler, and M. Fanning (2006). "Carboniferous to Lower Permian stratigraphy of the southern Tamworth Belt, southern New England Orogen, Australia: boundary sequences of the Werrie and Rouchel blocks". en. In: *Australian Journal of Earth Sciences* 53.2, pp. 249–284.

Robertson, Ian D.M. and Richard A. Eggleton (1991). "Weathering of granitic muscovite to kaolinite and halloysite and of plagioclase-derived kaolinite to halloysite". en. In: *Clays and Clay Minerals* 39.2, pp. 113–126.

Rosenthal, Y, AE Holbourn, DK Kulhanek, IW Aiello, TL Babila, G Bayon, L Beaufort, SC Bova, JH Chun, H Dang, et al. (2018). "International Ocean Discovery Program, Western Pacific Warm Pool". In: *Proceedings of the International Ocean Discovery Program, 363*. URL: http://publications.iodp.org/proceedings/363/363.PDF.

Rudnick, R.L., S. Gao, H.D. Holland, and K.K. Turekian (2003). "Composition of the continental crust". en. In: *The crust* 3, pp. 1–64.

Rudnick, Roberta L and S Gao (2003). "Composition of the continental crust". In: *Treatise on Geochemistry* 3.

Sakai, Shotaro, Kanako Seki, Naoki Terada, Hiroyuki Shinagawa, Takashi Tanaka, and Yusuke Ebihara (2018). "Effects of a weak intrinsic magnetic field on atmospheric escape from Mars". en. In: *Geophysical Research Letters* 45.18, pp. 9336–9343.

Saltzman, M.R., E. Thomas, and F.M. Gradstein (2012). "Carbon isotope stratigraphy". en. In: *The geologic time scale* 1, pp. 207–232.

Saltzman, Matthew R. (2005). "Phosphorus, nitrogen, and the redox evolution of the Paleozoic oceans". en. In: *Geology* 33.7, pp. 573–576.

Sano, S., R. Offler, H. Hyodo, and T. Watanabe (2004). "Geochemistry and chronology of tectonic blocks in serpentinite mélange of the southern New England Fold Belt, NSW, Australia". en. In: *Gondwana Research* 7.3, pp. 817–831.

Savage, Norman M., Apsorn Sardsud, and Werner Buggisch (2006). "Late Devonian conodonts and the global frasnian-famennian extinction event, thong pha phum, western Thailand". en. In: *Palaeoworld* 15.2, pp. 171–184.

Scheller, E.L., B.L. Ehlmann, D.J.Adams Renyu Hu, and Y.L. Yung (2021). "Long-term drying of Mars by sequestration of ocean-scale volumes of water in the crust". en. In: *Science* 372.6537, pp. 56–62.

Schrag, Daniel P, Robert A Berner, Paul F Hoffman, and Galen P Halverson (2002). "On the initiation of a snowball Earth". In: *Geochemistry, Geophysics, Geosystems* 3.6, pp. 1–21.

Secor Jr Donald T., Arthur W. Snoke and R. David Dallmeyer. (1986). "Character of the Alleghanian orogeny in the southern Appalachians: Part III. Regional tectonic relations". en. In: *Geological Society of America Bulletin* 97.11, pp. 1345–1353.

Seyfried Jr, William E. and Michael J. Mottl. (1982). "Hydrothermal alteration of basalt by seawater under seawater-dominated conditions". en. In: *Geochimica et Cosmochimica Acta* 46.6, pp. 985–1002.

Sharma, S. et al. (2023). "Diverse organic-mineral associations in Jezero crater, Mars". en. In: *Nature* 619.7971, pp. 724–732.

Shaulis, Barry J., Thomas J. Lapen, John F. Casey, and Douglas R. Reid (2012). "Timing and rates of flysch sedimentation in the Stanley Group, Ouachita Mountains, Oklahoma and Arkansas, USA: Constraints from U-Pb zircon ages of subaqueous ash-flow tuffs". en. In: *Journal of Sedimentary Research* 82.11, pp. 833–840.

Shaw, Henry F. and G.J. Wasserburg (1984). "Isotopic constraints on the origin of Appalachian mafic complexes". en. In: *American Journal of Science* 284.4-5, pp. 319–349.

Shayan, Ahmad (1984). "Hisingerite material from a basalt quarry near Geelong, Victoria, Australia". In: *Clays and Clay Minerals* 32.4, pp. 272–278.

Sheehan, Peter M (1973). "The relation of Late Ordovician glaciation to the Ordovician-Silurian changeover in North American brachiopod faunas". In: *Lethaia* 6.2, pp. 147–154.

Sheet, Julia M. and Rodney T. Tettenhorst (1997). "Crystallographic controls on the alteration of microcline perthites from the Spruce Pine District, North Carolina". en. In: *Clays and Clay Minerals* 45.3, pp. 404–417.

Shen, Yun-Hwei (2004). "Phenol sorption by organoclays having different charge characteristics". en. In: *Colloids and surfaces A: Physicochemical and engineering aspects* 232.2-3, pp. 143–149.

Sherwood, Steven C, Sandrine Bony, and Jean-Louis Dufresne (2014). "Spread in model climate sensitivity traced to atmospheric convective mixing". In: *Nature* 505.7481, pp. 37–42.

Siegel, D.I. and H.O. Pfannkuch (1984). "Silicate mineral dissolution at pH 4 and near standard temperature and pressure". en. In: *Geochimica et Cosmochimica Acta* 48.1, pp. 197–201.

Singh, Balbir and R.J. Gilkes (1991). "Weathering of a chromian muscovite to kaolinite". en. In: *Clays and Clay Minerals* 39.6, pp. 571–579.

Skrzypek, E., A.-S. Tabaud, J.-B. Edel, Karel Schulmann, Alain Cocherie, Catherine Guerrot, and Philippe Rossi (2012). "The significance of Late Devonian ophiolites in the Variscan orogen: a record from the Vosges Klippen Belt". en. In: *International Journal of Earth Sciences* 101.4, pp. 951–972.

Slagstad, Trond, Christian Pin, David Roberts, Christopher L. Kirkland, Tor Grenne, Greg Dunning, Simone Sauer, and Tom Andersen (2014). "Tectonomagmatic evolution of the Early Ordovician suprasubduction-zone ophiolites of the Trondheim Region, Mid-Norwegian Caledonides". en. In: *Geological Society, London, Special Publications* 390.1, pp. 541–561.

Soulet, Guillaume, Robert G Hilton, Mark H Garnett, Tobias Roylands, Sébastien Klotz, Thomas Croissant, Mathieu Dellinger, and Caroline Le Bouteiller (2021). "Temperature control on CO2 emissions from the weathering of sedimentary rocks". In: *Nature Geoscience* 14.9, pp. 665–671.

Staal, Cees R van, Sandra M Barr, JA Percival, FA Cook, and RM Clowes (2012). "Lithospheric architecture and tectonic evolution of the Canadian Appalachians and associated Atlantic margin". In: *Tectonic styles in Canada: The LITHOPROBE perspective: Geological Association of Canada Special Paper* 49, pp. 41–95.

Staal, Cees R van, Alexandre Zagorevski, William C McClelland, Monica P Escayola, James J Ryan, Andrew J Parsons, and Joaquin Proenza (2018). "Age and setting of Permian Slide Mountain terrane ophiolitic ultramafic-mafic complexes in the Yukon: Implications for late Paleozoic-early Mesozoic tectonic models in the northern Canadian Cordillera". In: *Tectonophysics* 744, pp. 458–483.

Stanley, Steven M (2016). "Estimates of the magnitudes of major marine mass extinctions in earth history". In: *Proceedings of the National Academy of Sciences* 113.42, E6325–E6334.

Steele, A. et al. (2018). "Organic synthesis on Mars by electrochemical reduction of CO2". en. In: *Science Advances* 4.10, p. 5118.

Stepanauskas, Ramûnas, Niels OG JØrgensen, Ole R Eigaard, Audrius Žvikas, Lars J Tranvik, and Lars Leonardson (2002). "Summer inputs of riverine nutrients to the Baltic Sea: bioavailability and eutrophication relevance". In: *Ecological monographs* 72.4, pp. 579–597.

Stern, Jennifer C, Charles A Malespin, Jennifer L Eigenbrode, Christopher R Webster, Greg Flesch, Heather B Franz, Heather V Graham, Christopher H House, Brad Sutter, Paul Douglas Archer Jr, et al. (2022). "Organic carbon concentrations in 3.5-billion-year-old lacustrine mudstones of Mars". In: *Proceedings of the National Academy of Sciences* 119.27, e2201139119.

Stevens, Robert K (1970). "Cambro-Ordovician flysch sedimentation and tectonics in west Newfoundland and their bearing on a Proto-Atlantic Ocean". In: *Geological Association of Canada, Special Paper* 7, pp. 165–176.

Stolfus, Brittany M, Bradley D Cramer, Ryan J Clark, Nicholas J Hogancamp, James E Day, Stephanie A Tassier-Surine, and Brian J Witzke (2020a). "An expanded stratigraphic record of the Devonian-Carboniferous boundary Hangenberg biogeochemical Event from Southeast Iowa (USA)". In: *Bulletin of Geosciences*.

Stolfus, Brittany M., Bradley D. Cramer, Ryan J. Clark, Nicholas J. Hogancamp, James E. Day, S.T.E.P.H.A.N.I.E.A. IER-SURINE, and Brian J. Witzke (2020b). "An expanded stratigraphic record of the Devonian-Carboniferous boundary Hangenberg biogeochemical Event from Southeast Iowa (USA". en. In: *Bulletin of Geosciences* 95.4.

Stone, Shane W., Roger V. Yelle, Mehdi Benna, Daniel Y. Lo, Meredith K. Elrod, and Paul R. Mahaffy (2020). "Hydrogen escape from Mars is driven by seasonal and dust storm transport of water". en. In: *Science* 370.6518, pp. 824–831.

Stouge, Svend (2012). "Middle Ordovician (late Dapingian–Darriwilian) conodonts from the Cow Head Group and Lower Head Formation, western Newfoundland, Canada". In: *Canadian Journal of Earth Sciences* 49.1, pp. 59–90.

Sturman, Tom (2012). "Organic matter preservation in clays from the basal 'Hot Shale'of the Arthur Creek Formation within the Georgina Basin, Australia". en. In: *PhD diss.*

Su, Wen, Jun Gao, Reiner Klemd, Ji-Lei Li, Xi Zhang, Xian-Hua Li, Neng-Song Chen, and Lu Zhang (2010). "U–Pb zircon geochronology of Tianshan eclogites in NW China: implication for the collision between the Yili and Tarim blocks of the southwestern Altaids". en. In: *European Journal of Mineralogy* 22.4, pp. 473–478.

Sun, Vivian Z. and Ralph E. Milliken (2015). "Ancient and recent clay formation on Mars as revealed from a global survey of hydrous minerals in crater central peaks". en. In: *Journal of Geophysical Research: Planets* 120.12, pp. 2293–2332.

Sun, Xiaole, John Higgins, and Alexandra V Turchyn (2016). "Diffusive cation fluxes in deep-sea sediments and insight into the global geochemical cycles of calcium, magnesium, sodium and potassium". In: *Marine Geology* 373, pp. 64–77.

Swanson-Hysell, Nicholas L and Francis A Macdonald (2017). "Tropical weathering of the Taconic orogeny as a driver for Ordovician cooling". In: *Geology* 45.8, pp. 719–722.

Swezey, Christopher (2002). *Regional stratigraphy and petroleum systems of the Appalachian Basin, North America*. en.

Syvitski, James PM, Charles J Vörösmarty, Albert J Kettner, and Pamela Green (2005). "Impact of humans on the flux of terrestrial sediment to the global coastal ocean". In: *science* 308.5720, pp. 376–380.

Tice, M.M. et al. (Mar. 2024). "Regional Paleoenvironments Recorded in Sedimentary Rocks of the Western Fan-Delta, Jezero Crater, Mars". en. In: *55th Lunar and Planetary Science Conference*.

Torres, Mark A, A Joshua West, and Gaojun Li (2014). "Sulphide oxidation and carbonate dissolution as a source of CO2 over geological timescales". In: *nature* 507.7492, pp. 346–349.

Tremblay, Alain, Gilles Ruffet, and Jean H. Bédard (2011). "Obduction of Tethyan-type ophiolites—A case-study from the Thetford-Mines ophiolitic Complex, Quebec Appalachians, Canada". en. In: *Lithos* 125.1-2, pp. 10–26.

Trupe, Charles H., Kevin G. Stewart, Mark G. Adams, Cheryl L. Waters, Brent V. Miller, and Lauren K. Hewitt (2003). "The Burnsville fault: Evidence for the timing and kinematics of southern Appalachian Acadian dextral transform tectonics". en. In: *Geological Society of America Bulletin* 115.11, pp. 1365–1376.

Tutolo, Benjamin M. and Nicholas J. Tosca (2023). "Observational constraints on the process and products of Martian serpentinization". en. In: *Science Advances* 9.5, p. 8472.

Valley, Peter M., Gregory J. Walsh, Arthur J. Merschat, and Ryan J. McAleer (2020). "Geochronology of the Oliverian Plutonic Suite and the Ammonoosuc Volcanics in the Bronson Hill arc: western New Hampshire, USA". en. In: *Geosphere* 16.1, pp. 229–257.

Veizer, Jan, Davin Ala, Karem Azmy, Peter Bruckschen, Dieter Buhl, Frank Bruhn, and Giles A.F. Carden (1999). "87Sr/86Sr, 13C and 18O evolution of Phanerozoic seawater". en. In: *Chemical geology* 161.1-3, pp. 59–88.

Velbel, Michael Anthony (1993). "Constancy of silicate-mineral weathering-rate ratios between natural and experimental weathering: implications for hydrologic control of differences in absolute rates". In: *Chemical Geology* 105.1-3, pp. 89–99.

Velde, Bruce B and Alain Meunier (2008). *The origin of clay minerals in soils and weathered rocks*. Springer Science & Business Media.

Viers, Jérôme, Bernard Dupré, and Jérôme Gaillardet (2009). "Chemical composition of suspended sediments in World Rivers: New insights from a new database". In: *Science of The Total Environment* 407.2, pp. 853–868. ISSN: 0048-9697. DOI: https://doi.org/10.1016/j.scitotenv.2008.09.053. URL: https://www.sciencedirect.com/science/article/pii/S0048969708010103.

Villalobos, Mario, Maya A. Trotz, and James O. Leckie (2003). "Variability in goethite surface site density: evidence from proton and carbonate sorption". en. In: *Journal of Colloid and Interface Science* 268.2, pp. 273–287.

Waldron, John W.F., Scott D. Anderson, Peter A. Cawood, Laurel B. Goodwin, Jeremy Hall, Rebecca A. Jamieson, Sarah E. Palmer, Glen S. Stockmal, and Paul F. Williams (1998). "Evolution of the Appalachian Laurentian margin: Lithoprobe results in western Newfoundland". en. In: *Canadian Journal of Earth Sciences* 35.11, pp. 1271–1287.

Wang, Bo, Michel Faure, Dominique Cluzel, Liangshu Shu, Jacques Charvet, Sebastien Meffre, and Qian Ma (2006). "Late Paleozoic tectonic evolution of the northern West Chinese Tianshan belt". en. In: *Geodinamica Acta* 19.3-4, pp. 237–247.

Wang, Bo, Michel Faure, Liangshu Shu, Koen Jong, Jacques Charvet, Dominique Cluzel, Bor-ming Jahn, Yan Chen, and Gilles Ruffet (2010). "Structural and geochronological study of high-pressure metamorphic rocks in the Kekesu section (northwestern China): Implications for the late Paleozoic tectonics of the Southern Tianshan". en. In: *The Journal of Geology* 118.1, pp. 59–77.

Wang, Bo, Liangshu Shu, Michel Faure, Bor-ming Jahn, Dominique Cluzel, Jacques Charvet, Sun-lin Chung, and Sébastien Meffre (2011). "Paleozoic tectonics of the southern Chinese Tianshan: insights from structural, chronological and geochemical studies of the Heiyingshan ophiolitic mélange (NW China". en. In: *Tectonophysics* 497.1-4, pp. 85–104.

Wang, Fred P. and Julia F.W. Gale (2009). *Screening criteria for shale-gas systems*. en.

Webster, C.R. et al. (2013). "Isotope ratios of H, C, and O in CO2 and H2O of the Martian atmosphere". en. In: *Science* 341.6143, pp. 260–263.

Wernicke, Liza J. and Bruce M. Jakosky (2021). "Martian hydrated minerals: A significant water sink". en. In: *Journal of Geophysical Research: Planets* 126.3, p. 2019 006351.

West, A Joshua, Albert Galy, and Mike Bickle (2005). "Tectonic and climatic controls on silicate weathering". In: *Earth and Planetary Science Letters* 235.1-2, pp. 211–228.

White, Shawna E, John WF Waldron, Greg R Dunning, and S Andrew Dufrane (2019). "Provenance of the Newfoundland Appalachian foreland basins". In: *American Journal of Science* 319.8, pp. 694–735.

White, Shawna E, John WF Waldron, and Nicholas B Harris (2020). "Anticosti foreland basin offshore of western Newfoundland: Concealed record of northern Appalachian orogen development". In: *Basin Research* 32.1, pp. 25–50.

Wieczorek, M.A. et al. (2022). "InSight constraints on the global character of the Martian crust". en. In: *Journal of Geophysical Research: Planets* 127.5, p. 2022 007298.

Williams, Lynda B., Brandon Canfield, Kenneth M. Voglesonger, and John R. Holloway (2005). "Organic molecules formed in a "primordial womb"". en. In: *Geology* 33.11, pp. 913–916.

Willner, A.P., T. Ermolaeva, U. Kramm, Y.N. Gorozhanina, V.N. Puchkov, M. Arzhavitina, V.N. Pazukhin, and R. Walter (2002). "Surface signals of an arc-continent collision: the detritus of the Upper Devonian Zilair Formation in the Southern Urals, Russia". en. In: *Geophysical Monograph Series* 132, pp. 183–209.

Wilson, M.J. (2004). "Weathering of the primary rock-forming minerals: processes, products and rates". en. In: *Clay Minerals* 39.3, pp. 233–266.

Won, Mun-Zu and William J Iams (2002). "Late Cambrian radiolarian faunas and biostratigraphy of the Cow Head Group, western Newfoundland". In: *Journal of Paleontology* 76.1, pp. 1–33.

Wong, Ah-San, Sushil K. Atreya, and Thérèse Encrenaz (2003). "Chemical markers of possible hot spots on Mars". en. In: *Journal of Geophysical Research: Planets* 108.E4.

Workman, Rhea K and Stanley R Hart (2005). "Major and trace element composition of the depleted MORB mantle (DMM)". In: *Earth and Planetary Science Letters* 231.1-2, pp. 53–72.

Wrafter, John P. and John R. Graham (1989). "Short Paper: Ophiolitic detritus in the Ordovician sediments of South Mayo, Ireland". en. In: *Journal of the Geological Society* 146.2, pp. 213–215.

Wright, I., M.M. Grady, and C. Pillinger (1992). "Chassigny and the nakhlites: Carbon-bearing components and their relationship to martian environmental conditions". en. In: *Geochimica et Cosmochim- ica Acta* 56, pp. 817–826.

Yong, Raymond N., Masashi Nakano, and Roland Pusch (2012). *Environmental soil properties and behaviour*. id. CRC Press.

Yoshinobu, Aaron S., Calvin G. Barnes, Øystein Nordgulen, Tore Prestvik, Mark Fanning, and R.B. Pedersen (2002). "Ordovician magmatism, deformation, and exhumation in the Caledonides of central Norway: An orphan of the Taconic orogeny?" en. In: *Geology* 30.10, pp. 883–886.

Young, R (2012). *Soil properties and behaviour*. Vol. 5. Elsevier.

Young, Seth A., Matthew R. Saltzman, William I. Ausich, André Desrochers, and Dimitri Kaljo (2010). "Did changes in atmospheric CO2 coincide with latest Ordovician glacial–interglacial cycles?" en. In: *Palaeogeography, Palaeoclimatology, Palaeoecology* 296.3-4, pp. 376–388.

Yu, Liu (2001). "Early Carboniferous radiolarian fauna from Heiyingshan South of the Tianshan Mountains and its geotectonic significance". en. In: *Acta Geologica Sinica-English Edition* 75.1, pp. 101–108.

Yu, Liu and Hao Shougang (2006). "Evolutionary significance of pylentonemid radiolarians and their Late Devonian species from southwestern Tianshan, China". en. In: *Acta Geologica Sinica-English Edition* 80.5, pp. 647–655.

Yuan, Chao, Min Sun, Simon Wilde, Wenjiao Xiao, Yigang Xu, Xiaoping Long, and Guochun Zhao (2010). "Post-collisional plutons in the Balikun area, East Chinese Tianshan: evolving magmatism in response to extension and slab break-off". en. In: *Lithos* 119.3-4, pp. 269–288.

Zachos, James, Mark Pagani, Lisa Sloan, Ellen Thomas, and Katharina Billups (2001). "Trends, rhythms, and aberrations in global climate 65 Ma to present". en. In: *Science* 292.5517, pp. 686–693.

Zhu, Xiaojun, Jingong Cai, Guoli Wang, and Junfeng Ji (2020). "The influence of organic matter on mineral surface area measurement of mudrocks by ethylene glycol monoethyl ether adsorption". en. In: *Applied Clay Science* 193, p. 105666.

Zuber, M.T. (2001). "The crust and mantle of Mars". en. In: *Nature* 412, pp. 220–227.